DISSERTATION

SYSTEMS ENGINEERING EVALUATION OF GPM DUAL-FREQUENCY RETRIEVAL ALGORITHMS

Submitted by

Chris R. Rose

Department of Electrical and Computer Engineering

In partial fulfillment of the requirements

for the Degree of Doctor of Philosophy

Colorado State University

Fort Collins, Colorado

Fall 2005

COLORADO STATE UNIVERSITY

August 29, 2005

WE HEREBY RECOMMEND THAT THE DISSERTATION PREPARED UNDER OUR SUPERVISION BY CHRIS R. ROSE ENTITLED SYSTEMS ENGINEERING OF GPM DUAL-FREQUENCY RETRIEVAL ALGORITHMS BE ACCEPTED AS FULFILLING IN PART REQUIREMENTS FOR THE DEGREE OF DOCTOR OF PHILOSOPHY.

Committee on Graduate Work

Advisor

Department Head/Director

ABSTRACT OF DISSERTATION

SYSTEMS ENGINEERING EVALUATION OF GPM DUAL-FREQUENCY RETRIEVAL ALGORITHMS

Following the success of the Tropical Rainfall Measuring Mission (TRMM), considerable effort has been directed at the next generation of space-based precipitation radar (PR) to be launched aboard the Global Precipitation Measuring (GPM) core satellite. While the TRMM PR uses a single-frequency radar at Ku-band (13.8 GHz) to measure and map tropical precipitation, the GPM PR will employ a dual-frequency precipitation radar (DPR) at Ku and Ka-bands (13.6 and 35.6 GHz) to more accurately measure global precipitation. Systems engineering tools are used in this work to help with model and algorithm analysis.

One of the retrieval algorithms being studied for use with GPM is a self-consistent, iterative, dual-frequency method that estimates drop-size-distribution (DSD) parameters, median volume diameter D_o, normalized intercept parameter N_w, in each radar resolution cell or bin. From the DSD values, the rain rate in each bin is calculated. The algorithm was recast in terms of a single-loop control-system model and discovered that the single-loop method accurately retrieves the DSD values in relatively low rain-rate regions where the DSD pairs are small. When the DSD pairs are larger, the algorithm can converge properly but yield incorrect solutions.

In this research, two alternative methods for DSD retrieval in those regions of incorrect convergence are presented and analyzed. The first method is a dual-loop control-system model which implicitly adds an additional system constraint on the N_w vertical profile. The second method is based on profile optimization and adds constraints on both the D_o and N_w profiles and uses a non-linear optimization technique to find suitable top and bottom-bin DSD values to best fit the input reflectivity profiles. The performance of these methods is discussed in detail.

It is important to know how the error in the input variables (factors) influence the output of the retrieval algorithms, and consequently which input factors are most important. Variance

decomposition, a systems engineering tool based on global sensitivity analysis techniques, is used to apportion error in the output of a model to the respective input factors and allow a quantitative determination of the importance of each factor.

Global sensitivity analysis performed on a TRMM-like algorithm, modelled for rainfall over both ocean and land, based on $k = \alpha Z^{\beta}$ and $R = a Z^{b}$ relationships, showed that at low rain rates, the error from a, b, and measured reflectivity Z_m dominate. At higher rain rates, the error from the surface reference technique dominates. Sensitivity analysis performed on the GPM profile-optimization algorithm for simulated near-vertical rainfall profiles show that the primary cause of model error is variability in the Ka-band radar signal with little variance contribution from the Ku-band signal.

Chris Randall Rose
Electrical and Computer Engineering Department
Colorado State University
Fort Collins, Colorado 80523
Fall 2005

ACKNOWLEDGEMENTS

First of all, I would like to thank God for everything. I also would like to thank everyone who helped me during this project. I am grateful to my advisor Dr. V. Chandrasekar for his kindness, support, guidance and encouragement during my graduate study. Also, I would like to express my gratitude to Dr. V. N. Bringi, Dr. R. Reinovsky and Dr. Y. K. Malaiya for serving as my committee members, for their support and guidance.

In particular, I wish to express my thanks to J. Repa, Dr. E. Heighway and Dr. R. Reinovsky from Los Alamos National Laboratory, for without their support, this work wouldn't have happened. I would also like to thank my sponsors in DX division and Los Alamos National Laboratory for their financial support and for being my sponsor during my study in Colorado.

During my research effort, I received much invaluable help from the crew at the Radar and Communication Group. Here, I would like to express my sincere thanks to N. Bharadwaj, Dr. D. Moisseev, Dr. W. Li, Dr. B. Zafar and Sang Lim for their friendship and for their help during this project. In particular, I wish to express my thanks to Dr. Tor A. Oigard whose inspiration and enthusiasm helped me to embrace and view statistics with new vigor.

Also, I would like to thank my parents, brother and sisters for their love and support while I was far away from home. Finally, and most important, I wish to thank my wife, Karen, my daughter Emily and son Christopher for their love, support and encouragement while I was working on this research and for their support and understanding during this work and for tolerating the many hours I was away from them.

The research was supported by the NASA Precipitation Measurement Program.

TABLE OF CONTENTS

LIST OF FIGURES

LIST OF TABLES

CHAPTER 1

INTRODUCTION

1.1 INTRODUCTION

It is becoming increasingly important to monitor the Earth's ecosystems in general, and more specifically to be able to measure and monitor the global water and energy cycle. Significant amounts of energy are transferred and move around the world through weather systems in the form of clouds and precipitation. For example, because water has a relatively large heat capacity, energy over the oceans is transferred into water vapor which rises, forms clouds, and by air movement is transferred to other parts of the world such as the continents. As the water vapor condenses and rain falls, energy is transferred. Additionally, it is important to monitor the amount and timeliness of rainfall and other precipitation such as snow that falls on various parts of the world to better understand the water cycle and ecosystems at a global scale.

One means of helping to meet the high-level science goals of monitoring global precipitation is the Tropical Rainfall Measuring Mission (TRMM) satellite that was launched in 1997. It was the first, space borne satellite to incorporate a downward looking radar to measure precipitation. With this satellite, scientists have been able to sample and measure both temporally and spatially, three-dimensional precipitation structures in the tropical latitudes. Information from TRMM has significantly increased our understanding of global precipitation and the movement of water around the globe.

Following on the success of TRMM, a new satellite cluster is being designed and readied for launch around 2009, the core satellite of which will incorporate the next generation precipitation radar, one that uses dual frequencies (DPR) that will have added capability in the

measurement of precipitation both in the form of rain and snow. This new mission is called Global Precipitation Measurement (GPM) and has as its main science objectives improved climate prediction, improved weather predictions, and improved global water cycle and hydrological predictions. The central element in the success of this mission is the core satellite that carries the new DPR operating at Ku- and Ka-bands. In addition to the core satellite, up to 10 constellation satellites will be networked together to passively monitor precipitation structures.

GPM is an international mission, and as such, it relies heavily upon sound systems engineering principles and procedures. The Japanese Aerospace Exploration Agency (JAXA) is the primary partner with the United States National Aeronautics and Space Administration (NASA). JAXA was formerly the National Space Development Agency of Japan (NASDA). Specific technology deliverables are split between NASA and JAXA with NASA supplying the satellite vehicle, some of the instruments and ground control. JAXA will supply the DPR. Both NASA and JAXA will jointly develop and implement the algorithms necessary to convert radar measurables into meaningful precipitation information. From a systems engineering perspective, the highest level is the science objectives followed by lower-level subsystems that are specified and implemented to meet the overall goals. Many organizations have standard procedures for implementing sound systems engineering procedures and NASA is no exception. It clear defines the role of the lower-level subsystems, how they help meet the overall goals, and how each subsystem must define its own specifications and requirements for any subsystems below it. Multiple links and feedback paths exist between subsystems to allow for scientific and technological innovation and monitoring of compliance with design specifications. For a given science objective, it is possible that iterations may be required in subsystems because of technological or budgetary limitations. With information fed back to the higher system levels, the objectives can be reviewed and perhaps adjusted to more fully utilize existing technology and methods. Nevertheless, it is common in large programs for technologists and scientists to

develop innovative solutions to problems and meet the overall objectives. There is constantly a trade-off between existing technology, what technology needs to be developed, innovation, and budgetary constraints.

1.2 LITERATURE REVIEW

The concepts of systems engineering, GPM, its algorithms, and means to measure the effectiveness of the algorithms and systems as a whole are presented in this section.

1.2.1 Systems Engineering

In general terms, systems engineering refers to the engineering and implementation of complex systems (these can be hardware or software of any combination) to provide an optimal solution or result given constraints in time, budget, technology, or any combination of the three. A considerable amount has been written on the concept of systems engineering and numerous texts exist. Some reference texts are [1] [2]. Some organizations develop their own methods. In fact, NASA has implemented its own internal document "Systems Engineering Management Plan" which defines the role and interactions between the science objectives and lower-level subsystems. It specifies the methodology used in defining subsystems to meet overall science objectives and how both requirements and constraints and pushed and pulled between subsystems. A fundamental assumption in systems engineering is that a flow exists between requirements and specifications and available technology to implement those requirements and specifications. It is normal to iterate on specifications and methods.

1.2.2 GPM

GPM, in the broadest sense, is the overall mission which is comprised of several subsystems including but not limited to the core satellite, dual-frequency precipitation radar (DPR), the algorithms necessary to convert radar measurements into meaningful precipitation information, ground-based validation and verification systems used to monitor the performance

of the spacecraft and algorithms, and data processing and control functions.

Given the fact that GPM is an international venture, many resources from both NASA and JAXA have written about the overall requirements, the satellite, the DPR, the algorithms, and the ground validation systems. References are cited in the body of the text.

1.2.3 Algorithms

Teams led by JAXA and NASA were the primary developers of the rain-rate estimation algorithms used for TRMM. The developers of the dual-frequency algorithms are from both NASA and JAXA. They again, are the primary scientists working on algorithms for the GPM that utilize its dual-frequency capabilities while building on the experience and expertise gained with the TRMM precipitation radar (PR). The NASA and JAXA teams have published numerous articles regarding dual-wavelength algorithms and how they might be applied to GPM. Some are based on the surface-reference-technique (SRT) as used in TRMM, and others are based on a self-consistent method that does not require the use of the SRT but can estimate the SRT value through iterations. All of these algorithms are based on microphysical properties and assumptions of precipitation whether they be snow, melting snow or rain and which regions in the atmosphere, based both on height and radar scattering measurements, are deemed snow, melting, and rain. Exact references are given in the main text.

1.2.4 Systems Engineering Analysis

As with any system or procedure, it is essential to understand how well it works as well as its limitations and strengths. One method of analyzing a system is by modelling its response and performing uncertainty and global sensitivity analysis. Uncertainty analysis describes the statistical mean and variance of a system as a function of uncertain input parameters. Global sensitivity analysis, which has its roots in classical feedback controls systems, on the other hand is able to apportion the variance in the output response back to the input variables allowing the systems designers to ascertain how much each input factor contributes to the uncertainty or

error in the output. With this information, they are able to concentrate or focus resources on those input factors that have the greatest influence on error in the output response and decrease the variables' error through more research in that area or through better information as to the actual response of the variable. In a way, with sensitivity analysis, the systems designers can perform a marginal cost to marginal benefit test and improve the overall system response.

The primary global sensitivity analysis technique used in this research is variance decomposition, a means to decompose the variance of the model response to the inputs. Numerous authors have written about global sensitivity analysis which are cited in this work. One in particular based his work on simple Monte Carlo integrations to find the variance of the conditional expectation, or Correlation Ratio as he called it. Another described a method that computes simpler integrals while decomposing the variance which allows for so-called first-order interactions and computation of higher or total-interaction terms.

After developing a thorough understanding of both the TRMM and GPM (proposed) algorithms, sensitivity analysis is performed on these algorithms with the intent of providing meaningful feedback to the systems designers as to which input factors are most important, what system parameters might be improved, and which factors are of little consequence.

1.3 PROBLEM STATEMENT

The primary observation of a space borne radar is the vertical profile of backscattering media. Based on the analysis presented in the background and in the relevant work sections of this proposal, this research attempts to address the unique and specific problems that exist in the field of space borne radar observations. In particular, this proposal focuses on the GPM satellite and its expected dual-frequency retrieval algorithms. The difficulty in modelling the microphysics of precipitation and assumptions about the system contribute to difficulty in modelling the system aspects of GPM. This effort is viewed as taking the first step in defining such an outline as more extensive experimentation and verification in many regions will be

needed to fully validate the GPM and its algorithms. A formal statement of the problem being addressed in this proposal is presented in the next section.

1.4 RESEARCH QUESTION

The goal of this research is to implement systems engineering principles in the study and analysis of the precipitation retrieval algorithms of GPM and be able to offer both qualitative and quantitative conclusions as to the applicability and feasibility of the retrieval algorithms being proposed for GPM.

1.5 OBJECTIVES OF THE RESEARCH

The following items summarize the objects of the research in this proposal. This section groups the tasks according to their major goals:

- Incorporate Systems Engineering Principles into the research
    - Examine how systems engineering is commonly performed on large, complex systems
    - Incorporate systems engineering principles in this research
    - Provide feedback to algorithms
- Study GPM and its subsystems, overall mission goals, and proposed implementation
    - Examine how the DPR is designed to work
    - Model the hardware and simulate the performance
    - Explain how the GPM system can meet the overall science objectives
- Algorithms
    - Examine the TRMM algorithm in detail
    - Examine proposed algorithms for GPM, dual-freq.-based
    - Determine performance of GPM algorithms

- Develop models for the GPM algorithm and determine its performance and limitations

- Systems Engineering Analysis (SEA) of Algorithm
  - Examine the current algorithm used in TRMM PR
  - Define the input factor variances
  - Model the TRMM algorithm
  - Determine the variance decomposition and factors' contribution to variance
  - Model the dual-frequency GPM algorithm
  - Define the input factor variances
  - Determine the variance decomposition
  - Provide feedback as to system response given expected input factors

1.6 OVERVIEW OF THE DISSERTATION

This dissertation is organized as follows:

Chapter 2 - GPM Overview

This chapter provides the overview of the Global Precipitation Measurement (GPM) spacecraft systems, the GPM radar parameters, the ground validation and systems overview.

Chapter 3 - Dual-Frequency Iterative Retrieval

This chapter describes the dual-frequency iterative retrieval algorithm to be used with the GPM dual-frequency precipitation radar (DPR). It discusses the mathematics and microphysics behind the algorithm, how it retrieves the drop-size-distribution (DSD) parameters in each bin. It incorporates the dual-frequency retrieval algorithm within a single-loop control system model and discusses the limitations of the method. It is shown that for certain DSD pairs, that the algorithm will incorrectly retrieve the DSD parameters and consequently, incorrectly estimate

the rain rate. It is shown that about half of the global rainfall will be incorrectly estimated by this algorithm. The algorithm incorrectly estimates high-valued DSD pairs because of a multi-valued solution space in which the retrieval must operate. It is shown that for these high-valued DSD pairs that the algorithm has one too few constraints.

Chapter 4 - Iterative Retrieval Method with DSD Profile Constraint

This chapter describes an alternative dual-frequency DSD retrieval method that adds a single additional constraint on Nw profile. A dual-loop control system model is described which assumes the profile of log(Nw) is linear to find DSD values in the incorrect convergence region. Several example cases are shown using both the single-loop and dual-loop retrieval methods. They are contrasted, and for those DSD pairs in the incorrect convergence region, the dual-loop method is able to retrieve the correct values and correct estimated rain rate.

Chapter 5 - Retrieval Algorithm: DSD Profile Optimization

This chapter describes an alternative dual-frequency DSD retrieval method for DSD values in the incorrect-convergence region. It adds two additional constraints on the DSD vertical profiles and assumes that the Do and log(Nw) profiles can be assumed to be linear, and optimizes them to minimize a cost function between externally supplied reflectivity and internally estimated profile values. During the process, the optimizer finds values for both the top and bottom Do and Nw values. After finding those values, it calculates linear profiles for both, then estimates rainfall rate based on the Do, Nw profiles. A random-restart method is used to provide seed values for the optimizer. It is shown that the profile optimization method does not add bias to the retrieved rain rate.

Chapter 6 - Systems Engineering Analysis: Background

This chapter describes how uncertainty (UA) and global sensitivity analyses (SA) can be applied to systems engineering problems. The necessary mathematics and methods are

explained and developed for use in sensitivity analysis. The difference between local SA and global SA is explained. Additionally, UA is described and its usefulness as part of systems engineering approach is detailed. A review of methods for performing global SA is given including the correlation ratio, the FAST method, and the method of Sobol'. UA typically only provides descriptive statistics such as the model output mean and standard deviation. This type of global SA is a part of the general variance-decomposition methods which are used to apportion the variance in a model output to each of the input factors. The importance of proper sampling techniques such as LPτ is emphasized.

Chapter 7 - Systems Engineering Analysis: TRMM-Like Algorithm

This chapter applies both UA and global SA using the method of Sobol' to an approximation of the Tropical Rainfall Measuring Mission (TRMM) rainfall retrieval algorithm. It first develops the algorithm, lists the assumptions, and describes the probability distribution functions for the input factors. The TRMM-like algorithm is fashioned into the required form for global SA. Both SA and UA are performed on the TRMM algorithm for both ocean and land where the error of the surface radar cross section can vary substantially. It is found that at low rain rates, where the algorithm reverts to the HB method, that the most important input factors are the coefficients a and b followed by the measured reflectivity. At higher rain rates, where the surface radar cross section is used in the modified-HB method, it shows that error in the surface radar cross section dominates the model output.

Chapter 8 - Systems Engineering Analysis: GPM Profile-Optimization Method

This chapter details the SA and UA analyses performed on the GPM profile-optimization algorithm. The UA/SA model requires only two inputs, the measured reflectivity at both Ku and Ka-bands. Results from the variance decomposition show that the error in Zm2 dominates the output variance throughout the simulated rain-rate region, from 1 to about 22 mm/hr. At low rain rates, input factor interactions contribute to higher-order interactions with a some of

the output variance being directly attributable to these higher-order interactions. At higher rain rates, above about 5 mm/hr, the higher-order interactions diminish and all the output variance can be described by the variance apportioned to the first-order indices of each factor.

Chapter 9 - Summary and Future Work

The results of this research are summarized and the major contributions of the dissertation are reviewed. Suggestions for future work are proposed.

CHAPTER 2

GPM OVERVIEW

2.1 INTRODUCTION

Following the success of the Tropical Rain Measuring Mission (TRMM) launched in 1997, the next generation of precipitation radar (PR) is expected to be launched aboard the Global Precipitation Measurement (GPM) core satellite around 2009. GPM's main science objectives focus on [3], [4]:

- Improving the scientific understanding of the global water cycle and fresh water availability,
- Improving the accuracy of precipitation forecasts and its impact on weather,
- Providing frequent and complete sampling of the Earth's precipitation.

At the highest level, GPM consists of a primary satellite spacecraft, a constellation of satellites, calibration/validation sites, and a global precipitation data center. Figure 2.1 shows a graphic of the GPM satellites and their coverage of the Earth. The primary satellite is called the core satellite and the others are referred to as constellation satellites. The core satellite will carry the next generation, dual-frequency precipitation radar (DPR) based on many of the successful technologies implemented with TRMM. Operational frequencies are 13.6 and 35.55 GHz. For example, the 13.6-GHz antenna/radar will be very similar to the 13.8-GHz antenna/radar currently deployed on TRMM. The constellation satellites will use similar radiometers and orbit the Earth in polar orbits.

The TRMM satellite is at an inclined Earth orbit of 35° allowing coverage up to ±35° of latitude. The GPM core satellite will be in a more inclined orbit of 65° allowing coverage up to ±65° latitude and correspondingly greater coverage of the Earth.

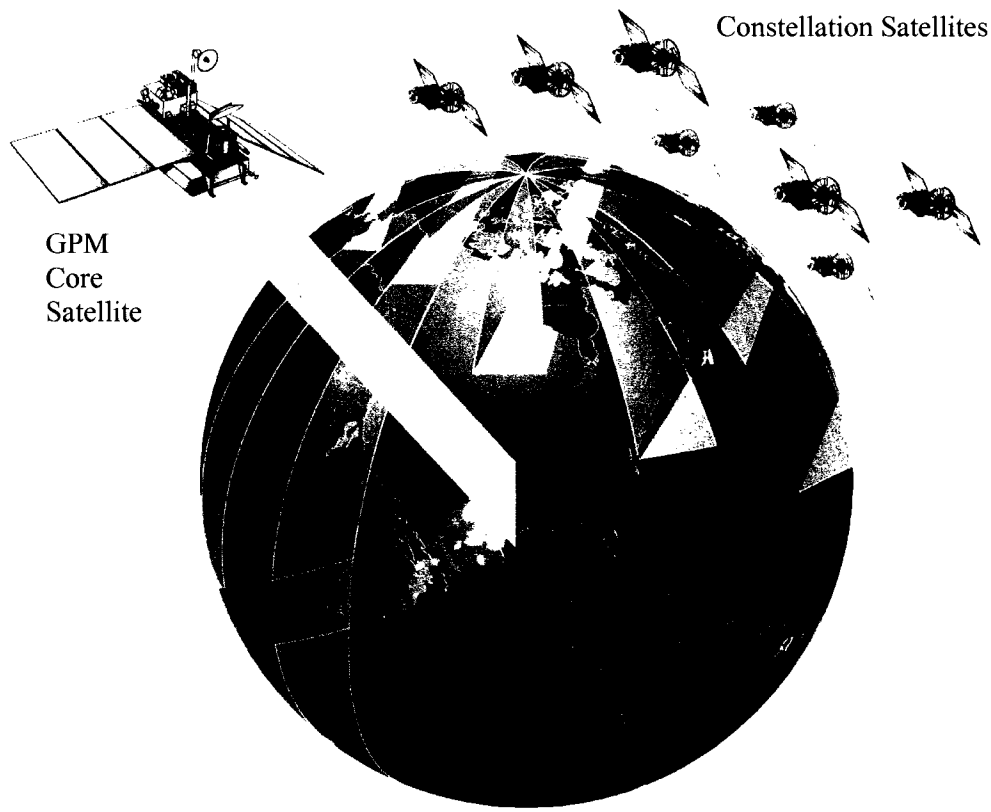

Figure 2.1. Graphic of the GPM core and constellation satellites and their coverage of the Earth.

As the primary mission of TRMM is the measurement of rainfall in the tropical regions, GPM will add to the tropical measurements the ability to measure snow and ice precipitation in the higher latitudes. The 35-GHz radar will be crucial to the success of those measurements.

GPM is a natural successor to the TRMM project. Even while TRMM was being specified and designed, the system architects desired to incorporate a second, higher-frequency radar for better measurement of precipitation. However, because of limited resources, TRMM was designed and launched with a single-frequency PR.

2.2 SYSTEM DESCRIPTION

The GPM system is comprised of many subsystems and functions. Figure 2.2 shows one set of interactions for GPM.

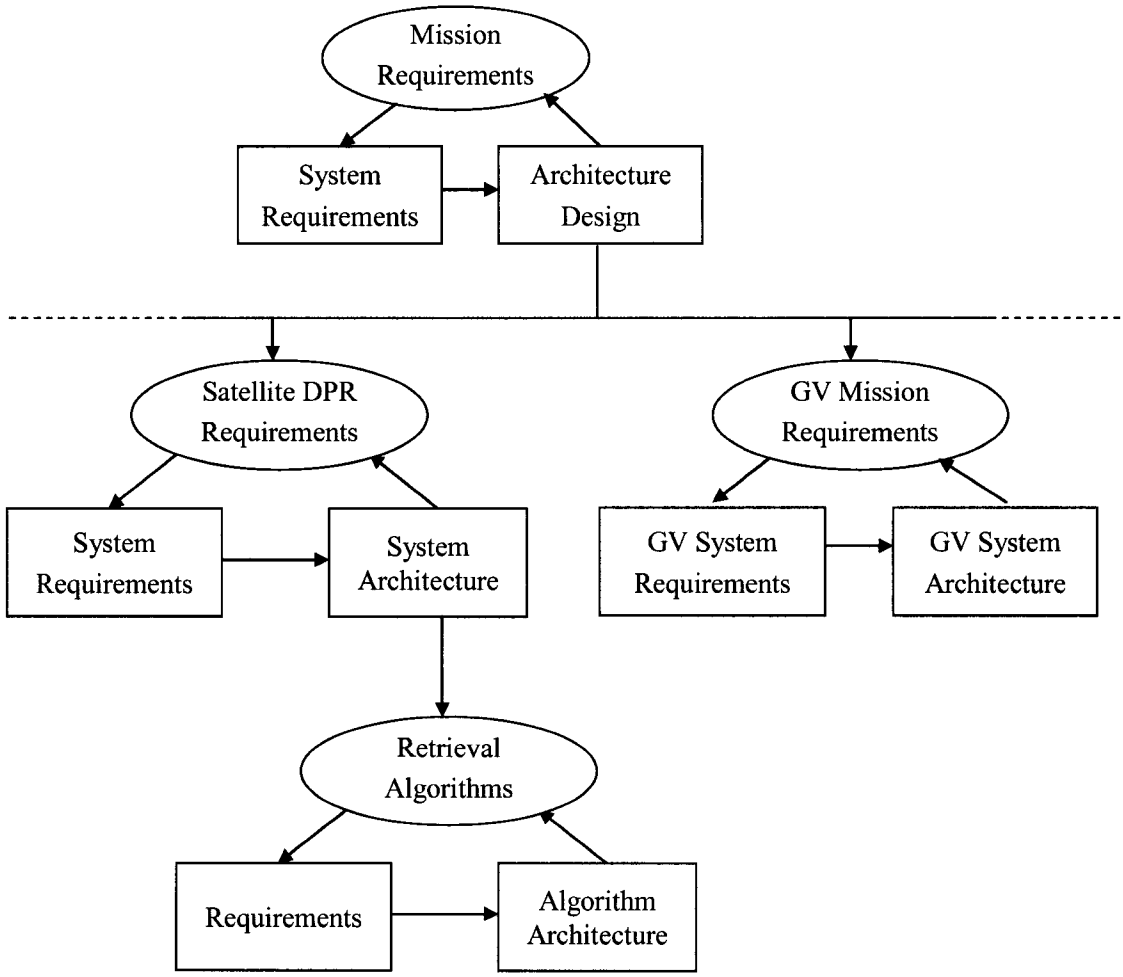

Figure 2.2. GPM system diagram showing links between mission, ground validation, satellite dual-frequency precipitation radar and retrieval algorithm requirements.

In the figure, the overall mission science requirements drive all aspects of the GPM project. Both the Ground Validation (GV) and Radar Systems are linked to the missions requirements so that those goals are obtained. Note that each subsystem has its own system requirements that are defined to ensure the success of the overall mission [5]. Additionally, feedback paths and links are provided between systems for verification of design objectives and necessary iterations in specification of requirements as might be necessary.

The GPM core satellite's DPR will point down and scan precipitation from right to left while it circles the Earth. Figure 2.3 shows a schematic of GPM's flight and scanning parameters.

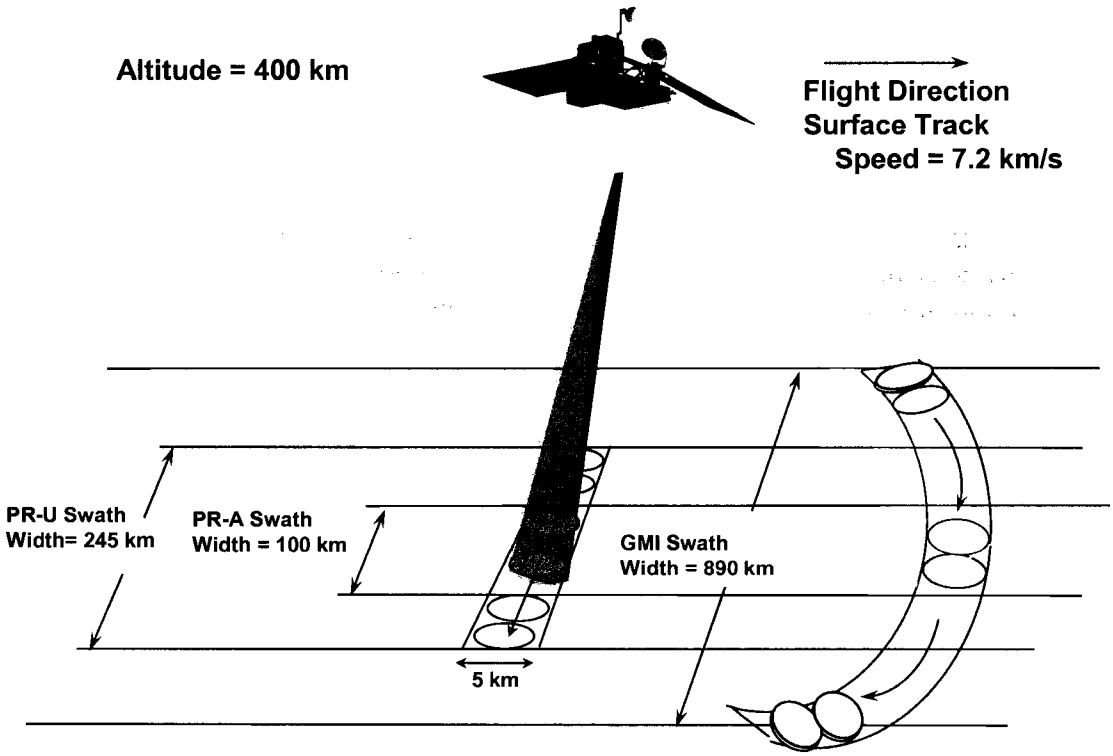

Figure 2.3. Diagram showing GPM's DPR scanning procedure.

Both radar beams are synchronized and adjusted to sample the same resolution volume with minimal error as they both scan across the field of view. The sample footprint or instantaneous field of view (IFOV) is about 5 km in diameter. The Ka-band radar, because of the much shorter wavelength, scans a swath of only 100 km wide while the Ku-band radar scans a width comparable to TRMM, about 245 km.

Table 2.1 shows some of the key radar and system parameters.

Table 2.1. DPR parameters. Adapted from G. M. Fleming, "Requirements for Global Precipitation Measurement," IGARSS 2002.

RADAR PARAMETER	VALUE
Radar Scanning Method	Active phased array
Antenna Type	128-element slotted waveguide
Altitude	400 km
Inclination angle	65°
Velocity	7.2 km/s
DPR Frequencies (PR-U, PR-A)	13.6 GHz (Ku), 35.55 GHz (Ka)
PR-U swath width	245 km
PR-A swath width	100 km
Horizontal Resolution, nadir	5 km
PR-U Sensitivity	17 dBZ
PR-A Sensitivity	11 dBZ
Beam width	0.71°
Peak Power PR-U	1000 W
Peak Power PR-A	180 W

2.3 GROUND VALIDATION

Successful implementation and operation of ground validation (GV) sites is crucial to the success of the GPM mission [6]. The goals of GV are:

- Evaluate: Quantifiable estimates on the quality of satellite precipitation products in terms of systematic and random error.
- Diagnose: Ascertain causes of errors within satellite products.
- Improve: Improvement of satellite algorithms and retrievals by refinement of physical assumptions and underlying models (e.g. cloud resolving models, radiative transfer equations).

To that end, considerable work has been done on the GV subsystem, and several sites have been proposed around the world that will facilitate the successful implementation of the GV goals. Figure 2.4 shows proposed GV sites around the world.

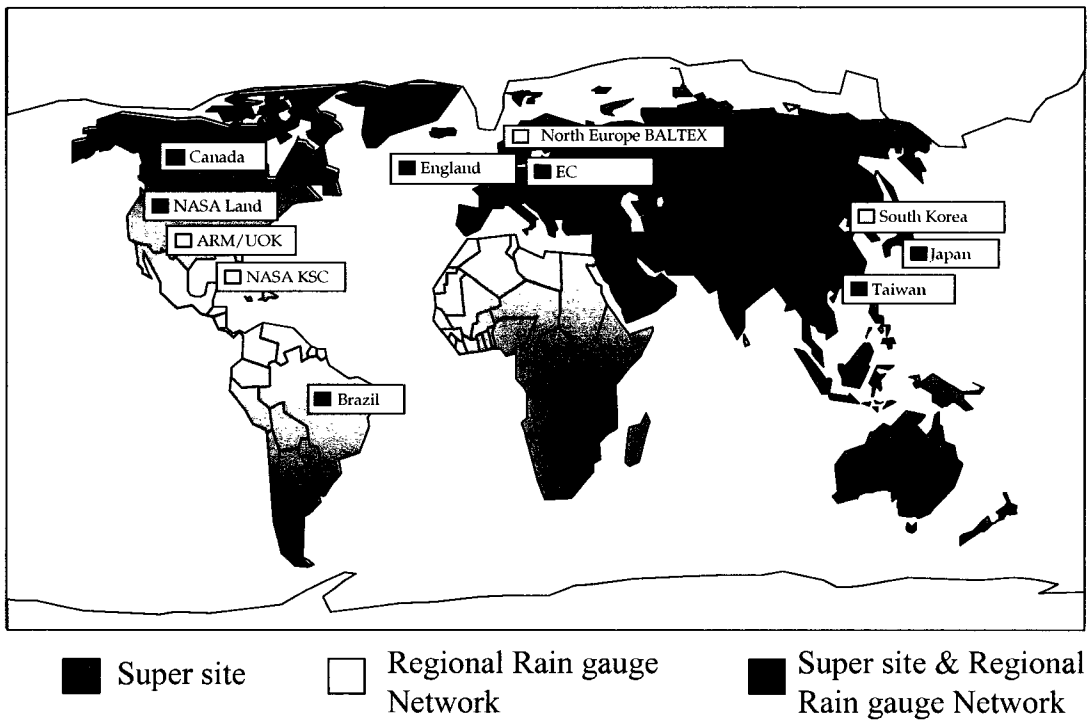

Figure 2.4. Diagram showing proposed GV super sites around the world.

At present, six super sites are planned with work continuing to finalize other locations. The super sites will field dual-polarimetric radars and other equipment necessary to characterize precipitation. Additionally, the super sites will be staffed. The rain gauge networks will largely be automated and deploy rain gauges to coordinate precipitation measurements with satellite overpass measurements.

2.4 RETRIEVAL METHODS

Because of the dual-frequency nature of the DPR, it can be used as two single-frequency radars or one dual-frequency radar with the switch over being in the algorithms that are used to estimate snow or rain precipitation.

2.4.1 Single Frequency

The TRMM retrieval algorithms are based on a single-frequency radar which work well for moderate to high rainfall rates. At low precipitation rates, the measured reflectivity values approach and can fall below the receiver noise threshold at which point they can't be measured. At very high rain rates, the precipitation can significantly attenuate the returned signal and reduce it below the noise floor. Additionally, the model deviates from its intrinsic assumptions and is less accurate. These algorithms are based on k-Z and Z-R relationships and use a modified Hitschfeld-Bordan method incorporating the surface radar cross section to correct for path attenuation.

2.4.2 Dual Frequency

The GPM DPR has several advantages over those of a single-frequency radar. First, if needed, it can operate as two, single-frequency radars utilizing the k-Z and Z-R relationships as TRMM does to estimate precipitation rates. The Ka-band frequency has greater sensitivity to low precipitation rates and will be able to measure lower rain rates than the 13.8-GHz radar. However, the down side of this is that the Ka-band will also be more susceptible to attenuation. Second, both frequencies can be used together with appropriate dual-frequency retrieval algorithms to more accurately estimate precipitation types and rates than can a single-frequency radar. One major advantage of the dual-frequency radar is that two of the three drop-size-distribution (DSD) parameters, N_w and D_o, can be retrieved, with μ assumed, whereas with the single-wavelength PR only one of the three can be retrieved with two being assumed. Using the DSD parameters directly is potentially a more accurate method to estimate rain rate than using the k-Z and Z-R relationships with their inherent assumptions.

At the present time, there are two types of dual-frequency retrieval algorithms that are being studied for implementation on GPM: 1) surface-reference-technique (SRT) based; and 2) non-SRT based. The SRT-based method uses a path-integrated-attenuation value derived from the

surface radar cross section similar to the method used by TRMM. The non-SRT algorithm is a self-consistent method whereby the integrated-path-attenuation values are calculated iteratively along with the DSD values. More details of these methods are given in the following chapters.

CHAPTER 3

DUAL-FREQUENCY ITERATIVE RETRIEVAL ALGORITHM

3.1 INTRODUCTION

Systems engineering principles and methods are very useful in large-scale complex systems for developing and analyzing the performance from end-user needs. Integrating research into system engineering is a challenging task. Following the success of the Tropical Rainfall Measuring Mission (TRMM) launched in 1997, the next generation of precipitation radar (PR) is expected to be launched aboard the Global Precipitation Measurement (GPM) core satellite around 2009. The TRMM PR presently operates at a single frequency of 13.8 GHz.

The TRMM PR algorithms rely on the surface-reference technique (SRT) to estimate path attenuation and correct the measured Ku-band reflectivity measurements [7]. After using a modified Hitschfeld-Bordan method, the attenuation-corrected reflectivities are then used to retrieve limited drop-size-distribution (DSD) information and the rain rate. A thorough description of the TRMM algorithm is given in [8]. This method works well for moderate to heavy rain fall where the SRT-derived attenuation value is large compared to its variance [9]. However, for low to moderate rain rates (less than 15 mm/hr), the variance of the measured SRT attenuation can be large resulting in poor rain estimates.

The proposed GPM-core satellite will use a dual-frequency precipitation radar (DPR) to measure and map global precipitation with unprecedented accuracy, resolution and areal coverage. The satellite vehicle, precipitation radar, retrieval algorithms, and ground validation (GV) functions are all critical subsystems of the overall GPM system and each contributes to the success of the mission. Errors in the radar measurements and models can adversely affect

the retrieved output values. Ground validation (GV) systems are intended to provide timely feedback to the satellite and retrieval algorithms based on ground observations.

The new, dual-frequency precipitation radar is proposed to operate at Ku (13.6 GHz) and Ka (35.6 GHz) bands. Figure 3.1(a) is a depiction of the downward looking satellite showing two rays, one for each wavelength, projected through a simple storm cloud and precipitation region.

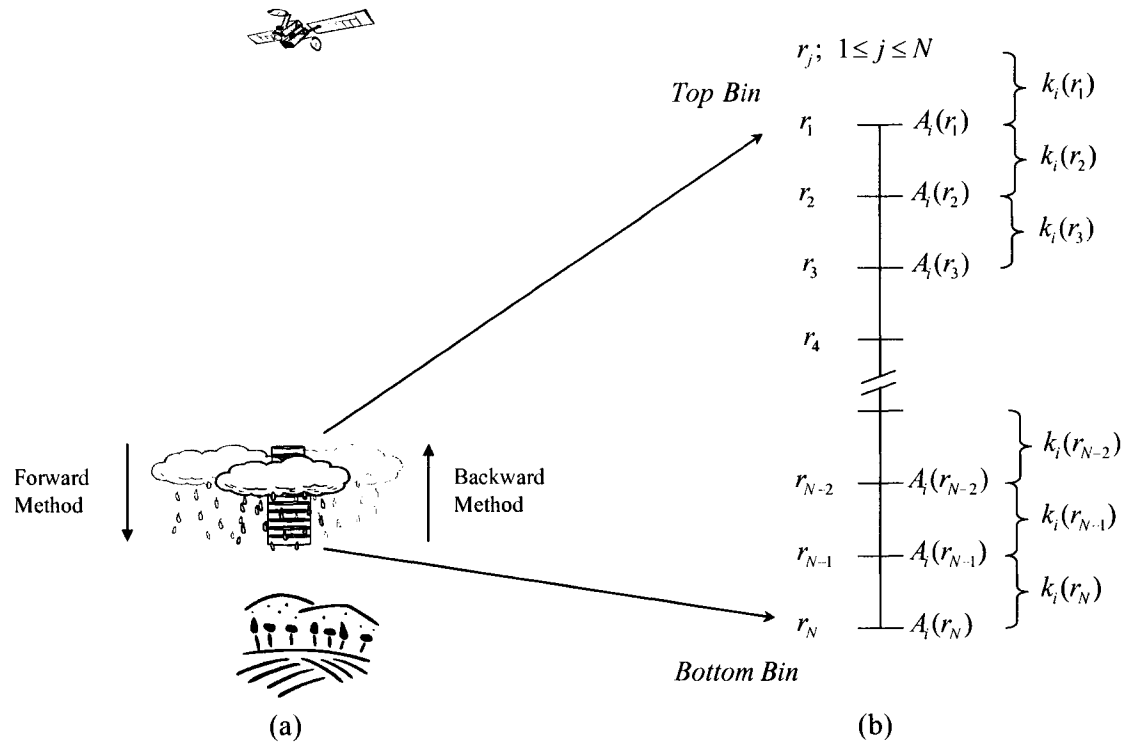

Figure 3.1. Part(a) shows a depiction of a downward looking GPM satellite. The discs represent sampling volumes. The forward method calculates DSD values starting at the top and moving to the bottom. The backward method calculates from the bottom to the top. Part(b) shows how the bin nomenclature and specific attenuation are defined.

The small discs represent the resolution volumes of the radars. Along with the new DPR, come new algorithms to measure and retrieve precipitation parameters such as the DSD in each resolution volume. The underlying microphysics of precipitation structures and DSDs dictate the types of models and retrieval algorithms that can be used to estimate precipitation. One of the retrieval algorithms being studied for use with GPM is a dual-wavelength algorithm that does not use the surface-reference technique.

The dual-frequency retrieval approach has been known since the 1970s, and has found renewed interest with the GPM DPR. Considerable work has already been done to evaluate the algorithm as a hybrid-SRT method [10] and as a stand-alone method with no SRT [9]. Additional work has been done by [11] to use the algorithm in the snow region. Inherent in the application of the dual-frequency algorithm are assumptions about the types of hydrometeors in each region: above the melting layer in snow; within the melting layer; and below the melting layer in rain. The types of hydrometeors assumed in the melting layer and above can significantly affect the retrieved DSDs and subsequent rain rate in the rain region. For GPM radar frequencies, the dual-frequency method appears to work best in low to moderate rain rates, and yields more detailed DSD information such as the intercept, N_o, and median volume diameter, D_o, than does the single-frequency approach. Because of the potentially large attenuation of the Ka-band signal in high rain rates, the algorithm has a firm limitation on the maximum rain-rate that it can be used to measure.

Generally, there are two main types of dual-frequency algorithms that can be used with a downward looking radar: a) The forward method, where the DSDs are calculated at each bin starting from the top bin and moving to the bottom (see Figure 3.1(a)) ; and b) the backward method, where the algorithm begins at the bottom bin and moves upward to the top calculating the DSD parameters and attenuation along the way [9], [12]. Figure 3.2 shows a summary diagram of these methods.

The assumption with the forward method is that there is known or at least assumed attenuation above the top bin. The integral equations are solved in a single pass through the hydrometeor regions.

The forward method can also be unstable in moderate to high attenuation levels coincident with moderate to high rain rates [12]. The backward type of algorithm can be further divided into three groups: a) standard dual-wavelength; b) surface-reference technique (SRT); and c) iterative non-SRT. The basic principle of the standard dual-wavelength approach is to estimate

the path attenuation (and rain rate) using the radar equation and the ratio of the returned power of both wavelengths.

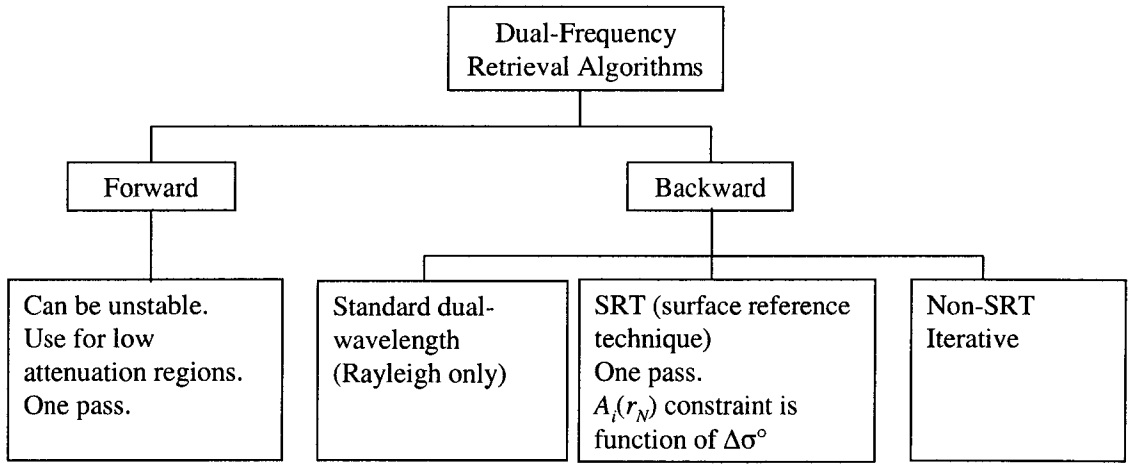

Figure 3.2. Diagram showing the two general types of dual-frequency retrieval algorithms, forward and backward. There are three types of backward retrieval algorithms: standard dual-wavelength; single-pass SRT-based; and non-SRT-based iterative.

This method requires one of two assumptions: first, the rain rate must be uniform over the measurement interval; or second, the reflectivity factor must be wavelength independent, meaning Rayleigh scattering at both frequencies [13]. The SRT method uses a backward calculation method assuming a total path-integrated-attenuation (PIA) value at the bottom for each wavelength. It is similar to the $\Delta\sigma^\circ$ method used in TRMM where $\Delta\sigma^\circ$ is defined as the difference between the normalized surface radar cross section without and with rain. This method solves the integral equations in a single pass using the $\Delta\sigma^\circ$ derived PIA. The third method, the non-SRT algorithm is a self-consistent algorithm wherein the total PIA for each frequency is first estimated using a seed value, and then through multiple iterations from bottom to top, the correct total PIA at each frequency (for each ray) at the bottom bin is calculated concurrently with the DSD values at each bin [14]

This chapter develops a system model primarily for the non-SRT dual-frequency retrieval algorithm. It is organized as follows: in section 3.2, algorithm development is included to reshape the necessary integral equations in terms of normalized DSD intercept parameter, N_w

instead of N_o. The dual-wavelength algorithm is developed and discussed in terms of a closed-loop control system model with feedback; in section 3.3, several test cases are used to evaluate the performance of the closed-loop (or single-loop) model as well as develop the relationship between observation error and convergence criteria. Errors at the top and bottom bins and the resulting impact are discussed; the fourth section describes D_o, N_w combinations where the closed-loop algorithm can not retrieve correct DSD values. An explanation is provided for the incorrect convergence region, why it occurs, and its limitations; section 3.5 presents an analysis of global DSD values, N_w and D_o, and is used to ascertain how much of the rain fall could be improperly estimated if the closed-loop dual-frequency retrieval model were used by itself. In other words, the trade space contribution of the closed-loop algorithm is defined; and section 3.6 summarizes the findings of this chapter.

3.2 GOVERNING EQUATIONS FOR A DUAL-FREQUENCY RADAR

3.2.1 Background

The dual-wavelength integral equations described by [10] solve for D_o and N_o at each range bin based on the assumed microphysical models for regions of hydrometeors and total path-integrated-attenuation. Mardiana et al. [9], [14], showed that those same equations could be used in a self-consistent iterative method to find the DSD values and PIA for each frequency without knowing beforehand the individual PIA values. This section briefly redevelops similar integral equations in terms of the normalized intercept parameter N_w instead of N_o.

Figure 3.1(b) shows a simple schematic describing the nomenclature for the model used in this work. Using the same nomenclature (for consistency) and descriptors as described by [9], [14], the measured, radar reflectivity factor, $Z_{mi}(r)$, at a specified range r can be expressed as

$$Z_{mi}(r) = Z_{ei}(r)\, A_i(r) \tag{3.1}$$

where $Z_{ei}(r)$ is the effective radar reflectivity and $A_i(r)$ is the two-way attenuation factor. The

subscript i, (i = 1, 2) represents the particular frequency, 13.6 and 35.6 GHz, respectively. The specific attenuation, k_i, for each frequency is defined for the region between bins.

The drop-size-distribution (DSD) is based on the normalized gamma [15], [16] of the form

$$N(D) = N_W f(\mu)\left(\frac{D}{D_o}\right)^{\mu} e^{-\Lambda D}\, dD \tag{3.2}$$

where

$$\Lambda = \frac{3.67+\mu}{D_o} \tag{3.3}$$

$$f(\mu) = \frac{6}{3.67^4}\frac{(3.67+\mu)^{\mu+4}}{\Gamma(\mu+4)} \tag{3.4}$$

and μ is the shape factor and is assumed to be constant in these algorithms. Γ is the gamma function, and D_o is the median volume diameter in mm.

The effective radar reflectivity factor, Z_{ei}, can be defined as

$$Z_{ei} = C_{Zi}\int_D \sigma_{bi}(D)N(D)\,dD \tag{3.5}$$

$$C_{Zi} = \frac{\lambda_i^4}{\pi^5 |K_w|^2} \tag{3.6}$$

where σ_{bi} is the radar backscatter cross section and is a function of the drop diameter D. λ_i is the wavelength and K_w is defined as

$$K_W = \frac{m^2-1}{m^2+2} \tag{3.7}$$

where m is the complex index of refraction. $|K_w|^2$ is about 0.93 for water at 20°C.

Substituting (3.2) for $N(D)$ in (3.5), we have

$$Z_{ei} = N_W\, f(\mu) D_o^{-\mu} C_{Zi}\int_D \sigma_{bi}(D) D^{\mu} e^{-\Lambda D}\, dD \tag{3.8}$$

and

$$Z_{ei} = N_W \, f(\mu) D_o^{-\mu} I_{bi}(D_o) \tag{3.9}$$

where

$$I_{bi}(D_o) = C_{Zi} \int_D \sigma_{bi}(D) D^{\mu} e^{-\Lambda D} \, dD \tag{3.10}$$

Note that Λ and D_o are related according to (3.3). Taking the ratio of Z_{ei} for both frequencies,

$$\frac{Z_{e1}}{Z_{e2}} = \frac{C_{Z1} \int_D \sigma_{b1}(D) D^{-\mu} e^{-\Lambda D} \, dD}{C_{Z2} \int_D \sigma_{b2}(D) D^{-\mu} e^{-\Lambda D} \, dD} \tag{3.11}$$

$$= \frac{I_{b1}(D_o)}{I_{b2}(D_o)} \tag{3.12}$$

$$= f_2(D_o) \tag{3.13}$$

and taking 10log of both sides (note that $log = log_{10}$, and $ln = log_e$), (3.13) can be rewritten as,

$$10\log(Z_{e1}) - 10\log(Z_{e2}) = 10\log[f_2(D_o)] \tag{3.14}$$

$$dBZ_{e1} - dBZ_{e2} = f_3(D_o) \tag{3.15}$$

where f_3 is a function of D_o and (3.15) is abbreviated as,

$$\delta dBZ_e = f_3(D_o) \tag{3.16}$$

Solving for D_o in simplified form, we have

$$D_o = f_4(\delta dBZ_e) \tag{3.17}$$

where the function f_4 is the mathematical inverse of f_3.

Several curves of D_o versus $\delta dBZe$ have been shown by [10] , [14], and [11], [17] for both snow and rain. Using (3.16), and appropriate microphysical models, the effective reflectivity values at both frequencies can be used to directly estimate the median volume diameter D_o.

The specific attenuation, k_i, at a particular range r can also be derived as,

$$k_i = C_{ki} \int_D \sigma_{ti}(D) N(D) dD \tag{3.18}$$

$$= C_{ki} N_W f(\mu) D_o^{-\mu} \int_D \sigma_{ti}(D) D^{\mu} e^{-\Lambda D} dD \tag{3.19}$$

$$= N_W f(\mu) D_o^{-\mu} I_{ti}(D_o) \tag{3.20}$$

and

$$C_{ki} = 4.343 \, x10^{-3} \tag{3.21}$$

$$I_{ti}(D_o) = C_{ki} \int_D \sigma_{ti}(D) D^{\mu} e^{-\Lambda D} dD \tag{3.22}$$

where σ_{ti} is the radar extinction cross section and is a function of drop diameter D.

The value of N_w at a particular range r can be found from (3.1) and (3.9), as

$$N_W = \frac{Z_{mi}}{f(\mu) D_o^{-\mu} I_{bi}(D_o) A_i} \tag{3.23}$$

With the backward-iteration method, the DSD parameters are first estimated at the bottom bin designated as r_N where N is the number of bins. Knowing the DSD parameters, N_w and D_o at the bottom bin, and an assumed initial attenuation, $A_i(r_N)$, the specific attenuation can be estimated between the bottom and the next-higher bin and consequently the next higher A_i.

Referring to Figure 3.1(b), the attenuation at the next higher bin, r_{j-1}, can be found from the information at the r_j bin using

$$A_i(r_{j-1}) = A_i(r_j) \exp\left[0.2 \ln(10) \int_{r_{j-1}}^{r_j} k_i(s) ds \right] \tag{3.24}$$

$$A_i(r_{j-1}) = A_i(r_j) \exp\left[0.2 \ln(10) \, h \, N_W \, f(\mu) \, D_o^{-\mu} \, I_{ti}(D_o) \right] \tag{3.25}$$

where h is the radar range resolution in km and j is the number of the range bin ($1 \le j \le N$). The top bin is designated as the first and the bottom is the *N-th* bin.

In contrast to the single-pass SRT-based algorithm described by [10] [12], the non-SRT algorithm described by [9] [14] iterates to find the correct attenuation factor and the subsequent DSDs. Note that path-integrated-attenuation (PIA) is defined as 10log(A) and is measured in decibels (dB). For a downward looking radar depicted in Figure 3.1, the algorithm calculates from the bottom, r_N bin just above the ground clutter, to the bin at the storm top, r_1. In this manner, it begins with $j = N$ and moves bin-by-bin to the top where $j = 1$. The process of calculating the DSD and attenuation values at each bin is described in the following paragraphs.

Values estimated or calculated by the algorithm are identified with a tilde (~) above the variable name. On the algorithm's first iteration, an initial guess for $A_i(r_N)$ must be used. Using the initial $A_i(r_N)$ and input $Z_{mi}(r_N)$ values, the effective radar reflectivity factor for each frequency at bin r_j can be estimated as,

$$\tilde{Z}_{ei}(r_j) = \frac{Z_{mi}(r_j)}{\tilde{A}_i(r_j)} \tag{3.26}$$

then $\tilde{D}_o$, $\tilde{I}_{bi}$ and $\tilde{I}_{ti}$ are calculated using,

$$\tilde{D}_o(r_j) = f_4\left[\delta dB\tilde{Z}_e(r_j)\right] \tag{3.27}$$

$$\tilde{I}_{bi}(\tilde{D}_o) = C_{Zi}\int_D \sigma_{bi}(D)\, D^{\mu}\, e^{-\Lambda D}\, dD \tag{3.28}$$

$$\tilde{I}_{ti}(\tilde{D}_o) = C_{ki}\int_D \sigma_{ti}(D)\, D^{\mu}\, e^{-\Lambda D}\, dD \tag{3.29}$$

$\tilde{N}_W$ is calculated using

$$\tilde{N}_W(r_j) = \frac{Z_{mi}\left(r_j\right)}{f(\mu)\,\tilde{D}_o^{-\mu}\,\tilde{I}_{bi}(\tilde{D}_o)\,\tilde{A}_i(r_j)} \tag{3.30}$$

and $\tilde{k}_i$ are found from

$$\tilde{k}_i(r_j) = \tilde{N}_W(r_j)\, f\left(\mu\right)\tilde{D}_o^{-\mu}\,\tilde{I}_{ti}(\tilde{D}_o) \tag{3.31}$$

Finally, both $\tilde{A}_i(r_{j-1})$ are calculated at the next higher bin using,

$$\tilde{A}_i(r_{j-1}) = \tilde{A}_i(r_j)\exp\left[0.2\ln(10)\, h\, \tilde{N}_W\, f(\mu)\tilde{D}_o^{-\mu}\, \tilde{I}_{ti}(\tilde{D}_o)\right] \tag{3.32}$$

where $\tilde{D}_o = \tilde{D}_o(r_j)$ in (3.27) – (3.32).

The estimation process described above continues up along each ray until the DSD, k_i and A_i values have been calculated for each bin. After each iteration, the bottom, measured-reflectivity values, $Z_{mi}(r_N)$, are compared to the bottom, estimated-reflectivity values, $\tilde{Z}_{mi}(r_N)$ calculated in the forward direction from the retrieved DSD profile. The algorithm iterates until

$$\tilde{Z}_{mi}(r_N) \approx Z_{mi}(r_N) \tag{3.33}$$

or

$$\frac{\tilde{Z}_{mi}(r_N)}{Z_{mi}(r_N)} \approx 1 \tag{3.34}$$

where

$$\tilde{Z}_{mi}(r_N) = \tilde{Z}_{ei}(r_N)\,\tilde{A}_i(r_N) \tag{3.35}$$

$$\tilde{Z}_{ei}(r_N) = \tilde{N}_W(r_N)\, f(\mu)\tilde{D}_o^{-\mu}\, \tilde{I}_{bi}(\tilde{D}_o) \tag{3.36}$$

$$\tilde{A}_i(r_N) = \exp\left[-0.2\ln(10)\, h \sum_{j=1}^{N} \tilde{k}_i(r_j)\right] \tag{3.37}$$

where $\tilde{D}_o = \tilde{D}_o(r_N)$ in (3.36).

Using the measured Z_{mi} values as a ratio, is mathematically identical to the ratio of $A_i(r_N)$ as described by [14] under certain assumptions. However, our analysis has shown that slightly more accurate results for the retrieved attenuation values are found using the input Z_{mi} values instead of the fixed-point iteration method.

3.2.2 Single-Loop Control-System Model

The dual-frequency algorithm convergence process can be modelled as a simple, feedback system. The idea of casting these equations into a feedback system is that further

system principles can be used to analyze the algorithm (system) performance. While exploring all aspects of this system is beyond the scope of this paper, we use this feedback system model to stage the subsequent discussion of algorithms. A block diagram of this approach is shown in Figure 3.3 where the feedback path consists of a closed loop on radar reflectivity factor. For the first iteration, a seed value for both $A_1(r_N)$ and $A_2(r_N)$ is chosen (in this work, 0.0 dB is used). The system inputs are the measured radar reflectivity values at both frequencies. After each iteration, the estimated Z_{mi} are calculated at the r_N–th bin using (3.35) and compared to the r_N–th bin of the input measured Z_{mi}.

Any error between the input and estimated $Z_{mi}(r_N)$ values is fed to a proportional-integral (PI) gain stage in which the next $A_{i,n+1}(r_N)$ values are calculated. These new $A_{i,n+1}(r_N)$ values, one for each frequency, are then used by the dual-frequency algorithm for its next iteration. The subscript n refers to the iteration number, and $n + 1$ is the next iteration.

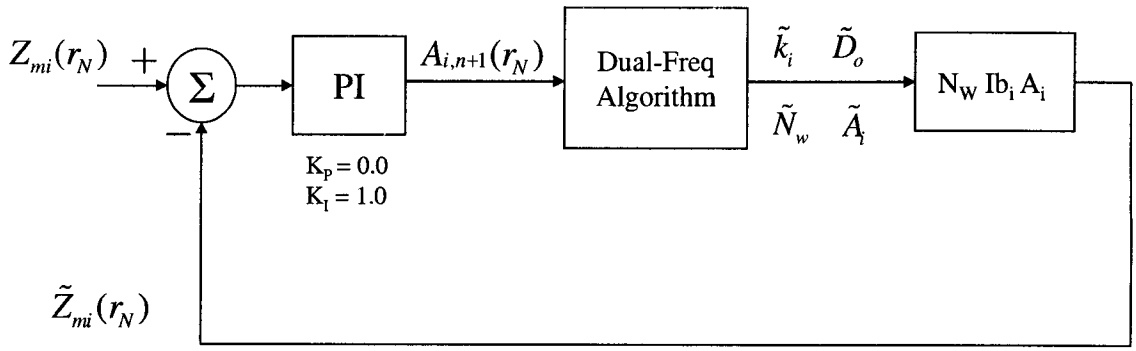

Figure 3.3. Block diagram of a single-loop control system model using the dual-wavelength algorithm. Any error between the input and estimated $Z_{mi}(r_N)$ values is fed to a proportional-integral (PI) gain stage in which the next $A_{i,n+1}(r_N)$ values are calculated. The loop ceases when a predefined convergence tolerance is reached.

The outputs from the algorithm are the $\tilde{k}_i$, $\tilde{D}_o$, $\tilde{N}_W$ and $\tilde{A}_i$ values at each bin. Present values for the PI gain stage are $K_P = 0$ and $K_I = 1$. Using an integrator term, the steady-state error tends to zero. Several studies have been done with small proportional gain, such as $K_P = 0.1$ and the net result was a reduced number of iterations for convergence. However, given no system-level requirement to minimize the number of iterations, nor step-response time as in a feedback control system, the use of a single integral gain term is sufficient for calculating the DSDs.

Nevertheless, the parameter K_P is available for future control while integrating this algorithm to the rest of the GPM system.

In practice, the error between the measured and estimated reflectivity factors is monitored, and when

$$\left| \frac{\tilde{Z}_{mi}(r_N)}{Z_{mi}(r_N)} - 1 \right| \leq \varepsilon_i \tag{3.38}$$

where ε_i is a predefined upper bound, the iterations cease.

It has been shown by [14] that an equivalent method (instead of using $Z_{mi}(r_N)$) for calculating the next $A_{i,n+1}(r_N)$ values is to use the attenuation factor values $A_i(r_N)$ and estimated $\tilde{A}_i(r_N)$ from (3.37). In this method, the attenuation and estimated attenuation values can also be used as tests for convergence. The fundamental operating principle of this algorithm is that by performing a sufficient number of iterations with a sufficiently small error tolerance, that the true $A_i(r_N)$ values can be found thereby negating any need for an SRT implementation. With the correct or true $A_i(r_N)$ values, it is implied that the DSD values will be correct based on whatever model assumptions are used. This iterative method using $\tilde{A}_i(r_N)$ instead of $Z_{mi}(r_N)$ will work except for one shortcoming, the attenuation values calculated in the iterations and resulting bins are estimated and can not be compared directly to input control data such as the $Z_{mi}(r)$ values. Using the $\tilde{A}_i(r_N)$ values for calculation of the next $A_{i,n+1}(r_N)$ values and convergence testing yields less accurate attenuation results than using the input Z_{mi} values.

3.3 CONVERGENCE TO CORRECT SOLUTION

The algorithm shown in Figure 3.3 has been evaluated using various simulations of known D_o, N_w combinations for regions of only rain and rain/melting/snow. In each case, models based on microphysical properties of the assumed precipitation, were made for the k_i, I_{ti}, I_{bi}, and D_o vs. $\delta dBZe$ relationships. The D_o vs. $\delta dBZe$ relationship is shown in (3.17) and uses the

difference in Z_{ei} values (in dBZ scale) to directly compute D_o. It can be implemented using a look-up table or curve-fit equations.

In this section, we consider only a single hydrometeor region of uniform rain for simulation and testing. Reflectivity profiles for both GPM frequencies can be synthesized using equations (3.1), (3.17), (3.10), (3.22), (3.23), (3.18) and (3.25). The rain drops are assumed spherical, at 20° C with $\mu = 1$. (Note that $N_w = N_o$ when $\mu = 0$, and the DSD becomes the exponential distribution.) It should be noted here that spheroidal models for raindrops were also developed, but for the purposes of analysis for downward looking radars, spherical drop models were sufficient.

An example of retrieved profiles for a simulated vertical rain column 0.5 to 3.5-km in height using $D_o = 2$ mm, $N_w = 1500$ is shown in Figure 3.4. Figure 3.4(a) shows the simulated, measured-reflectivity profiles in dBZ for the GPM frequencies 13.6 and 35.6 GHz as well as the difference between the two reflectivities. Figure 3.4(b) shows the correctly retrieved D_o profile which in this case is 2 mm. Figure 3.4(c) shows the retrieved N_w values and that they are correct per the known $N_w = 1500$ profile.

The retrieved N_w value is 1495 yielding an error of -0.33 % from the known value. Figure 3.4(d) shows the estimated rain-rate profile calculated from the retrieved DSDs at each bin using

$$R = 0.6x10^{-3}\,\pi \tilde{N}_w\, f(\mu)\, \tilde{D}_o^{-\mu} \int_D v(D)\, D^{\mu+3}\, e^{-\Lambda D}\, dD \tag{3.39}$$

where

$$v(D) = 4.854\, D\, e^{-0.195D} \tag{3.40}$$

is the Gunn-Kinzer terminal velocity. The retrieved rain-rate profile is constant at 9.6 mm/hr. This simulation assumes no measurement error on the inputs. Using initial $A_i(r_N)$ values of 0 dB, the algorithm converges to the proper DSD values in 238 iterations using the closed-loop feedback model with a convergence tolerance of 0.01 percent.

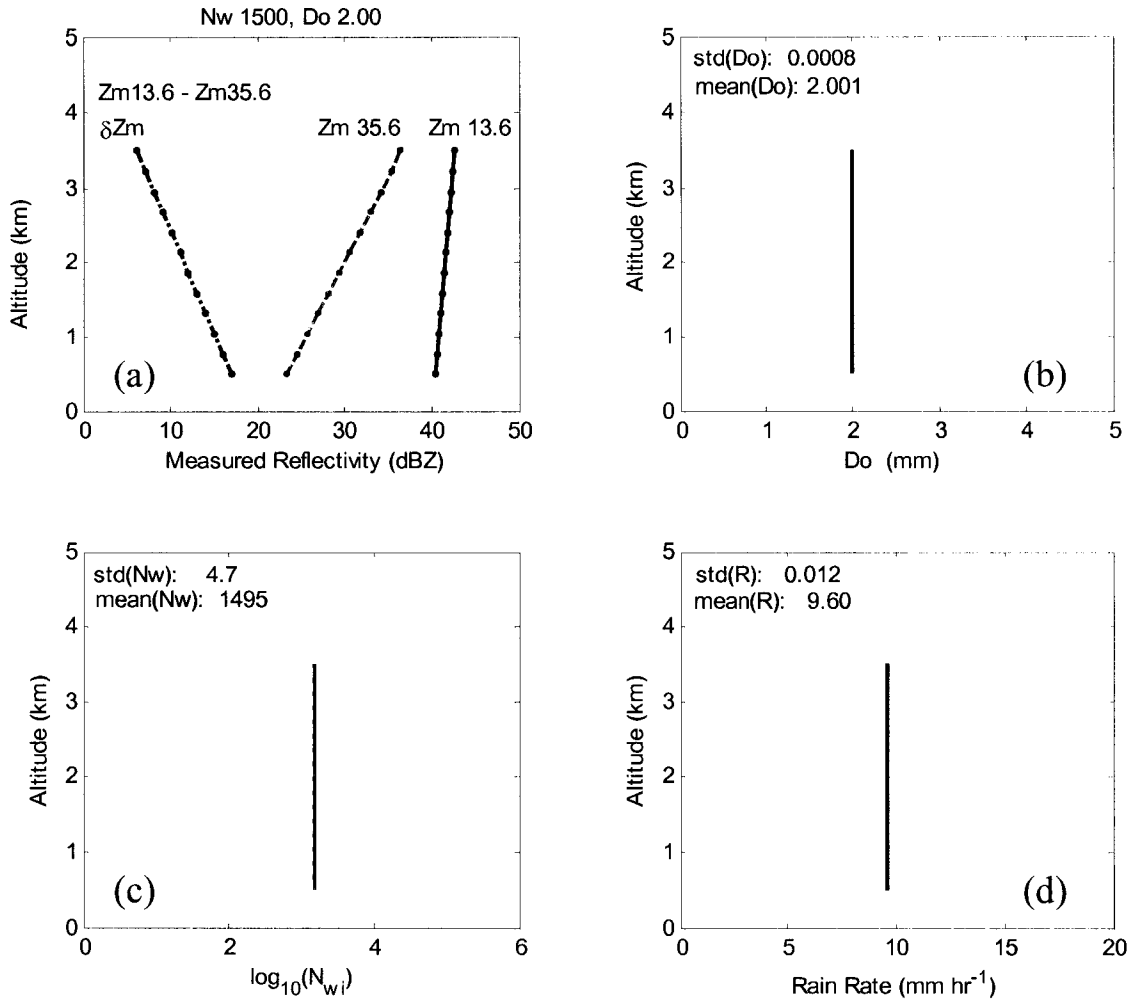

Figure 3.4. Plots showing simulated results for a vertical rain column 3-km in height above a 0.5-km base using known DSD parameters (N_w = 1500, D_o = 2) when the algorithm retrieves the correct values. Part(a) shows the input Z_{mi} values, Parts (b),(c),(d) show the profiles for D_o, N_w, and rain rate. Convergence tolerance is 0.01 percent and required 238 iterations.

This small error tolerance is unrealistic for actual measurements. However, for this model, a relatively small tolerance is required to retrieve the correct DSD values. As the tolerance value is increased, the bottom portions of the profiles will begin to deviate from the known DSD values as the algorithm is unable to determine the correct $A_i(r_N)$ values.

3.3.1 Impact of Measurement Error

The following analyses study the measurement errors to learn how the algorithm responds and to gauge its sensitivity to such errors. The measurement error of the GPM DPR is expected to be less than 0.5 dBZ [18]. To simulate fluctuations in the measurement, Gaussian

random noise was added to the 13.6 and 35.6-GHz reflectivity profiles in known D_o, N_w data sets at various range bins. While in reality there is measurement error in each bin, the following analyses evaluate the relative impact of the error in three separate simulations, namely, a) measurement error was injected at the top, b) injected at the bottom, and c) at each observation point along the path.

3.3.2 Sensitivity to Error at the Top Measurement Bin

When random measurement error is injected into only the top reflectivity bin of each ray, the algorithm incorrectly retrieves the DSD values below. This result is shown in Figure 3.5 for a simulated uniform vertical rain column 5.25 km in height based on $N_w = 4000$, $D_o = 1.35$ mm. Figure 3.5(a) shows the input Z_{mi} values and the distorted Z_{mi} values at the top bin where 0.10 and 0.07 dBZ-rms (-0.45 dBZ_{peak} and -0.325 dBZ_{peak}) have been randomly added to the 13.6 and 35.6-GHz signals respectively. Figure 3.5(b) shows the retrieved D_o profile, and Figure 3.5(c) shows the retrieved N_w profile. The profile for D_o should be a constant 1.35 mm with altitude. At the top, it is 1.34 mm and diverges to about 1.48 mm at the bottom. Likewise, N_w should be a constant 4000 with altitude. At the top, it starts at about 3905 but decreases to 1930 at the bottom. The rain profile is calculated and displayed in Figure 3.5(d) using (3.38). With incorrect DSD profiles, the rain profile is also incorrect. It is clearly seen that error in the top bin propagates down through the lower, estimated DSD values because the lower $Z_{mi}(r)$ values are based on the intrinsic attenuation of the top bin. With error at the top, the algorithm tries to account for an incorrect attenuation as best it can. In reality, the top bin will have very little attenuation, and can be easily retrieved or estimated. In fact, in all the simulations, nearly correct DSD values can be retrieved at the top bin in just the first iteration when there is no measurement error in the simulated data set. This is because the attenuation factor used in (3.26) is close to unity (or negligible in log scale) indicating that $Z_{ei}(r_1) \approx Z_{mi}(r_1)$. Many more iterations will be required to obtain the correct DSD values for the bottom bins when moderate

to large amounts of attenuation are present. Depending on the value and sign of the injected error at the top bin, the retrieved DSD values below will be over- or under-estimated.

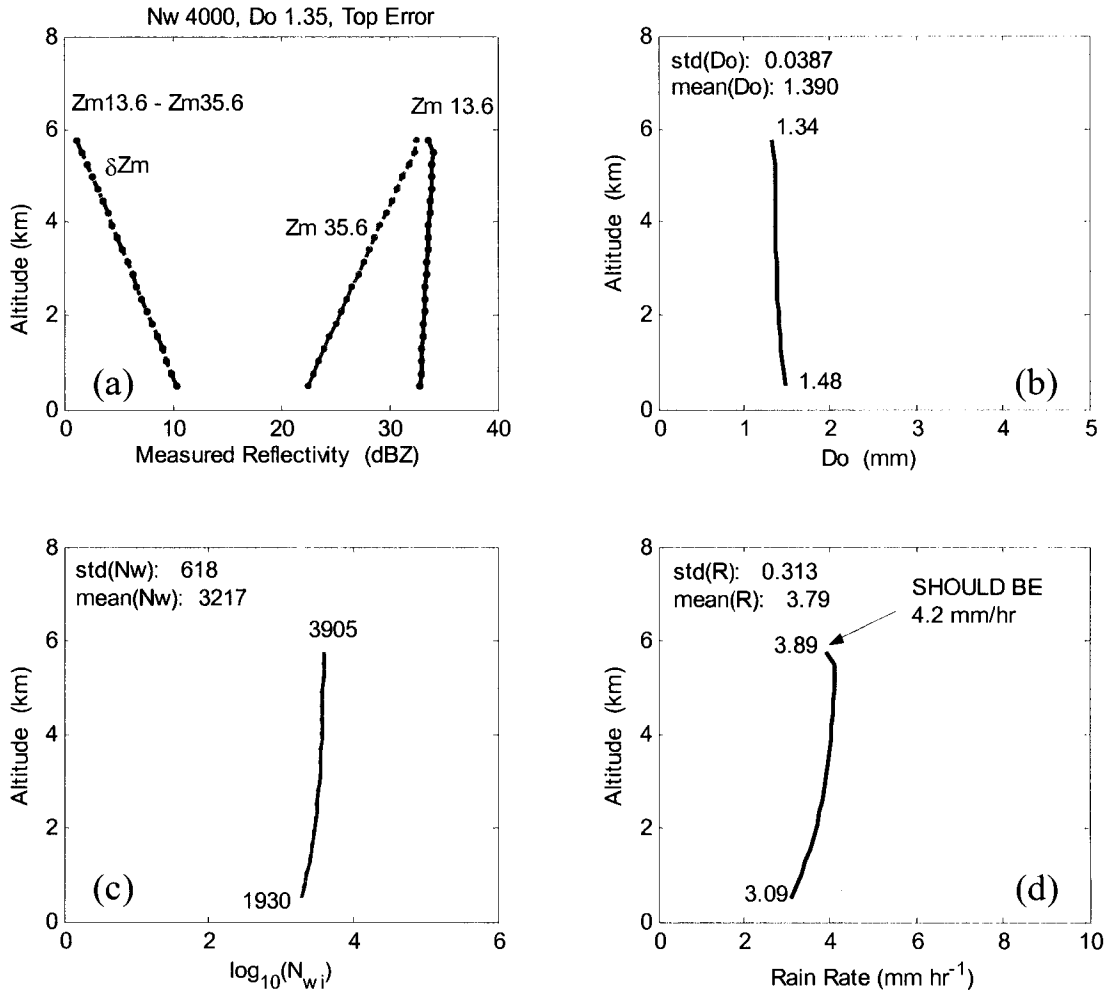

Figure 3.5. Plots showing simulated results for a vertical rain column 0.5 to 5.75-km in height using known DSD parameters (N_w = 4000, D_o = 1.35) with measurement error in the top bin. With error at the top, the algorithm incorrectly retrieves D_o, N_w and then incorrectly estimates the rain rate in all bins. Convergence tolerance is 0.01 percent and required 141 iterations.

Proper convergence, or simply convergence, occurs when iterations cease due to the conditions of (3.38) being satisfied.

3.3.3 Sensitivity to Error at the Bottom Measurement Bin

Figure 3.6 shows the retrieved profiles with measurement error in the bottom bin for a simulated uniform vertical rain column 5.25 km in height based on N_w = 4000, D_o = 1.35 mm. In this simulation, 0.112 and 0.111-dBZ-rms error disturbances (0.51 dBZ_{peak} and -0.50 dBZ_{peak},

13.6 and 35.6-GHz inputs respectively) have been randomly added to the bottom bin, and as a result, only the bottom retrieved DSD values are incorrect.

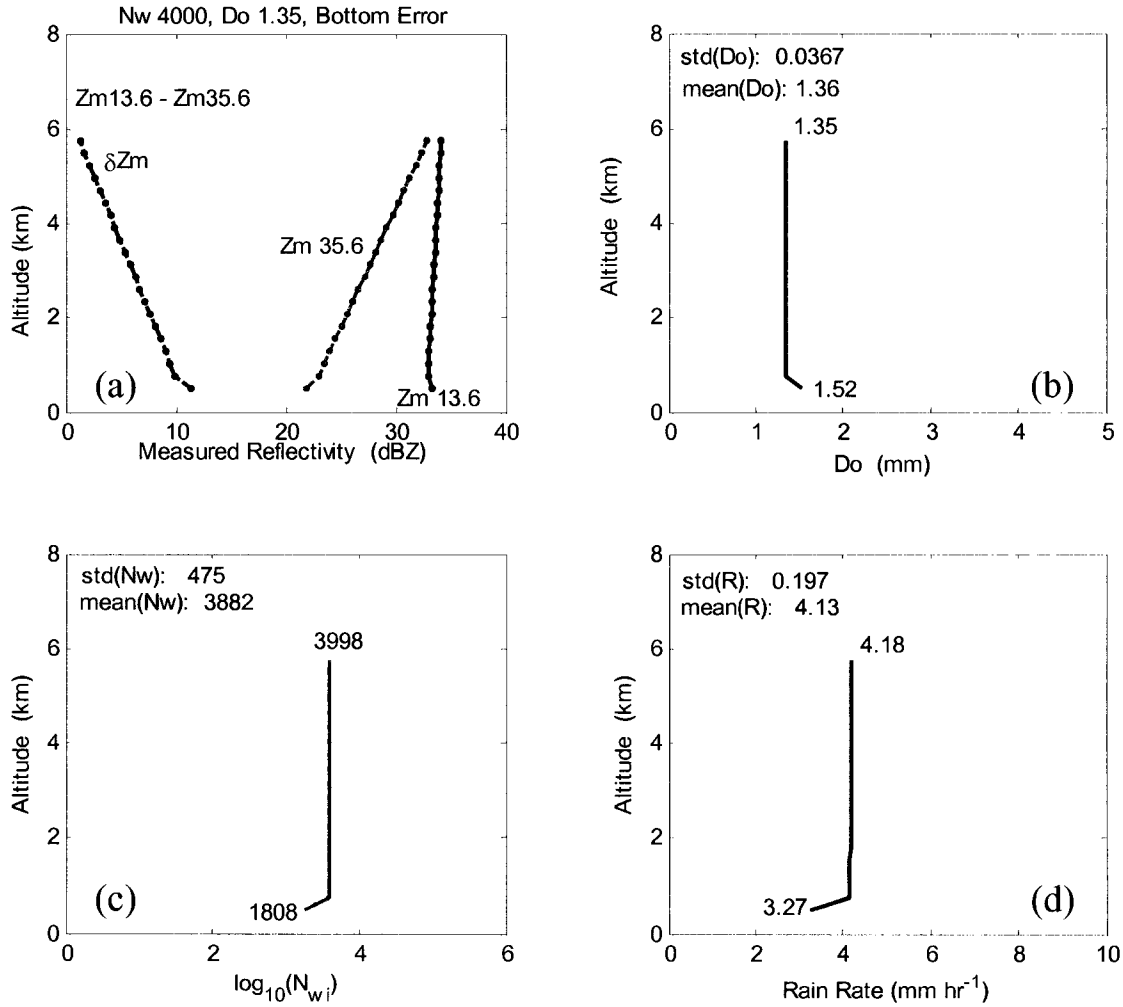

Figure 3.6. Plots showing simulated results for a vertical rain column 0.5 to 5.75-km in height using known DSD parameters (N_w = 4000, D_o = 1.35) with measurement error in the bottom bin. The algorithm correctly retrieves the DSD values above the error bin. As expected, at the error bin, the DSD values deviate substantially from expected values. Convergence tolerance is 0.01 percent and required 164 iterations.

Figure 3.6(b) shows that the D_o profile, 1.35 mm, is correctly retrieved from the top down to the disturbance where it diverges to 1.52 mm. Figure 3.6(c-d) show correct N_w and rain profiles from the top, down to the incorrect bottom bin where they both diverge. The N_w value at the top bin is correct at 3998 but decreases to 1808 at the bottom bin with the added measurement error. Similar to the previous case, depending on the sign and magnitude of the additional error, the

bottom-bin retrieved values can be curved right or left. Clearly, the error in the bottom bin has little impact on the bins above as the correct DSDs are retrieved in those bins.

3.3.4 Sensitivity to Measurement Error Along the Path

Gaussian random error, 0.50-dBZ standard deviation, was added to all the bins of both rays to simulate measurement error. Figure 3.7(a) shows the 13.6 and 35.6-GHz measured reflectivity profiles of a simulated uniform vertical rain column 5.25 km in height based on N_w = 4000, D_o = 1.35 mm with added measurement errors.

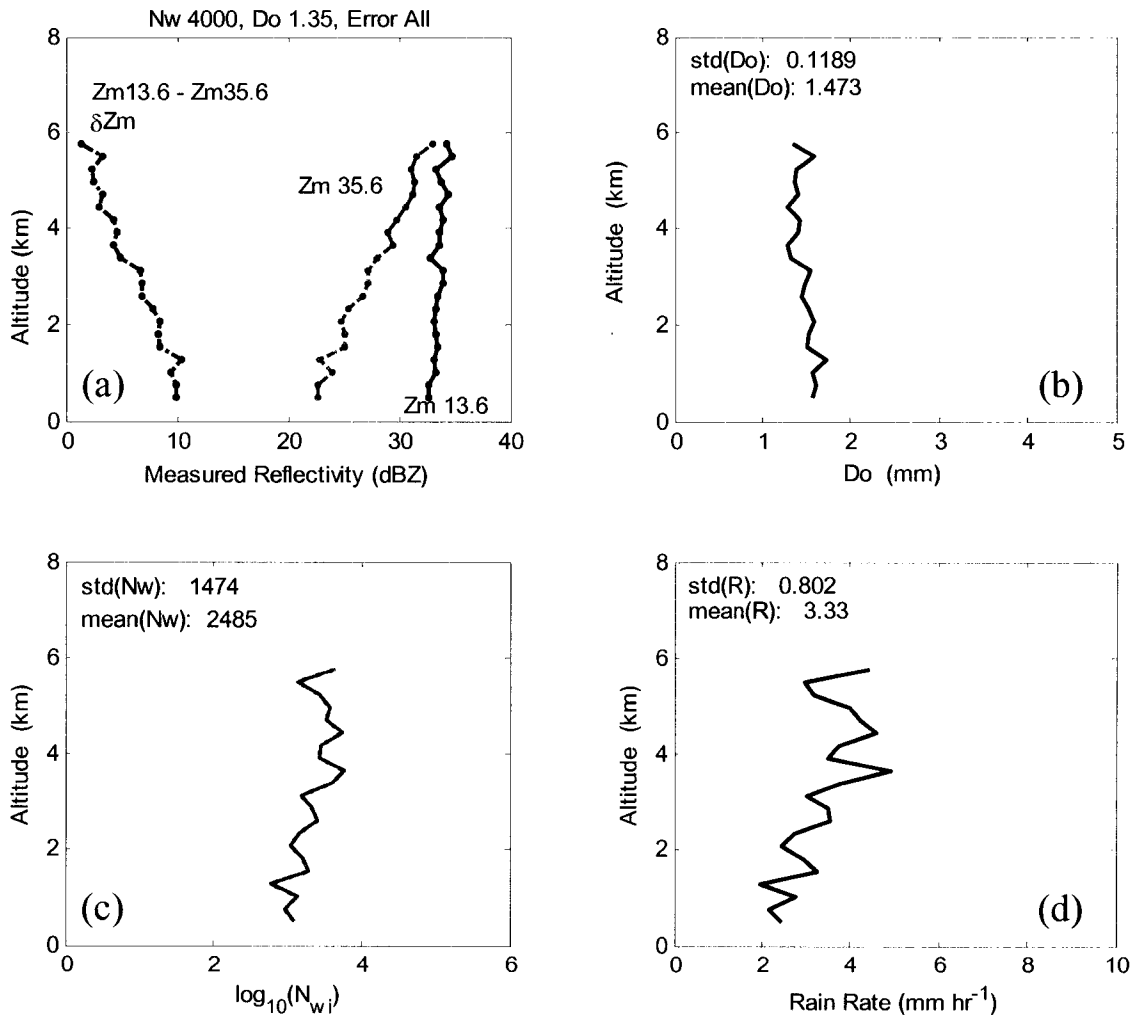

Figure 3.7. Plots showing simulated results for a vertical rain column 0.5 to 5.75-km in height using known DSD parameters (N_w = 4000, D_o = 1.35) with 0.5-dB standard deviation Gaussian random error added to each bin of both rays. Convergence tolerance is 0.01 percent and required 89 iterations.

Without the errors, these inputs would be straight lines. The standard deviation of the 13.6-GHz profile with respect to its true profile is 0.38 dBZ, and the standard deviation of the 35.6-GHz profile with respect to its true profile is 0.52 dBZ. These standard deviation values are calculated as the standard deviation of $Z_{mi,with\text{-}error}(r_j) - Z_{mi,error\text{-}free}(r_j)$ for $j = 1$ to N. Because the added errors in each bin are random from a Gaussian distribution of specified standard deviation (zero mean), the actual overall standard deviation values for each profile will vary from one realization or simulation to another. Figure 3.7 shows a representative case with a significant amount of error in both input rays and retrieved outputs. The DSD profiles—D_o should be a constant 1.35 mm, and N_w should be a constant 4000—vary from their expected values. As expected, both are slightly noisy and skewed with altitude in panels (b) and (c). The rain profile shown in Figure 3.7(d) is also skewed as a result of incorrect DSD values. Rain rate varies from about 4.2 mm/hr at the top to about 2.3 mm/hr at the bottom and has a normalized standard error (NSE) of 0.24. It is underestimated in the lower altitudes. The NSE of D_o is 0.08.

With measurement error in the reflectivity data set, the convergence tolerance in (3.38) normally must be increased to allow the algorithm to converge without generating internal errors. These internal errors occur when mathematical impossibilities such as negative attenuation are required or calculated. There are cases, however, as above, that even with a low tolerance and significant error, that the algorithm will still converge without internal errors. These situations are generally the exceptions and not the rule. From a systems perspective, the algorithm must be robust enough to converge for all of the error-laden reflectivity data sets. To make it more robust, the convergence tolerance must be increased to account for the wide variation in measurement error. To ascertain how the algorithm convergence tolerance must be adjusted with respect to differing amounts of error, Monte Carlo-type simulations were analyzed. Table 3.1 shows the relationship between measurement error in the data sets and

maximum convergence tolerance for an N_w = 4000, D_o = 1.35 data set in order to have the simulations converge without internal errors.

Table 3.1. Maximum convergence tolerance as it relates to measurement error in dBZ for N_w = 4000, D_o = 1.35 mm data set. The measurement errors are random, one standard deviation. Convergence tolerance percentages are values that would allow all data sets to converge without internal errors.

Measurement Error: dBZ	Max. Convergence Tolerance
0.5	8 %
0.4	5.5 %
0.3	4 %
0.2	1 %
0.1	0.1 %

The numbers in Table 3.1 are approximations and are viewed most appropriately as showing a measurable trend rather than exact tolerance values. It is clear that with large error a large convergence tolerance is required. In practice, the tolerance would be set small and be incrementally increased as internal errors occur.

3.4 CONVERGENCE TO INCORRECT SOLUTION

Many DSDs with constant D_o, N_w profiles for rain have been simulated and tested with the dual-frequency retrieval algorithm within the single-loop model. It has been found that with certain combinations of DSD pairs the algorithm converges but does not yield the proper, expected DSD values along the entire profile. Figure 3.8 shows the retrieval output for a simulated vertical uniform-rain profile 3-km in height based on N_w = 4000, D_o = 1.85 mm.

Figure 3.8(a-c) show the input Z_{mi} values, the retrieved D_o profile and the retrieved N_w profile, respectively. The rain profile is shown in Figure 3.8(d). The algorithm retrieves the proper DSD values for a portion of the profile but deviates in the lower region. With similar large D_o, N_w combinations, the required number of iterations to convergence is greatly increased. In this example, it required 4508 iterations to converge with 0.01% tolerance.

Correct convergence is when the algorithm meets the requirement of (3.38) and the retrieved DSD profiles match the known inputs, i.e., for known vertical profiles, vertical profiles are retrieved. Incorrect convergence is when the algorithm converges but the retrieved DSD profiles do not match the known input values. Note that even though the D_o and N_w profiles are incorrect in the bottom portions, they should be 1.85 mm and 4000 respectively, that the algorithm correctly retrieved the estimated reflectivity values for both frequencies.

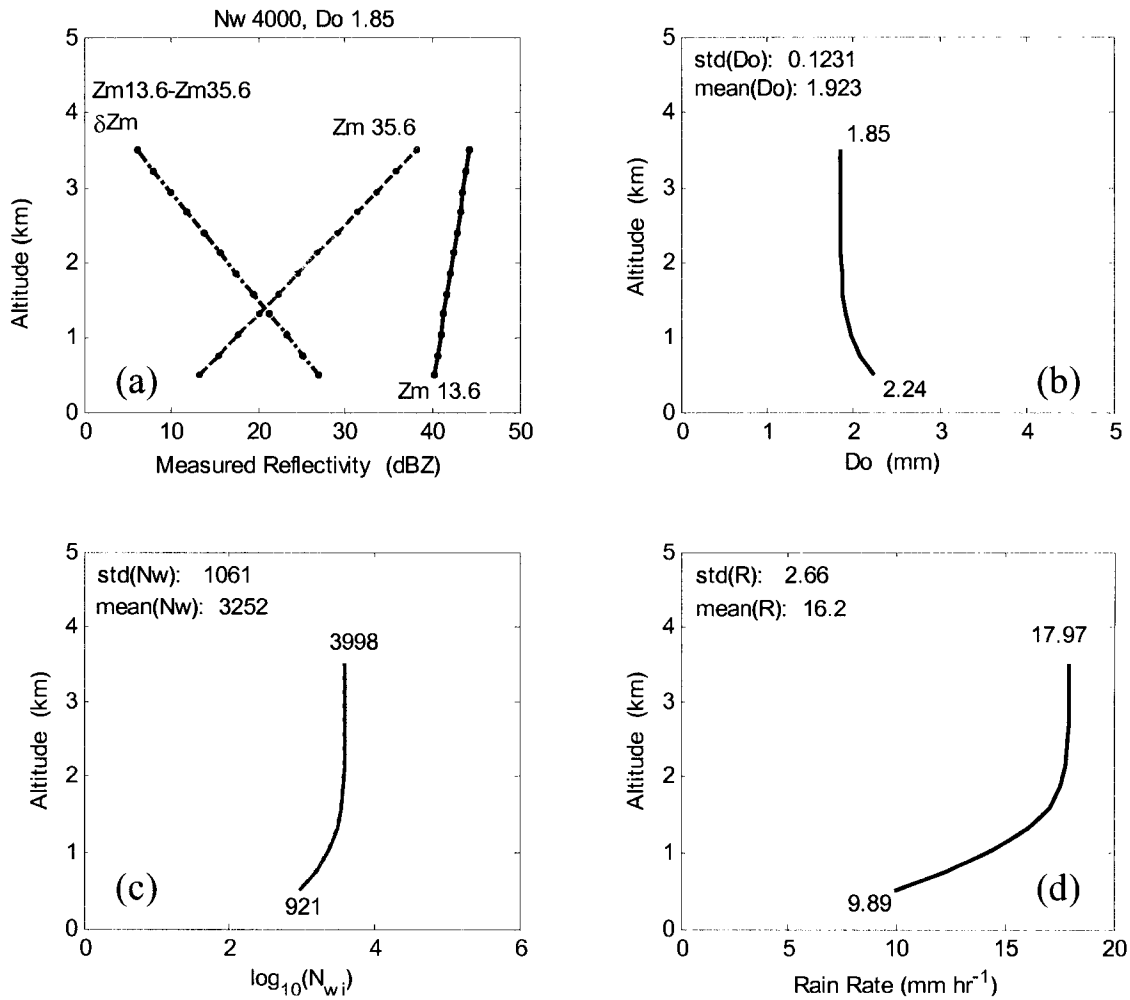

Figure 3.8. Plots showing simulated results for a vertical rain column 0.5 to 3.5-km in height using known DSD parameters (N_w = 4000, D_o = 1.85). The algorithm converges but is unable to retrieve correct DSD values for the full profile. Part (d) shows the rain rate with a 45% underestimate at the bottom bin. Convergence tolerance is 0.01 percent and required 4508 iterations.

Referring to (3.35), it is clear that $\tilde{Z}_{mi}(r_j)$ is a function of the retrieved N_w, D_o and A_i. They can all be incorrect but have correctly estimated $\tilde{Z}_{mi}(r_j)$ values. In this case, and in other large D_o, N_w combinations, that is exactly what happens.

3.4.1 Regions of Correct Convergence

Figure 3.9 shows contours of constant rain rate in a D_o, N_w diagram. Superimposed on the diagram are three curves corresponding to simulated total path lengths of six, nine and twelve bins which separate the D_o, N_w space into regions of correct and incorrect convergence.

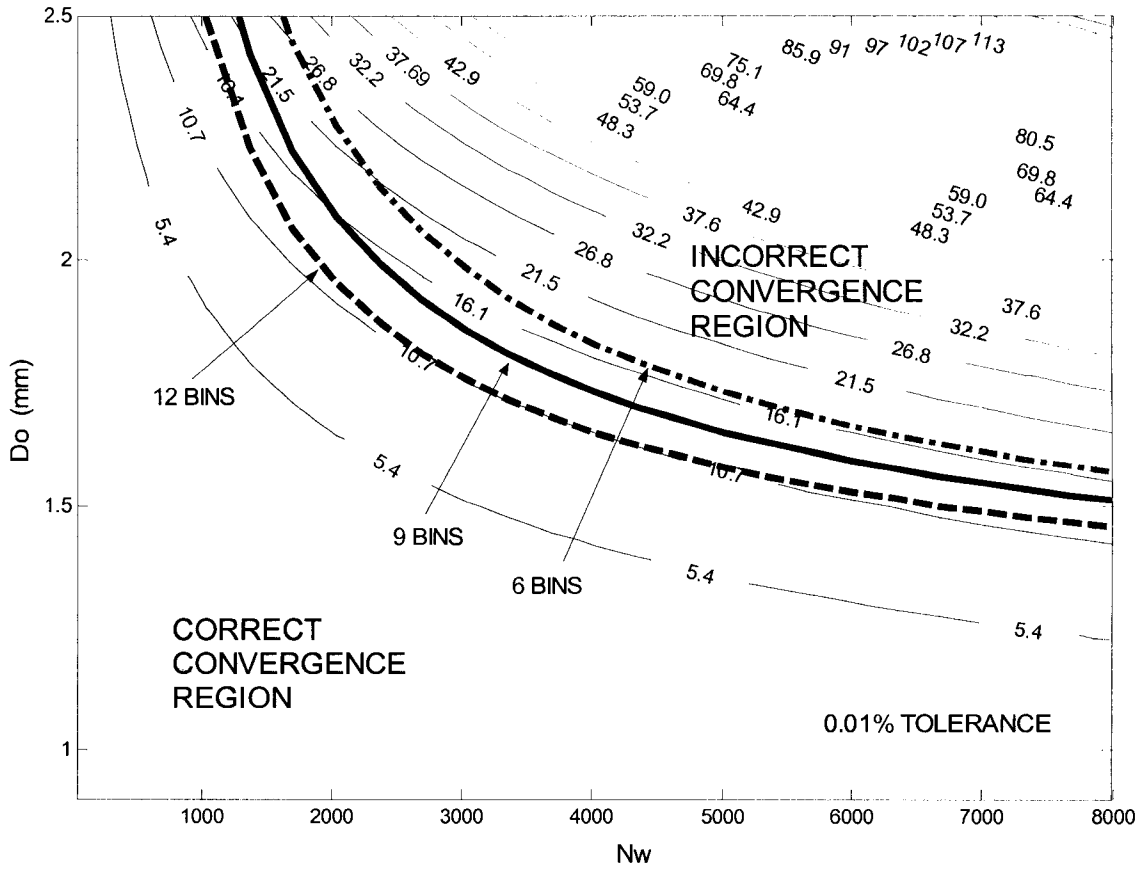

Figure 3.9. Contour plot of constant rain rate versus D_o, N_w. Three approximate boundary lines separate regions of correct and incorrect DSD retrieval for six, nine and twelve bins of path length. D_o, N_w combinations below a respective line converge correctly, and above a boundary curve converge incorrectly.

The PIA for a distance of 12 bins is obviously greater than that for nine and six bins. For a given number of bins, or associated *PIA*, the region above the selected curve yields

"incorrect" convergence, and in the region below, the algorithm outputs "correct" convergent solutions. The regions below a curve are called correct convergence solutions as the algorithm retrieves the correct solution throughout the profile and the region above a curve is called the incorrect convergence region. The solutions where the DSD values curve at the bottom are referred to as incorrect convergence solutions because the input data set is based on known, constant DSD values, but the algorithm retrieves multiple values in the lower portions instead of the one correct value. An example of incorrect convergence is shown in Figure 3.8. An example of correct convergence is shown in Figure 3.4. It is clear that by reducing the amount of PIA the incorrect-solution-region boundary shifts upward. With $\mu = 1$ for all cases, the boundary line between the two regions has been approximated as

$$D_o = \left[a + \frac{b}{N_w^{0.5}} \right]^2 \tag{3.41}$$

where a = 0.9913, b = 23.21 for six bins (dash-dot line); a = 0.9922, b = 20.72 for nine bins (solid heavy line); and a =0.9989, b = 18.31 for 12 bins (dashed line).

Note that in all these data sets, the closed-loop dual-frequency algorithm converges properly and correctly calculates the $\tilde{Z}_{mi}(r_j)$ values. It is important to reiterate that even though the $\tilde{Z}_{mi}(r_j)$ values may be correct, the DSDs can be incorrect. Also note that the existence or not of a correct solution is not entirely dependent on the rain rate as it varies from about 12 mm/hr on the boundary line at the bottom right of the figure to about 18 mm/hr on the upper left assuming 12 bins.

The reason for two convergence regions lies in the D_o, N_w combination and the amount of inherent attenuation associated with a large D_o, N_w combination. Additionally, in the dual-wavelength algorithm, a Z_{mi} noise floor was set to 15 and 10 dBZ for the 13.6 and 35.6-GHz inputs respectively. It is clear that the total amount of PIA (relating to D_o, N_w) is a significant factor in determining whether or not the algorithm performs properly. By eliminating some of

the bottom points in high D_o, N_w combination data sets, the algorithm can be made to properly retrieve correct solutions. However, doing this also shortens the vertical profile eliminating valuable data.

The convergence tolerance was set to 0.01 % for these simulations in Figure 3.9. Changing the error tolerance, such as increasing it to say 0.1%, shifts the boundary region separators down reducing the area of the region of correct convergence.

Figure 3.10 shows two scatter plots of Z_e vs. Z_m from widely varying DSD pairs, with $\log(N_w)$, and D_o varying uniformly in the range, $3 \le \log(N_w) \le 5$, $0.5 \le D_o \le 2.5$, and $\mu = 1$. The computations were done for spherical water drops. (It is not necessary to assume spherical water drops but is done only for simplification purposes.) Figure 3.10(a) shows the results for 13.6 GHz and Figure 3.10(b) shows the results for 35.6 GHz. The simulation procedure directly calculates the specific attenuation, k_i, and effective radar reflectivity, Z_{ei} values from the above input DSD random variables. The Z_{mi} values are then calculated by subtracting the theoretical PIA from the effective radar reflectivity factor,

$$Z_{mi}(dBZ) = Z_{ei}(dBZ) - 2\,h\,M\,k_i \tag{3.42}$$

where h is the radar range resolution (0.25 km), M is the number of bins, and k_i is the specific attenuation (assumed constant over the range) in dB/km.

It is clear from the lower-left portions of both Figure 3.10(a) and (b) (ignore the upper-left portions where the Z_{mi} values wrap back), that at low reflectivity values, the Z_{ei} values are proportional to the Z_{mi} values, and Z_{ei} is a single-valued function of Z_{mi}. As the value of Z_{mi} increases however, the plots show that the retrieval algorithm can encounter a region or regions where multiple solutions exist for Z_{ei} and consequently for N_w and D_o. The multi-valued region is entered more quickly for the 35.6 than for 13.6-GHz signal. To illustrate how regions of correct and incorrect convergent solutions, as described and shown in Figure 3.9 relate to these

scatter plots, three D_o, N_w pairs of known retrieval response are marked on the plots as squares and diamonds on Figure 3.10.

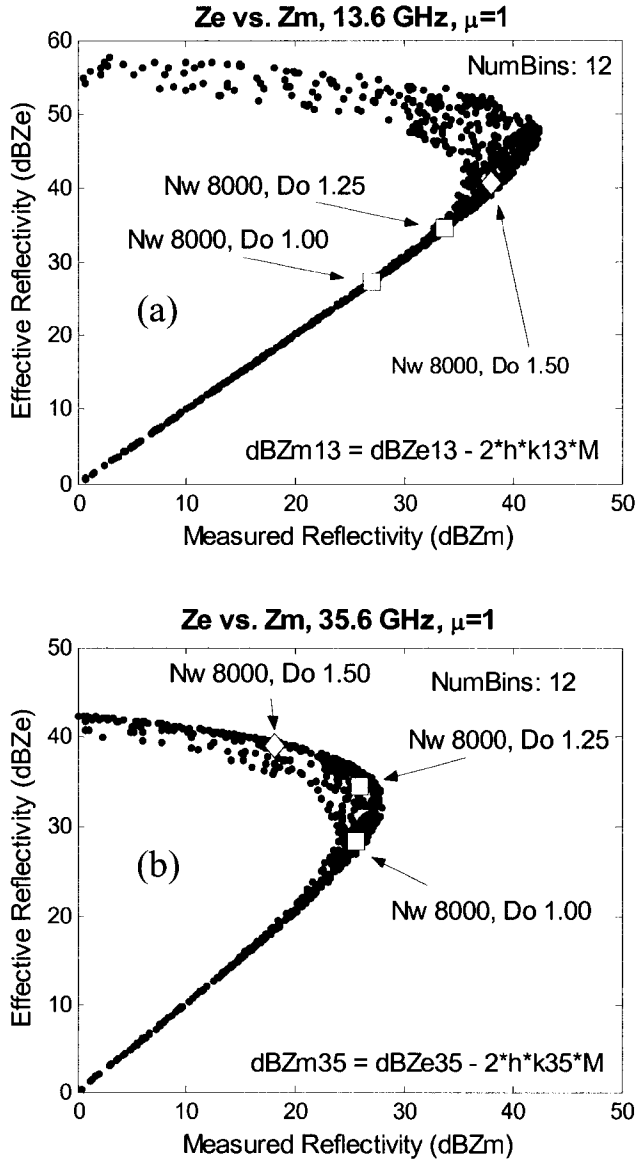

Figure 3.10. 1000-point scatter plots of effective versus measured reflectivity values based on random N_w and D_o values. Panel (a) is for 13.6 GHz, and panel (b) is for 35.6 GHz. The lower left portions of both curves show a one-to-one relationship between Z_m and Z_e, but at higher Z_m values, the Z_e solutions become multi-valued.

These pairs correspond to: N_w 8000, D_o 1.00; N_w 8000, D_o 1.25; and N_w 8000, D_o 1.50. Each pair has one point marked on the 13.6 GHz [Figure 3.10(a)] and another in the 35.6-GHz plot, [Figure 3.10(b)]. For the N_w 8000, D_o 1.00 pair, marked as squares, the 13.6-GHz point is

in the single-valued region on the lower part of the curve in Figure 3.10(a) and the 35.6-GHz point is in the multi-valued region in Figure 3.10(b). The algorithm properly retrieves this D_o, N_w pair and outputs a correct convergent solution.

For the N_w 8000, D_o 1.25 pair, marked as the middle squares, again the 13.6-GHz point is in the single-valued region on the lower portion of curve [Figure 3.10(a)] and the 35.6-GHz point is in the multi-valued region on Figure 3.10(b). The algorithm again retrieves the correct DSD values for this pair.

For the N_w 8000, D_o 1.50 pair, indicated as diamonds, both the 13.6 and 35.6-GHz points are in the multi-valued regions. As a result, the algorithm incorrectly retrieves the DSD values for this pair and does not yield the correct profile solution as is expected. From the simulations, it is shown that the single-loop algorithm retrieves the correct DSD values when at least one point of the D_o, N_w pair is in the singular-valued lower region. However, when both points fall in the multi-valued regions, then the algorithm incorrectly retrieves the DSD values.

It is clear that a combination of N_w, D_o and A_i limit the performance of the non-SRT dual-wavelength algorithm in retrieving correct DSD values. Leaving the N_w and D_o values as they are and simply decreasing the total attenuation that the algorithm must resolve can allow it to retrieve the correct DSD values. One way this can be done is by eliminating points from the bottom of the data set, but that will shorten the hydrometeor profile. Figure 3.11 shows two scatter plots that illustrate this concept. They are based on the same DSD values shown in Figure 3.10, but the number of bins, M, is varied to simulate truncating points from the bottom of a reflectivity data set. The lower curves are calculated using M = 10. Reducing the number of bins to M = 5, and M = 2, hence the two-way attenuation, shifts the curves up and to the right, effectively moving the multiple-value solution region up and to the right. The points, asterisk and diamond, on the graphs correspond to both straight and curved retrieval results for paired-input data.

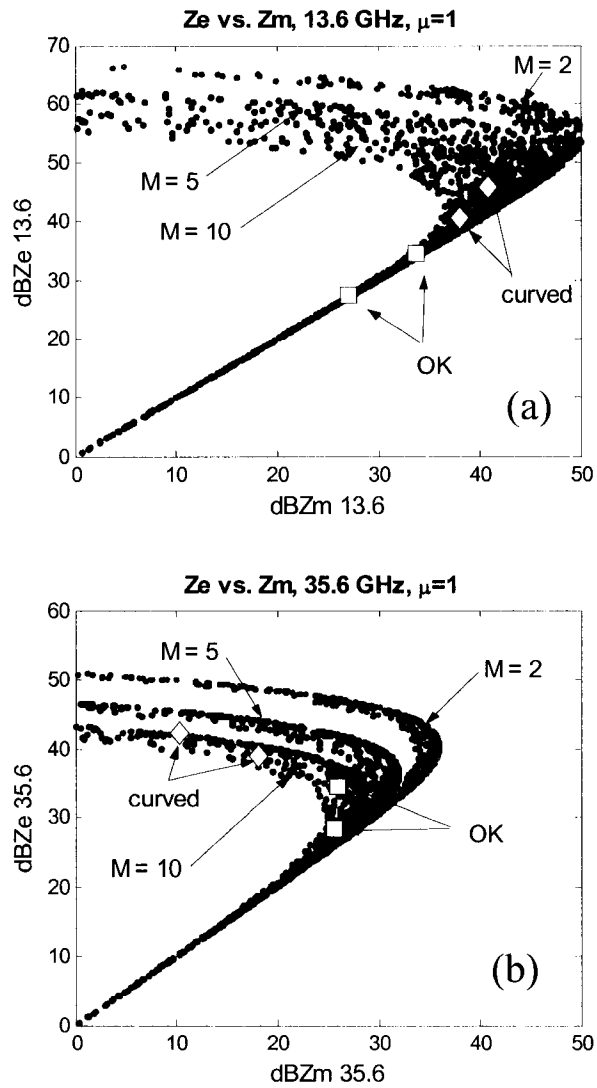

Figure 3.11. Scatter plot of measured and effective reflectivity as a function of PIA for 13.6 and 35.6 GHz. By reducing the number of bins, or PIA, the curves can be made to shift up and to the right and effectively reducing the multi-value solution region.

For example, a D_o, N_w pair that yielded an incorrect solution with $M = 10$, but provided a correct solution with $M = 5$. The same effect can be achieved by eliminating bins or points from the bottom of the profile.

3.5 NATURAL VARIABILITY OF DSD

Knowing that under high N_w, D_o, A_i conditions the single-loop dual-wavelength algorithm will incorrectly retrieve the DSD values and the rain-fall rate, it is important to determine what

percentage of rainfall is likely to be incorrectly retrieved if this algorithm is used. A joint distribution of D_o, N_w pairs was constructed using data from the global DSD variability study in [19]. The data set was constructed from long-term disdrometer observations from four locations, namely: Darwin, Australia; Graz, Austria; Florida, USA; and Papua New Guinea. The D_o, N_w distribution is shown as a scatter plot in Figure 3.12. The convergence-region boundary line described by (3.41) is superimposed to show the two regions of correct and incorrect retrievals.

Of the total D_o, N_w pairs analyzed, roughly 12% of them lie above the boundary line and will suffer from retrieval error. As a percentage of points, 12% is a relatively small number. However, when examining rain rate, the higher rain rates will be associated with the higher D_o, N_w pairs. It is useful to estimate what percent of global rain is affected by incorrect convergence.

To answer this question, some simplistic estimates and approximations are used. The D_o, N_w pairs in Figure 3.12 are assumed to be distributed around the globe. Rainfall rates above 10 mm/hr are assumed to be convective, and those less than 10 mm/hr are stratiform. In an attempt to apply proper scales to the data, convective rain-rate values are multiplied by 0.30 and stratiform values by 0.70 implying stratiform rain is encountered 70% of the time and convective 30% of the time [20]. Analyzing the four data sets under the simplistic assumptions, and applying the approximations above, shows that about half of the global rain falls in the region above the boundary line where the algorithm will incorrectly retrieve the DSD and rain-rate values. About half of the time, the dual-frequency algorithm will correctly determine the world-wide DSD and rain-rate values. The above numbers should be treated as very approximate estimates. On a global scale, this will be significant in the mission and system performance of GPM if only the single-loop, dual-frequency algorithm is used to estimate rain rate.

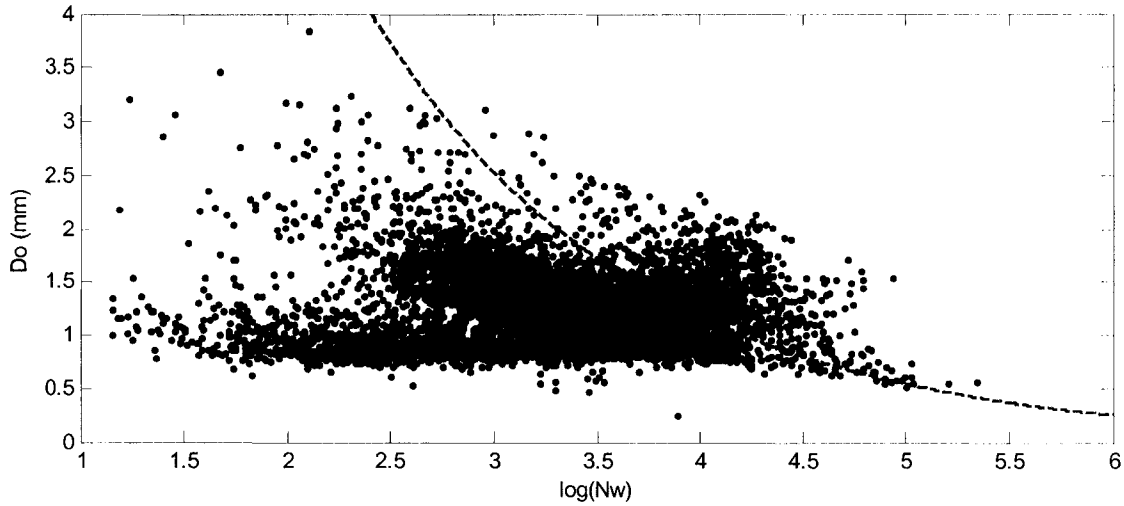

Figure 3.12. Scatter plot of disdrometer data from four regions of the world (Bringi et al. 2003). The boundary line between correct and incorrect convergence, assuming 12 bins, is superimposed to show which N_w, D_0 pairs the closed-loop algorithm will correctly retrieve. Data points below the line will be correctly retrieved and points above incorrectly.

3.6 SUMMARY AND CONCLUSIONS

This chapter has used a systems approach to develop and evaluate the space borne dual-frequency algorithm. To that goal, the governing equations for the dual-frequency method are redeveloped in terms of the normalized DSD parameters that are becoming increasingly popular. The self-consistent dual-frequency method relies on an iterative process to calculate the correct attenuation values in the bottom bins of the two rays and the DSD values in each bin.

A closed-loop feedback system with integral gain is used to retrieve the DSD parameters with an option to also use proportional gain. This system is further improved by replacing the attenuation with observed reflectivity in the feedback loop. The closed-loop system model with reflectivity feedback is directly connected to observations and lends itself to easier diagnostics. Using the closed-loop model developed here, the impact of measurement error on system convergence is studied. An ideal precipitation model with constant DSD in the vertical

dimension is studied for widely varying DSD parameters. Based on the uniform precipitation model, it is shown that the retrieval yields correct DSDs only if they fall in a certain region, defined by a combination of N_w, D_o and cumulative attenuation A_t. An empirical equation is developed to define the region of correct convergence.

It was shown that the closed-loop feedback model is applicable for about half of the global DSD values and will converge to the correct DSD values. The GPM DPR, in moderate to high rain rate regions, will be limited by both the large attenuation of the Ka-band signal as well as algorithm uncertainties caused by high D_o, N_w combinations where the closed-loop algorithm will be forced to operate in the multi-valued solution space.

CHAPTER 4

ITERATIVE RETRIEVAL METHOD WITH DSD PROFILE CONSTRAINT

4.1 INTRODUCTION

Results in Chapter 3 showed that the dual-frequency single-loop control-system retrieval model in Figure 3.3 can yield convergent but incorrect DSD values when the N_w, D_o, A_i combinations are large. This incorrect estimation of the true DSDs occurs when the solution space to the integral equations becomes multi-valued and the method has insufficient constraints to reach the correct solution. With reduced attenuation, such as deleted bins (data points) from the bottom, the correct N_w, D_o values can be retrieved in the higher bins with a corresponding reduction in vertical DSD profile. The factors in determining whether or not the algorithm will retrieve the correct solution are N_w, D_o and A_i.

It has been shown previously that about half of the global rain rate will be correctly retrieved by the iterative dual-frequency algorithm [21]. For those rainfall-rate situations that could be incorrectly estimated, this chapter describes a method to improve the retrieval performance of the iterative dual-frequency algorithm by constraining the vertical N_w profile to be linear in log scale, i.e., linear $\log(N_w)$. (Note that $log = \log_{10}$, and $ln = \log_e$).

This chapter is organized as follows. Section 4.2, introduces the concept of a dual-loop control-system model to be used for DSD retrieval using a vertical-profile constraint on N_w. The constraint is implemented on $\log(N_w)$ and employs a residual minimization algorithm as part of the outer dual-loop. The model is described and how it aids DSD retrieval. In section 4.3, four, incorrect-convergence-region test cases are analyzed to demonstrate the capability of

the technique. These test profiles are based on: 1) constant, vertical N_w, D_o; 2) sloped $\log(N_w)$, D_o; 3) sloped $\log(N_w)$, D_o with added measurement error; and 4) non-linear $\log(N_w)$ with linearly-sloping D_o. In each of these test cases, the single-loop model is first used to retrieve the DSD profiles which are then tested for region of convergence. The dual-loop model is then executed to retrieve the correct or "best fit" DSD values. It is demonstrated that even with significant measurement error, the proposed dual-loop constrained-$\log(N_w)$ model accurately retrieves the DSD values. Section 4.4 provides a summary of this chapter.

4.2 DUAL-LOOP CONSTRAINT

For almost half of the expected global rainfall the single-loop Z_{mi}-feedback method of Figure 3.3 will retrieve the correct DSDs and rain rate [21]. However, for the remainder of DSD pairs, an alternative procedure is required to obtain correct retrievals. Thus, for those D_o, N_w combinations that are in the incorrect-solution region (above the boundary line in Figure 3.9), an additional constraint (essentially an additional assumption about the DSD profile) is proposed to assist the iterative algorithm in retrieving the correct DSD profiles.

The additional constraint can be on any number of variables such as D_o, k_i, N_o, or N_w. In previous work, results using k_i as the additional constraint [22] were shown but a constraint on N_w is more general, and is preferred. Simulations and analyses show that in cases of high D_o, N_w, A_i combinations, where the single-loop algorithm does not correctly retrieve the DSD profiles, the $A_i(r_N)$ values in the bottom bins, after the iterative algorithm converges, are smaller than they should be. Also, in those same lower bins, the D_o is larger than it should be and the N_w values are smaller. The net effect, because the algorithm converges, is that the $\tilde{Z}_{mi}(r_j)$ values are correct throughout the retrieved profile while the DSD values are incorrect. This result can be illustrated by examining (3.35) where $\tilde{Z}_{mi}(r)$ is the product of $\tilde{Z}_{ei}(r)$ and $\tilde{A}_i(r)$. If $\tilde{A}_i(r)$ is smaller than expected and $\tilde{Z}_{ei}(r)$ is large than expected, $\tilde{Z}_{mi}(r)$ can still be correct.

Figure 4.1 shows a block diagram of the single-loop model expanded into a dual-loop feedback structure with the intent of forcing additional attenuation to both $A_i(r_N)$ values. Once again, the system construct developed in [21] enables easy modifications of the original single-loop system to a dual-loop system. The inner loop, on Z_{mi}, is the same as the single-loop method described earlier. The outer loop incorporates the constraint on $\log(N_w)$ by adding additional error (attenuation) to the summation block, in addition to that which would be added by the single loop on Z_{mi}.

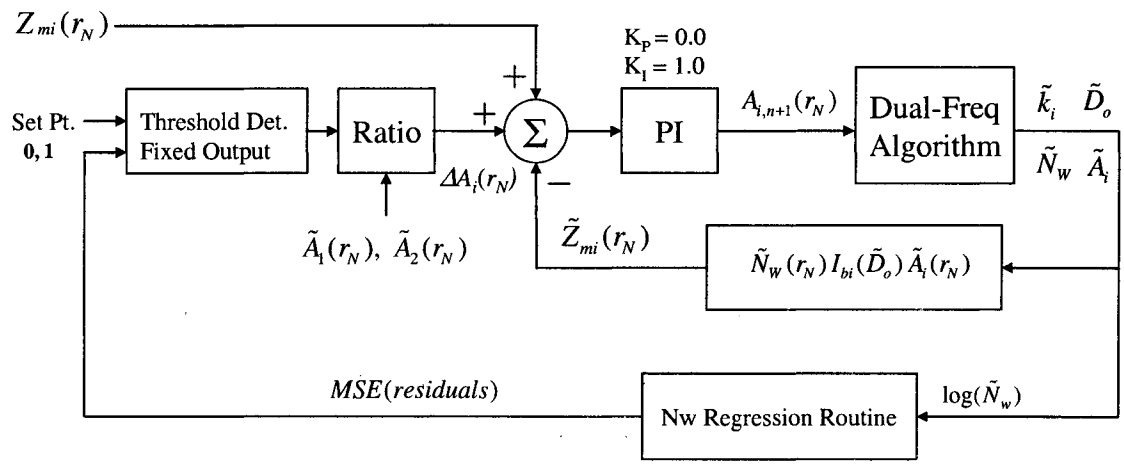

Figure 4.1. Block diagram of a dual-loop control-system model around the dual-frequency algorithm. The inner loop is the same as the single loop model and uses reflectivity as feedback. The outer loop is used to add an incremental amount of attenuation to each $A_i(r_N)$ value each iteration while monitoring the linear-regression fit of the retrieved $\log(N_w)$ profile. The model is stopped when the mean-square-error of the $\log(N_w)$-fit residuals is a minimum.

This is done by fitting the retrieved $\log(N_w)$ profile, measuring the residuals, and then using a ratio technique to add an incremental amount of error (attenuation), $\Delta A_i(r_N)$, each iteration. The threshold detector block is used to control the functioning of the outer loop. If the set point is low (e.g., a binary zero), the outer loop is turned off and the system reverts to the single-loop model of Figure 3.3. Setting the threshold to a binary one causes the outer loop to be activated.

4.2.1 Constraint on Nw

The iterative dual-frequency algorithm described in Chapter 3, [14], [21] theoretically allows significant bin-to-bin variability in the N_w, D_o profile values and imposes no specific

DSD profile constraints, i.e., whether or not the DSD profiles should adhere to any specific vertical profile function. It is clear that the constraint on linear $\log(N_w)$ is an approximation to actual N_w profiles, but empirical evidence suggests that it is a valid approximation for both convective and stratiform rain precipitation. In stratiform precipitation, it is understood that the $\log(N_w)$ profile can be approximated as either constant or linearly varying with altitude. Several precipitation regions, coincident with both the Tropical Rainfall Measuring Mission (TRMM) Precipitation Radar (PR) overpass and ground radar measurements, have been studied and the DSD profiles estimated giving results that show that the ground radar and PR both estimated the $\log(N_w)$ profile to be approximately linear in the rain region [23]. In fact, the TRMM PR-derived N_w profile was constant in those analyses. Bringi et al. [16] showed that $\log(N_w)$ can also be reasonably approximated by a linear vertical profile for a convective storm beginning at the early growth phase and developing into an intense microburst. Stratiform precipitation is less variable than convective, consequently, the linear approximation seems to be a reasonable assumption. Constraints could also be imposed on D_o profiles, but in order to add a minimal number of constraints to the DSD profiles and to the iterative algorithm, only the $\log(N_w)$ constraint is implemented in this work and the D_o profile is allowed to vary as calculated by the algorithm.

4.2.2 Minimize Residuals Method

The proposed method for adding an additional constraint on $\log(N_w)$ (an additional control method loop on N_w) is a four-step process:

4.2.2.1 Step One

The dual-loop model of Figure 4.1 is first executed as a single-loop model with the outer feedback-loop turned off. After running the algorithm using only $\tilde{Z}_{mi}(r_N)$ as feedback, and determining if the DSDs in the top bins are in the incorrect-convergence region using (3.41),

and are therefore likely to be in error in the lower bins, then the N_w-constraint method can be implemented. The top bins (or the top bin) are used for region testing because the attenuation levels are lowest, the DSD values are the most correct in those bins (even after one or just a few iterations), and based on simulations, they indicate the likelihood and magnitude of incorrect DSD values below.

The $\tilde{A}_i(r_N)$ values at the completion of *Step One* in the process, even though too small (i.e., too little attenuation) if the solution is in the incorrect convergence region, are used as seed inputs to *Step Two* such that it begins the attenuation estimation process where the first step ended.

4.2.2.2 Step Two

The dual-loop model is run with the outer-loop enabled. During each iteration, a linear least-squares fit of the retrieved log(N_w) profile is performed, the mean-square-error (MSE) of the residuals is calculated, and a small amount of attenuation is added to each $\tilde{A}_i(r_N)$ based on the relative magnitude of each $\tilde{A}_i(r_N)$. The MSE of the residuals is calculated as

$$MSE(n) = \sqrt{\frac{1}{N}\sum_{j=1}^{N}\left\{\log\left[N_{W,R}(r_j)\right] - \log\left[N_{W,F}(r_j)\right]\right\}^2} \tag{4.1}$$

where N is the number of bins, n is the iteration number, $N_{W,R}(r_j)$ are the retrieved $\tilde{N}_W$ values, and $N_{W,F}(r_j)$ are the fitted N_w values. Because the $\tilde{A}_i(r_N)$ values for the two frequencies can be significantly different in magnitude, e.g., for a uniform-vertical-rain column, 2.5-km in height, based on N_w = 4000 and D_o = 2.00, $\tilde{A}_1(r_N)$ = 3.80 dB and $\tilde{A}_2(r_N)$ = 18.95 dB, it is necessary to properly apportion the incremental attenuation $\Delta A_i(r_N)$ and add an amount to each frequency according to,

$$\Delta A_1(r_N) = \frac{\tilde{A}_{1,n}(r_N)}{\tilde{A}_{1,n}(r_N) + \tilde{A}_{2,n}(r_N)}\Delta A_{N_w} \tag{4.2}$$

$$\Delta A_2(r_N) = \frac{\tilde{A}_{2,n}(r_N)}{\tilde{A}_{1,n}(r_N) + \tilde{A}_{2,n}(r_N)} \Delta A_{N_W} \tag{4.3}$$

where ΔA_{N_W} is a fixed amount of error (attenuation) based on the MSE of the residuals calculated from (4.1). In this manner, apportioned attenuation is added to each $\tilde{A}_i(r_N)$ while maintaining convergence of $\tilde{Z}_{mi}(r_j)$ and $Z_{mi}(r_j)$ within the inside loop.

The underlying principle of the dual-loop mode is that a minimum in the MSE of the residuals, where the $\log(\tilde{N}_W)$ profile is linear or nearly linear, can be found by scanning the solution space of $\tilde{A}_i(r_N)$. Iterations cease when a predefined number of iterations is reached or the $\tilde{A}_i(r_N)$ values are increased to a preset level—typically a percentage of the initial value found in *Step One*.

4.2.2.3 Step Three

In this step, the array of MSE(n) values that was created in *Step Two* is analyzed to find the iteration number of the minimum fit error. The index number of the minimum MSE is extracted and provided to *Step Four*.

4.2.2.4 Step Four

The dual-loop algorithm, using the final $\tilde{A}_i(r_N)$ values from *Step One*, is then re-run and stopped at the index of the minimum MSE iteration number, i.e., n = index of minimum MSE. The retrieved DSD profiles are then based both on the best linear fit of the $\log(N_w)$ profile and on the Z_{mi} input profiles. At present, the algorithm and method to find the minimum MSE of the residuals is preliminary and still being developed but shows good promise for those cases that require an additional constraint.

4.3 TEST CASES

Hundreds of simulations have been analyzed using various combinations of N_W, and D_o both with and without simulated measurement error. To demonstrate the performance of the

dual-loop method for DSD retrieval in the incorrect region of convergence, four representative D_o, log(N_w) vertical-profile examples are described in the following paragraphs—one each for constant, sloped, sloped with measurement error, and non-linear log(N_w).

4.3.1 Constant Do, Nw

Single-Loop Retrieval: Figure 4.2 shows the input reflectivity and retrieved profiles of a simulated uniform rain column, 2.5-km in height, using N_w = 4000, D_o = 2.0 after applying the single-loop Z_{mi} method described in Figure 3.3 (or *Step One* of the N_w constraint method).

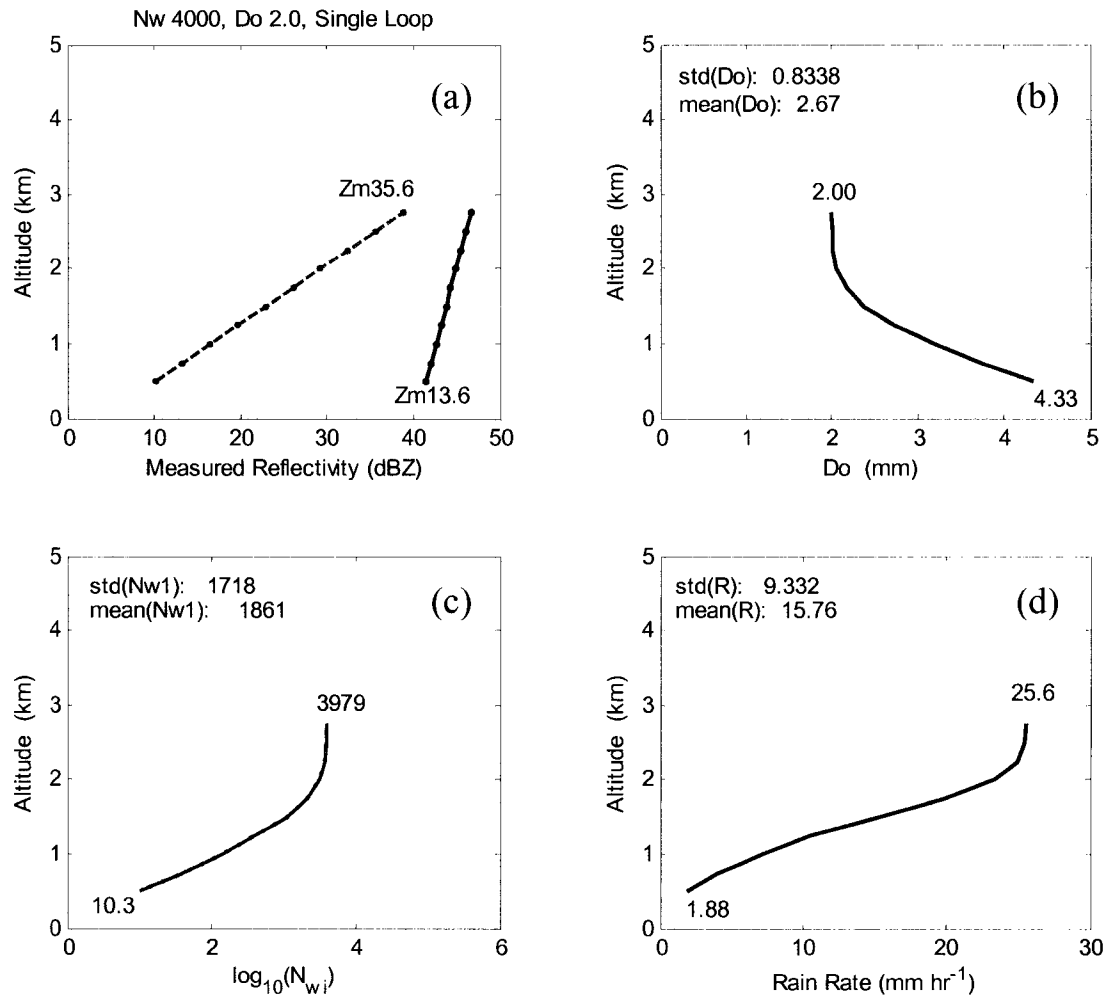

Figure 4.2. Plots of simulated results for a uniform vertical rain column 2.5-km in height (10 bins x 0.25 km) above a 0.5-km base showing incorrect DSD retrievals using the single-loop Z_{mi} feedback method. Part(a) shows the input Z_{mi} values. Parts (b),(c),(d) show the profiles for D_o, N_w, and rain rate. For this D_o, N_w combination (N_w = log(4000), D_o = 2) there is significant error in the bottom bins. Convergence tolerance is 0.01 percent.

The bottom bins clearly suffer from incorrect DSD retrieval as a result of incorrect $\tilde{A}_i(r_N)$. Figure 4.2(b) shows that the D_o profile varies widely from 2.0 at the top to 4.33 mm at the bottom, and Figure 4.2(c) shows that the retrieved N_w values vary from 3979 at the top to about 10 at the bottom. Figure 4.2(d) shows the rain profile varying from 25.6 at the top to about 1.9 mm/hr at the bottom, a 93% underestimation of the rain rate in the bottom altitudes.

At the top bin, the retrieved DSD values are N_w = 3979 and D_o = 2.00. Using (3.41) with 12 bins, and retrieved N_w = 3979 and solving for D_o, gives D_o = 1.66 mm which is less than the retrieved value of 2.00. Because the retrieved D_o value exceeds the maximum allowable threshold value, we conclude that this particular N_w, D_o combination is in the incorrect convergence region. By comparison, at the bottom bin, N_w = 10.3, D_o = 4.33, and assuming 12 bins, (3.41) indicates that the maximum allowable D_o is about 45 mm showing that D_o = 4.33 mm is in the correct convergence region. However, a D_o of 4.33 mm though not impossible, is very unlikely. The upper bound of 45 mm is impossible thus indicating that this test for region of convergence should be discounted.

N_w Constraint: Implementing the dual-loop model described above, the MSE of the residuals was calculated at each iteration, n, up to and including the iteration index of the minimum MSE of the residuals. The results are shown in Figure 4.3 for the same uniform vertical rain column retrieved DSD profiles. The inner-loop convergence tolerance is 0.01 percent. Figure 4.3(b) shows the correct D_o profile at a constant 2.00 mm and Figure 4.3(c) shows the correct N_w profile. Rain rate is shown in Figure 4.3(d) and is constant at 25.6 mm/hr. This is a moderately-high rain rate and will be measurable through most, but not all, of the rain region because of the associated large attenuation of the Ka-band signal. This phenomenon is demonstrated in Figure 4.3(a) where the Ka-band signal is attenuated to approximately its noise floor. The noise floor was set to 15 and 10 dBZ, for the 13.6 and 35.6-GHz rays, respectively.

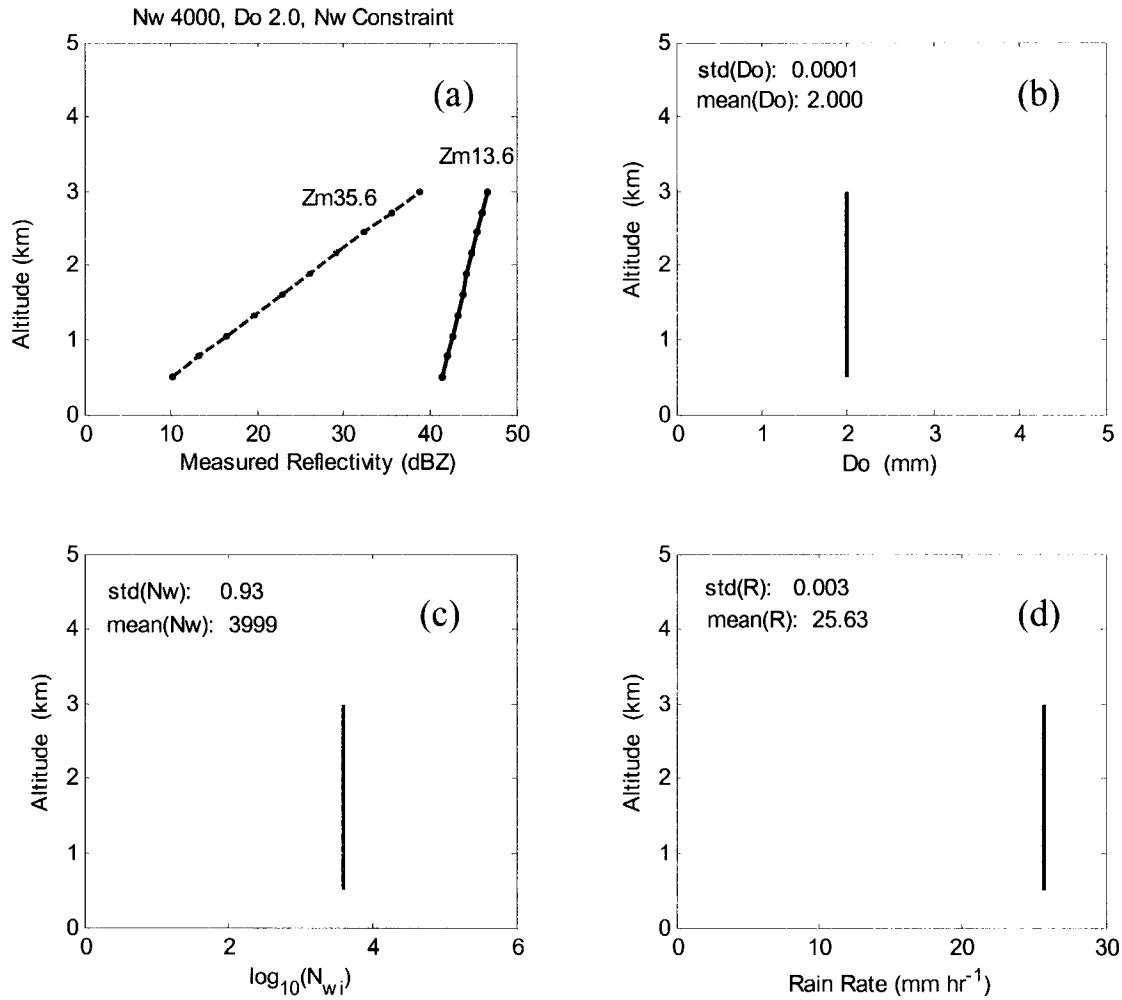

Figure 4.3. Simulated results for a uniform vertical rain column 2.5-km in height (10 bins x 0.25 km) above a 0.5-km base showing correctly retrieved DSD values using an additional constraint on linear log(N_w). Part(a) shows the input reflectivity values, part(b) shows the correctly retrieved D_o profile. Parts(c), (d) show the correct N_w and rain rate profiles. Convergence tolerance is 0.01 percent. N_w = log(4000), D_o = 2.

4.3.2 Linear Do and log(Nw) Profiles, No Error

Single-Loop Retrieval: In this example, the retrieval process for a linearly-varying DSD profile based on N_w: log(4000)-log(8000) and D_o: 1.75-1.60 for a vertical rain column 3.0-km in height is demonstrated. The D_o, N_w combinations chosen at the top and bottom are both in the incorrect-convergence regions and are impossible to correctly retrieve using the single-loop method. Figure 4.4 shows the retrieved DSD and rain-rate profiles with a 0.01% convergence tolerance using the single-loop method.

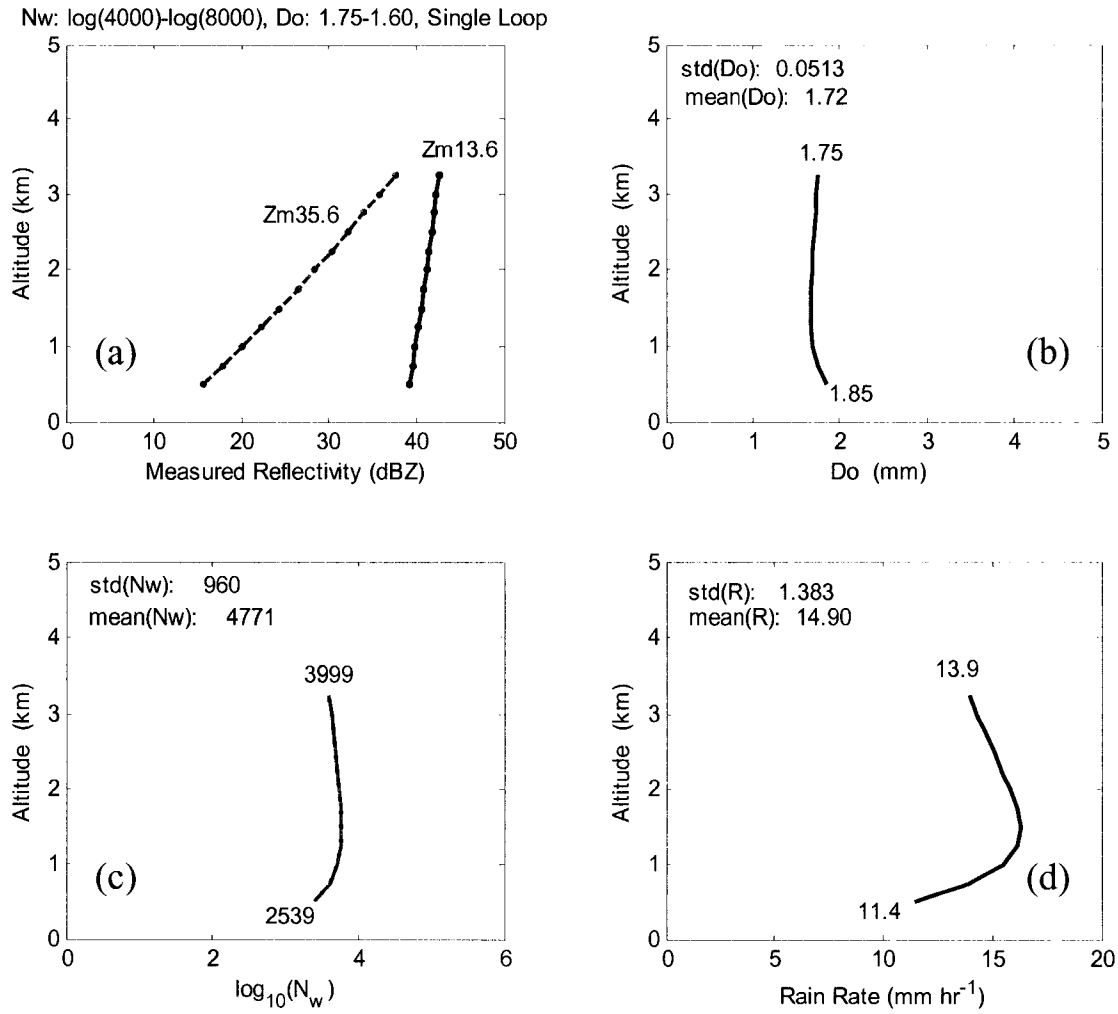

Figure 4.4. Graphic showing the retrieval results for a vertical rain column 3.0-km in height (12 bins x 0.25 km) above a 0.5-km base using the single-loop method for sloped N_w: log(4000)-log(8000), D_o: 1.75-1.60. Parts (b-d) show incorrect retrieval in the lower bins. At the top bin, the D_o, N_w combination exceeds the values used to test for region of correct convergence. Convergence tolerance is 0.01 percent.

Figure 4.4(b) shows that there is considerable non-linear variation in the D_o profile with it ranging from 1.75 at the top to 1.85 mm at the bottom when it should vary between 1.75 and 1.60 mm. Figure 4.4(c) shows the distortion in the retrieved N_w profile, and Figure 4.4(d) shows significant inaccuracies in the retrieved rain profile. Testing the N_w, D_o combination at the top bin using (3.41) gives a maximum allowable D_o of 1.66 mm which is less than the retrieved D_o of 1.75 mm. We conclude that the top bin is in the incorrect convergence region

and that the bottom bins are retrieved incorrectly and the N_w constraint should be implemented via the dual-loop model.

N_w Constraint: Using the final values of $\tilde{A}_i(r_N)$ from the single-loop retrieval, the dual-loop algorithm with the additional N_w constraint was executed. The retrieved DSD profiles, with minimum MSE, based on the same vertical rain column 3.0-km in height are shown in Figure 4.5.

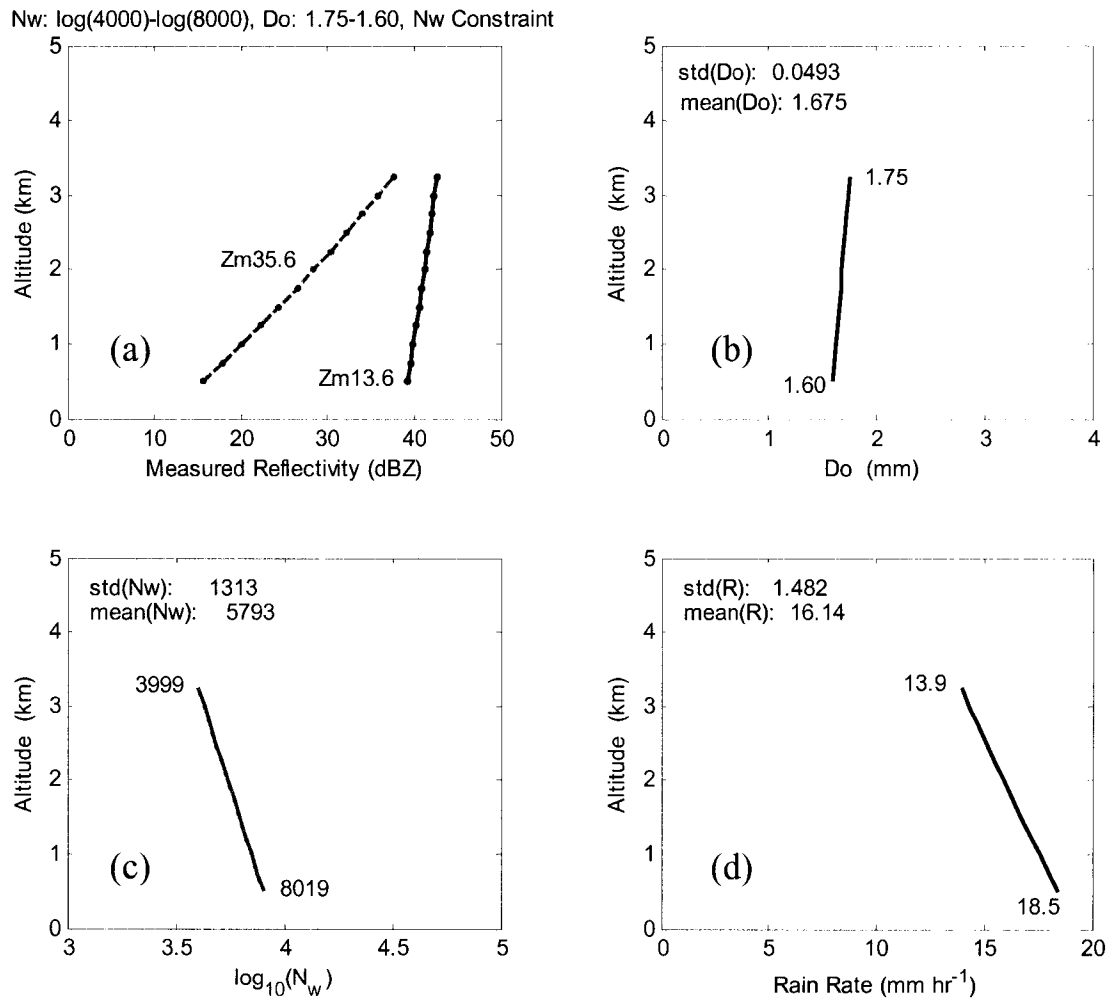

Figure 4.5. Graphic showing correctly retrieved DSD values (N_w: log(4000)-log(8000), D_o: 1.75-1.60) for a vertical rain column 3.0-km in height above a 0.5-km base using the linear-log(N_w) constraint. Part(b) shows the D_o profile, part(c) the correct N_w values, and part(d) shows the correct rain rate profile. The dual-loop method was run till iteration 110 and stopped at the minimum of the residuals. Convergence tolerance is 0.01 percent.

The inner-loop convergence tolerance is 0.01 percent. Figure 4.5(b) shows the correct, linear D_o values ranging from 1.75 at the top to 1.60 mm at the bottom, and Figure 4.5(c) shows the correct N_w profile. The correct rain-rate profile is shown in Figure 4.5(d). It is clear that constraining $\log(N_w)$ allows the algorithm to find the correct DSD values. This retrieval simulation was done with no added measurement error and was accurate in its results.

4.3.3 Linear Do, log(Nw) Profiles with Measurement Error

Single-Loop Retrieval: In this DSD-profile retrieval example, random-error sampled from a 0.5-dB standard-deviation, zero-mean Gaussian distribution, was added to each bin of the 3-km high, N_w = log(4000)-log(8000), D_o: 1.75-1.60, vertical-rain-column reflectivity profiles used in the previous case study. After adding measurement error to each bin of each ray, the overall error in each reflectivity profile is characterized by computing the standard deviation of the difference between the error-laden and the error-free profile at each bin. Because the added error is randomly sampled from a statistical distribution, the amount of error in each reflectivity profile will vary from simulation to simulation. In this case, the actual standard deviation of the 13.6-GHz error is 0.47 dBZ, and the standard deviation of the 35.6-GHz error is 0.35 dBZ. The single-loop method was executed first to extract the DSD and rain-rate profiles shown in Figure 4.6. Figure 4.6(a) shows the input reflectivity profiles at 13.6 and 35.6 GHz with added error. Figure 4.6(b) shows the retrieved D_o profile. With no measurement error, it should begin at 1.75 mm at the top and linearly decrease to 1.60 mm at the bottom bin. From the retrieved profile, there is a considerable amount of distortion and obvious incorrect retrieval of D_o in the lower bins. Testing for region of convergence at the top bin using (3.41), gives a maximum allowable D_o of 1.70 which is less than the retrieved value of 1.84 mm. We conclude that the top bins are in the incorrect region of convergence and the lower bins are incorrectly estimated. Figure 4.6(c) shows the incorrectly retrieved $\log(N_w)$ profile. As an additional test of the

validity of the single-loop DSD retrievals, the N_w and D_o bottom-bin values from the single-loop method are examined.

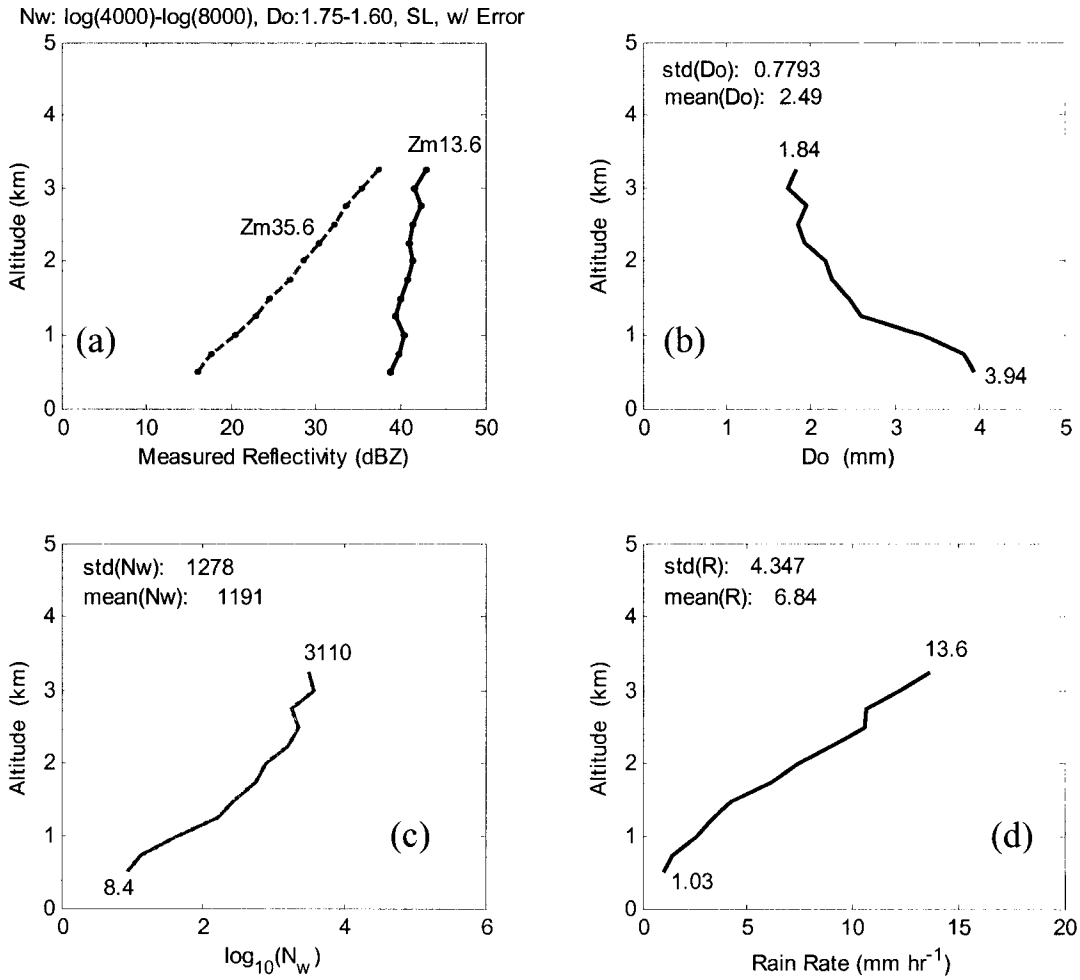

Figure 4.6. Plots of retrieved values for a sloped combination N_w: log(4000)-log(8000), D_o: 1.75-1.60 for a vertical rain column 3.0-km in height above a 0.5-km base using the single-loop Z_{mi} model with added 0.5-dBZ standard-deviation random error in each reflectivity bin. Convergence tolerance is 0.01 percent. Standard error of Z_{m1} is 0.47, and of Z_{m2} is 0.35 dBZ.

D_o is unrealistically large, and N_w is unrealistically small. Again, these values indicate that the single-loop method has not retrieved correct values. The rain-rate profile is shown in Figure 4.6(d). It can be compared to the correct rain rate profile, with no error, in Figure 4.5(d) where the values range from 13.9 to 18.5 mm/hr. It is clear that additional measurement error can greatly influence the accuracy of the retrieved values.

N_w Constraint: Using the final $\tilde{A}_i(r_N)$ values from the single-loop simulation, the dual-loop algorithm was run with the additional N_w constraint. It should be noted here that with error in the reflectivity data, the index of the minimum MSE(residual) is not as pronounced or well defined as in the error-free case. Nevertheless, there is a clear MSE minimum. The results from the dual-loop method are shown in Figure 4.7.

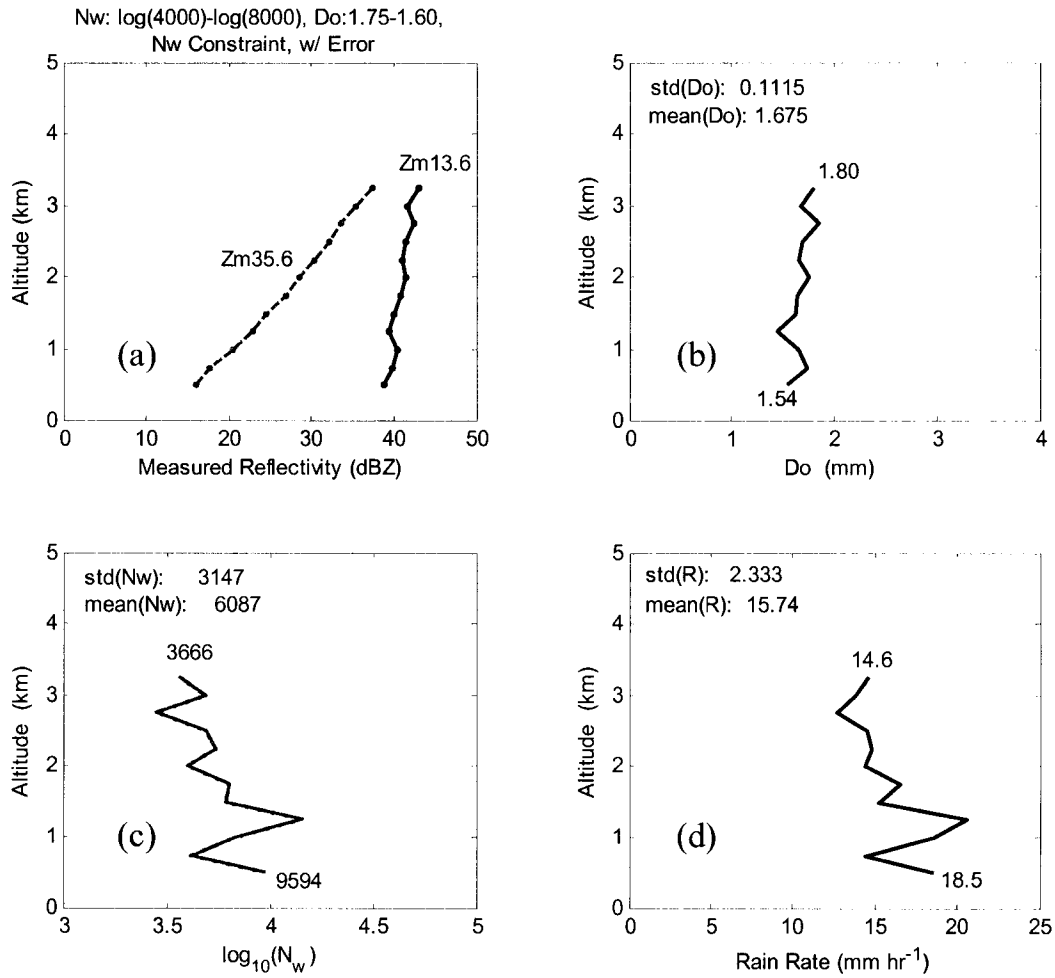

Figure 4.7. Graphic showing retrieved outputs for a vertical rain column 3.0-km in height above a 0.5-km base using N_w: log(4000)-log(8000), D_o: 1.75-1.60 with added measurement error using the dual-loop method with a linear constraint on Log(N_w). In this case, iterations cease at 124 where the MSE(residuals) is a minimum. Convergence tolerance is 0.01 percent. Standard error with respect to true profiles on Z_{m1} is 0.47, and on Z_{m2} is 0.35 dBZ.

Figure 4.7(b) shows the retrieved 3-km-high D_o profile ranging from 1.80 mm at the top to 1.54 mm at the bottom. The expected values with no measurement error are 1.75 and 1.60 mm.

Figure 4.7(c) shows the log(N_w) profile, which is expected to vary linearly from log(4000) at the top to log(8000) at the bottom (3.602 to 3.903 in log scale), varying from log(3666) to log(9594). The rain profile is shown in Figure 4.7(d) and can be compared to expected values of 13.9 to 18.5 mm/hr. In comparing these error-laden, N_w-constrained retrieved DSD with the error-free N_w-constrained profiles, it is clear that there is a strong correlation in values and slopes between the two cases. However, because of the measurement error, the two profiles will not agree exactly.

To illustrate some of the uncertainty in the dual-loop method with added measurement error, it is useful to examine a profile of log($\tilde{N}_W$).

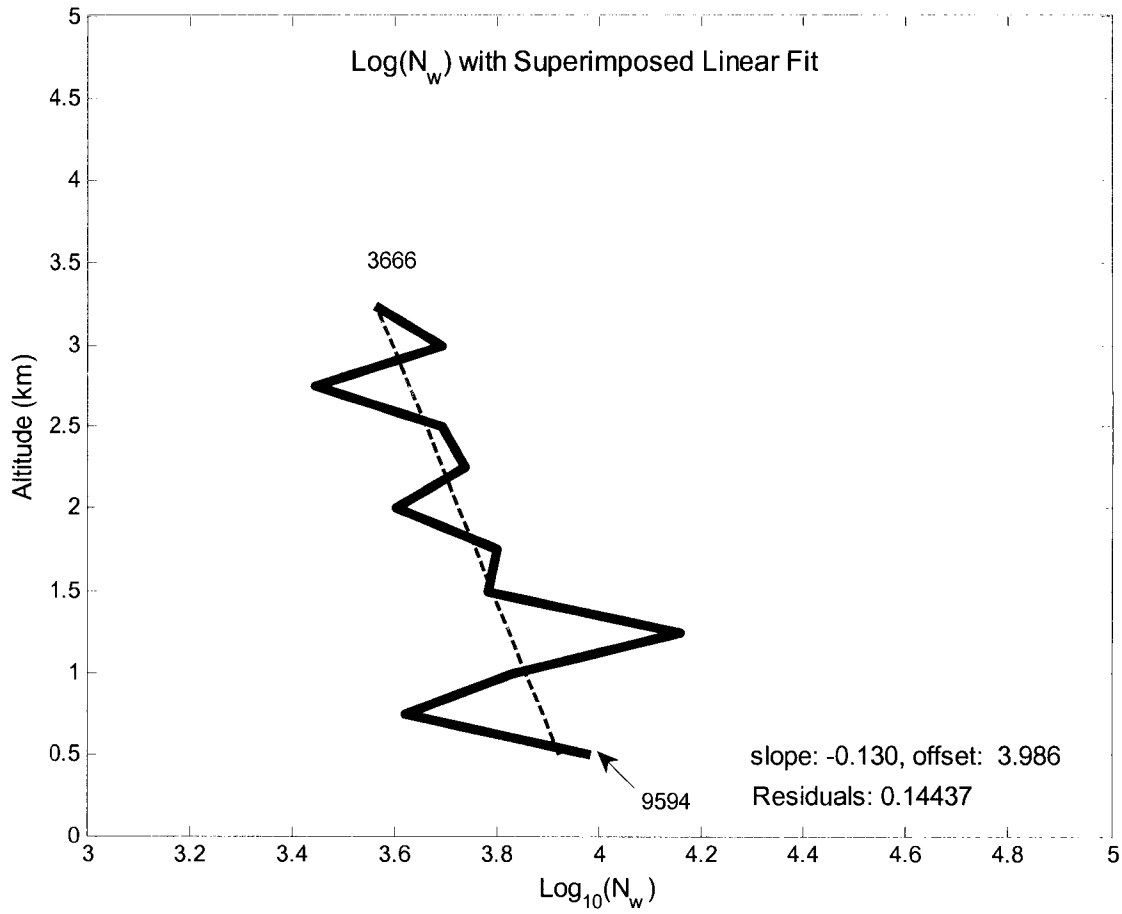

Figure 4.8. Graphic showing the retrieved log(N_w) profile with the superimposed linear-least-squares fit line at the final iteration value of 124 as used in the outer loop. Because of added measurement error, it is impossible that the two would be exactly the same, but there is an overall agreement between the two.

Figure 4.8 shows the retrieved log($\tilde{N}_W$) profile for the final iteration value of 124 along with the superimposed least-squares linear-fit line. The additional uncertainty in Z_{mi} causes significant bin-to-bin error, but the overall trend and top and bottom retrieved values are close to expected values.

4.3.4 Linear Do, non-linear Log(Nw) profiles

In this example, to contrast the cases shown for linear profiles, we demonstrate how the dual-loop model performs when the log(N_w) profile is not linear in its vertical profile. Though myriad combinations are possible, the log(N_w) profile is arbitrarily modelled using a second-order polynomial equation such that the top bin starts at log(4000), the bottom bin ends at log(8000) and a non-linear perturbation of log(6500) occurs in the middle. The D_o profile is as before, 1.75 at the top, linearly decreasing to 1.60 mm at the bottom. For brevity, the results from the single-loop retrieval have been omitted which show significant errors in the retrievals of D_o, log(N_w) and of course estimated rain rate. The bottom, retrieved values from the single-loop method were: D_o = 2.23, log(N_w) = log(609), and rain rate = 6.4 mm/hr. Expected or true values were: D_o = 1.60, log(N_w) =log(8000), and rain rate = 18.4 mm/hr. The top-bin retrieved values for D_o, log(N_w) and rain rate were in agreement with expected values.

Figure 4.9 shows the retrieval results from the dual-loop method. Figure 4.9(a) shows the input reflectivity profiles for 13.6 and 35.6 GHz for a 3-km in height rain column. Figure 4.9(b) shows the retrieved D_o profile. The top bin is correct, and the bottom bin is slightly underestimated at 1.56 mm (true value is 1.60 mm). Figure 4.9(c) shows the retrieved (solid line) and simulated non-linear log(N_w) (dashed line with dots) profiles. The bottom, N_w value is expected to be 8000 but is overestimated at 9829. The retrieved and simulated log(N_w) profiles agree over most of the profile but deviate in the lower bins. Figure 4.9(d) shows the simulated (dashed-line with dots) and retrieved rain (solid line) profiles. In this example, the retrieved rain rate is slightly overestimated in the bottom bin at 20.1 mm/hr while the true value is 18.4

mm/hr. The top-bin rain-rate expected and retrieved values are in agreement. Given the assumption that the dual-loop model assumes a linear profile for $\log(N_w)$, it is reasonable that the retrieved and expected DSD values differ somewhat. However, it is important to note that the dual-loop method retrieved significantly more accurate results for the DSDs and rain rate than the single-loop method even with a non-linear $\log(N_w)$ profile. One reason for this improvement in performance is that the dual-loop method fits a "best estimate" to the $\log(N_w)$ profile.

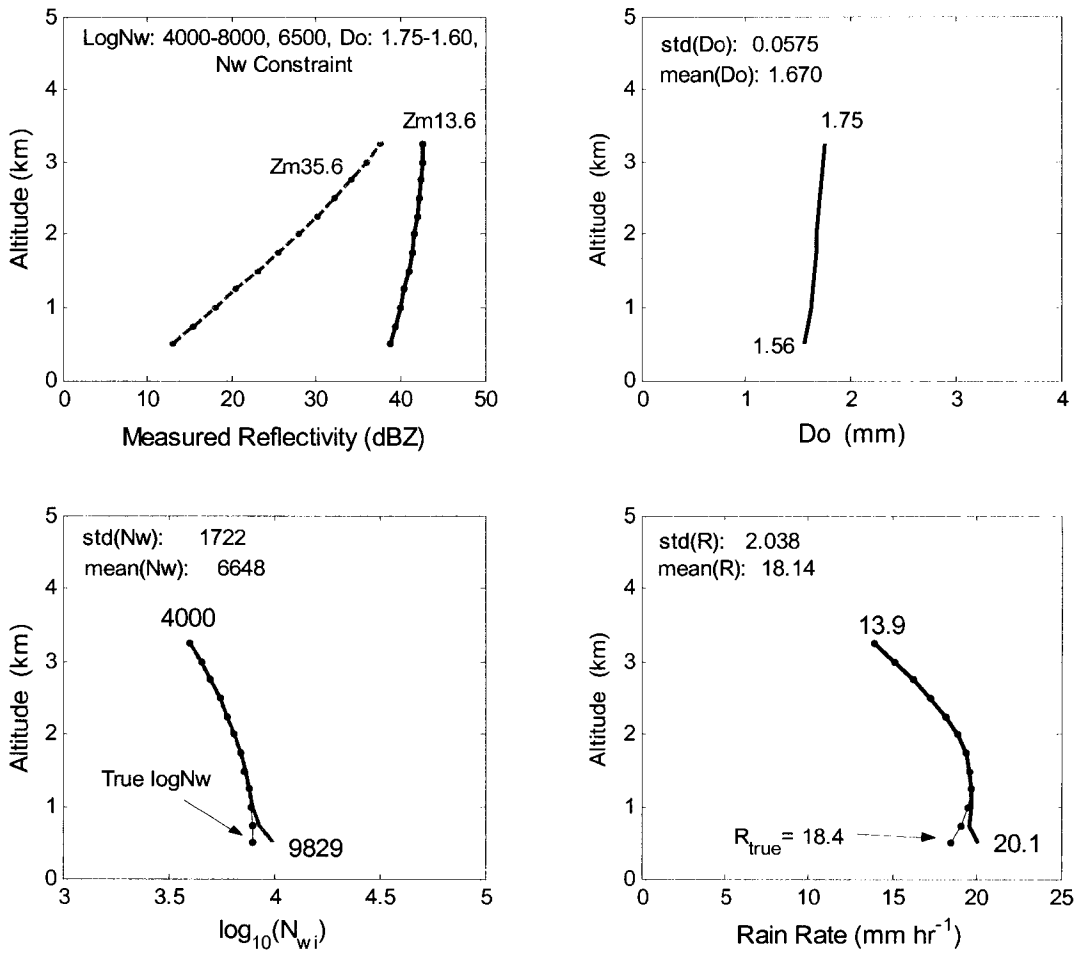

Figure 4.9. Plots showing input and retrieved profiles for a vertical rain column 3.0-km in height above a 0.5-km base using the linear-$\log(N_w)$ constraint. Profiles based on N_w: log(4000)-log(8000) with a mid-range perturbation of log(6500); D_o: 1.75-1.60. Part(a) shows the 13.6 and 35.6-GHz measured reflectivity profiles. Part (b) shows the retrieved D_o profile. Both the simulated (dashed with dots) and retrieved (solid) N_w profiles are shown in part (c). The simulated (dashed with dots) and retrieved (solid line) rain profiles are shown in part (d). The dual-loop method was run till iteration 556 and stopped at the minimum of the residuals. Convergence tolerance is 0.01 percent.

The retrieved log(N_w) profile (solid line) at the final iteration of 556 is shown in Figure 4.10 along with the linear fit of the retrieved log(N_w) (dashed line) and the true log(N_w) profile (dashed with asterisks). Note that in spite of the linear-fit assumption, the dual-loop method is able to correctly retrieve nearly all the N_w profile as it deviates only in the bottom bins. In comparing the linear fit and the retrieved log(N_w) profiles, the algorithm provides a best estimate of the retrieved log(N_w) profile.

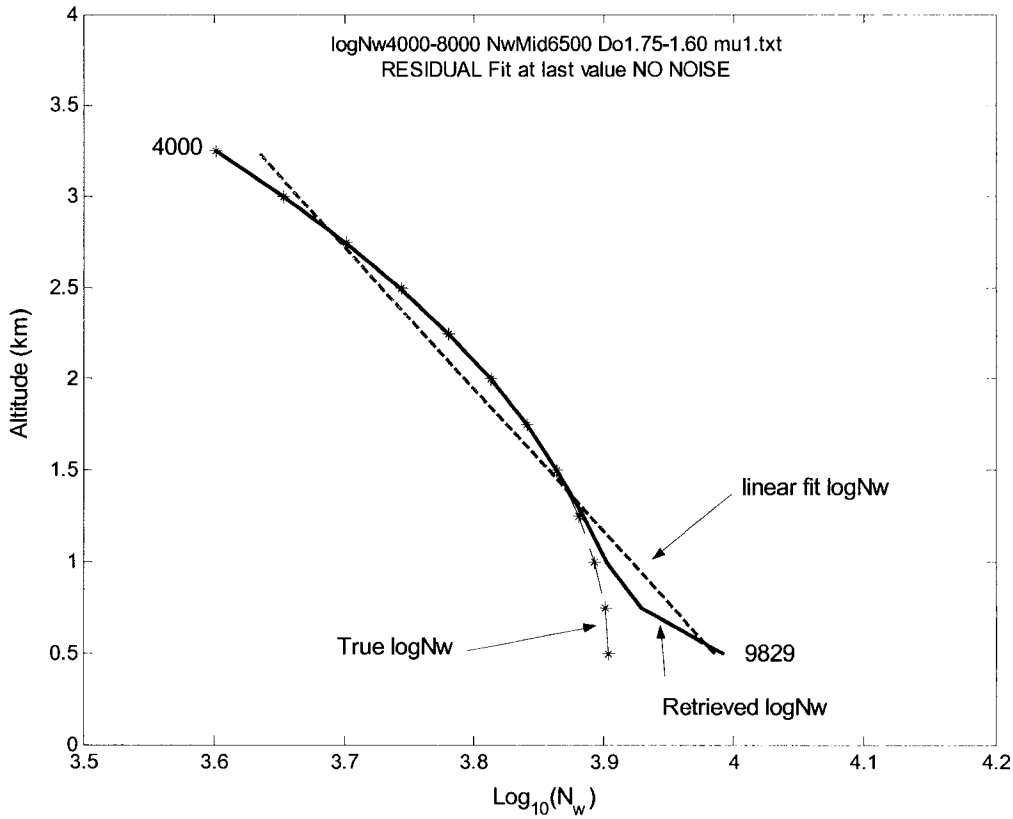

Figure 4.10. Graphic showing the retrieved log(N_w) profile along with a superimposed linear-least-squares fit line at the final iteration value of 556. The retrieved Log(N_w) profile is the solid line, the fit is the dashed, and the true log(N_w) profile is the dashed-asterisk curve. This fit is based on a non-linear log(N_w) profile.

4.4 SUMMARY AND CONCLUSIONS

The GPM DPR, in moderate to high rain-rate regions, will be limited by both the large attenuation of the Ka-band signal as well as algorithm uncertainties caused by high D_o, N_w combinations where the single-loop Z_{mi} algorithm will be forced to operate in the multi-valued

solution space. From previous work, about half of the global rainfall rates (based on DSD pairs) fall in the correct convergence region in which the single-loop Z_{mi}-feedback model will correctly retrieve the DSDs [21]. Using the same single-loop Z_{mi}-feedback model for the other half will yield incorrect DSD values and incorrect rain-rate estimates in the lower profile regions.

To better estimate global rain fall using the dual-frequency algorithm, an additional constraint is proposed for operation in those regions where the D_o, N_w combination is large. This chapter has shown a method to impose a linear constraint on $log(N_w)$, and shows results using that method, and that it can yield marked improvement in DSD estimation when required due to incorrect convergence of the single-loop method.

Four test cases were examined and discussed. In the first case, a constant vertical rain column based on a D_o, N_w combination from the incorrect convergence region was analyzed using the single-loop method resulting in incorrect DSD-profile retrieval. The data were then analyzed using the dual-loop method and correct DSD profiles were retrieved. In the second case, a simulated data set from the incorrect convergence region consisting of linearly-sloped D_o, $\log(N_w)$ profiles was examined. It was first analyzed using the single-loop method and then with the additional constraint on linear $\log(N_w)$. In the third test case, the same linearly-sloped D_o, $\log(N_w)$ profiles were analyzed with added random measurement error of 0.5-dBZ standard deviation, zero mean, added bin-by-bin, to each reflectivity profile. Using the linear-$\log(N_w)$ constraint, the dual-loop algorithm was able to retrieve reasonable DSD and rain-rate profiles. In the fourth case, a non-linear $\log(N_w)$ profile was examined. It was shown that the dual-loop method found a best estimate to the non-linear N_w profile and estimated reasonable values for the DSDs and rain-rate profiles.

Based on empirical evidence, the vertical profile of $\log(N_w)$ can be reasonably approximated as linear. In the estimation or retrieval process, any non-linearity of $\log(N_w)$ profiles (non-compliance with the linear-model assumptions) will contribute to the error in the

retrieval. Note that if the true profile of $\log(N_w)$ is not linear, the solution presented here will yield an equivalent linear $\log(N_w)$. It should be mentioned that this chapter and similar research should be placed in the context of dual-wavelength retrieval of precipitation estimates for the GPM era.

CHAPTER 5

RETRIEVAL ALGORITHM: DSD PROFILE OPTIMIZATION METHOD

5.1 INTRODUCTION

This chapter describes an alternative, dual-frequency, random-restart, four-variable profile-optimization method for DSD retrieval. It is based on a linear model of vertical profiles for D_o and $\log(N_w)$ and the ability to accurately estimate the D_o, N_w values in both the top and bottom bins. Note that log = $\log_{10}$, and ln = $\log_e$. It offers advantages over the single-loop model in that it does not suffer from the multi-valued solution-space problem relating to large D_o, N_w, A_i combinations. It also is not susceptible to the bi-valued D_o-ambiguity for rain described in detail by [9] [10] [11] [12] [14].

Bringi et al. [16] showed that $\log(N_w)$ can also be reasonably approximated by a linear vertical profile for a convective storm beginning at the early growth phase and developing into an intense microburst. Stratiform precipitation is less variable than convective, consequently, we believe the linear approximation is a reasonable assumption.

Following this introduction, section 5.2 describes the theory and mathematical background behind the applicability and solution space for the optimized linear-DSD-profile model. In section 5.3, four test cases are analyzed and discussed showing the performance and limitations of the proposed method. Two simulations are performed using input reflectivity data with no intrinsic measurement error; and two are performed using simulated profiles with added measurement error. The results of error and error-free data are discussed and analyzed. Data from a 1000-profile simulation is included showing the mean and standard error of the method

when measurement error is randomly added to multiple profiles. Section 5.4 briefly summarizes the optimization method.

5.2 OPTIMIZATION METHOD

5.2.1 Background

The single-loop feedback method using the iterative dual-frequency retrieval algorithm finds the DSD parameters D_o, N_w, as well as A_i and k_i for each bin. The retrieval method described in this chapter assumes that $\log(N_w)$ and D_o can be approximated by linear vertical profiles, and given a set of input $Z_{mi}(r_j)$ values, that an optimal solution can be found for the top and bottom-bin values of D_o, N_w such that the cost function between the $Z_{mi}(r_j)$ and estimated $\tilde{Z}_{mi}(r_j)$ is minimized. A flow chart of the four-variable optimization method is shown in Figure 5.1.

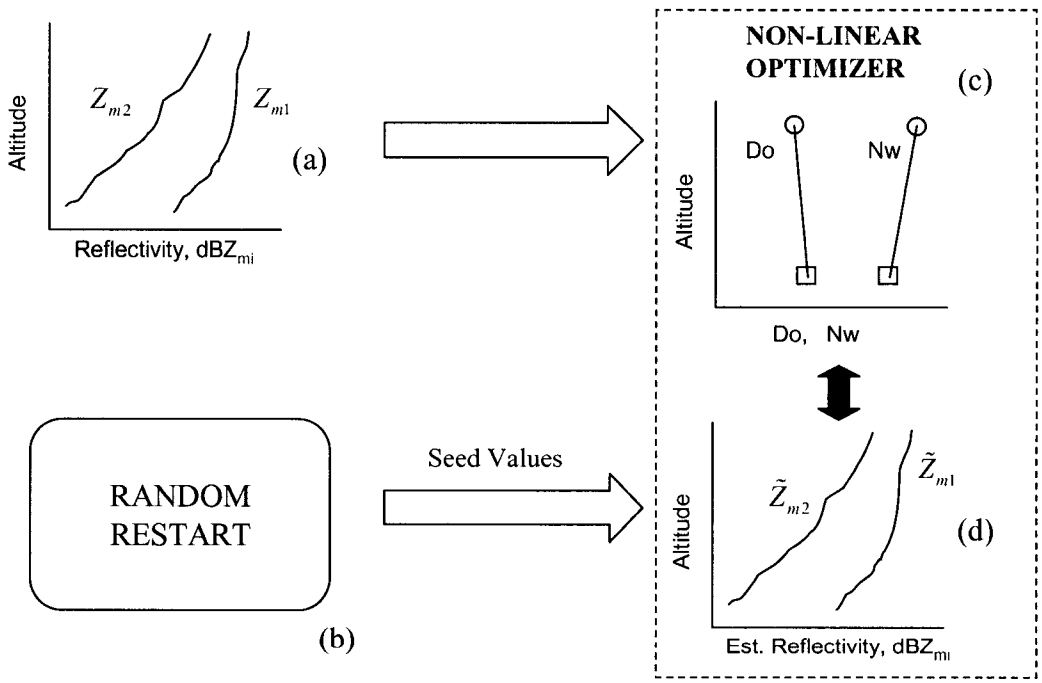

Figure 5.1. Flow chart illustrating the four-variable random-restart optimization method. Panel (a) depicts input reflectivity values with unknown D_o, N_w profiles. Random seed values are generated in panel (b). Panels (c) and (d) depict the interaction within the optimization routine to find the top and bottom D_o, N_w values to minimize a cost function relating to the input Z_{mi} and internally calculated Z_{mi} values.

Note that $1 \leq j \leq N$. A tilde (~) over a variable name indicates that it is an algorithm-derived value. The $Z_{mi}(r_j)$ values (in dBZ scale) are depicted in Figure 5.1(a) and are inputs to the optimizer shown in parts (c) and (d). Seed values for the optimizer, depicted in Figure 5.1(b), are generated using the random restart method [24]. Using both the $Z_{mi}(r_j)$ and seed values, the optimizer finds a solution for the top and bottom D_o, N_w values, indicated by circles and squares in Figure 5.1(c), to minimize the cost function. In early simulations and modelling, the top and bottom bin D_o, N_w outputs from the single-loop retrieval algorithm were used with limited success as seed values for the optimizer. It became clear that simply using the single-loop retrieved values was inadequate and a better method to generate seed values was required. As a result, the random restart method, which uses randomly generated top and bottom seed values for each optimization cycle, has been implemented.

To illustrate the process of finding the best or optimal solution, and the necessity of using the random-restart method, the following example is given. Figure 5.2 shows a plot of the bottom-bin surface-solution space for N_w: log(8000)- log(4000); D_o: 1.60-1.75, top to bottom respectively, using top-bin values of D_o: 1.60 and N_w: log(8000). The top-bin values are fixed in this example, and the bottom D_o, N_w values are swept between 0.5 to 2.5, and 10^3 to 10^6 ($3 \leq \log(N_w) \leq 5$), respectively, using 50 steps, to create the plot. The heavy line indicates the bottom of the trough and the dot indicates the minimum value, or optimal bottom-bin solution given a top-bin DSD pair. In this case, the top-bin pair is correct. Note that due to the relatively coarse step size of the grid in this figure, the minimum value of the cost function occurs at D_o: 1.77, N_w: log(3728) instead of at the expected values, D_o: 1.75, N_w: log(4000). If the plot is calculated and drawn with more than 150 grid-divisions instead of the 50 used in this example, the expected bottom-bin D_o, N_w values are found. It is important to note that Figure 5.2 depicts the solution space for correct top-bin D_o, N_w values. If they are incorrect, then the shape of the plot changes (e.g., the location of the trough moves, the slopes of the sides change,

and the location of the cost function minimum changes) and the optimal bottom-bin solution will be found at a different D_o, N_w pair. In general, during the optimization process, when the optimizer is simultaneously searching for both top and bottom D_o, N_w pairs to minimize the cost function, the shape of the surface curve changes and the final bottom-bin values can and do change as a result of variation or inaccuracies in the top-bin values. The optimizer automatically adjusts the search step-size to a much finer scale than depicted here.

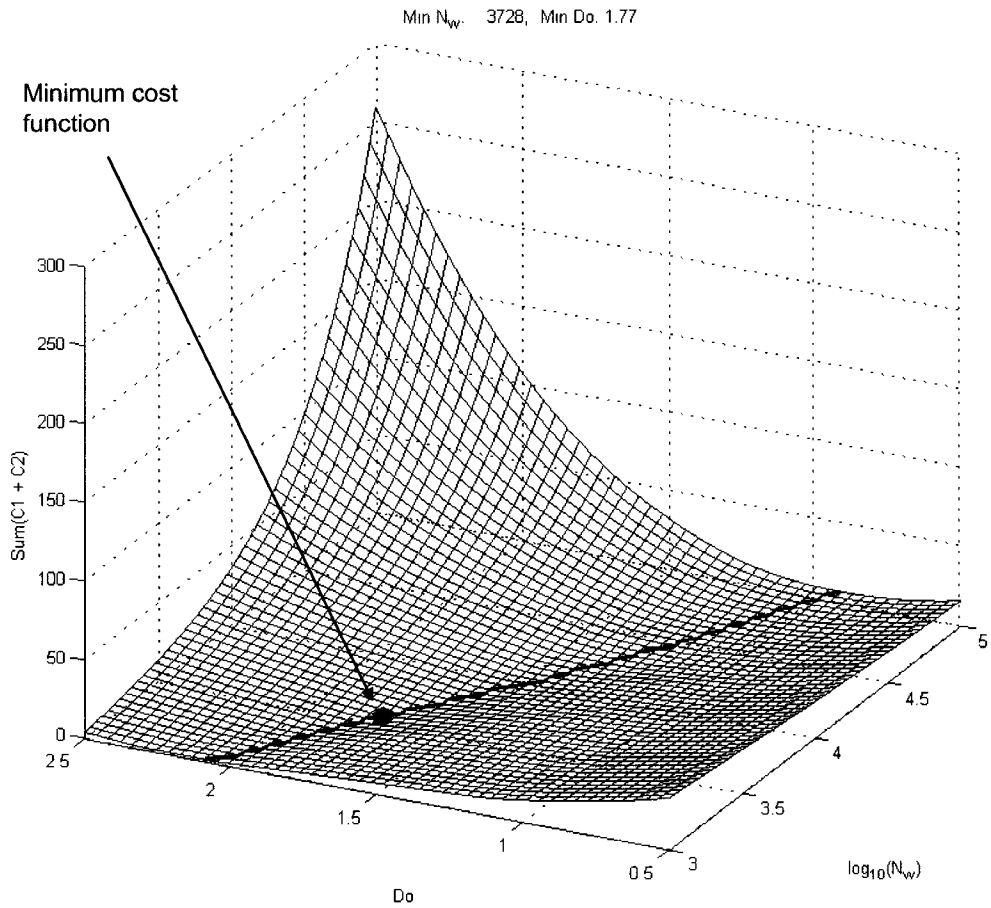

Figure 5.2. Plot of the bottom-bin surface-solution space for N_w: log(8000)-log(4000); D_o: 1.60-1.75, top to bottom using top-bin values of D_o: 1.60, N_w: log(8000). The heavy line indicates the bottom of the trough. The minimum D_o, N_w pair is indicated by the dot. Because of relatively coarse grid size, the minimum point on the graphs is not at the correct D_o: 1.75, N_w: log(4000) value. The algorithm uses an automatically-determined step size which is much smaller than that depicted here allowing it to determine the correct D_o, N_w pairs.

The necessary integral equations used in this method are similar to those used with the single-loop method described in Chapter 3, some of which are repeated here to ease reading. Rewriting (3.1) in terms of estimated measured reflectivity (with the superscript ~),

$$\tilde{Z}_{mi}(r) = \tilde{Z}_{ei}(r)\,\tilde{A}_i(r) \tag{5.1}$$

where

$$\tilde{Z}_{ei}(r) = \tilde{N}_W(r)\, f(\mu)\, \tilde{D}_o^{-\mu}\, I_{bi}(\tilde{D}_o) \tag{5.2}$$

$$\tilde{A}_i(r) = \exp\left[-0.2\ln(10)\, h \sum_{j=1}^{N} \tilde{k}_i(r_j)\right] \tag{5.3}$$

and I_{bi} is a function of $\tilde{D}_o$ expressed as

$$I_{bi}(\tilde{D}_o) = C_{Zi} \int_D \sigma_{bi}(D)\, D^{\mu}\, e^{-\Lambda D}\, dD \tag{5.4}$$

$$C_{Zi} = \frac{\lambda_i^4}{\pi^5 |K_w|^2} \tag{5.5}$$

where $\tilde{D}_o = \tilde{D}_o(r_N)$ in (5.2) - (5.4). σ_{bi} is the radar backscatter cross section and is a function of the drop diameter D. λ_i is the free-space wavelength in meters, and K_w is defined as

$$K_W = \frac{m^2 - 1}{m^2 + 2} \tag{5.6}$$

where m is the complex index of refraction of water at 20° C at these wavelengths.

The specific attenuation k_i in (5.3) at a particular range $r = r_j$ is defined as,

$$\tilde{k}_i(r) = \tilde{N}_W\, f(\mu)\, \tilde{D}_o^{-\mu}\, I_{ti}(\tilde{D}_o) \tag{5.7}$$

where

$$I_{ti}(\tilde{D}_o) = C_{ki} \int_D \sigma_{ti}(D)\, D^{\mu}\, e^{-\Lambda D}\, dD \tag{5.8}$$

$$C_{ki} = 4.343\, x10^{-3} \tag{5.9}$$

and σ_{ti} is the radar extinction cross section and is a function of drop size D and $\tilde{D}_o = \tilde{D}_o(r_j)$ in (5.7) and (5.8).

At the beginning of each optimizer iteration [see Figure 5.1(c),(d)] the top and bottom D_o, N_w seed values are used to create linear D_o, log(N_w) profiles. Using the internally generated

linear DSD profiles, the method then calculates estimated $\tilde{Z}_{mi}(r_j)$ using (5.2) - (5.7). The optimizer compares the internally-generated $\tilde{Z}_{mi}(r_j)$ profiles to the input $Z_{mi}(r_j)$ profiles during each iteration as it searches the DSD-variable space to minimize the cost function. The PIA values in dB, at each frequency and at each bin, are calculated using (5.3).

In terms of dB scale, (5.1) can be written as

$$\tilde{Z}_{mi}(r_j) = \tilde{Z}_{ei}(r_j) - PIA(r_j) \tag{5.10}$$

noting that in linear scale, attenuation factor $A_i(r_j)$ is ≤ 1, and in dB scale, path-integrated attenuation PIA ≥ 0. The cost function is the minimum of $C_1 + C_2$ stated as

$$\min(C_1 + C_2) \tag{5.11}$$

where

$$C_1 = \sqrt{\frac{1}{N}\sum_{j=1}^{N}\left[\tilde{Z}_{m1,dBZ}(r_j) - Z_{m1,dBZ}(r_j)\right]^2} \tag{5.12}$$

$$C_2 = \sqrt{\frac{1}{N}\sum_{j=1}^{N}\left[\tilde{Z}_{m2,dBZ}(r_j) - Z_{m2,dBZ}(r_j)\right]^2} \tag{5.13}$$

and N is the number of bins. $Z_{mi,dBZ}(r_j)$ and $\tilde{Z}_{mi,dBZ}(r_j)$ in (5.12) and (5.13) are in units of dBZ.

5.2.2 Methodology

The optimization method requires top- and bottom-bin seed values for D_o, N_w. As a general procedure, the single-loop feedback method should be executed first to retrieve the D_o, N_w and rain-rate profiles and a test using (3.41) should be performed to determine if the top bins are in the incorrect convergence region. Note that the single-loop retrieval method estimates the top bin values very accurately, even on the first iteration, because $Z_{ei}(r_1) \approx Z_{mi}(r_1)$. Depending on the test result, the four-variable optimization method can be executed to retrieve the "best-fit" D_o, N_w profiles for those cases where the single-loop method is insufficient. The optimizer

used in this work allows for non-linear optimization of multiple variables. D_o is constrained between 0.5 and 2.5 mm, and N_w is constrained between 10^3 and 10^5 ($3 \leq \log(N_w) \leq 5$). The random variables used in the random-restart method as seed values are uniformly distributed, $0.75 \leq D_o \leq 2.25$ and $10^3 \leq N_w \leq 6 \times 10^4$, with N_w seed having a slightly narrower range than the expected N_w final values. Additionally, the slopes of the random D_o and $\log(N_w)$ profiles are opposite to each other such that if the top D_o value is greater than the bottom D_o value, then the top N_w value will be smaller than the bottom N_w value.

The optimization method, though computationally more expensive than a single-loop approach, yields much more accurate results for certain D_o, N_w profiles. In normal operation, 10 to 50 random-restart iterations are performed. After the iterations are completed, the cost function minimum is found along with the corresponding top and bottom D_o, N_w values. Using the optimum D_o, N_w values, the retrieved rain profile and each range r is calculated using (3.39).

5.3 TEST CASES

To illustrate the four-variable optimization method for D_o, N_w pairs in the incorrect convergence regions, the following four test cases are analyzed and discussed. The simulated data sets discussed in the following examples are each for a 3-km in height, vertical rain column, based on DSD values of D_o: 1.60 to 1.75, and N_w: log(8000) to log(4000), top to bottom respectively. In each of these cases, the "true" measured reflectivity values, $Z_{mi}(r_j)$ are derived from this DSD profile. This particular D_o, N_w combination is chosen to illustrate the difficulty the single-loop method has in retrieving the correct DSD-profile values and demonstrate the retrieval performance of the optimization method. Many other DSD-profile combinations could have been used from the hundreds of simulated pairs, but this example suffices for illustrative purposes. No constant vertical-DSD-profile data sets are analyzed here as they are viewed as subsets of the more general, linear profiles.

5.3.1 Linear Vertical Profile for D_o, N_w, Single-Loop Retrieval, No Measurement Error

In this example the single-loop retrieval method is demonstrated to establish a base-line retrieval to which the remaining simulations can be compared. Figure 5.3 shows the output profiles from the single-loop retrieval method.

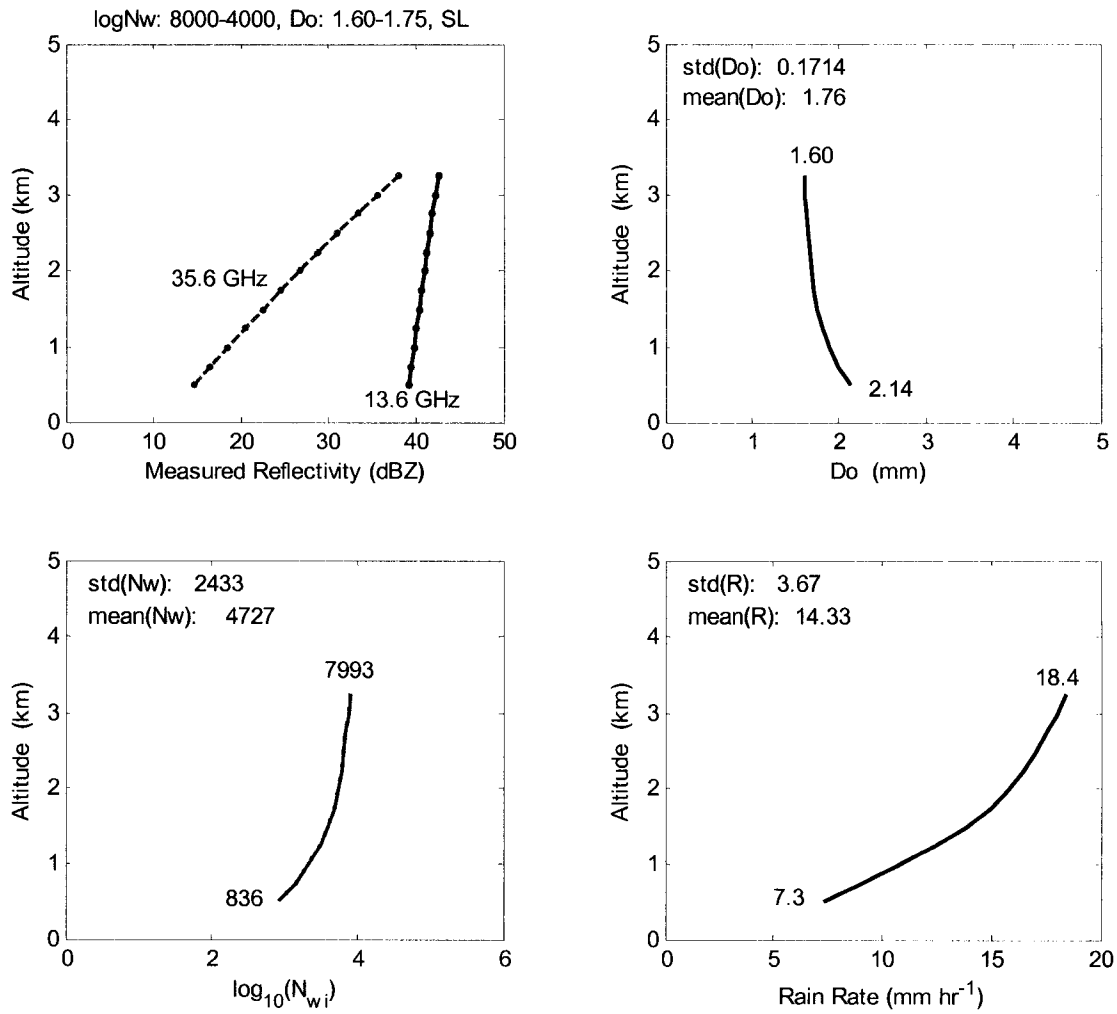

Figure 5.3. Plots of the output profiles using the single-loop feedback retrieval model for a vertical rain column 3-km in height based on D_o: 1.60-1.75, log(N_w): log(8000)-log(4000). Panel (a) shows the corresponding input reflectivity values. Panels (b), (c), and (d) show the profiles for D_o, log(N_w), and rain rate. There is considerable error in the lower bins due multiple possible solutions with these N_w, D_o combinations. Convergence tolerance was 0.01% and required 3966 iterations.

Figure 5.3(a) shows the input Z_{mi} values (dBZ scale) based on the above-mentioned D_o: 1.60 – 1.75, and N_w: log(8000) – log(4000) profiles with no measurement error in $Z_{mi}(r_j)$. Because this D_o, N_w combination is in the incorrect convergence region both in the top and bottom bins,

the single-loop method incorrectly estimates the DSD values in the lower bins. Figure 5.3(b) shows the D_o profile and that it is correct at the top bin at 1.60 mm and incorrect at the bottom, 2.14 mm (true value 1.75). Figure 5.3(c) shows the N_w profile (log scale) and shows a nearly correct retrieved value at the top of log(7993) (true value is 8000), and an inaccurate N_w value in the bottom bin of log(436) (true value 4000). The rain-rate profile is shown in Figure 5.3(d) and illustrates how distorted the rain-rate estimate can become. The value at the top bin is correct at 18.4 mm/hr, but the retrieved bottom value, 7.3 mm/hr, should be 13.9 mm/hr, yielding a 47% underestimation.

5.3.2 Linear Vertical Profile for D_o, Nw, Optimization, No Measurement Error

Given the input $Z_{mi}(r_j)$ values, the four-variable optimization method can be executed with random-restart seed values for the top and bottom bins. Figure 5.4 shows the results of using this method. Figure 5.4(a) shows profiles of the true D_o, (solid line on the left) and optimizer-found $\tilde{D}_o$ values indicated by dots. The solid line on the right is true log(N_w) and asterisks are optimizer-found log($\tilde{N}_w$). Note that the optimizer-retrieved values for both D_o and N_w overlay exactly. The seed values for this optimization cycle which yielded a minimum cost function were *Do*: 1.53, 1.50; log(N_w): 3.82, 4.34. Figure 5.4(b) shows the true (solid line) and retrieved rain-rate profiles (dots). The true rate in the bottom bin is 13.9 mm/hr and the rate calculated by the optimizer is 13.9 mm/hr. Figure 5.4(c) compares the $Z_{ei}(r_j)$ profiles (solid and dashed lines in dBZ scale) based on the true D_o, N_w and retrieved values shown as dots and asterisks. Again, the retrieved values overlay the true values exactly. Figure 5.4(d) shows comparisons of the input $Z_{mi}(r_j)$ (solid and dashed lines) and retrieved $Z_{mi}(r_j)$ values (dots and asterisks) based on optimized D_o, N_w values. The minimum value of the cost function was found at iteration number two of the 20 random-restart operations performed. Optimization tolerance was set to 10^{-6}.

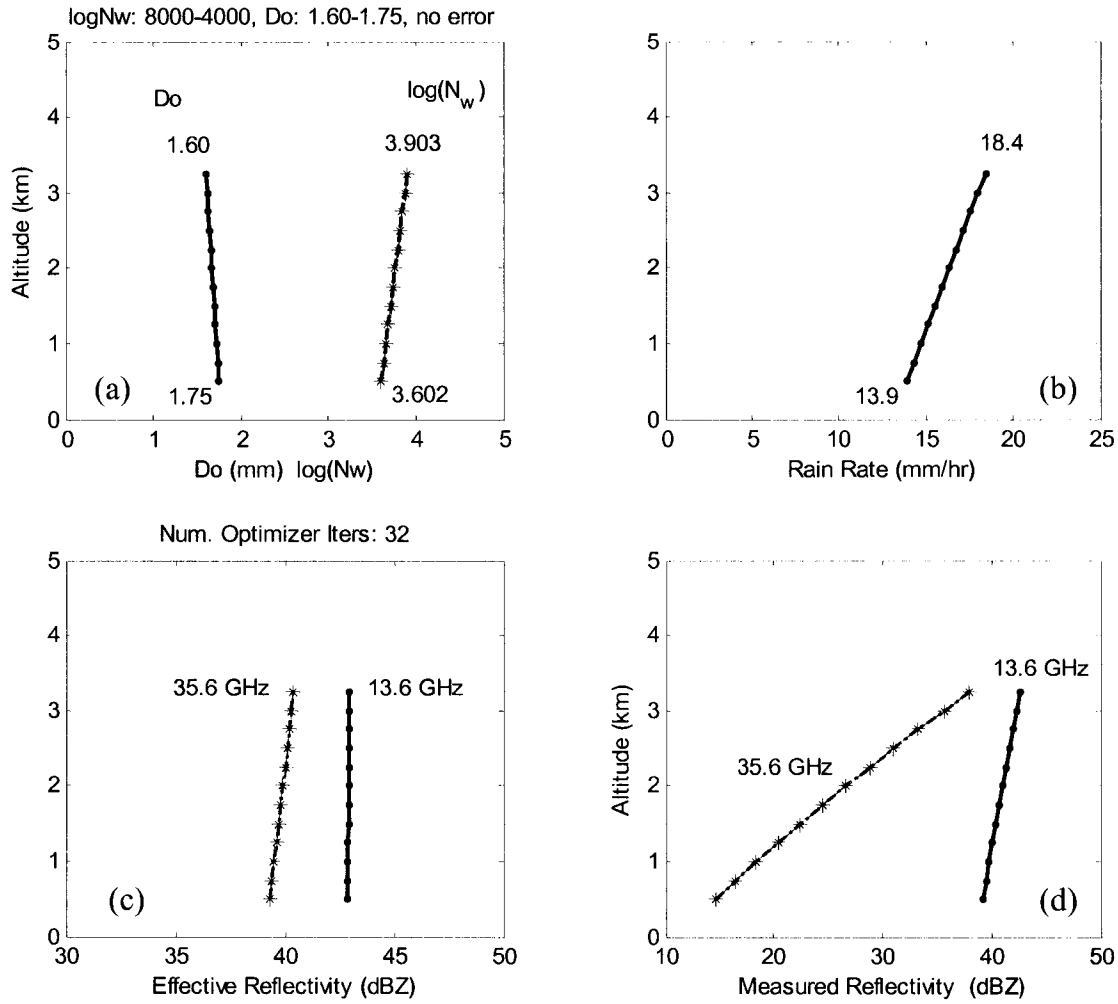

Figure 5.4. Plots showing the output of the four-variable optimization method using input profiles for a 3-km vertical-rain-column based on D_o: 1.60-1.75, N_w: log(8000)-log(4000). The left portion of panel (a) shows the true (solid line) and estimated (dots) D_o profiles. The right portion of panel (a) shows the true log(N_w) (solid) and estimated (asterisks) profiles. Panel (b) shows the rain-rate profile obtained via the optimizer (dots) with the true profile (solid). Panel (c) shows the effective radar reflectivity factors (solid lines) along with the estimated profiles (asterisks and dots), and panel (d) shows the input Z_{mi} values (solid) and optimizer outputs (dots and asterisks) at both frequencies. Twenty random-restart cycles were used, with cycle two being selected.

5.3.3 Linear Vertical Profile for D_0, N_w, Single-Loop Retrieval, Measurement Error

In this section, the effects of measurement error on the single-loop retrieval method are analyzed and discussed. The same D_o, N_w and Z_{mi} profiles are used from *section 5.3.1*. However, Gaussian error, 0.5-dBZ standard deviation, is added to the Z_{mi} profiles in each bin to simulate measurement error in the system. Figure 5.5(a) shows the input $Z_{mi}(r_j)$ profiles with

the additional error. Note that they are not smooth as in Figure 5.3(a) because of the measurement error.

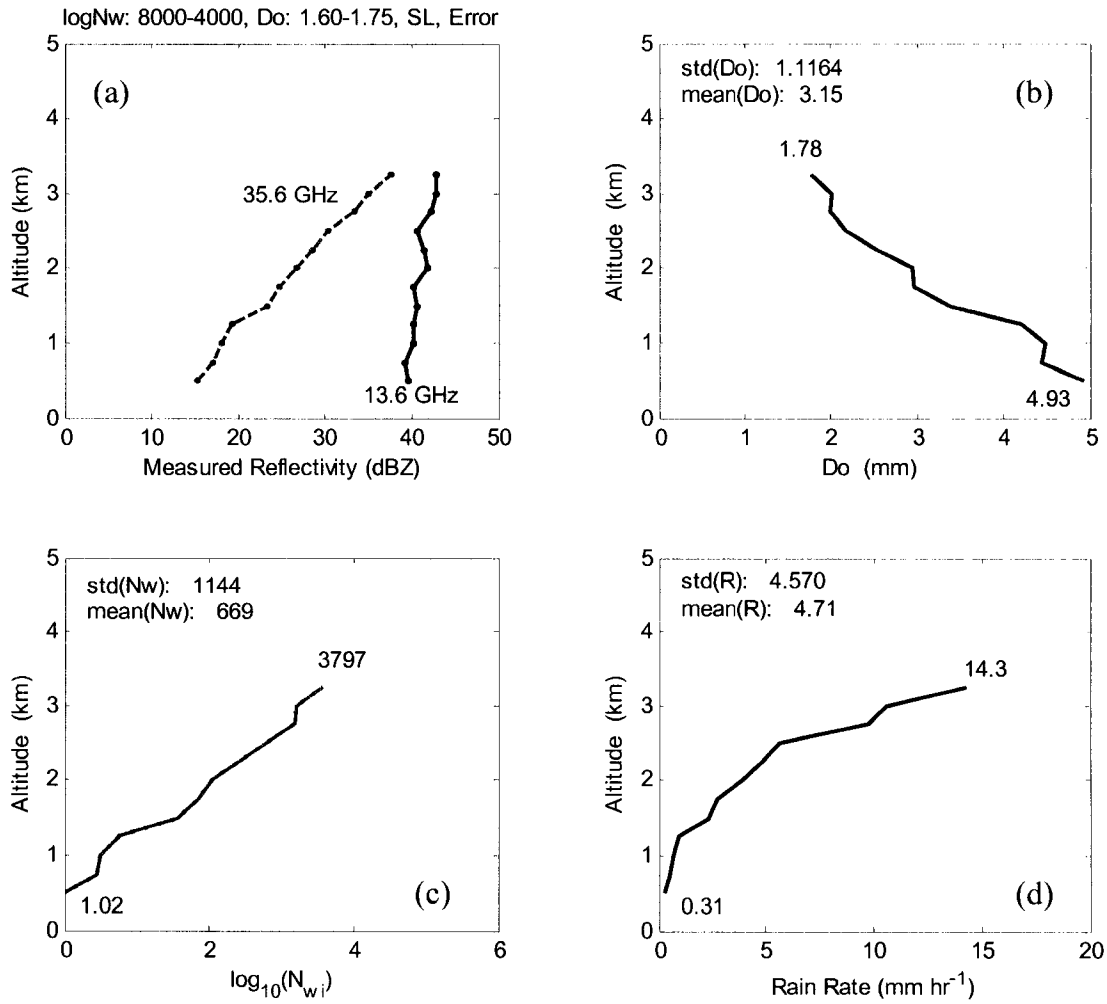

Figure 5.5. Plots of the input reflectivity and retrieved output profiles using the single-loop retrieval model for a 3-km vertical-rain-column based on D_o: 1.60-1.75, N_w: log(8000)-log(4000) with 0.5-dBZ standard-deviation added random measurement error. Panel (a) shows the input reflectivity values for both 13.6 and 35.6 GHz. Panels (b), (c), and (d) show the retrieved profiles for D_o, log(N_w), and rain rate. Convergence tolerance was 0.01% and required 42 iterations. Error added to the 13.6-GHz profile was 0.49 dBZ, and error added to the 35.6-GHz profile was 0.64 dBZ, both one standard deviation.

The standard deviation of the random error on the 13.6-GHz reflectivity profile is 0.49 dBZ, and the standard deviation on the 35.6-GHz reflectivity profile is 0.64 dBZ where these error numbers are calculated as the standard deviation of $Z_{mi}(r_j)$-noise minus $Z_{mi}(r_j)$-true-profile at each bin in the profile. Note that because the error is random, the amount of error in each bin will vary from simulation to simulation as will the total error in each profile. Figure 5.5(b)

shows the retrieved D_o profile. At the top bin, the retrieved value of 1.78 mm differs from the true value without error of 1.60 mm. Even more error is present in the bottom-bin retrieval with a value of 4.3 mm and a true value of 1.75 mm. The error in the lower bins is caused both by the incorrect convergence region and the error in the $Z_{mi}(r_j)$ profiles. Figure 5.5(c) shows the retrieved $\log(N_w)$ profile with log(3797) at the top to log(1.02) at the bottom. It obviously differs greatly from the true values of log(8000) at the top and log(4000) at the bottom. Figure 5.5(d) shows the rain-rate profile and that it also varies significantly from the true profile shown in Figure 5.4(b). The top rain-rate value should be 18.4 mm/hr but 14.3 mm/hr is estimated. The bottom value should be 13.9 mm/hr but 0.31 mm/hr is retrieved, a 98% underestimation.

5.3.4 Linear Vertical Profile for D_o, N_w, Optimization, Measurement Error

Given the same input $Z_{mi}(r_j)$ values from *section 5.3.3* including the same simulated error, the four-variable random-restart optimization method was executed. Figure 5.6 shows the results from this simulation. Figure 5.6(a) shows the true D_o and $\log(N_w)$ profiles (D_o is the solid line and N_w is the dashed line) with superimposed D_o, $\log(N_w)$ profiles (dots and asterisks) from the optimizer. Note that the top D_o points agree but the bottom true value is 1.75 and the retrieved values is 1.85 mm. The optimizer slightly overestimates the $\log(N_w)$ value at the top at 3.923 but underestimates it at the bottom. The bottom, true value is 3.602 = log(4000) but the retrieved value is 3.429. Figure 5.6(b) shows the true and estimated rain-rate profiles. The top value should be 18.4 but is estimated as 19.2. At the bottom, the expected value is 13.9 but is retrieved as 11.9 mm/hr, a 14% underestimation. Figure 5.6(c) shows the true (solid line, dashed line) and estimated Z_{ei} values (dots and asterisks) at both 13.6 and 35.6 GHz. The retrieved values for 13.6 GHz are very close to expected but there is some underestimation in the 35.6-GHz values in the lower part of the profile. Figure 5.6(d) shows the input $Z_{mi}(r_j)$ values with added error (solid line for 13.6, and dashed line for 35.6 GHz) with the optimizer-found $Z_{mi}(r_j)$ values superimposed (dashed lines with dots, 13.6 GHz, and asterisks, 35.6 GHz).

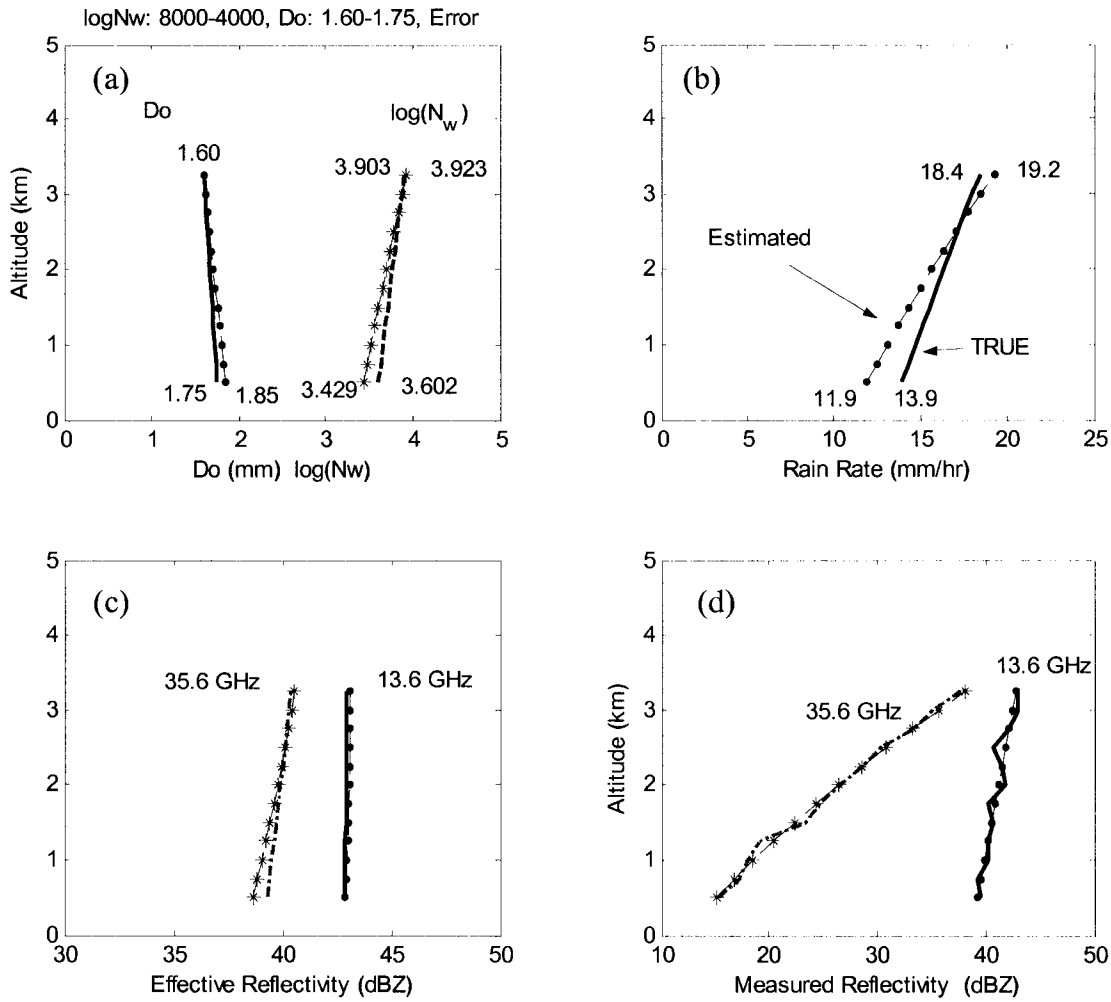

Figure 5.6. Output of the four-variable random-restart optimization method using the input data set of Fig. 7. Dashed lines with dots and asterisks are profiles estimated by the optimization procedure. Panel (a) shows the true D_o, $\log(N_w)$ profiles along with the estimated values. Due to the added noise, there is some error in the bottom bins. Panel (b) shows true and estimated rain-rate profiles again with some underestimation of rain rate in the bottom. True and estimated effective reflectivity are depicted in panel (c). Panel (d) shows the input and estimated measured reflectivity profiles. Note that the method found very good approximations to the input reflectivity profiles. Fifty random-restart cycles were performed with the residual minimum found at cycle number 35.

It is clear from the graph that in the 50 random-restart cycles, that the optimization method found the best approximation in cycle number 35 given the input reflectivity data and constraints. The estimated reflectivity profiles closely overlay the input reflectivity profiles.

The optimization method is not able to retrieve the true DSD profiles exactly because of errors in the input $Z_{mi}(r_j)$ data. It is however, able to minimize the cost function and find the resulting top and bottom D_o, N_w values along with the corresponding rain profile that best match

the input reflectivity data set. Note that even in this scenario of inaccurate input $Z_{mi}(r_j)$ values, the four-variable random-restart optimization method was able to find reasonably-estimated $Z_{mi}(r_j)$ profiles.

Because the added measurement error to the reflectivity profiles in this example was random, the retrieved rain-rate values based on this method will vary from simulation to simulation in accordance with the amount and location of random error in each of the profiles. Figure 5.7 shows a histogram of the bottom-bin estimated-rain-rate values using the non-linear optimization method for 1000 simulated profiles (based on N_w: log(8000)-log(4000),D_o: 1.75-1.60, vertical rain column 3-km high), each with added 0.5-dBZ standard-deviation random error as described above.

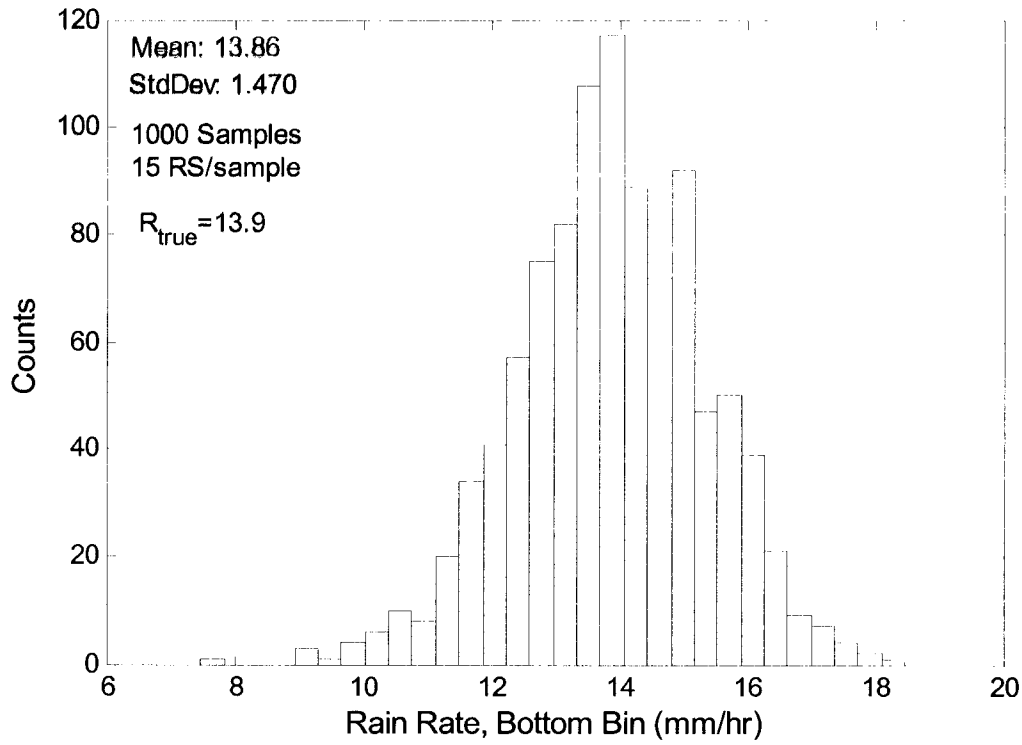

Figure 5.7. Plot showing a histogram of the bottom-bin rain-rate estimation for 1000 simulated profile pairs, each with added random 0.5-dBZ standard-deviation measurement error and using 15 random-restart iterations per simulation. The reflectivity profiles are for a 3-km high, vertical rain column based on N_w: log(8000)-log(4000), D_o: 1.75-1.60. The mean of the histogram is 13.86 mm/hr close to the true mean of 13.9. The standard deviation is 1.470.

Additionally, for each simulated profile, the optimizer was configured for 15 random-restart cycles. The results show that the estimated mean of the histogram is 13.86 mm/hr, close to the correct value of 13.9 mm/hr, demonstrating the important result that the optimization process is not biased. The standard error of the distribution is 1.47.

5.4 SUMMARY AND CONCLUSIONS

It has been shown that the single-loop retrieval method will correctly estimate DSD values and subsequent rain-rate profiles based on retrieved DSDs for about half the world-wide rainfall. For those DSD pairs that the single-loop method is unable to determine correctly, another method or set of constraints is required. This chapter has described an alternative, dual-frequency method to retrieve DSD values based on assumed linear vertical profiles for the DSD using a non-linear optimization technique. The optimization technique requires as inputs the $Z_{mi}(r_j)$ values for both wavelengths, and top and bottom seed values for the random-restart function. Outputs from the method are the top and bottom values of D_o, N_w that minimize a cost function relating to the input $Z_{mi}(r_j)$ and internally calculated $\tilde{Z}_{mi}(r_j)$ profiles. From the retrieved top and bottom DSD values, linear profiles for D_o, N_w can be calculated. From these D_o, N_w profiles, the rain-rate profile can be estimated.

To illustrate the performance of the technique, it was compared with the single-loop method both with and without measurement error using simulated DSD linear profiles based on D_o, N_w pairs found in the incorrect convergence region. As expected, the single-loop model incorrectly retrieved the DSD values in the lower altitudes both with and without measurement error. The optimization technique was able to retrieve the correct DSD profiles throughout the vertical profile when no measurement error was included. When measurement error was present, the optimization technique retrieved a "best-estimate" of the true DSD profiles that closely matched the known values. A simulation of 1000 profiles with added measurement error showed that the

mean value of the simulation was nearly the same as the correct or expected value in the bottom bin.

Based on empirical evidence, we have assumed that the vertical profile of $\log(N_w)$ can be reasonably approximated as linear. In the estimation process, any non-linearity of $\log(N_w)$ profiles (non-compliance with the linear-model assumptions) will contribute to error in the retrieval. However, for this work, the assumption of linear $\log(N_w)$ profiles is reasonable.

CHAPTER 6

SYSTEMS ENGINEERING ANALYSIS: BACKGROUND

6.1 INTRODUCTION

In general, systems engineering consists of the methods and/or processes used to evaluate and optimize the performance of a system which is limited by time, technology and/or resources. By analyzing the system, the designers are able to trade off resources, time and technology, determining which parts contribute little to the overall success or outcome. Likewise, in satellite-based precipitation-retrieval algorithms, some input variables, parameters and model assumptions are more important than others. An algorithm can be sensitive to errors in some factors and insensitive to errors in others. It is important to know how the algorithm responds to these errors and how the errors affect the output of the model so that resources can be applied to the factors that will yield the greatest benefit. Sensitivity analysis (SA) and uncertainty analysis (UA) techniques can be used to assist in systems engineering analysis by providing insight as to the relative importance of each input factor. In general terms, SA is the study of how the output of a model (numerical or mathematical) varies as a function of its input parameters [25]. The input variables to the model are also referred to as input factors. This chapter provides an introduction to sensitivity and uncertainty analysis methods and how they can be used as tools in systems engineering. Figure 6.1 shows the relationship between systems engineering and two of the many tools that can be used to perform it, namely, SA and UA. Links below the SA block show how it can be categorized into three main types, and some of the many methods and techniques used to implement it. For more in-depth descriptions of SA and UA, the reader is referred to some of the references such as [25], [26], [27].

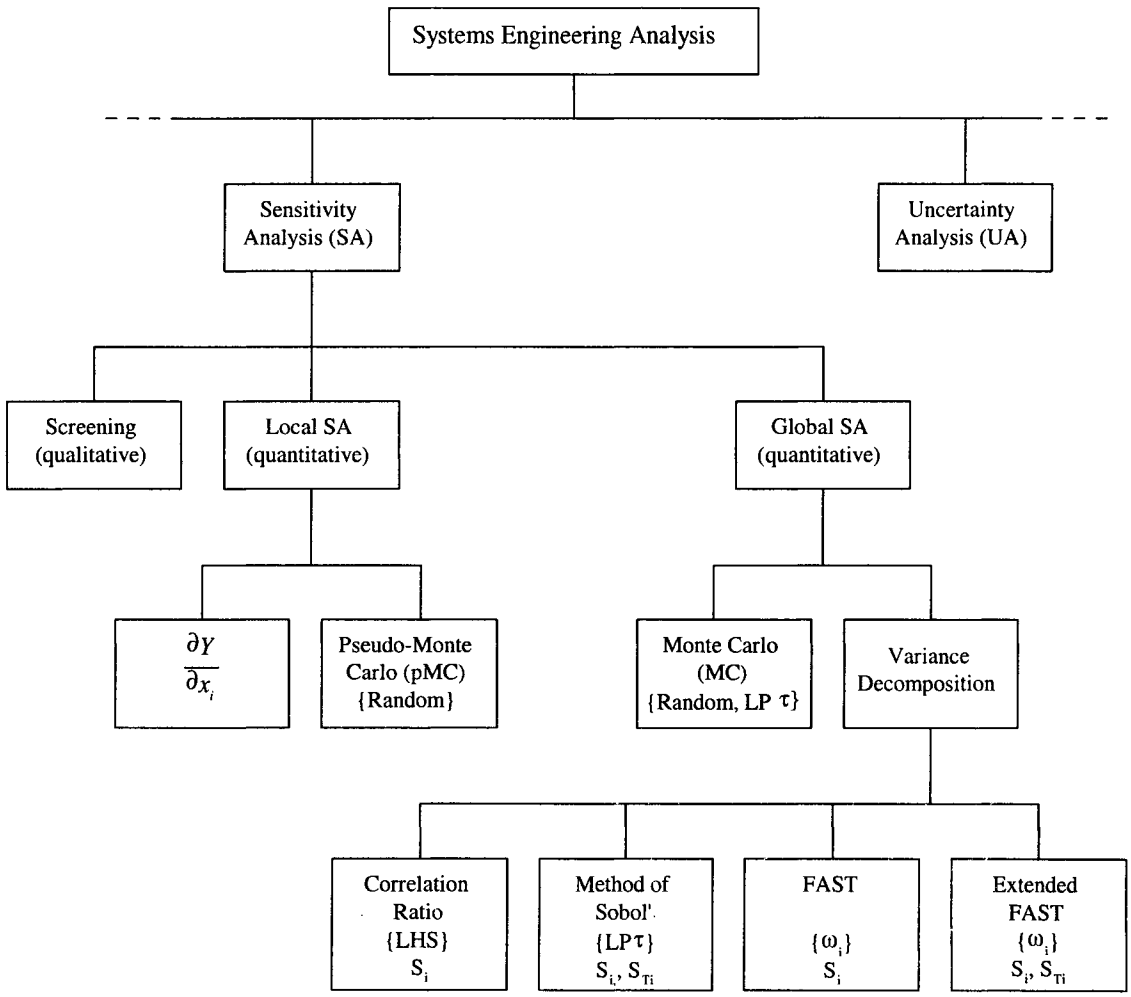

Figure 6.1. Flow chart showing the relationships between systems engineering analysis and SA/UA. Uncertainty analysis provides descriptive statistics of the model output. Sensitivity analysis methods are grouped by screening, local SA, and global SA. Local SA methods consist of the partial derivative technique and pseudo-Monte Carlo techniques. Global SA can be grouped into MC and variance decomposition methods. Four techniques are used to perform variance decomposition—Correlation Ratio, Method of Sobol', Fourier Amplitude Sensitivity Test (FAST), and Extended FAST. The items in braces { } refer to the dominant sampling method used for the particular method.

Sensitivity analysis methods can be grouped into three main categories: 1) screening; 2) local; and 3) global [26]. Screening methods are used for large and computationally-expensive models to provide a qualitative measure of the relative importance of the input factors. They rank the input factors by order of importance but do not quantify how much more important one factor is in relation to another.

Local SA methods are based on the partial-derivative technique where the sensitivity S_i of the model output Y, with respect to an input factor, x_i , $i = 1,\ldots,k$ factors, is given by

$$S_i = \frac{\partial Y}{\partial x_i} \tag{6.1}$$

where each input factor is varied, one at a time, around some small percentage of its nominal value while fixing the other factors at their nominal values. The technique provides more quantitative information about the input factors and model than the screening method. The SA method shown in (6.1) has been used for decades in the feedback control discipline to study and quantify how a system output can be affected by variations in each of the input factors or model parameters [28]. This method assumes that the input factors' nominal values are known, and that the model is linear in the region about the nominal set points. It also provides, at best, a crude method of apportioning the output variance to the input factors. When an explicit analytical expression can not be obtained for a model, a variation on the linear SA method of (6.1) is done by pseudo-Monte Carlo (MC) simulations in which one-by-one, each parameter is sampled from its distribution and the others remain fixed at their nominal values. In the figure, the descriptions in braces { }indicate the method of sampling. In contrast to local sensitivity analysis, global SA techniques calculate the model output by simultaneously varying all the input factors throughout their ranges as opposed to one at a time.

Global sensitivity analysis can be implemented by two principal techniques (with greatly differing results): MC analysis; and variance decomposition. MC methods, pioneered at Los Alamos National Laboratory in 1947, randomly sample the distributions of each of the input factors and provide a means to analyze the statistical output of the model in relation to the statistical properties of the input factors. Variance-decomposition techniques, on the other hand, provide detailed information as to the relationships between the input factors and model output and apportion the error in the model output back to the input factors. Each of these techniques is sampling based, meaning that samples are drawn from the probability density functions (PDFs) of each of the factors and the model is executed once for each set of sampled values. When model linearity and nominal values are not known or can not be reasonably

assumed, global SA methods are better suited to determine sensitivity as a function of input factor variability. Other difficulties arise when models are non-linear, or non-monotonic.

A simplified block diagram of SA and UA processes, based on the variance decomposition technique, adapted from [29], is shown in Figure 6.2.

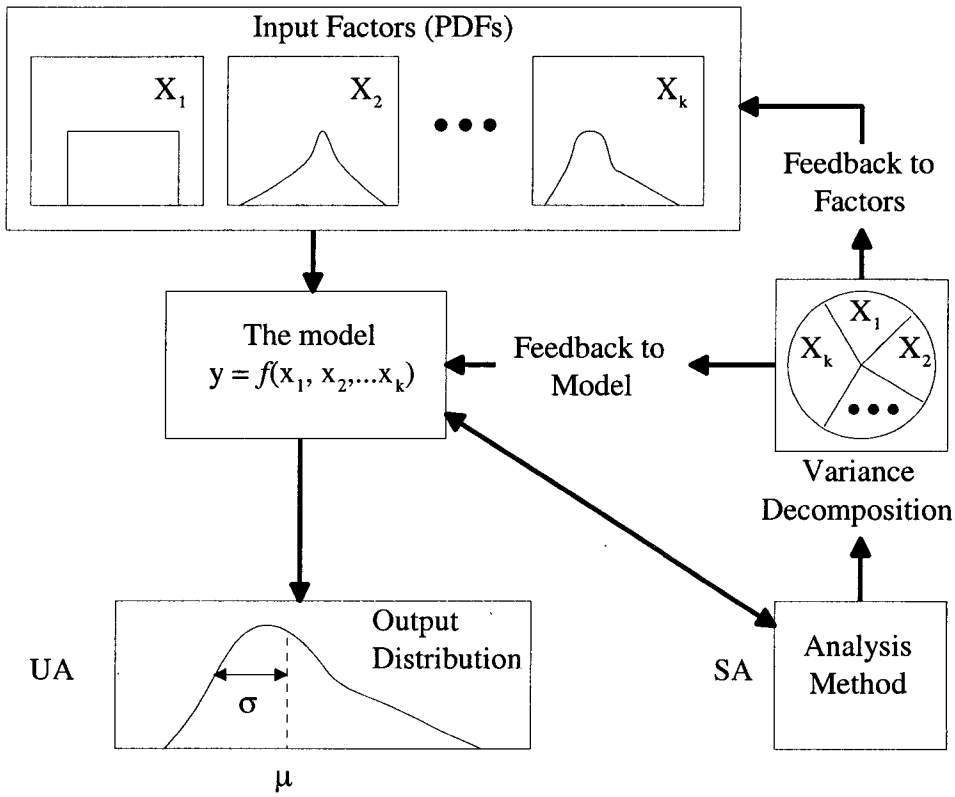

Figure 6.2 A simplified flow chart and schematic view of sampling-based sensitivity and uncertainty analysis. Adapted from [29].

The top portion of the figure depicts the input factors. The downward path on the left indicates the flow for UA and the path on the right, pointing upwards, depicts the flow of SA using the variance-decomposition technique. Note that any of several analysis methods to perform the variance decomposition type of SA can be used. The model being studied, $Y = f(X_i)$, where $X_i = \{X_1, X_2, ...X_k\}$, for k input factors, uses sampled values from the distribution space of each factor. After being executed multiple times, the model output values (assuming a single model output value with multiple instances) will exhibit some type of empirical distribution as depicted in the bottom left of Figure 6.2. Sensitivity analysis, shown on the right side of Figure

6.2, uses both the statistical properties of the input factors and model output along with an appropriate analysis method to decompose the variance of the output. The output of SA (using variance decomposition) can be best illustrated as a pie chart in Figure 6.2 showing the relative importance (quantitative) of each of the factors in relation to the total output variance. A factor that has a large impact on the total variance will be shown in the pie chart with a large percentage while a factor that has minimal influence on the output variance will have a correspondingly small percentage of the pie chart. Once SA (in this case the variance decomposition technique) is completed, feedback can be provided to the model structure and to the underlying assumptions used in the factor distributions.

Uncertainty and sensitivity analysis are related and are sometimes confused as to what each analysis provides. Uncertainty analysis (UA) is a method used to quantify the uncertainty in the model output as a result of uncertain inputs. The end products of UA are typically a histogram of the model output along with its mean and standard deviation and possibly other descriptive statistics as required by the experimenter [30]. UA determines how uncertain the model output is given a set of input factors. Generally speaking, highly variable inputs yield a higher statistical variance in the output distribution than input factors with small variances. For example, consider the simple *Z-R* relationship, $R = a\, Z_e^{\,b}$, where R is the rain rate (mm/hr), Z_e is the effective radar reflectivity ($mm^6\ m^{-3}$), a and b are coefficients. If each of the three input factors, a, b, Z_e, is assumed to have some probability density function, or statistical distribution, then the output R will also exhibit a statistical distribution related in magnitude to the input variables' distributions. Sensitivity analysis, as defined and used in this work, is implemented using variance decomposition which is a global SA technique. Several methods of implementing variance decomposition are described in section 6.3. (In the rest of the chapter, when the term SA is used, it implies global SA variance decomposition unless otherwise stated.) Before proceeding, an explanation of notation and terminology is needed.

6.2 NOTATION AND TERMINOLOGY

For a given model with k input factors and function, f, the output Y can be expressed as

$$Y = f(X_1, X_2, ..., X_k) \tag{6.2}$$

where X_1, X_2, ..., X_k are the input factors. Each of the factors is an N by 1 dimensional vector comprised of samples from its respective probability density function (PDF). In practice, N samples are obtained from the PDF of each factor and the model is executed N-times in MC fashion. This equation can be written as

$$Y_i = f[X_1(i), X_2(i), ..., X_k(i)] \tag{6.3}$$

where $i = 1 \ldots N$, the number of samples or realizations.

6.3 VARIANCE-DECOMPOSITION METHODS

6.3.1 Introduction

Referring to Figure 6.1, variance-decomposition methods or techniques include the Correlation Ratio [31], the Method of Sobol' [32] [33] [34], and the Fourier Amplitude Sensitivity Test (FAST) [35]. The original FAST method, described in [35], is limited to output analyses equivalent to those of the correlation ratio, that is, first-order terms. Saltelli later extended the FAST method to include both first and higher-order sensitivity terms and named it Extended FAST [36]. Note that any of these four methods could be used as the "analysis method" in Figure 6.2.

6.3.2 General

For a given model, [26] and [31] showed that the unconditional total variance of model output Y can be written as

$$Var(Y) = V_{X_i}[E(Y|X_i)] + E_{X_i}[V(Y|X_i)] \tag{6.4}$$

where

$$V_{X_i}\left[E(Y|X_i)\right] = \int \left[E[Y|X_i] - E[Y]\right]^2 p_{X_i}(X_i)dX_i \tag{6.5}$$

$$E_{X_i}\left[V(Y|X_i)\right] = \iint \left(y - E[Y|X_i]\right)^2 p_{Y|X_i}(y)dy\, p_{X_i}(X_i)dX_i \tag{6.6}$$

and

$$E[Y|X_i] = \int y\, p_{Y|X_i}(y)dy \tag{6.7}$$

The two right-side components of (6.4) are called the variance of the conditional expectation (VCE) and the residual. The integrals associated with (6.4) could be easily calculated assuming PDFs for the input factors but the conditional probability density functions are not generally known and hence explicit analytical solutions can not be derived. As a result, MC-type simulations are needed to solve the integrals.

6.3.3 Correlation Ratio

Using (6.4), the magnitude of the VCE with respect to the total variance is defined as

$$\eta^2 = \frac{V_{X_i}\left[E(Y|X_i)\right]}{Var(Y)} \tag{6.8}$$

and is termed the Correlation Ratio. It is computationally expensive to solve for η using MC simulations as both inner and outer loops are required for each factor. However, the method is conceptually simple and relatively easy to implement. McKay recommended Latin-Hypercube sampling (LHS) instead of random sampling because LHS more fully covers the distribution space of each factor when evaluating the integrals and yields faster convergence in the model [37].

6.3.4 Method of Sobol'

The Method of Sobol' is used to perform variance decomposition much more efficiently than the Correlation Ratio while yielding more information [38]. It is based on the decomposition of total variance given as

$$V = \sum_{i=1}^{k} V_i + \sum_{i}^{k} \sum_{j>i}^{k} V_{ij} + \ldots + V_{12\ldots k} \tag{6.9}$$

where V is the total unconditional variance, V_i is the variance due to each input factor X_i by itself. V_{ij} is the variance due to each pair of input factors, X_{ij}. Additionally, higher-order interaction terms are included all the way up to $V_{12\ldots k}$ which is the variance due to the interaction of all the input factors. A measure of sensitivity S_i for a factor can be derived by dividing each term in (6.9) by the total unconditional output variance V giving

$$S(i_1,\ldots i_k) = \frac{V(i_1,\ldots,i_k)}{V} \tag{6.10}$$

where the subscripts, $i_1,\ldots,i_k$ represent the input factors X_i and their combinations, $X_1 \ldots X_k$. From (6.9) and (6.10), the sensitivity indices can be written as,

$$\sum_{i=1}^{k} S_i + \sum_{i}^{k} \sum_{j>i}^{k} S_{ij} + \ldots + S_{12\ldots k} = 1 \tag{6.11}$$

with the useful property that the sum of all the sensitivity indices and interactions sum to one. The S_i variables are called the first-order sensitivity indices. The S_{ij} are called the second order indices. Likewise, S_{ijm} are called third order and so on up to the highest order, $S_{12..k}$, which accounts for the interaction of all k input factors. For a model that is additive,

$$\sum_{i=1}^{k} S_i = 1 \tag{6.12}$$

meaning the sum of the first-order sensitivity indices is one. If the S_i do not sum to one, then higher-order interactions are present. Rather than compute directly all the first and higher-order sensitivity indices, it if often sufficient to compute only the S_i and total sensitivity indices, S_{Ti} for each input factor X_i. The S_{Ti} indices measure the contribution to the total variance as a result of the first and higher-order interactions of each factor X_i. For example, assuming k = 3, the total sensitivity index for X_1 would be

$$S_{T1} = S_1 + S_{12} + S_{13} + S_{123} \tag{6.13}$$

which accounts for all the interactions of input factor X_1 with X_2 and X_3. For factor X_2, the total sensitivity index is

$$S_{T2} = S_2 + S_{12} + S_{23} + S_{123} \tag{6.14}$$

Similar expressions would be generated for X_3 factors thereby accounting for their interactions as well. Rather than compute each sensitivity term to compute the S_{Ti}, a more efficient method is to recognize and use the relationship between the factors,

$$S_{Ti} = 1 - S_{\sim i} \tag{6.15}$$

where $\sim i$ indicates the sensitivity terms which do not include the index i, that is, the total fractional variance complementary to parameter X_i.

The Correlation Ratio computes only first-order sensitivity terms while the Method of Sobol' computes both first-order and total-sensitivity terms. The computational cost of Sobol', measured in number of model evaluations $[2N(k + 1)]$, is much less than the MC integrals associated with the Correlation Ratio method (kN^2). Using the Correlation ratio, with $k = 3$, and $N = 128$; 49,152 model evaluations are required to obtain only the first-order sensitivity indices. For the Method of Sobol', with $k = 3$, and $N = 128$, 1024 model evaluations are required to obtain both first and total-order sensitivity indices for all three factors.

Sobol' included a quasi-random sampling method, known as LPtau (LPτ), to be used in the Sobol' variance-decomposition method. It helps yield a faster convergence rate in the model output, approximately on the order of N^{-1}, rather than the rate using the purely random sampling of the factor distribution spaces which converges at approximately $N^{-0.5}$ [39]. The Sobol' sampling method is designed to fully sample the space of each factor in a hyper-dimensional unit cube of dimension k [40]. This means that the sampled LPτ values range between 0 and 1 with a uniform distribution. The sampled LPτ values can be transformed into the appropriate PDFs by using the properties of each factor's inverse cumulative distribution function (CDF). Even though [31] recommended LHS for the computation of the Correlation

Ratio, others have shown that the LPτ method yields superior results even when computing the Correlation Ratio [39]. Therefore, in this work, when the Correlation Ratio is computed, the input factors are sampled using the LPτ method instead of random or LHS.

6.3.5 FAST and Extended FAST

The Fourier Amplitude Sensitivity Test (FAST) methods are based on Fourier analysis procedures involving sampling the factor distribution spaces in a manner similar to sampling time-domain signals at fundamental and harmonic frequencies. The FAST method only provides first-order sensitivity terms. The extended FAST technique provides both first and total-order terms. Though the four variance-decomposition methods shown in Figure 6.1 give equivalent results for similarly-ordered outputs (i.e., similar results for first or total-order terms), the FAST methods are very cumbersome to implement in comparison to the Method of Sobol' and Correlation Ratio. For more information regarding FAST and Extended FAST, the reader is referred to [35] and [36].

6.4 SUMMARY

There are many tools that can be used by systems designers to perform systems engineering analysis. Two of those tools described in this chapter, are sensitivity and uncertainty analysis. In general terms, SA is the study of how the output of a model varies as a function of its inputs. Uncertainty analysis describes the level of uncertainty in a model's output given uncertain inputs. Both are tools that can be used to assist in systems engineering analysis. In this chapter, it was shown that SA methods can be divided into three groups: screening, local and global.

Screening methods rank the input factors by importance but provide no quantitative analysis of how much more important one factor is over another. Local SA methods provide more quantitative information about factor importance and consist of the common control-

system partial derivative and the pseudo-Monte Carlo techniques. Global SA differs from local SA methods in that global techniques simultaneously vary all the input factors during model execution as opposed to varying one factor at a time.

Global SA can be performed using Monte Carlo and variance decomposition techniques. The variance decomposition techniques have an advantage over MC methods a they apportion the error in the model output variance back to the input factors. In this way, the exact contribution to model output variance (error) can be quantitatively determined for each factor.

There are four techniques or methods used to perform variance decomposition: Correlation Ratio; Method of Sobol'; FAST; and Extended FAST. The correlation ratio is relatively simple to implement, but is computationally very expensive, and provides only first-order sensitivity terms. The method of Sobol' is slightly more complicated to implement, but computationally much more efficient, and provides both first and total-order sensitivity terms. The FAST and Extended FAST methods are very cumbersome to implement, require about the same level of computational expense as the Method of Sobol', and provide first, and first plus total-order terms, respectively.

A word of caution is in order. At times, there can be significant confusion when discussing sensitivity analysis, what it means, and how it is implemented. The objective of this work is to perform SA using the global SA method of variance decomposition and apportion the error in the output to the input factors. In the next chapter, the Method of Sobol' will be used to perform SA.

CHAPTER 7

SYSTEMS ENGINEERING ANALYSIS: TRMM-LIKE ALGORITHM

7.1 INTRODUCTION

In November 1997, the Tropical Rainfall Measuring Mission (TRMM) satellite was launched from the Tanegashima Space Center in Japan by the H-II F6 launch vehicle [41]. TRMM was and continues to be a joint project between the United States National Aeronautics and Space Administration (NASA) and the Japanese Aerospace Exploration Agency (JAXA). The precipitation radar (PR) on board the satellite, is the first weather radar to be deployed in space and is one of several instruments being used to provide a three-dimensional structure of rainfall by measuring the radar reflectivity of the cloud system and the attenuation of the microwave signal as it passes through the precipitation. The major advantages of such a system are its global coverage and frequent sampling of global precipitation. Important applications of this project are immediate practical benefits to agriculture, water resources management, and flood warning systems [42].

Satellite systems such as TRMM are complex and rely on the proper design and functioning of each of its many subsystems—satellite vehicle, ground validation (GV) sites, precipitation radar (PR), calibration, and retrieval algorithms—to ensure high quality data products. The retrieval algorithms employed in TRMM are based on mathematical models and assumptions about the microphysics of precipitation. Errors in the model assumptions, variables input to the model, and model parameters can lead to errors in the output, which in this case, is the retrieved rain rate.

This chapter describes and implements systems engineering analysis on a TRMM-like (TL) retrieval algorithm using sensitivity analysis (SA) and uncertainty analysis (UA) tools. It is referred to as TL to convey the notion that the tested algorithm is based on the TRMM algorithm but deviates in select aspects. In section 7.2, a brief overview is given of the TRMM satellite and its rainfall-retrieval algorithm. Next, the TL rain-rate estimation model is developed which will be used for the SA and UA. In section 7.3, the TL model is analyzed using the UA/SA methods described in Chapter 6 which use the Method of Sobol' variance-decomposition technique. The input factors are described along with their respective probability density functions (PDFs). The SA/UA results are presented in section 7.4 and a summary is given in section 7.5.

In the context of systems engineering, when analyzing the performance of a new system, it is important to be able to benchmark its performance with that of some other reference system. The TL retrieval/rainfall estimation system serves as that comparative reference for future work.

7.2 TRMM OVERVIEW

In a limited systems view, TRMM is comprised of three major subsystems: the earth-orbiting satellite with its PR; the ground functions including the Ground Validation (GV) systems; and the microphysical-based retrieval or rainfall estimation algorithms. Other subsystems are the data processing, communications, and launch vehicle, but these are not covered in this work.

7.2.1 Spacecraft

The TRMM satellite is in earth orbit at an altitude of about 350 km as shown in Figure 7.1. The 13.8-GHz PR uses a 128-element phased-array antenna to scan from right to left as the satellite moves through its inclined orbit with a scan angle of about ± 17°.

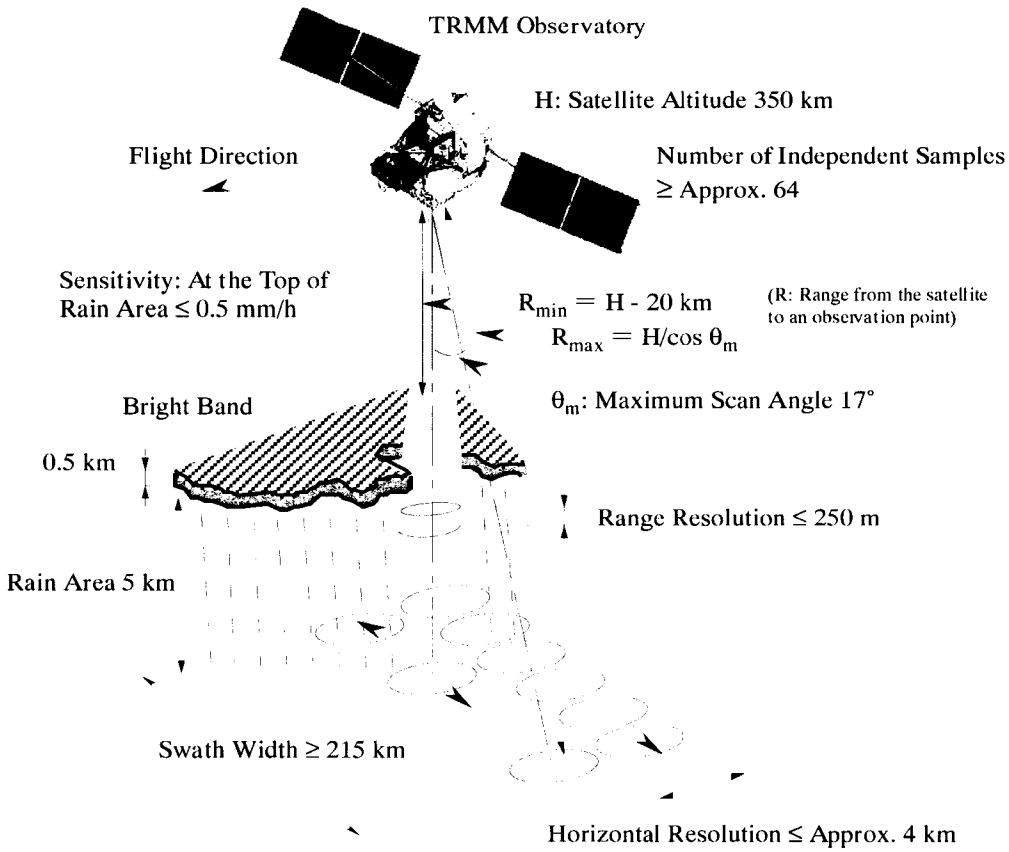

Figure 7.1. Measurement concept of the precipitation radar on board the TRMM satellite. Source: TRMM Data Users Handbook, 2001.

The radar footprint, at ground level, is about 4 km in diameter and the vertical resolution is 0.25 km. In the figure, the bright band (melting layer) is depicted as being approximately 0.5-km in height at an altitude of 5 km. Because of ground clutter up to about 2 km above ground, the vertical distance of the PR-measured rain region is typically about 3 km.

7.2.2 Ground Validation Program

In conjunction with the goals of TRMM, several ground validation (GV) sites are operated by the GV Program. These sites are operated on a continual basis and provide independent verification and validation of the PR performance and algorithm data products. The TRMM science team suggested having 10 GV sites, representing a reasonable variety of tropical rain regimes in place at the time of launch. The TRMM program focused on four of the highest

priority sites, e.g., Florida, Kwajalein, Australia and Texas. The operational sites are equipped with Doppler weather radars and networks of surrounding rain gauges. The data retrieved by these sites is correlated with the data retrieved by the satellite and necessary adjustments or modifications are sent to the satellite subsystems or data processing subsystems [43] [44]. Proper site planning, facilities planning and operations of the GV sites are crucial to the overall success and attainment of the TRMM mission goals.

7.2.3 Retrieval Algorithm

The retrieval algorithm used to estimate the TRMM rainfall rates is designated as 2A25 in the data products [45] and is thoroughly described in [8] but a brief overview of the fundamental equations, methods and assumptions of the retrieval algorithm will be given here. The underlying assumption of the retrieval method is that specific attenuation $k(r)$ in dB/km, at some range r from the satellite, can be modelled as

$$k(r) = \alpha Z_e^{\beta}(r) \tag{7.1}$$

and that the rainfall rate in mm/hr can be modelled as

$$R(r) = a Z_e^{b}(r) \tag{7.2}$$

where α, β, a and b are empirically-derived coefficients and the true radar reflectivity factor is designated as $Z_e(r)$ (mm^6 m^{-3}). Because of attenuation, $Z_e(r)$ is masked and must be estimated. Note that the subscript i is dropped in Z_e from that used in earlier chapters because this is a single frequency radar. The observed or measured radar reflectivity factor $Z_m(r)$ (mm^6 m^{-3}) at range r is related to $Z_e(r)$ by the two-way attenuation factor $A(r)$,

$$Z_m(r) = Z_e(r)A(r) \tag{7.3}$$

and $A(r)$ is given by

$$A(r) = \exp\left[-0.2\ln(10)\int_0^r k(s)ds\right] \tag{7.4}$$

Using the assumption of (7.1), (7.3) can be solved for $Z_e(r)$ and written as

$$Z_e(r) = \frac{Z_m(r)}{A_{HB}(r)} \tag{7.5}$$

where $A_{HB}(r)$ is the Hitschfeld-Bordan (HB) derived attenuation factor,

$$A_{HB}(r) = \left[1 - q\beta \int_0^r \alpha(s) Z_m^{\beta}(s) ds\right]^{1/\beta} \tag{7.6}$$

with $q = 0.2 \ln 10$. It should be noted that log = $\log_{10}$ and ln = $\log_e$. The method requires that β is constant and describes $A_{HB}(r)$ in terms of measured $Z_m(r)$ instead of $Z_e(r)$. The HB total path-integrated-attenuation, in dB scale, can be written as

$$PIA_{HB} = -\frac{10}{\beta} \log(1 - \zeta) \tag{7.7}$$

where

$$\zeta = q\beta \int_0^{r_s} \alpha(s)\, Z_m^{\beta}(s) ds \tag{7.8}$$

and r_s is the range to the surface or the distance to the last bin of measured reflectivity above clutter ($r = r_s$). The weakness in (7.7) and the Hitschfeld-Bordan method in general, is that for large rainfall rates and correspondingly large attenuation values, ζ can approach or become larger than one, at which point (7.7) becomes invalid. To help remedy this situation, the Surface Reference Technique (SRT) is used to adjust the value of ζ such that the difference in (7.7) is always greater than zero.

The SRT method gives an independent estimate of the total path-integrated-attenuation, and is defined as

$$PIA_{SR} = \Delta\sigma^0 = \left\langle \sigma^0_{no-rain} \right\rangle - \left\langle \sigma^0_{rain} \right\rangle \tag{7.9}$$

where $\langle \sigma^\circ_{\text{no-rain}} \rangle$ indicates the average of the surface radar cross section with no rain, and $\langle \sigma^\circ_{\text{rain}} \rangle$ is the average when rain is present [46]. The PIA_{SR} is frequently referenced as simply $\Delta\sigma^\circ$.

The objective is to find the best or most accurate PIA_e using a combination of both PIA_{SR} and PIA_{HB}. If the assumption is made that under high rain-rate conditions (corresponding also to high-attenuation conditions) that $\Delta\sigma^0$ is correct or at least more accurate than PIA_{HB}, then the true PIA_e can be estimated using (7.7) and (7.9),

$$PIA_e = \Delta\sigma^0 = -\frac{10}{\beta}\log(1-\varepsilon\zeta) \tag{7.10}$$

where ε is a correction term to ensure that the difference in (7.10) is always positive. From (7.10), the correction factor ε_s for SRT is,

$$\varepsilon_s = \frac{1-10^{-0.1\beta\Delta\sigma^0}}{\zeta} \tag{7.11}$$

The final value of ε is between 1 and ε_s and is given by the simple linear equation [47]

$$\varepsilon = 1+\zeta(\varepsilon_s - 1) \tag{7.12}$$

instead of the more detailed maximum-likelihood calculations described in [8]. With this final value of ε, the attenuation-corrected $Z_e(r)$ can be calculated at all ranges using

$$Z_e(r) = \frac{Z_m(r)}{\left[1-\varepsilon q\beta\int_0^r \alpha(s)Z_m^{\beta}(s)ds\right]^{1/\beta}} \tag{7.13}$$

Because multiplying by ε in the denominator is equivalent to adjusting the α in the integral, this method is referred to as the α-adjustment method.

The TRMM 2A25 algorithm also adjusts for non-uniform beam filling (NUBF), but as the adjustment is small, it is not implemented in this work. Normally, after the final ε value is calculated using (7.12), the a and b terms in (7.2) are adjusted according to

$$\log(a) = a_0 + a_1 x + a_2 x^2 \tag{7.14}$$

$$\log(b) = b_0 + b_1 x + b_2 x^2 \tag{7.15}$$

where

$$x = \log(\varepsilon) \tag{7.16}$$

and

$$a' = 10^{\log(a)} \tag{7.17}$$

$$b' = 10^{\log(b)} \tag{7.18}$$

to provide the final, adjusted *Z-R* relationship used to estimate rain rate,

$$R(r) = a' Z_e^{b'}(r) \tag{7.19}$$

with $R(r)$ in mm/hr. The coefficients in (7.14) and (7.15) are contained in the TRMM 2A25 reference document .

7.3 UA AND SA APPLIED TO TL ALGORITHM

This section describes how uncertainty and sensitivity analyses are applied to a TL algorithm with the objective of determining the importance of each of the input factors in the variance (error) of the rainfall-rate estimation in the bottom bin. The assumptions and values used for the input factors are also described.

7.3.1 Model

Using equations (7.1) through (7.19), a model for the TL algorithm can be constructed according to the sensitivity analysis guidelines in Chapter 6 of the form,

$$R(r) = f\left(Z_m, \alpha, \beta, a, b, \Delta\sigma^0\right) \tag{7.20}$$

where the rain-rate $R(r)$ is a function of the input factors and range r. Using this model, for inputs consisting of Z_m, α, β, a, b, $\Delta\sigma^\circ$, the estimated rain-rate profile can be calculated at each bin of the input Z_m profile. Although the input profile, Z_m, is many bins high, the sensitivity analysis is performed using only the values from the bottom bin nearest the ground. That is, the remaining bins are used to calculate the rain profile, but only the rain rate from the bottom bin is used to perform UA and SA.

7.3.2 Input Factors

Each of the input factors listed in (7.20) must have an assigned probability density function (PDF) that can be sampled as part of the SA process.

Factor Z_m In this case, the input factor, Z_m is a vector, a vertical profile of reflectivity values. It is understood that there is random measurement error in each bin, and that the error is normally distributed, zero mean, with a 1-dB standard deviation [48]. With random error in the Z_m profile, some bins within any particular profile will have more or less error than others, but in general, it is assumed that the error can be up to 1 dB and is normally distributed in each bin. Without accounting for measurement error, the model could be run with the Z_m profile constant at its nominal values (based on known N_w, D_o pairs and known rain rate) and it could be used directly in the model with the SA method calling the same Z_m profile each time. However, doing this would not allow the computation of the sensitivity index of the variance (error) of the Z_m profile. The objective of SA is to incorporate measurement error (statistical variance) in the Z_m profile along with variance in each of the other input factors. Because the sensitivity and uncertainty analysis methods don't allow for a direct mapping of an error vector in (7.20), the Z_m profiles must first be mapped to another random variable called a trigger factor [49]. A schematic diagram showing how a trigger factor is used with sensitivity analysis is shown in Figure 7.2. To simulate Z_m with measurement error, Figure 7.2 shows η profiles based on a known N_w, D_o pair, and corresponding rain rate, with random error added to each bin of each profile. In this work, $\eta = 1200$, but it could be any reasonably large number such as 1000 or 1500. The dashed lines in the upper-right of Figure 7.2 represent the intrinsic or baseline Z_m profile to which error is added resulting in the solid lines. The trigger factor serves as an index to select specific Z_m profiles for SA. It is a discrete random variable, in this case uniform, 1 to η, corresponding to the number of error-laden Z_m profiles. When performing SA, the Z_m profiles (vectors) are generated and sorted from least to greatest overall error based on the

average error of each profile, then the trigger factor is sampled and used to select the appropriate Z_m profile to be inserted in each model evaluation.

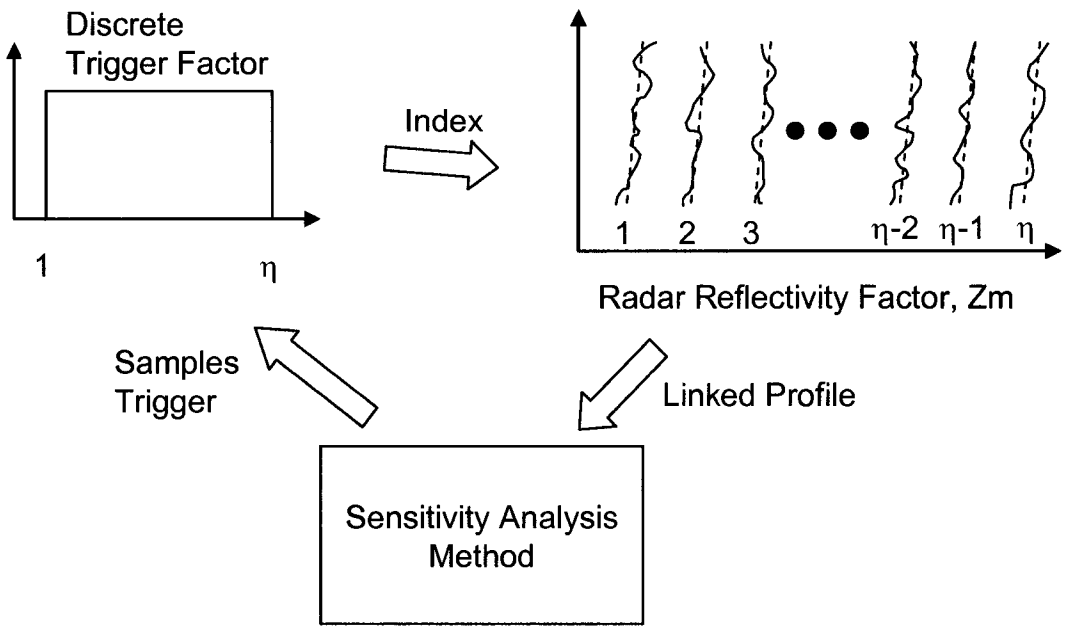

Figure 7.2. Diagram showing the relationship between trigger variables, the sensitivity analysis method and input factors with error distribution.

In this way, the error in the Z_m profiles can be integrated into the model evaluations and be linked to their error distribution range and the SA process.

Factor: α In this work, α is assumed to be uniform and vary ± 20% about its nominal value specified for rain, 20° C, stratiform [8].

Factor: β This must be a constant and is fixed at its defined value for rain, 20° C, stratiform.

Factors *a* and *b* In practice, the factors *a* and *b* are derived from power-law fits of the Z-R relationship of the form $R = a\,Z^{b}$. Considerable work has been done to analyze global precipitation data, model it, then compute the *a* and *b* coefficients as functions of ε such that the values of *a* and *b* are linked to the α-adjustment method in the TRMM algorithm [50]. Using that method, the log polynomials of (7.14) and (7.15) are derived and statistical information as

to the actual distribution of a and b are unfortunately not available. Note that even small variations in a and b in (7.2) (or a′ and b′ in (7.19)) can cause large variation in estimated rainfall rate, and consequently, the distributions of a and b can be very important to accurate rainfall estimation.

In the TRMM algorithm, the a and b factors are computed using (7.14) and (7.15) where (7.19) is used to compute rain rate. As this work focuses on a TL algorithm, the calculation and usage of a and b is somewhat differently depending on the rain rate and HB PIA. For low rainfall rates, where ε is unity (or close to unity), and α-correction is not performed, the *Z-R* relationship of (7.2) is used in SA/UA with estimated PDFs for a and b, and for higher rainfall rates, the a and b correction method shown in (7.14) and (7.15) is used without sampling the PDFs. The TL algorithm automatically transitions from one method to the other depending on the values of PIA from (7.9) and ζ from (7.8). For this method to work, it is necessary to obtain reasonable estimates of PDFs for a and b under low rainfall conditions. Using this method, at higher rain rates, errors in Z_m and $\Delta\sigma^\circ$ both propagate through the model and are implicit in the calculation of ε and the values of a' and b'.

In order to obtain a reasonable estimate of the probability density functions of a and b for low rainfall rates, the four global regions of disdrometer data (same data sets) shown in Figure 3.12 were analyzed using the method described by [51]. Figure 7.3 shows a scatter plot of filtered, stratified log(R) vs. log(Z) with the assumption of low rainfall-rate stratiform precipitation determined by, $R < 15$ mm/hr, $Z > 18$ dBZ to account for noise floor, and $Z < 35$ dBZ. In the plot, reflectivity Z is in linear scale, $mm^6\ m^{-3}$.

In the method described by [51], the Z-R relations are stratified or grouped by α and ε using the equation

$$\alpha_s = \frac{k_s}{Z_s^{\beta}} \tag{7.21}$$

where $\beta = 0.7923$, and the subscript s represents the subgroup of the total data set. For each point in the plot, a specific attenuation value, k_s is calculated. After calculating each k_s value, then an α_s value is calculated using (7.21). Following that, the *Z-R* points are grouped or stratified according to α and least-square first-order curve fits are performed on the grouped *Z-R* points. The lines in Figure 7.3 are the resultant *Z-R* curve fits, each with a different *a* and *b* value described by (7.2). Regressions were not performed on groups with fewer than five points. Some of these unused outlier points are shown below and above the main body of scatter points and show no fitted lines. It should be noted that in order to obtain better distributions of *a* and *b*, more curve fits are necessary, and hence more data are necessary. However, for this work, these data seemed to be sufficient as a preliminary estimation of *a* and *b* PDFs.

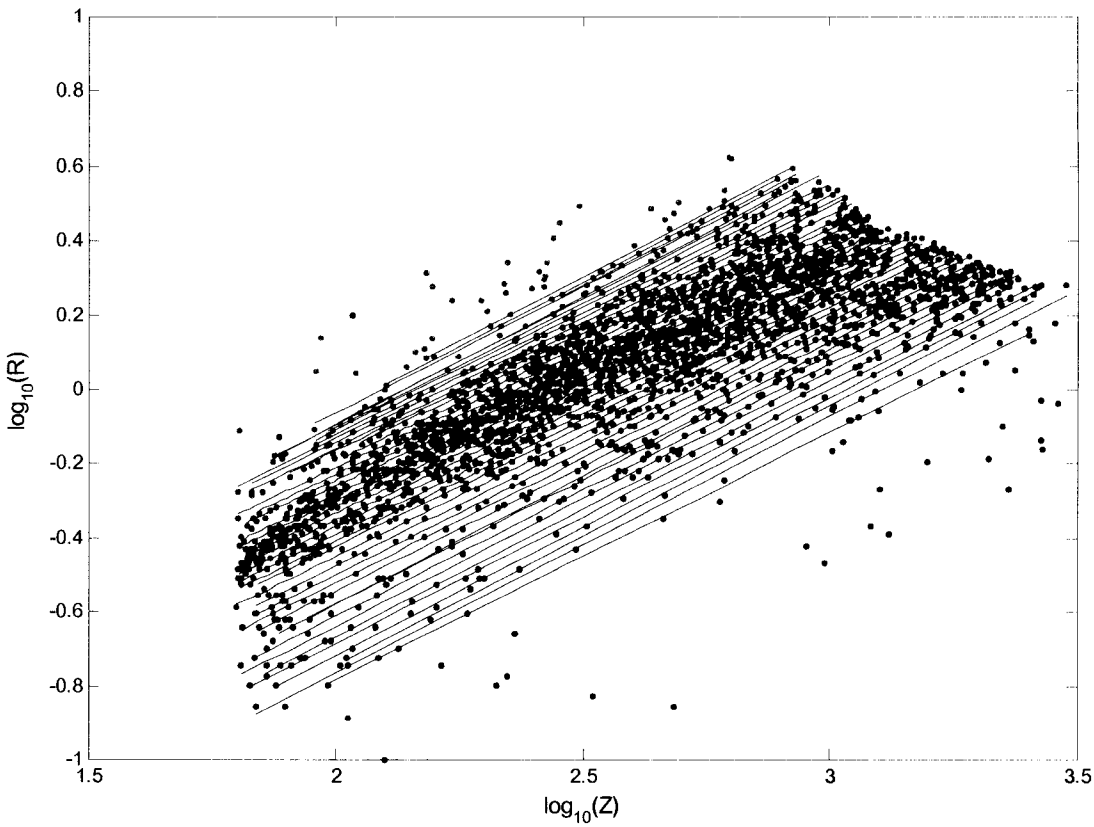

Figure 7.3. Scatter plot of log(R) versus log(Z) showing $R = a Z^b$ fit. The lines are R-Z curve fits based on grouped points. For each line, a set of *a* and *b* coefficients is obtained. The scatter plot assumes stratiform rain, $R < 15$ mm/hr and $Z < 35$ dBZ.

In Figure 7.3, of the 6271 available DSD sets, 2775 met the imposed low-rainfall-rate conditions expressed above and are shown in the figure. Of those points (pair of Z and R values), 43 sets of *a* and *b* coefficients were obtained and plotted in histogram form in Figure 7.4.

The dashed lines in Figure 7.4(a) and (b) represent the nearly uniform PDFs estimated for the *a* and *b* coefficients. These plots use 10 bins, and the shape of each histogram will vary somewhat depending on the number of bins. The distribution for *a* is assumed to be uniform, roughly ± 0.014 about its mean. The distribution for *b* is also assumed uniform and about ± 0.036 about its mean.

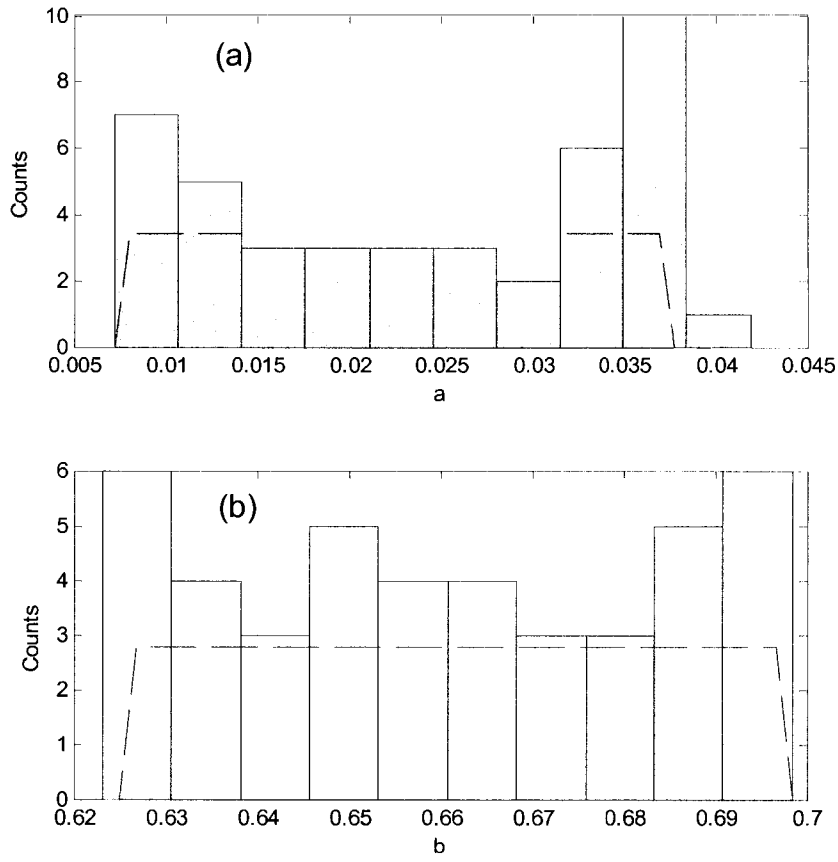

Figure 7.4. Histograms of the *a* and *b* coefficients for the $R = a Z^b$ relationship. In each case, a uniform distribution is fitted to the histograms. Part (a) shows the histogram for the *a* coefficient. The mean values is 0.0243. There is obviously some higher percentage of counts around 0.35, but a uniform PDF is assumed between 0.008 and 0.037. Part (b) shows the *b* coefficient with a mean value of 0.661and assumed uniform distribution between 0.626 and 0.698. Each histogram consists of 43 points or samples.

An alternative procedure is to keep b fixed and relate all variabilities of Z-R through the concept of normalized DSD [52].

7.4 RESULTS

In order to obtain boundaries of rainfall rates for simulation purposes, Figure 7.5 shows a graph of measured global-rainfall rates for the month of July 2000 from TRMM courtesy of Dr. Wanyu Li. For stratiform rain over ocean, the data indicate that about 99% of the measured rainfall rate is between 5 and 20 mm/hr and for stratiform rain over land, 79% of the rainfall rate is between 5 and 20 mm/hr. For convective rain over ocean, 87% occurs between 5 and 20 mm/hr, and for convective over land, about 79% occurs between 5 and 20 mm/hr. Given these data, a generous analysis range for TRMM simulations is 5 to 35 mm/hr which accounts for a large percentage of global rainfall rate.

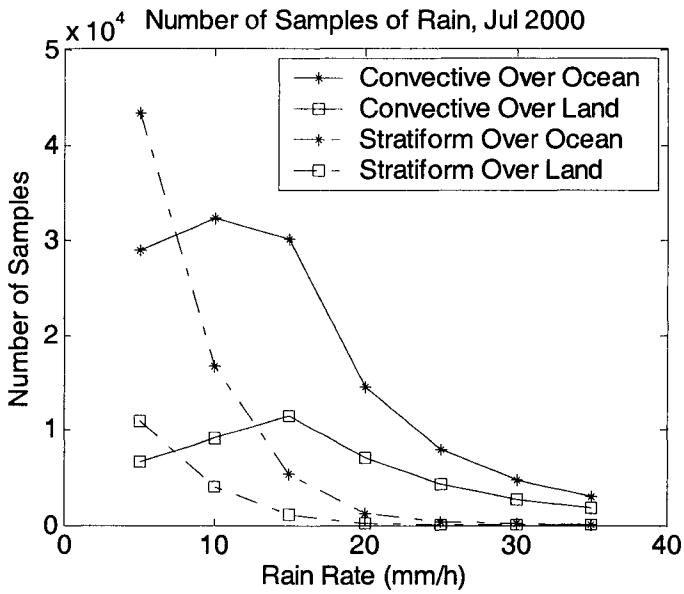

Figure 7.5. Graph showing a breakdown of global rainfall rates from TRMM categorized as convective over land and ocean, and stratiform over both land and ocean. Data are from the month of July 2000 courtesy of Dr. W. Li.

It is important to analyze global rainfall also based on the percentage that occurs over land and over ocean. Figure 7.6 shows a chart based on the same July 2000 data which shows a breakdown of measured rainfall rate by region for global rainfall rate less than 35 mm/hr. The

percentage of measured global rainfall rate occurring over ocean is about 76% and over land about 24%.

Additionally, in simulating representative profiles, the TRMM receiver noise-floor of about 18 dBZ was used to eliminate profiles that could not be measured by the radar. The noise-floor constraint is especially critical at low rain rates where the measured reflectivity values are small. It also plays a role at very high rain rates where large attenuation can reduce the measured Z_m values.

Many Z_m profiles were simulated using known N_w, D_o pairs for use in the UA and SA computations. The parameters for these profiles are listed in Table 7.1 and are representative of the range of rainfall rates that TRMM typically measures. In the reflectivity profiles, the actual N_w and D_o values were chosen to provide increasing rainfall rates with reasonable N_w, D_o values in accordance with empirical data that indicate actual ranges for N_w and D_o are, $3 \leq \log N_w \leq 5$, and $0.5 \leq D_o \leq 2.5$ [19].

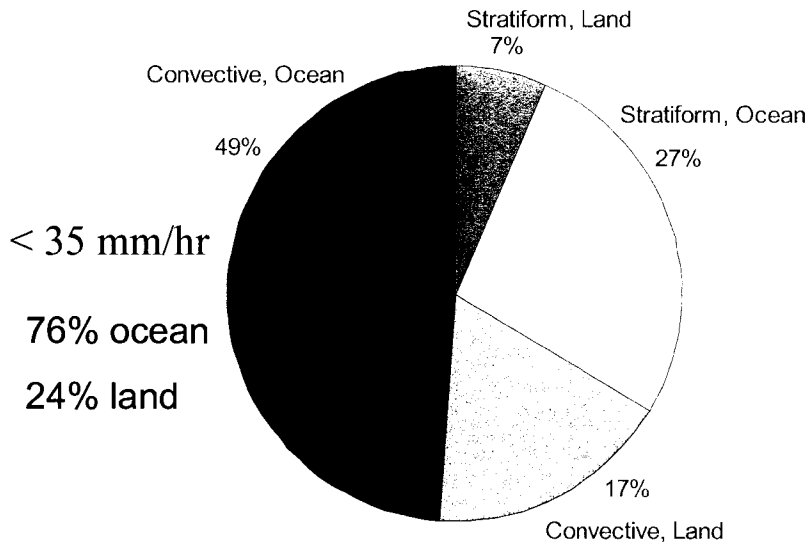

Figure 7.6. Breakdown of measured rainfall rate less than 35 mm/hr by region--ocean and land. Global data from July 2000. Courtesy of Dr. W. Li, CSU Radar Laboratory.

Using the Method of Sobol' (global SA using the variance-decomposition technique), both UA and SA were performed on the TL function of (7.20) for the N_w, D_o pairs listed in Table 7.1 for

both ocean and land conditions. Each profile is based on a vertical rain column, 3-km high assuming 12 bins, each with a radar range resolution of 0.25 km. The nominal values for input factors α and β are taken from [8] assuming stratiform rain and 20° C water with no temperature or height-based interpolation.

Table 7.1. List of the N_w, D_o pairs that were used to create Z_m profiles. The expected rain rate in mm/hr is shown in the right column.

D_o (mm)	N_w	Rain Rate (mm/hr)
0.65	33,800	1.09
0.75	33,900	2.14
0.85	34,300	3.87
0.90	34,600	5.10
0.95	35,000	6.65
1.00	35,500	8.56
1.10	36,700	13.52
1.15	37,400	17.33
1.25	38,900	26.64
1.30	39,700	32.65
1.35	40,500	39.73

Although many other combinations of N_w, D_o and rain rate could be used for these sensitivity analyses, the above sets meet the purpose here to cover the expected rainfall range, measure the importance of error on the output variance of estimated rain rate, and to quantitatively determine the importance of each of the factors listed in (7.20).

7.4.1 Ocean

For ocean, the TL-algorithm input-factor distributions are shown in Table 7.2. The uniform distribution is represented by U{range}, and the normal distribution is represented by N{mean, standard deviation}.

Table 7.2. List of the input factors and their distributions for the TRMM-like algorithm rainfall rate sensitivity analyses over OCEAN. The nominal values for these factors were obtained from [8], assuming 20° C stratiform rain.

Factor Name	Probability Distribution
α	U{ 2.851 e-4 ± 20% }
β	constant = 0.792 30
a	U{0.022 82 ± 0.014 }
b	U{ 0.672 7 ± 0.036}
$\Delta\sigma^\circ$	N{ $\Delta\sigma^\circ_{true}$, 1 dB }
Z_m *(error in each bin)*	N{0, 1 dB}

In this scenario, the error associated with Z_m is assumed to be from a normal distribution, zero mean, with a 1-dB standard deviation. The distribution associated with $\Delta\sigma^\circ$ is based on its true mean value from the simulated data set with added zero mean, 1-dB standard deviation error. The SA and UA results for D_o = 0.65 through D_o = 1.35 listed in Table 7.1 are shown in the following pages in Figure 7.7 through Figure 7.17. In each figure, a pie chart is shown in parts (a) and (b). Part (a) shows the variance decomposition for the inputs with the percentage contributed by each factor listed by the factor name. Part (b) shows a pie chart for the total sensitivity indices. Each pie wedge is identified by input factor, but since the sum of the total sensitivity indices can be larger than one, the total sensitivity index percentages are not shown. The histogram in part (c) of each figure is a distribution of estimated rainfall rate in the bottom bin of each profile. Part (d) of each figure shows the raw values output from the SA procedure using the method of Sobol'.

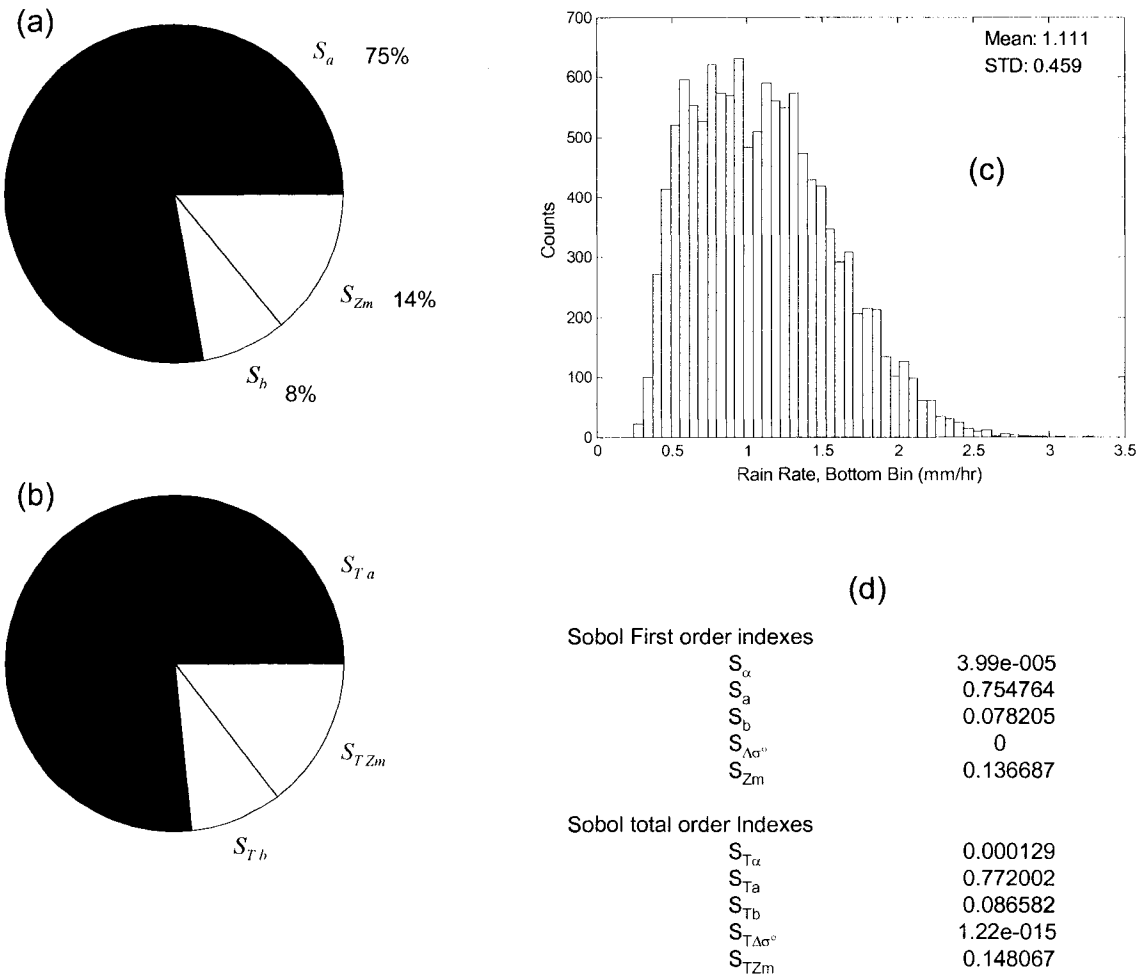

Figure 7.7. $N_w = 33{,}800$ $D_o = 0.65$, TRMM-like over ocean. The pie chart in part (a) shows the variance decomposition of the first-order sensitivity indices. Part (b) shows the total sensitivity indices. A histogram of the bottom-bin estimated rainfall is shown in part (c). Part (d) is a listing of the raw outputs from the method of Sobol' sensitivity analysis method. In this simulation, there is little higher-order interaction.

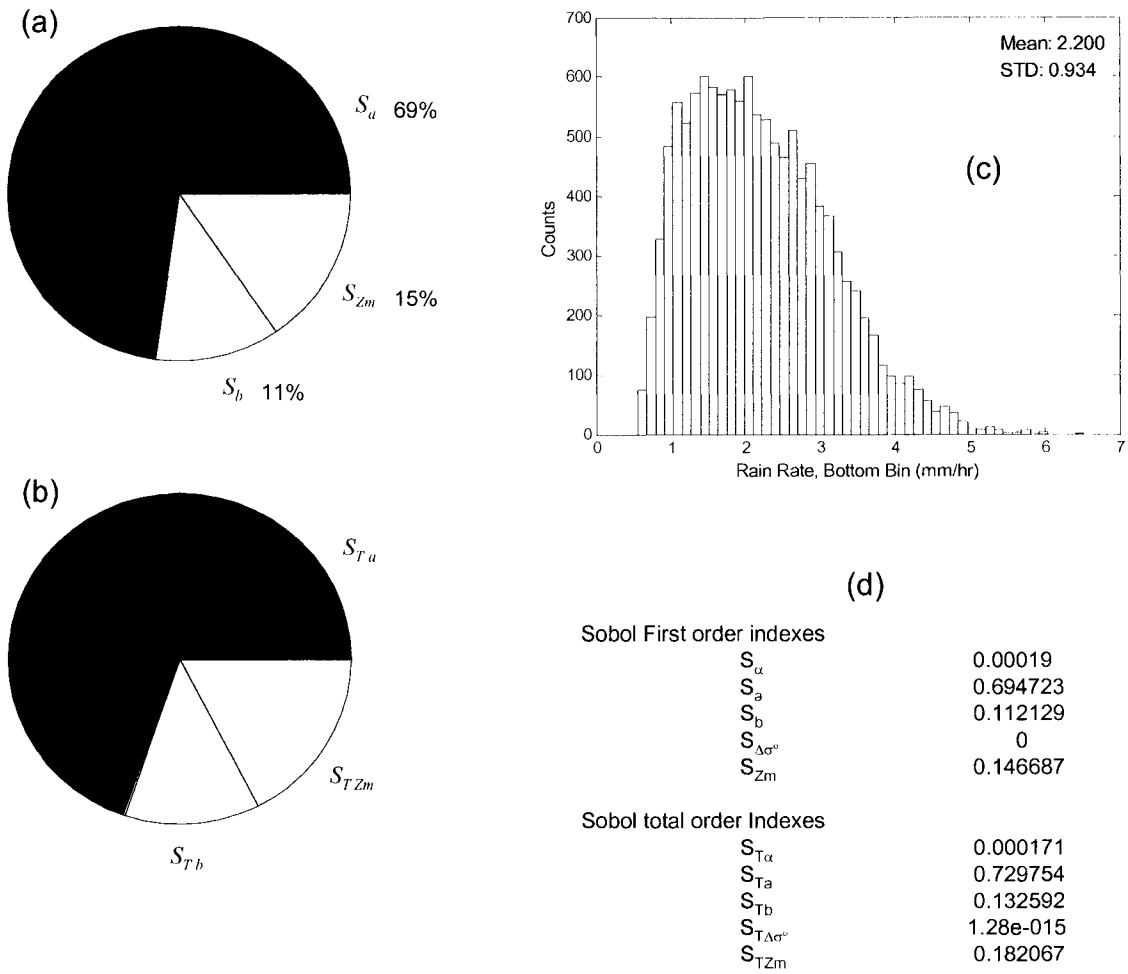

Figure 7.8. $N_w = 33{,}900$ $D_o = 0.75$, TRMM-like over ocean. The pie chart in part (a) shows the variance decomposition of the first-order sensitivity indices. Part (b) shows the total sensitivity indices. A histogram of the bottom-bin estimated rainfall is shown in part (c). Part (d) is a listing of the raw outputs from the method of Sobol' sensitivity analysis method. In this simulation, there is little higher-order interaction.

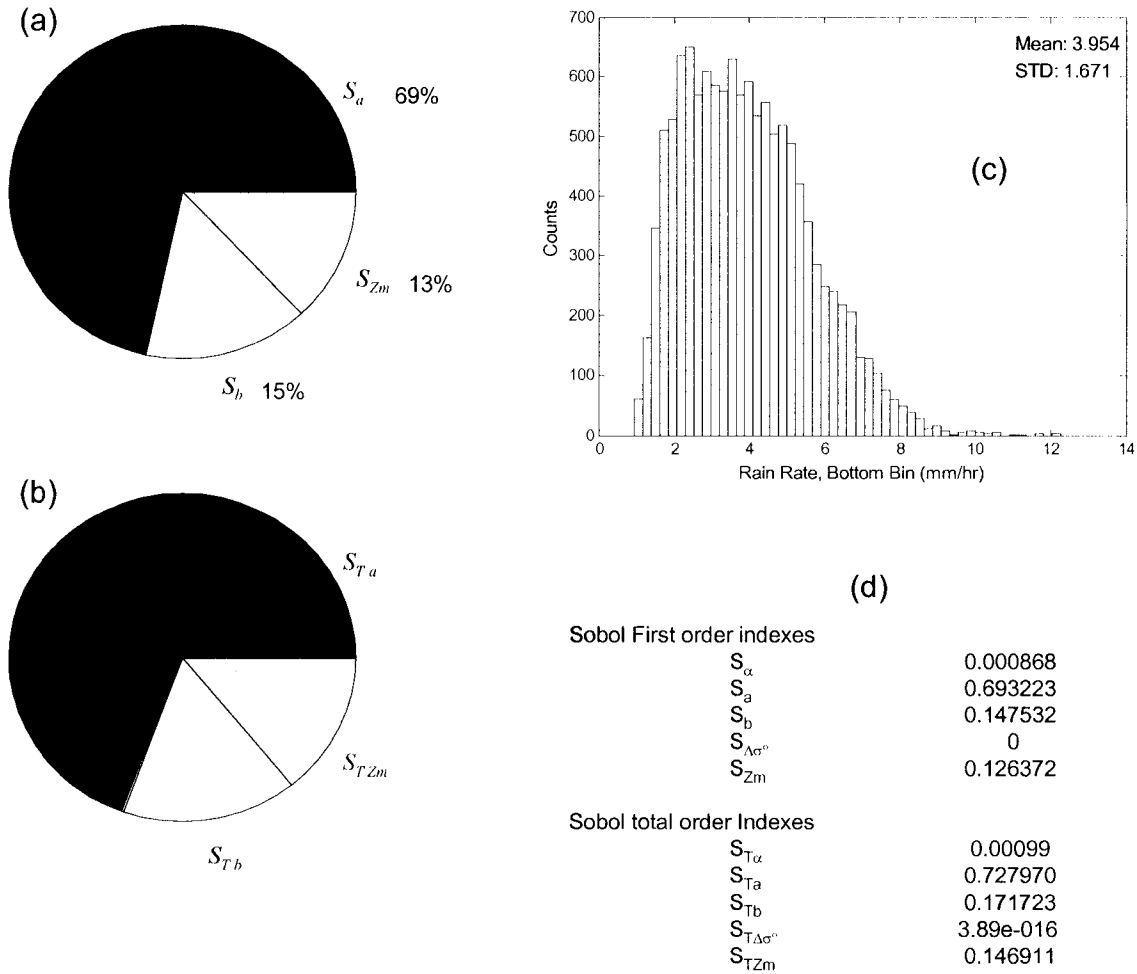

Figure 7.9. $N_w = 34{,}300$ $D_o = 0.85$ TRMM-like over ocean.. The pie chart in part (a) shows the variance decomposition of the first-order sensitivity indices. Part (b) shows the total sensitivity indices. A histogram of the bottom-bin estimated rainfall is shown in part (c). Part (d) is a listing of the raw outputs from the method of Sobol' sensitivity analysis method. In this simulation, there is little higher-order interaction.

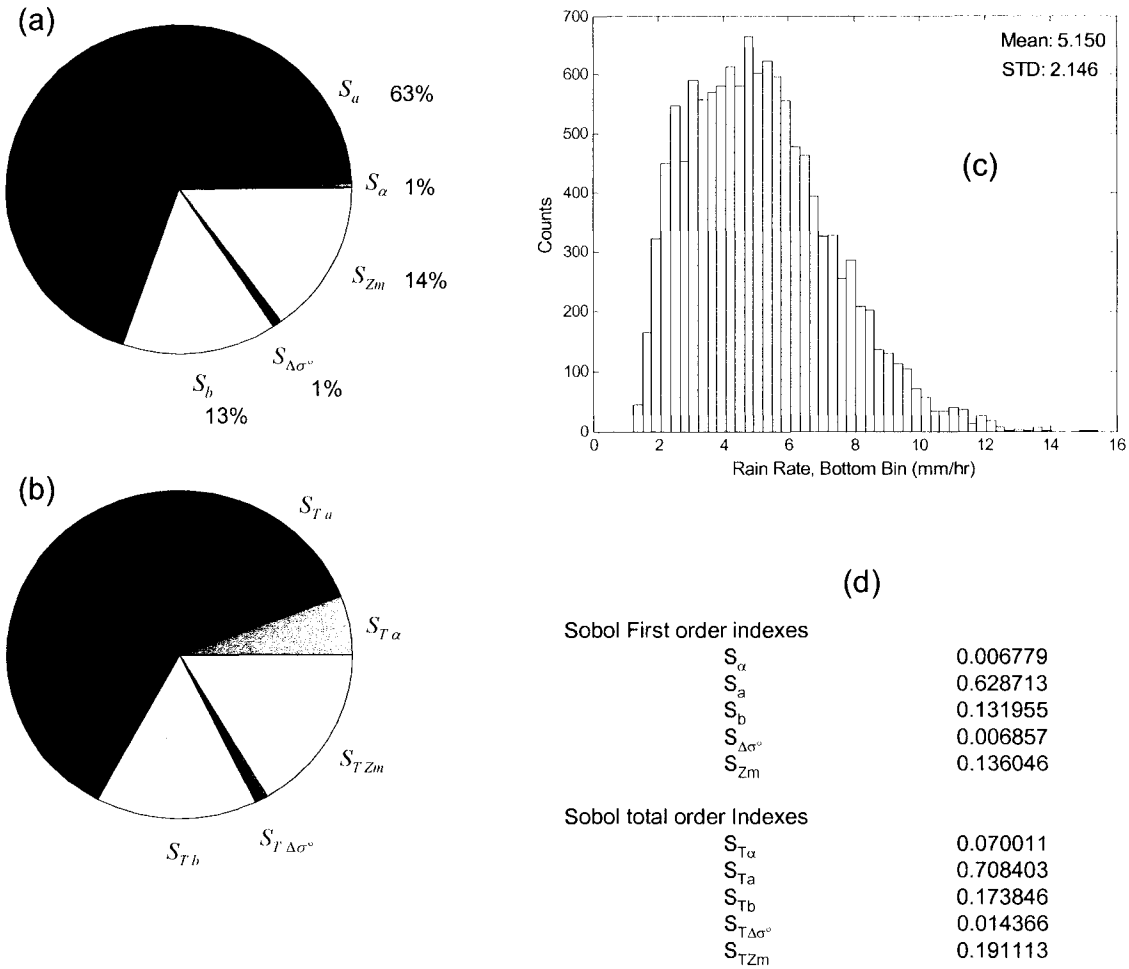

Figure 7.10. $N_w = 34{,}600$ $D_o = 0.90$ TRMM-like over ocean.. The pie chart in part (a) shows the variance decomposition of the first-order sensitivity indices. Part (b) shows the total sensitivity indices. A histogram of the bottom-bin estimated rainfall is shown in part (c). Part (d) is a listing of the raw outputs from the method of Sobol' sensitivity analysis method. In this simulation, there is little higher-order interaction.

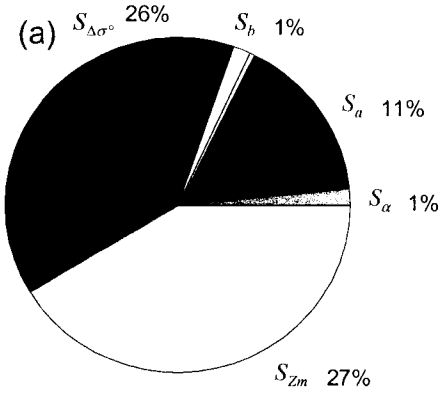

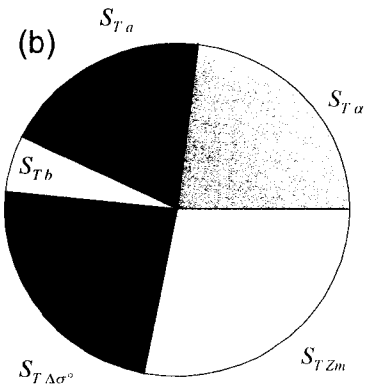

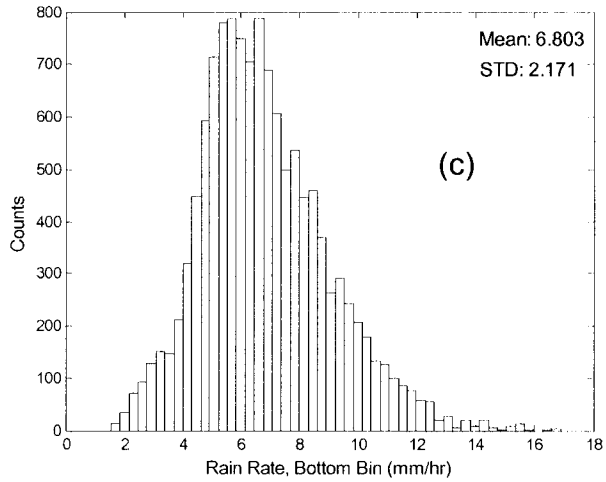

(d)

Sobol First order indexes

S_α	0.01185
S_a	0.107469
S_b	0.012485
$S_{\Delta\sigma^\circ}$	0.25678
S_{Zm}	0.273459

Sobol total order Indexes

$S_{T\alpha}$	0.356383
S_{Ta}	0.304695
S_{Tb}	0.086697
$S_{T\Delta\sigma^\circ}$	0.362880
S_{TZm}	0.431739

Figure 7.11. $N_w = 35{,}000$ $D_o = 0.95$ TRMM-like over OCEAN. The pie chart in part (a) shows the variance decomposition of the first-order sensitivity indices. Part (b) shows the total sensitivity indices. A histogram of the bottom-bin estimated rainfall is shown in part (c). Part (d) is a listing of the raw outputs from the method of Sobol' sensitivity analysis method. In this simulation, there is significant higher-order interaction.

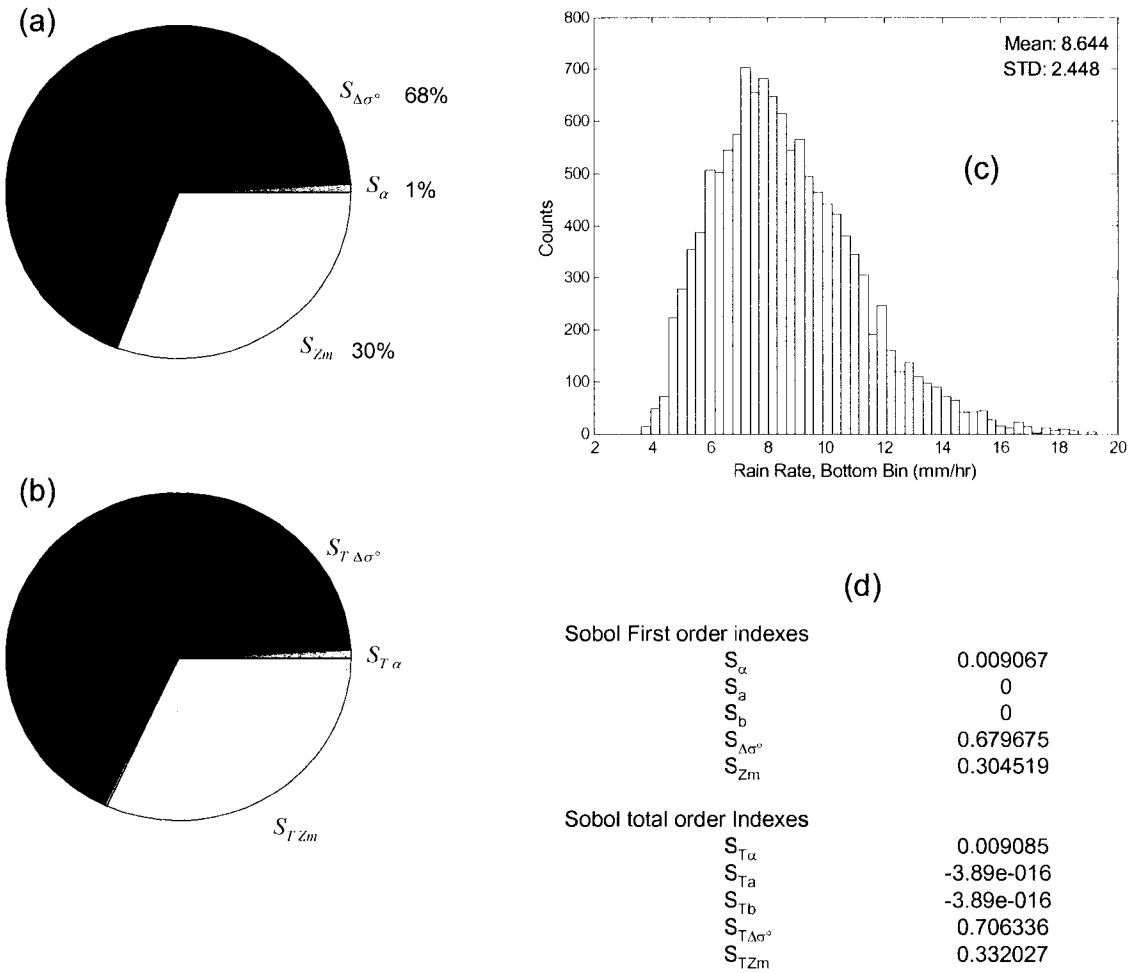

Figure 7.12. $N_w = 35{,}500$ $D_o = 1.00$ TRMM-like over ocean. The pie chart in part (a) shows the variance decomposition of the first-order sensitivity indices. Part (b) shows the total sensitivity indices. A histogram of the bottom-bin estimated rainfall is shown in part (c). Part (d) is a listing of the raw outputs from the method of Sobol' sensitivity analysis method. In this simulation, there is little higher-order interaction and the model is additive.

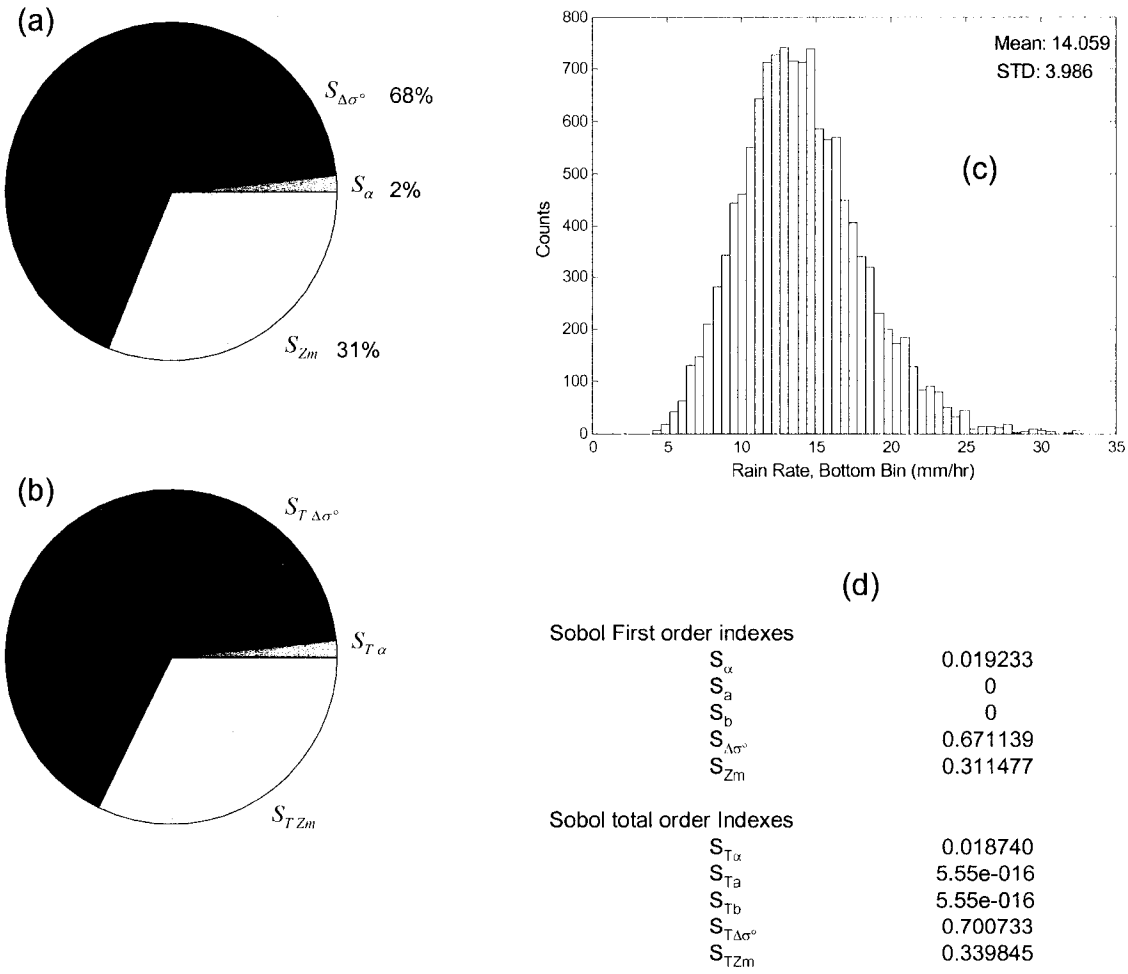

Figure 7.13. $N_w = 36{,}700$ $D_o = 1.10$ TRMM-like over ocean. The pie chart in part (a) shows the variance decomposition of the first-order sensitivity indices. Part (b) shows the total sensitivity indices. A histogram of the bottom-bin estimated rainfall is shown in part (c). Part (d) is a listing of the raw outputs from the method of Sobol' sensitivity analysis method. In this simulation, there is little higher-order interaction and the model is additive.

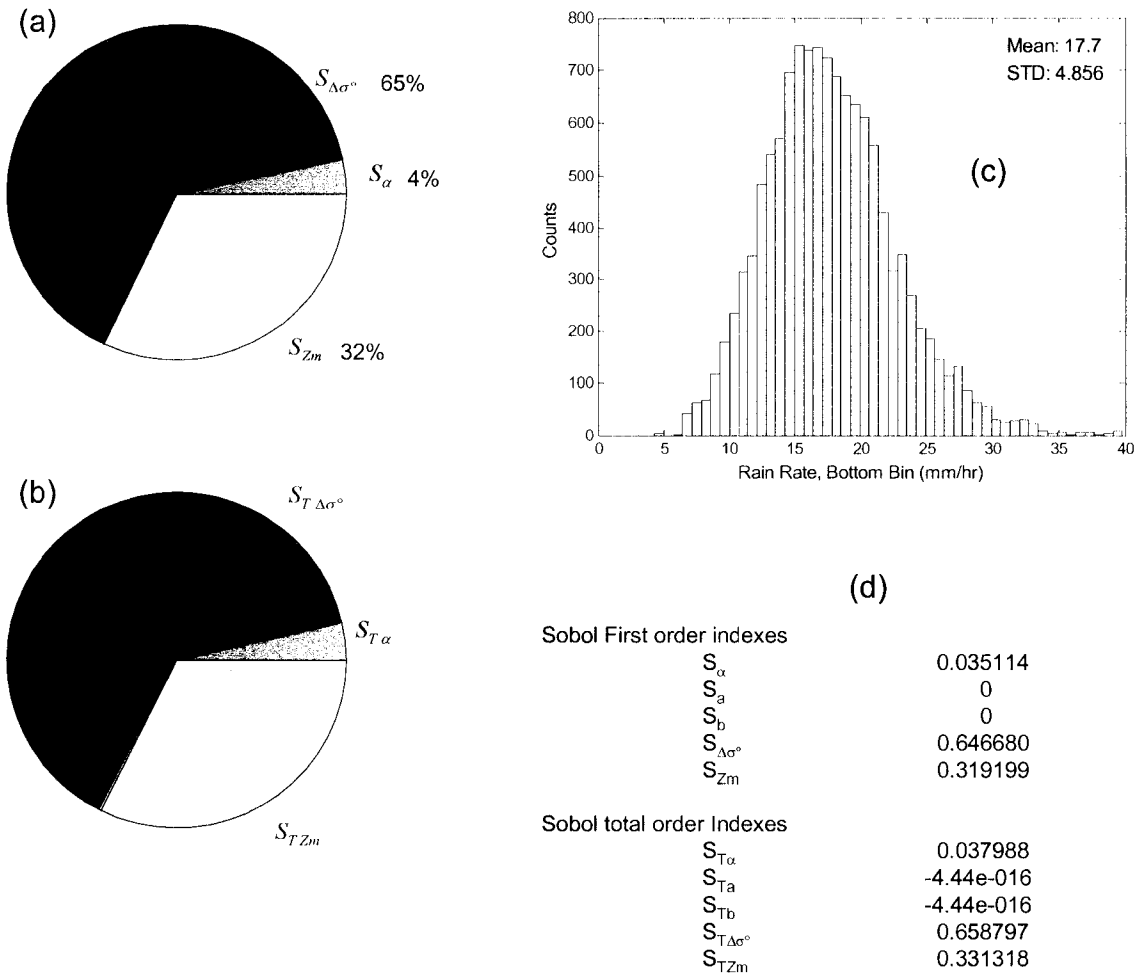

Figure 7.14. $N_W = 37{,}400$ $D_o = 1.15$ TRMM-like over ocean. The pie chart in part (a) shows the variance decomposition of the first-order sensitivity indices. Part (b) shows the total sensitivity indices. A histogram of the bottom-bin estimated rainfall is shown in part (c). Part (d) is a listing of the raw outputs from the method of Sobol' sensitivity analysis method. In this simulation, there is little higher-order interaction and the model is additive.

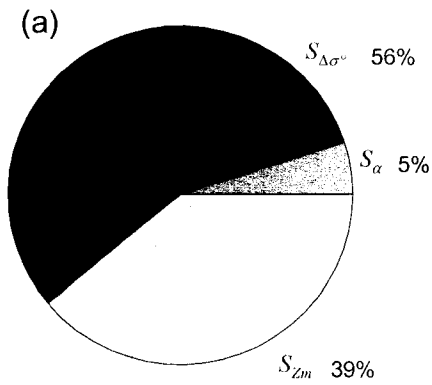

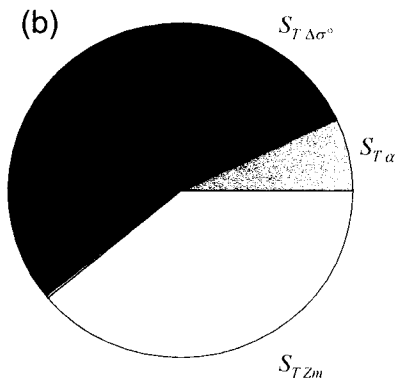

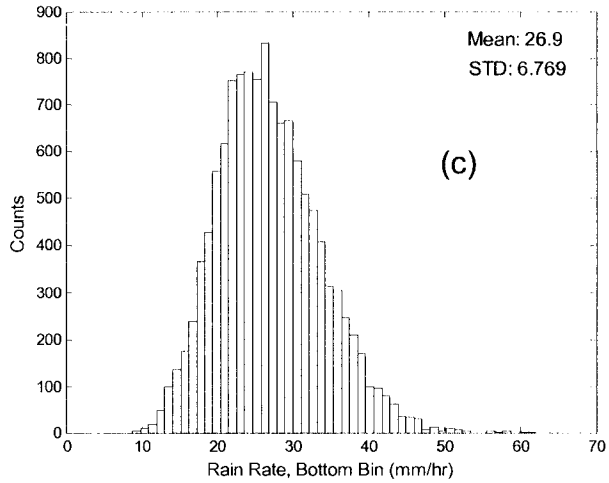

(d)

Sobol First order indexes	
S_α	0.052818
S_a	0
S_b	0
$S_{\Delta\sigma^o}$	0.561887
S_{Zm}	0.390923
Sobol total order Indexes	
$S_{T\alpha}$	0.077045
S_{Ta}	9.99e-016
S_{Tb}	9.99e-016
$S_{T\Delta\sigma^o}$	0.581084
S_{TZm}	0.419172

Figure 7.15. $N_W = 38{,}900$ $D_o = 1.25$ TRMM-like over ocean. The pie chart in part (a) shows the variance decomposition of the first-order sensitivity indices. Part (b) shows the total sensitivity indices. A histogram of the bottom-bin estimated rainfall is shown in part (c). Part (d) is a listing of the raw outputs from the method of Sobol' sensitivity analysis method. In this simulation, there is little higher-order interaction and the model is additive.

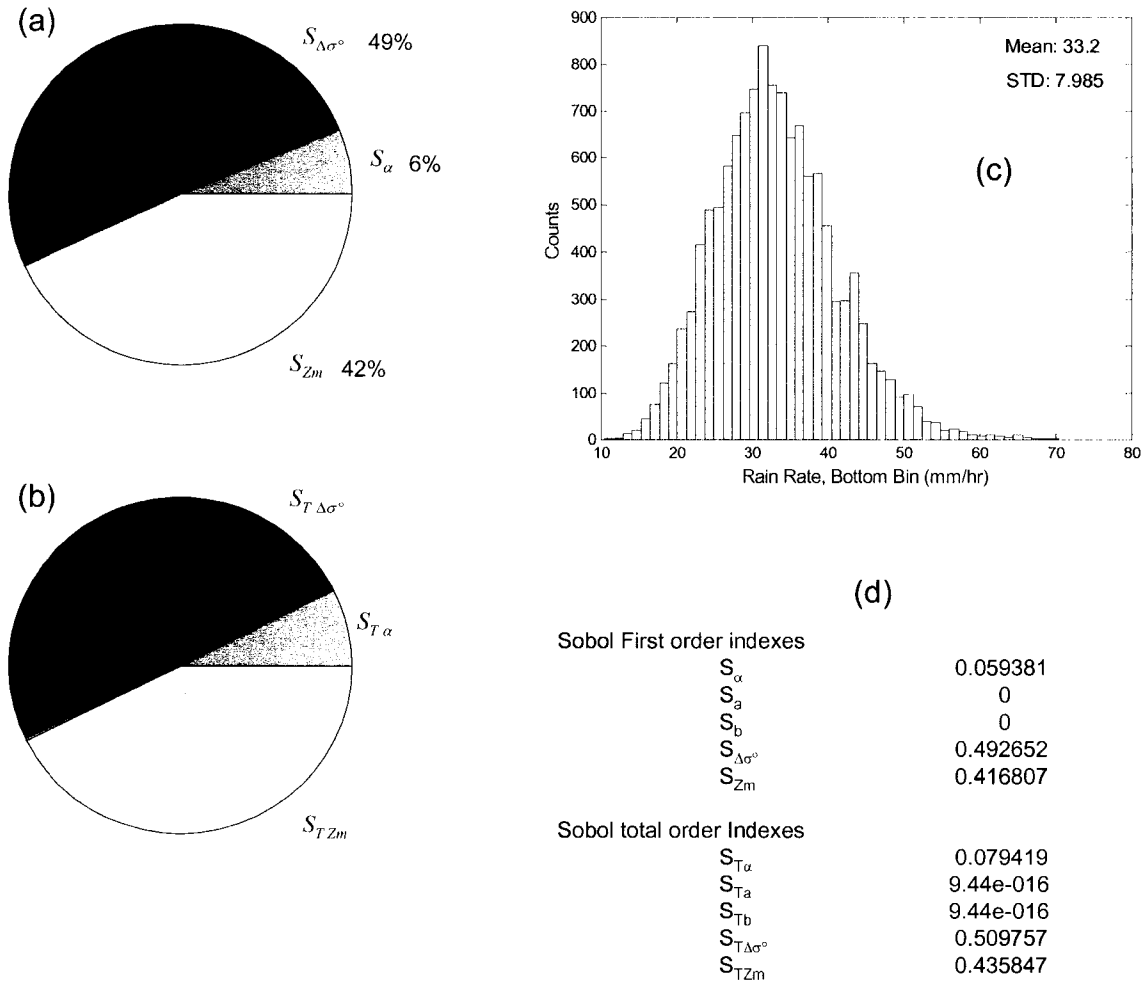

Figure 7.16. $N_w = 39{,}700$ $D_o = 1.30$ TRMM-like over ocean. The pie chart in part (a) shows the variance decomposition of the first-order sensitivity indices. Part (b) shows the total sensitivity indices. A histogram of the bottom-bin estimated rainfall is shown in part (c). Part (d) is a listing of the raw outputs from the method of Sobol' sensitivity analysis method. In this simulation, there is little higher-order interaction and the model is additive.

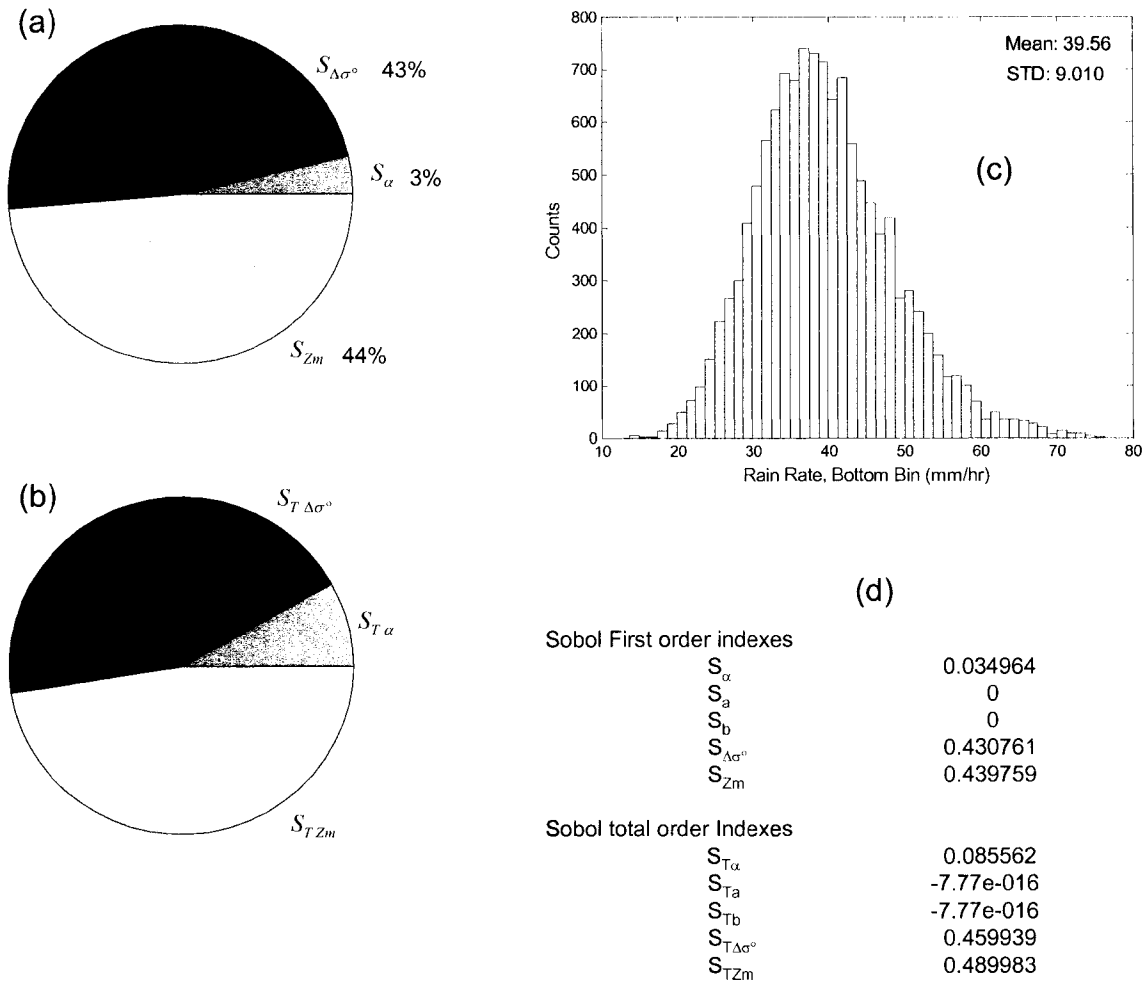

Figure 7.17. $N_w = 40{,}500$ $D_o = 1.35$ TRMM-like over ocean. The pie chart in part (a) shows the variance decomposition of the first-order sensitivity indices. Part (b) shows the total sensitivity indices. A histogram of the bottom-bin estimated rainfall is shown in part (c). Part (d) is a listing of the raw outputs from the method of Sobol' sensitivity analysis method. In this simulation, there is little higher-order interaction and the model is additive.

The SA results of the N_w, D_o pairs listed in Table 7.1 are shown in graph form in Figure 7.18.

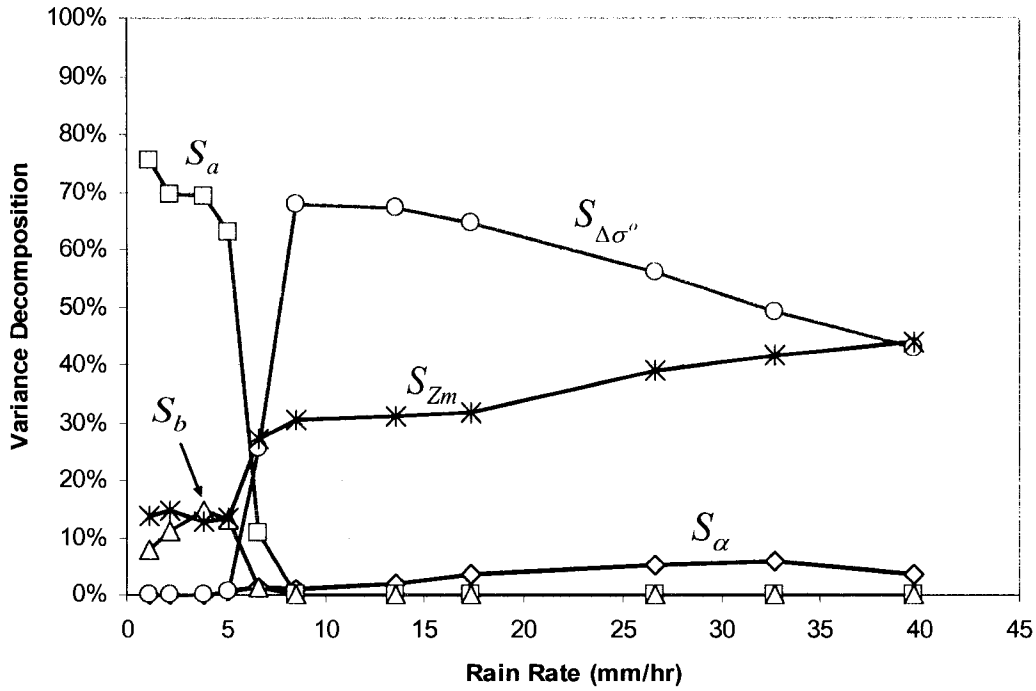

Figure 7.18. Graph showing the first-order variance decomposition of the important factors in the TRMM-like algorithm over OCEAN. The above assumptions are used for the PDFs for the input factors listed in Table 7.2. The factors *a* and *b* have significant impact in the low rainfall region but diminish as the algorithm transitions to higher region where the log polynomials are used to calculate *a* and *b*. At low rain rates, *a* and *b* dominate. At high rain rates, the error in $\Delta\sigma^\circ$ dominates. As the rain rate and attenuation levels increase, attenuation becomes more important and requires more correction, thus α also becomes somewhat more important in the variance of the calculated rain rate.

From the SA results, there is a clear peak in the contribution of α to the total output variance around the 30 mm/hr range after which its contribution to total variance declines. At low rain rates, the error in *a* dominates while the contribution from α and $\Delta\sigma^\circ$ are negligible. The coefficient *b* is the second-most important factor at low rain rates. In low rain-rate region, the TRMM algorithm mainly uses the HB solution which does not use the $\Delta\sigma^\circ$ input values. In the higher rain rate region, the $\Delta\sigma^\circ$ input is used in the retrieval algorithm. A transition between HB and $\Delta\sigma^\circ$ methods occurs in the range between about 5-8 mm/hr. In both the lower and upper regions, the sum of the three first-order sensitivity factors is approximately 100% at each

rain-rate point indicating that the TRMM model of (7.20) is additive meaning there are no higher-order interactions between the input factors. However, in the transition region, the model is not completely additive and higher-order sensitivity interactions occur. Above the transition, the error in $\Delta\sigma^\circ$ dominates the rain rate variance. As expected, the contribution from the error in $\Delta\sigma^\circ$ declines with increasing rain rate because the true-$\Delta\sigma^\circ$ values increase and the error associated with this variable decreases as a percentage of its true value and hence its contribution to output variance decreases. Throughout the entire rain-rate region, the contribution from α is small in comparison to that of the other factors.

From UA, the standard and normalized standard error vs. rain rate for the profiles of Table 7.1 are shown in Figure 7.19.

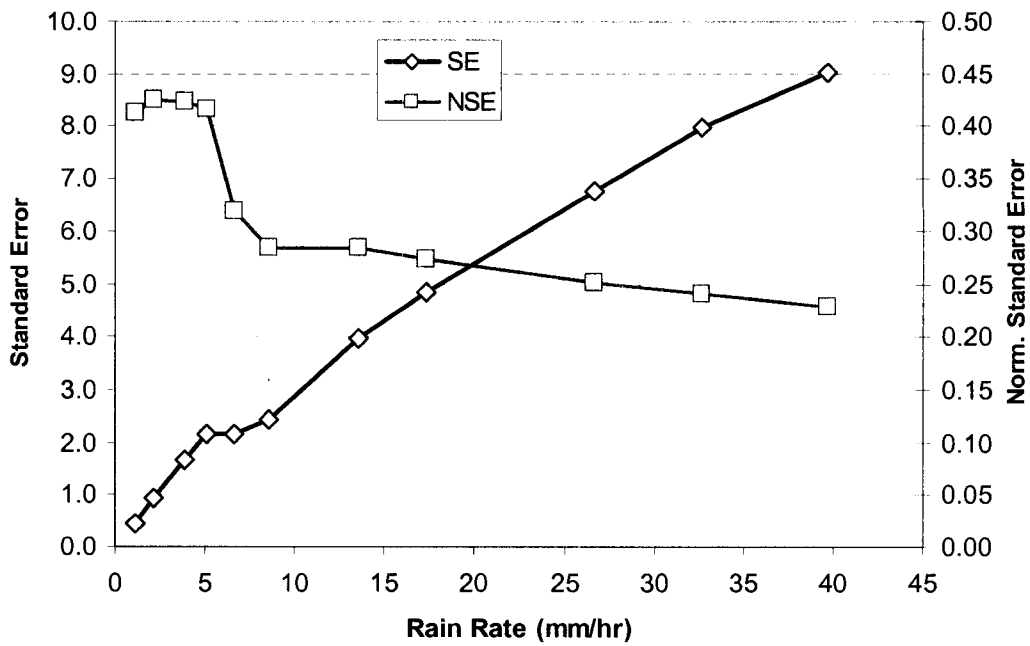

Figure 7.19. Plot showing the standard error and normalized standard error of the simulated rain rate only in the bottom bin. Data from TRMM-like algorithm over Ocean.

As expected, with increasing rain rates, the standard error increases, but the normalized standard error remains below approximately 0.43. Table 7.3 shows a listing of the variance decomposition outputs for the TRMM-like algorithm over ocean. The left column is estimated rain rate in mm/hr based on the N_w and D_o parameters listed in Table 7.1.

Table 7.3. List of the variance decomposition results for the TRMM-like algorithm over ocean. The column on the left is estimated rain rate in mm/hr based on the N_w, D_o pairs listed in Table 7.1

Rain Rate (mm/hr)	S_α	S_a	S_b	$S_{\Delta\sigma^\circ}$	S_{Zm}
1.09	0.0%	75.5%	7.8%	0.0%	13.7%
2.14	0.0%	69.5%	11.2%	0.0%	14.7%
3.87	0.1%	69.3%	14.8%	0.0%	12.6%
5.10	0.7%	62.9%	13.2%	0.7%	13.6%
6.65	1.2%	10.7%	1.2%	25.7%	27.3%
8.56	0.9%	0.0%	0.0%	68.0%	30.5%
13.52	1.9%	0.0%	0.0%	67.1%	31.1%
17.33	3.5%	0.0%	0.0%	64.7%	31.9%
26.64	5.3%	0.0%	0.0%	56.2%	39.1%
32.65	5.9%	0.0%	0.0%	49.3%	41.7%
39.73	3.5%	0.0%	0.0%	43.1%	44.0%

7.4.2 Land

For land, the TL-algorithm input-factor PDFs are shown in Table 7.4. The error associated with $\Delta\sigma^\circ$ over land is assumed to be from a normal distribution, mean equal to the true PIA from simulations, with 3-dB standard deviation.

Table 7.4. List of the input factors and their distributions for the TRMM-like rainfall rate sensitivity analyses over LAND. The nominal values for these factors were obtained from [8], assuming 20° C stratiform rain.

Factor Name	Probability Distribution
α	U{ 2.851e-4 ± 20% }
β	constant = 0.792 30
a	U{0.022 82 ± 0.014 }
b	U{ 0.672 7 ± 0.036}
$\Delta\sigma^\circ$	N{ $\Delta\sigma^\circ_{true}$, 3 dB }
Z_m *(error in each bin)*	N{0, 1 dB}

Pie charts for TL algorithm over LAND showing the first order sensitivities, S_i, and total sensitivity indices, S_{Ti} are shown for D_o = 0.65 through D_o = 1.35 listed in Table 7.1 are shown in the following pages in Figure 7.20 through Figure 7.30. In each figure, a pie chart is shown in parts (a) and (b). Part (a) shows the variance decomposition for the inputs with the percentage contributed by each factor listed by the factor name. Part (b) shows a pie chart for the total sensitivity indices. Each pie wedge is identified by input factor, but since the sum of the total sensitivity indices can be larger than one, the total sensitivity index percentages are not shown. The histogram in part (c) of each figure is a distribution of estimated rainfall rate in the bottom bin of each profile. Part (d) of each figure shows the raw values output from the SA procedure using the method of Sobol'.

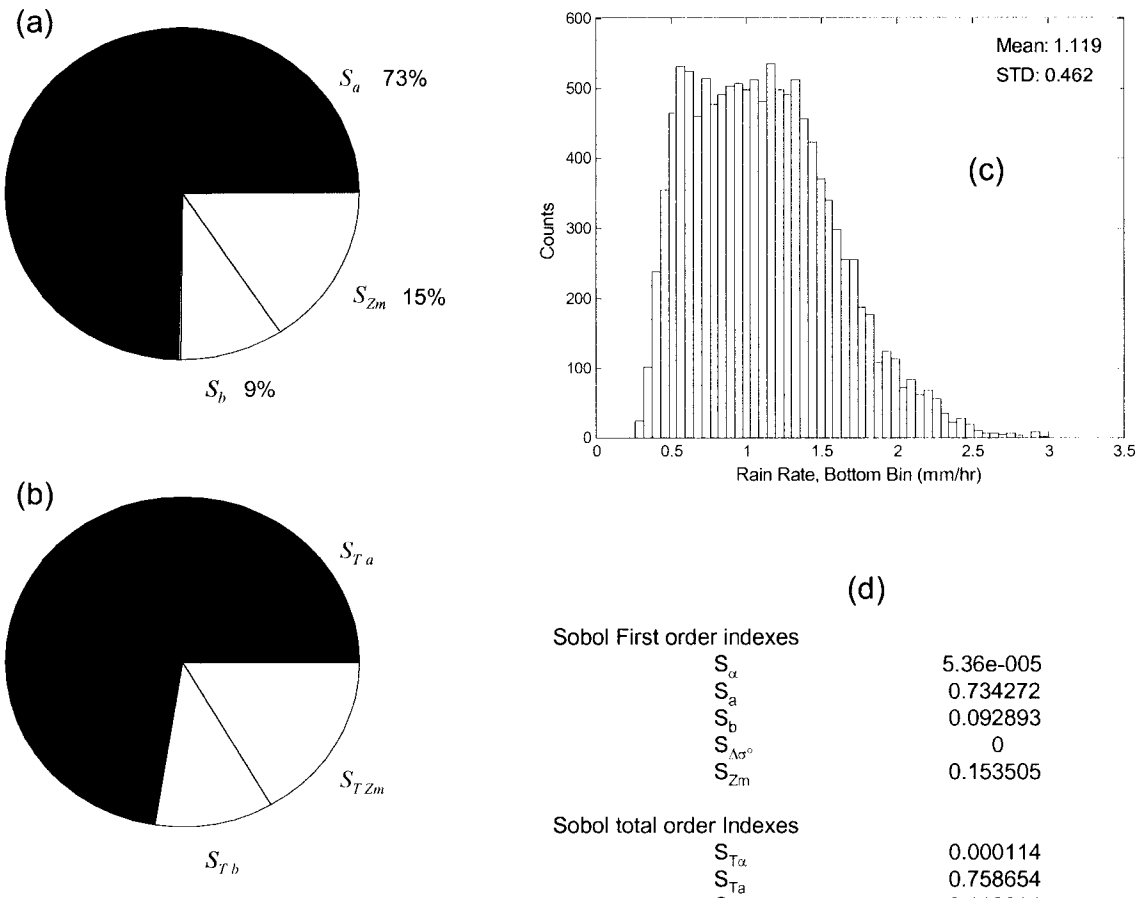

Figure 7.20. $N_w = 33{,}800$ $D_o = 0.65$. TRMM-like over land. The pie chart in part (a) shows the variance decomposition of the first-order sensitivity indices. Part (b) shows the total sensitivity indices. A histogram of the bottom-bin estimated rainfall is shown in part (c). Part (d) is a listing of the raw outputs from the method of Sobol' sensitivity analysis method. In this simulation, there is little higher-order interaction and the model is additive.

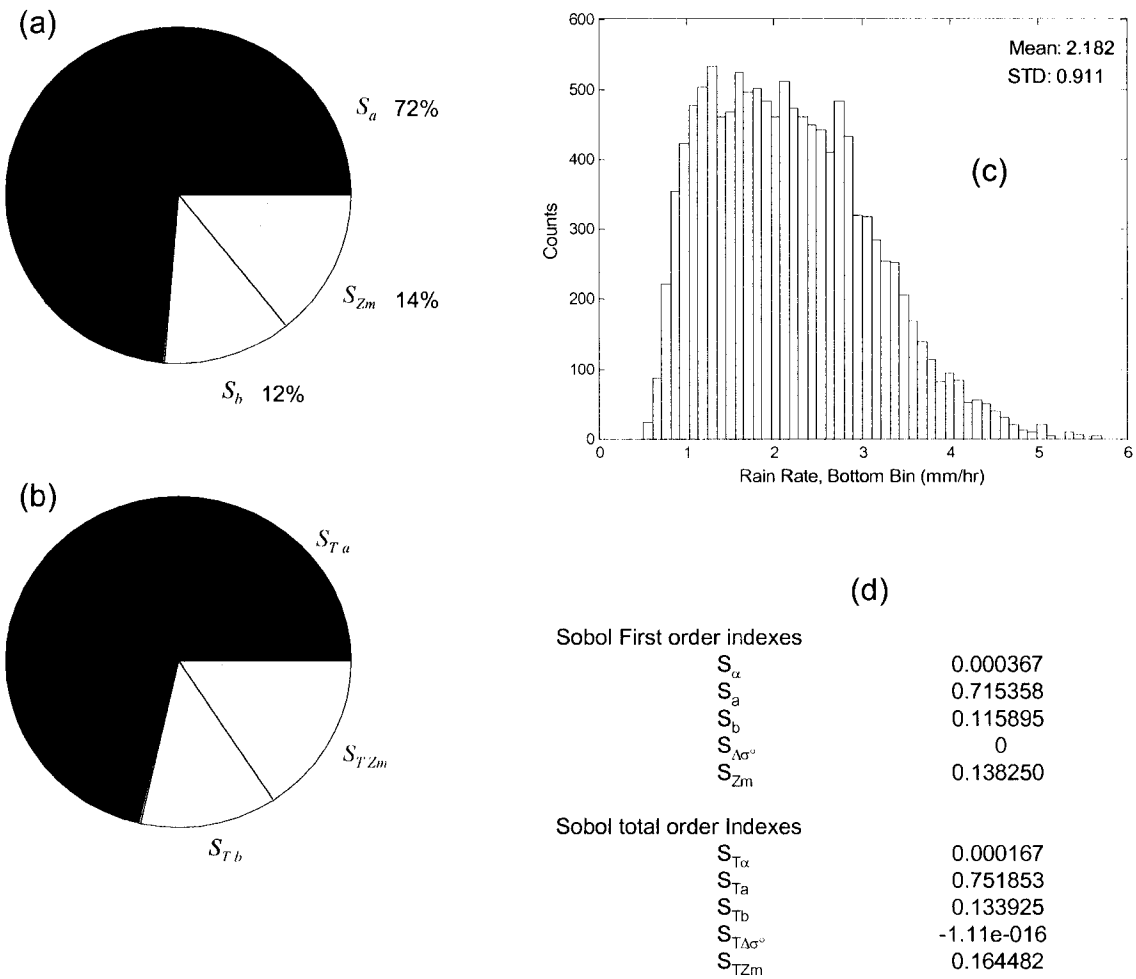

Figure 7.21. $N_w = 33{,}900$ $D_o = 0.75$. TRMM-like over land. The pie chart in part (a) shows the variance decomposition of the first-order sensitivity indices. Part (b) shows the total sensitivity indices. A histogram of the bottom-bin estimated rainfall is shown in part (c). Part (d) is a listing of the raw outputs from the method of Sobol' sensitivity analysis method. In this simulation, there is little higher-order interaction and the model is additive.

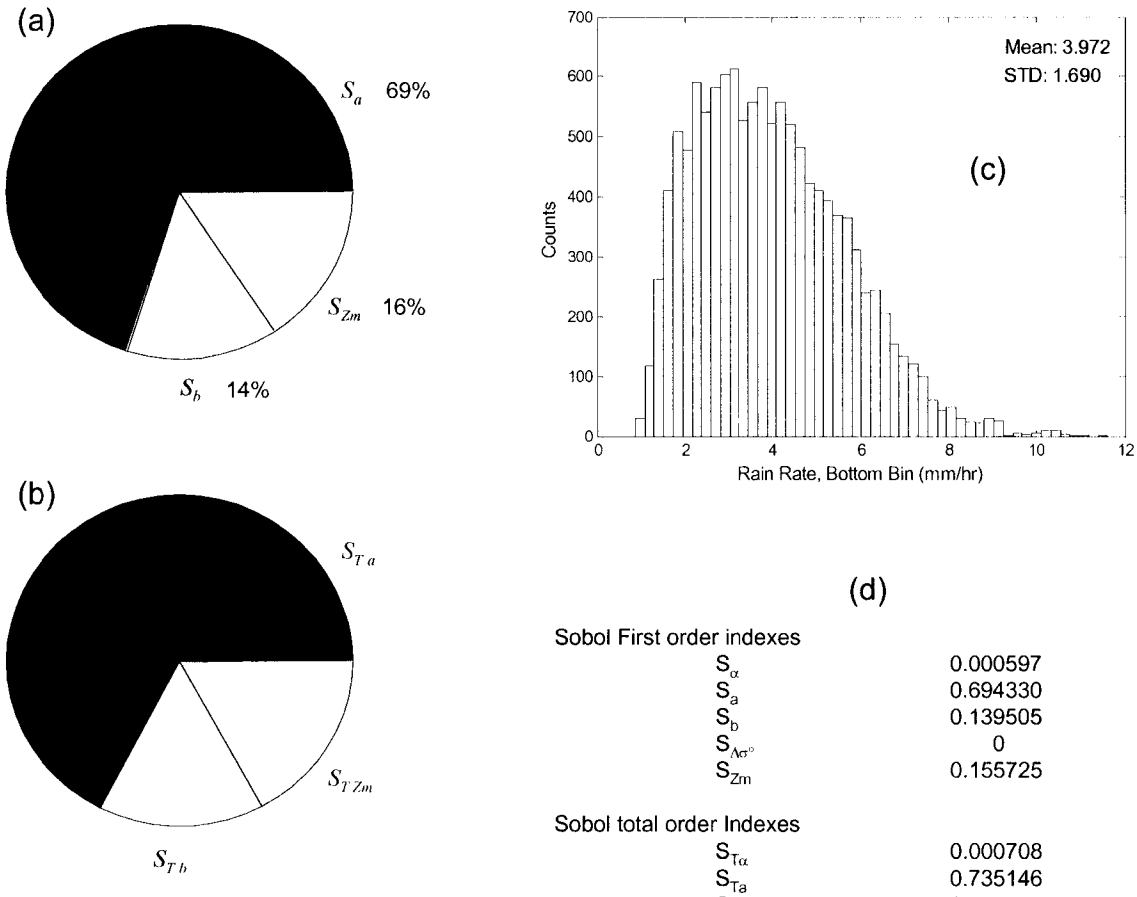

Figure 7.22. N_w = 34,300 D_o = 0.85. TRMM-like over land. The pie chart in part (a) shows the variance decomposition of the first-order sensitivity indices. Part (b) shows the total sensitivity indices. A histogram of the bottom-bin estimated rainfall is shown in part (c). Part (d) is a listing of the raw outputs from the method of Sobol' sensitivity analysis method. In this simulation, there is little higher-order interaction and the model is additive.

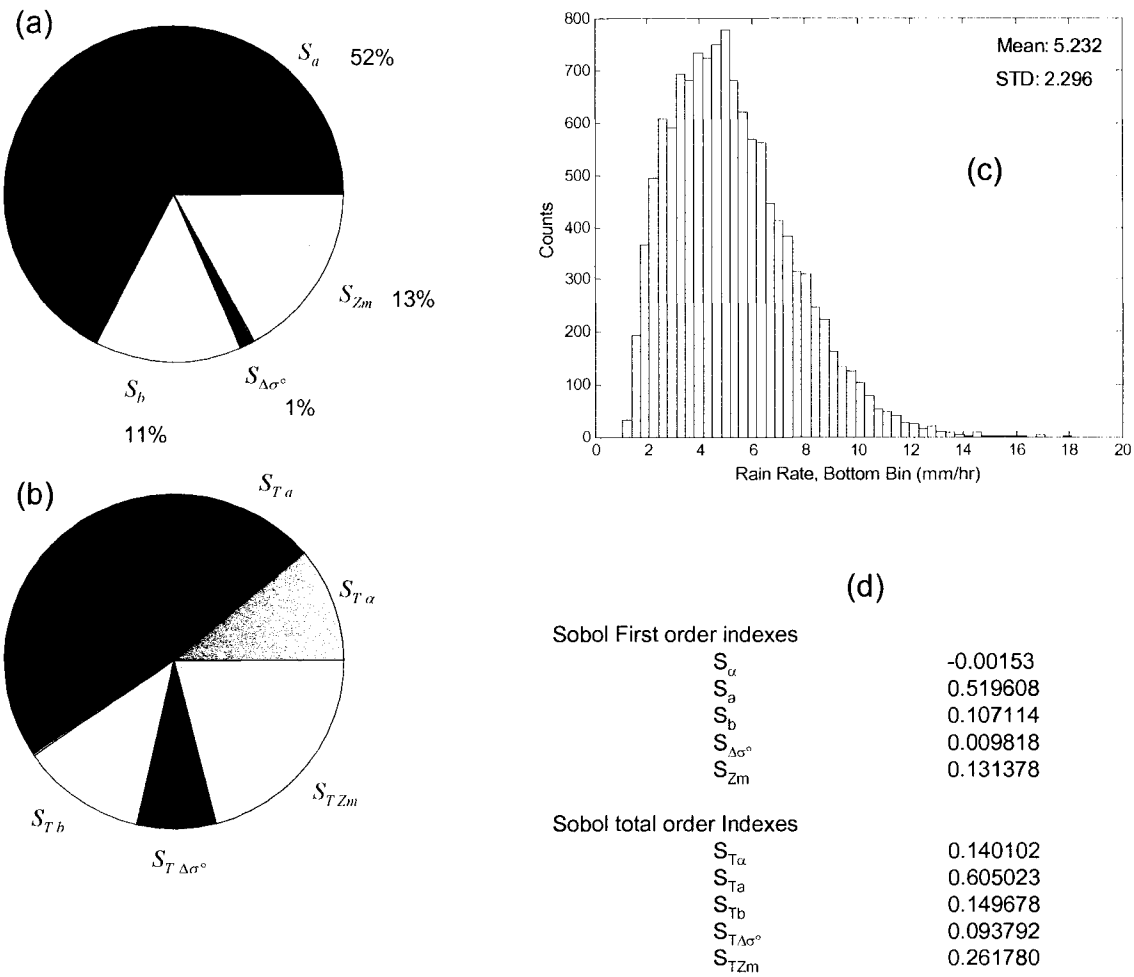

Figure 7.23. $N_w = 34{,}591$ $D_o = 0.90$. TRMM-like over land. The pie chart in part (a) shows the variance decomposition of the first-order sensitivity indices. Part (b) shows the total sensitivity indices. A histogram of the bottom-bin estimated rainfall is shown in part (c). Part (d) is a listing of the raw outputs from the method of Sobol' sensitivity analysis method. In this simulation, there is significant higher-order interaction and the model is not additive.

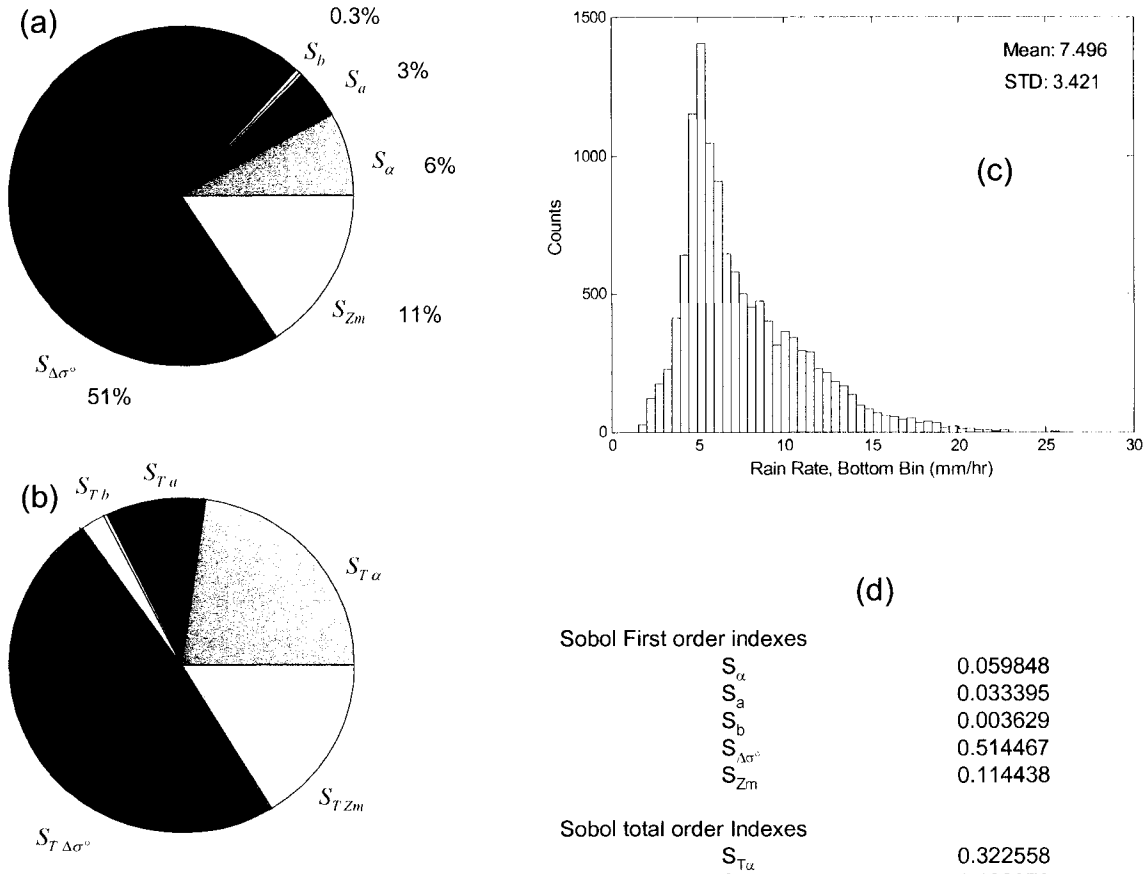

Figure 7.24. $N_w = 35{,}000$ $D_o = 0.95$. TRMM-like over land. The pie chart in part (a) shows the variance decomposition of the first-order sensitivity indices. Part (b) shows the total sensitivity indices. A histogram of the bottom-bin estimated rainfall is shown in part (c). Part (d) is a listing of the raw outputs from the method of Sobol' sensitivity analysis method. In this simulation, there is significant higher-order interaction and the model is not additive.

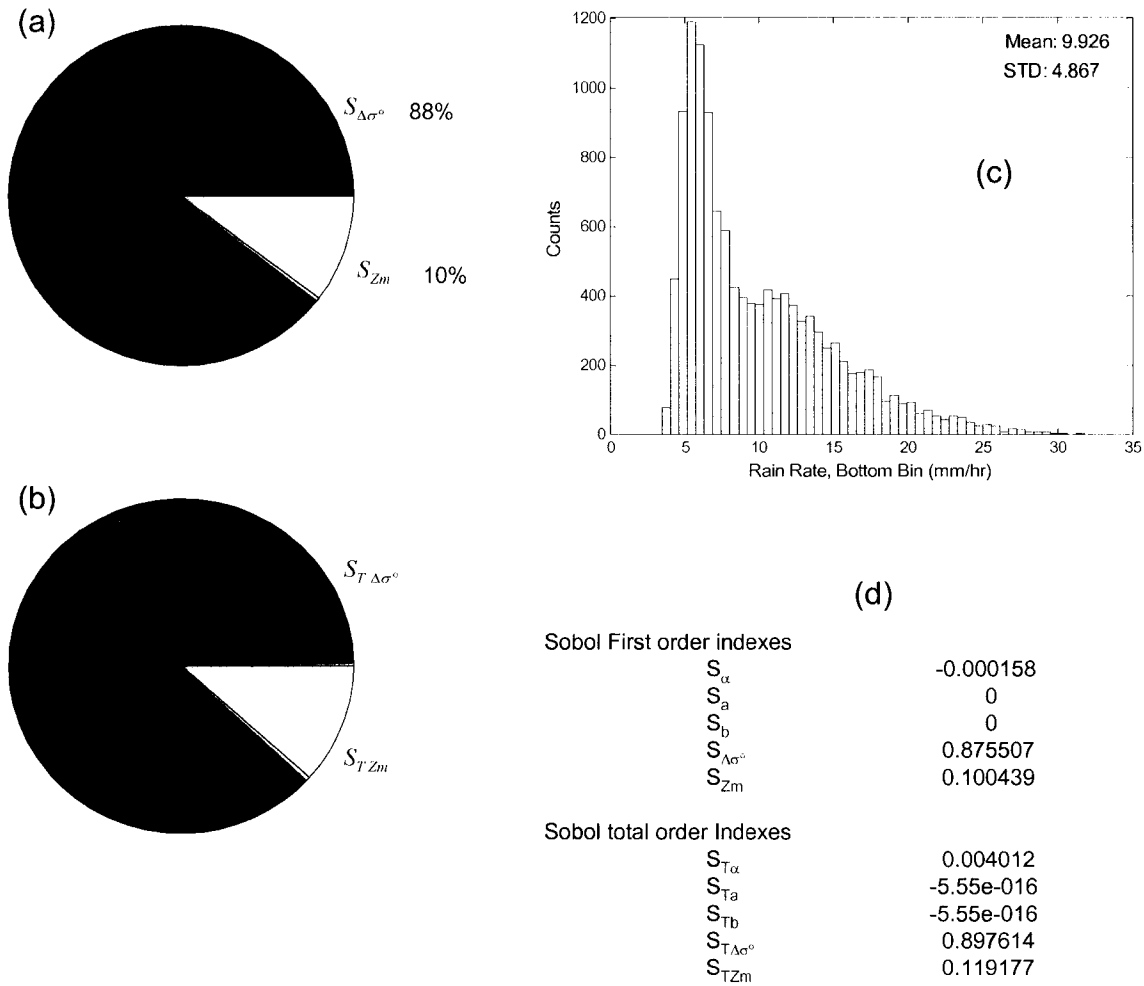

Sobol First order indexes

S_α	-0.000158
S_a	0
S_b	0
$S_{\Delta\sigma^o}$	0.875507
S_{Zm}	0.100439

Sobol total order Indexes

$S_{T\alpha}$	0.004012
S_{Ta}	-5.55e-016
S_{Tb}	-5.55e-016
$S_{T\Delta\sigma^o}$	0.897614
S_{TZm}	0.119177

Figure 7.25. $N_w = 35{,}500$ $D_o = 1.00$. TRMM-like over land. The pie chart in part (a) shows the variance decomposition of the first-order sensitivity indices. Part (b) shows the total sensitivity indices. A histogram of the bottom-bin estimated rainfall is shown in part (c). Part (d) is a listing of the raw outputs from the method of Sobol' sensitivity analysis method. In this simulation, there is little higher-order interaction and the model is additive.

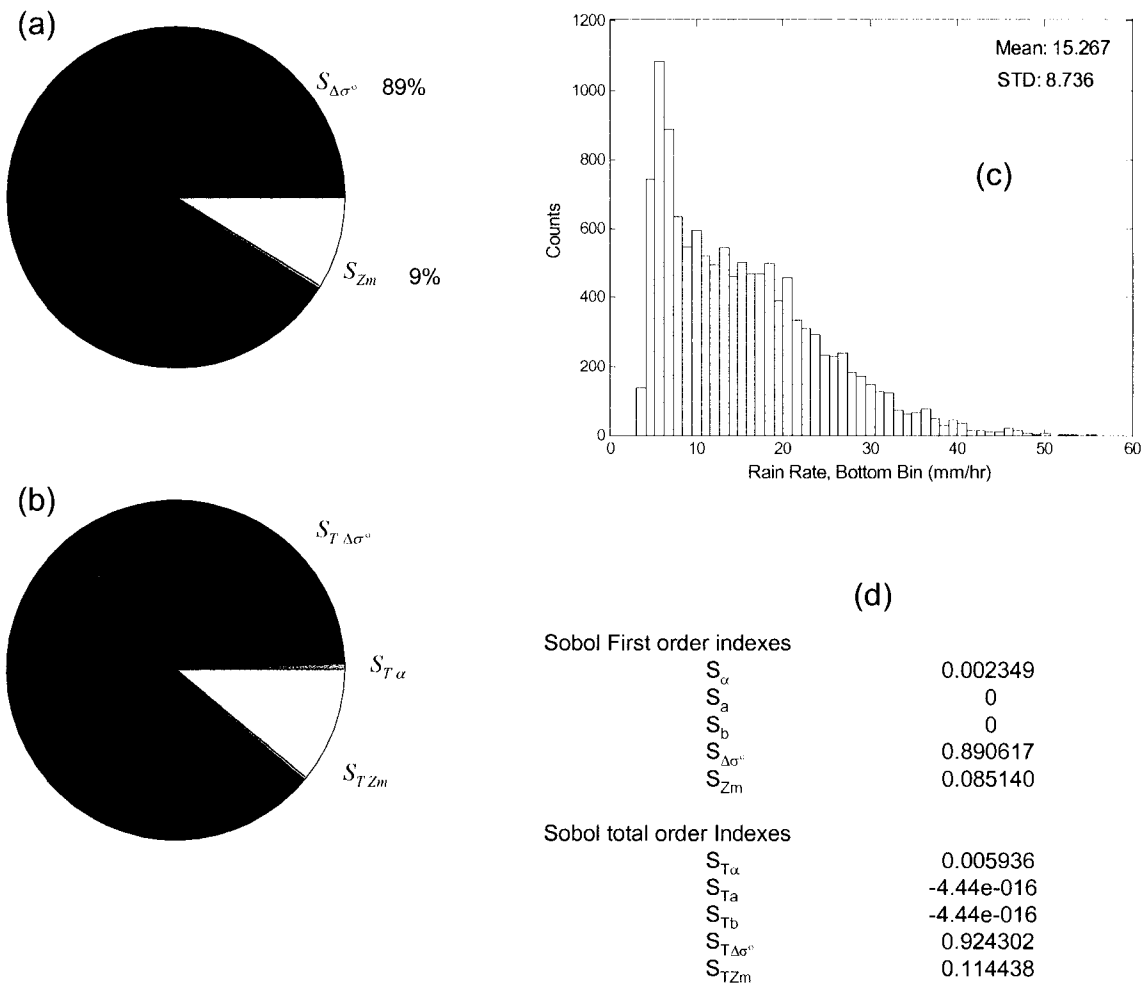

Figure 7.26. $N_w = 36{,}700$ $D_o = 1.10$. TRMM-like over land. The pie chart in part (a) shows the variance decomposition of the first-order sensitivity indices. Part (b) shows the total sensitivity indices. A histogram of the bottom-bin estimated rainfall is shown in part (c). Part (d) is a listing of the raw outputs from the method of Sobol' sensitivity analysis method. In this simulation, there is little higher-order interaction and the model is additive.

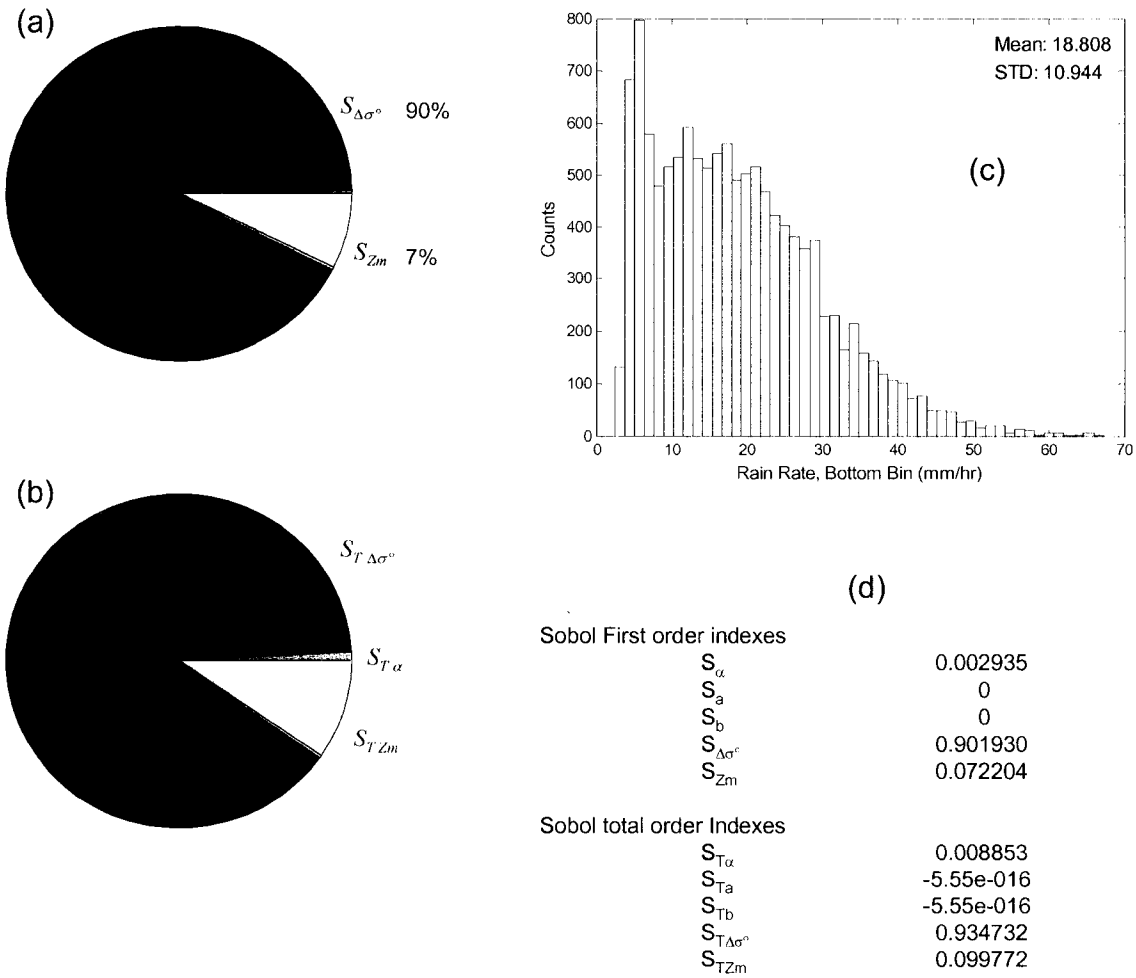

(d)

Sobol First order indexes	
S_α	0.002935
S_a	0
S_b	0
$S_{\Delta\sigma^o}$	0.901930
S_{Zm}	0.072204
Sobol total order Indexes	
$S_{T\alpha}$	0.008853
S_{Ta}	-5.55e-016
S_{Tb}	-5.55e-016
$S_{T\Delta\sigma^o}$	0.934732
S_{TZm}	0.099772

Figure 7.27. $N_w = 37{,}400$ $D_o = 1.15$. TRMM-like over land. The pie chart in part (a) shows the variance decomposition of the first-order sensitivity indices. Part (b) shows the total sensitivity indices. A histogram of the bottom-bin estimated rainfall is shown in part (c). Part (d) is a listing of the raw outputs from the method of Sobol' sensitivity analysis method. In this simulation, there is little higher-order interaction and the model is additive.

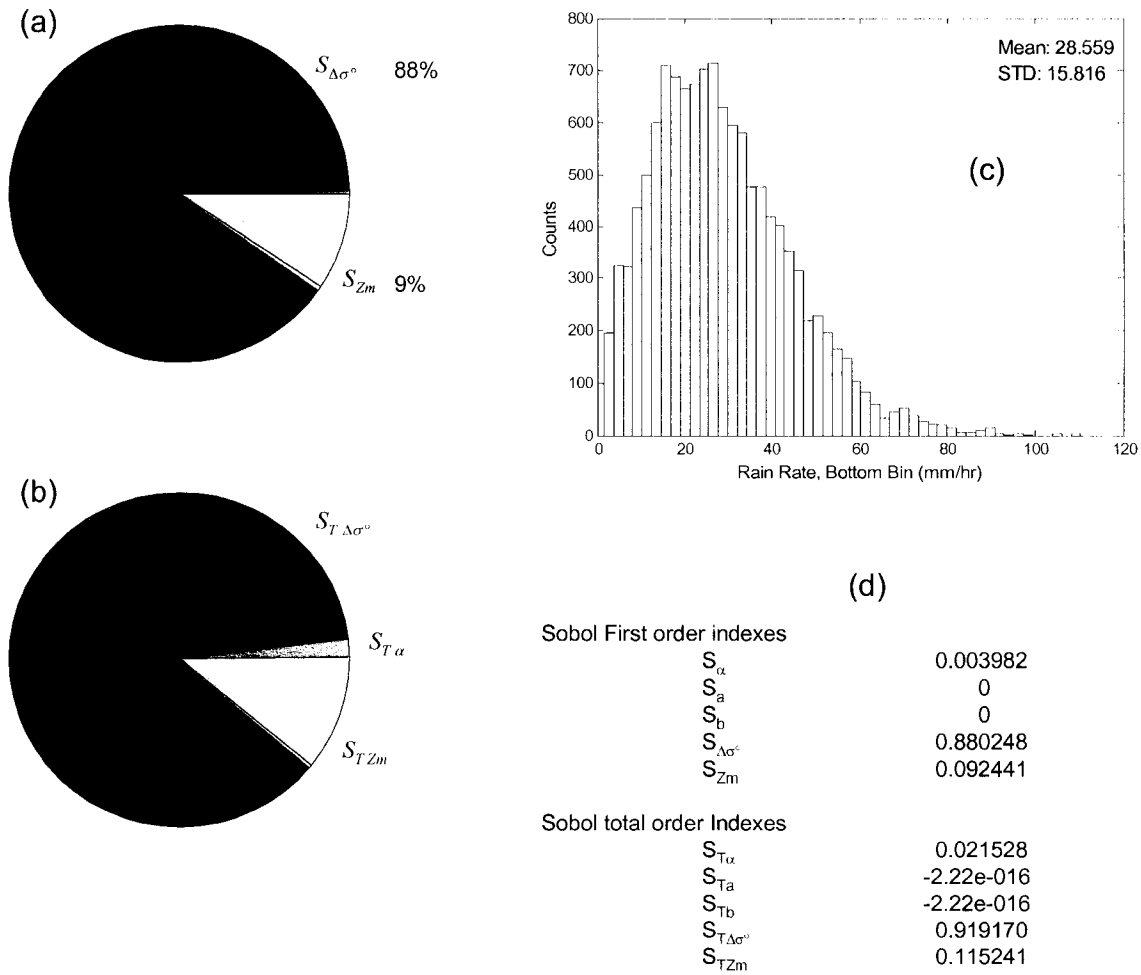

(d)

Sobol First order indexes	
S_α	0.003982
S_a	0
S_b	0
$S_{\Delta\sigma^o}$	0.880248
S_{Zm}	0.092441
Sobol total order Indexes	
$S_{T\alpha}$	0.021528
S_{Ta}	-2.22e-016
S_{Tb}	-2.22e-016
$S_{T\Delta\sigma^o}$	0.919170
S_{TZm}	0.115241

Figure 7.28. $N_w = 38{,}900$ $D_o = 1.25$. TRMM-like over land. The pie chart in part (a) shows the variance decomposition of the first-order sensitivity indices. Part (b) shows the total sensitivity indices. A histogram of the bottom-bin estimated rainfall is shown in part (c). Part (d) is a listing of the raw outputs from the method of Sobol' sensitivity analysis method. In this simulation, there is little higher-order interaction and the model is additive.

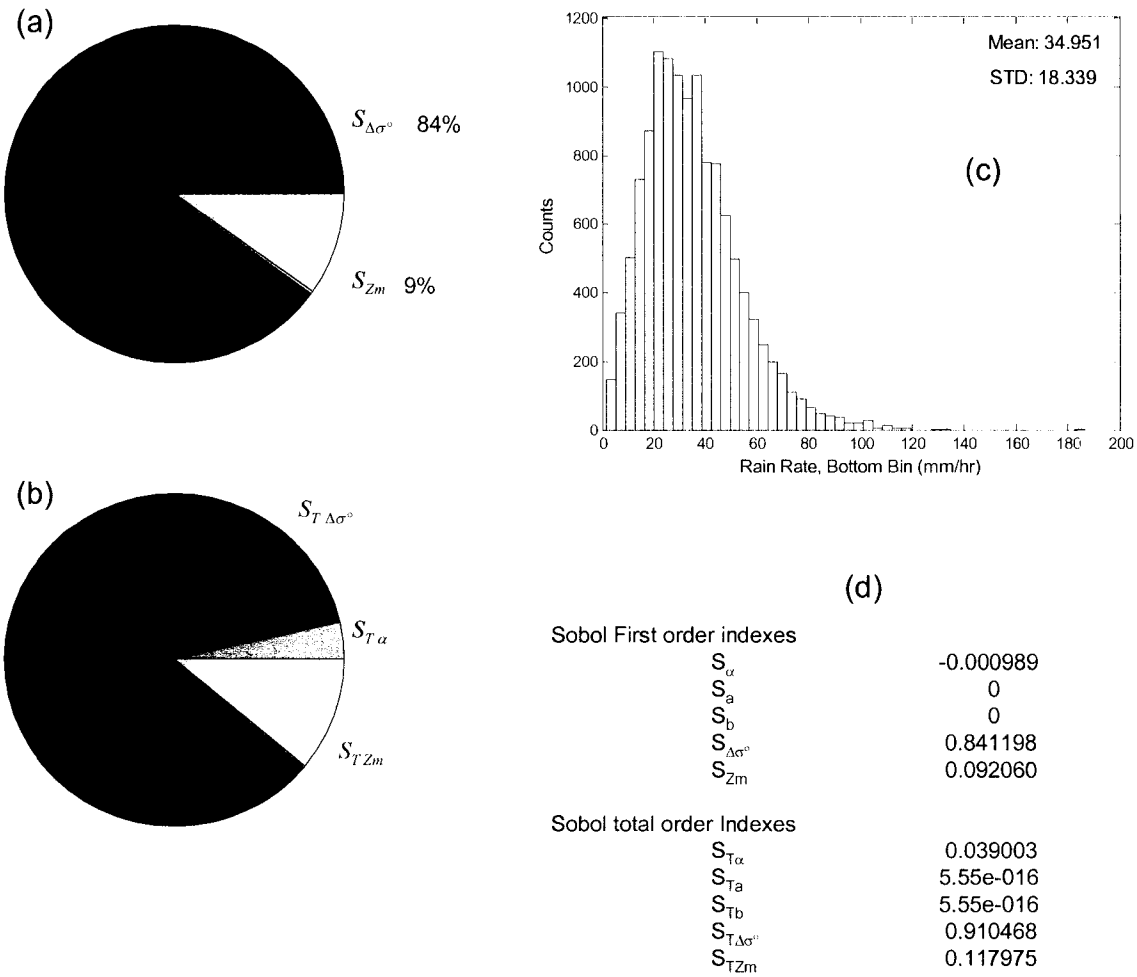

Figure 7.29. $N_w = 39{,}700$ $D_o = 1.30$. TRMM-like over land. The pie chart in part (a) shows the variance decomposition of the first-order sensitivity indices. Part (b) shows the total sensitivity indices. A histogram of the bottom-bin estimated rainfall is shown in part (c). Part (d) is a listing of the raw outputs from the method of Sobol' sensitivity analysis method. In this simulation, there is little higher-order interaction and the model is additive.

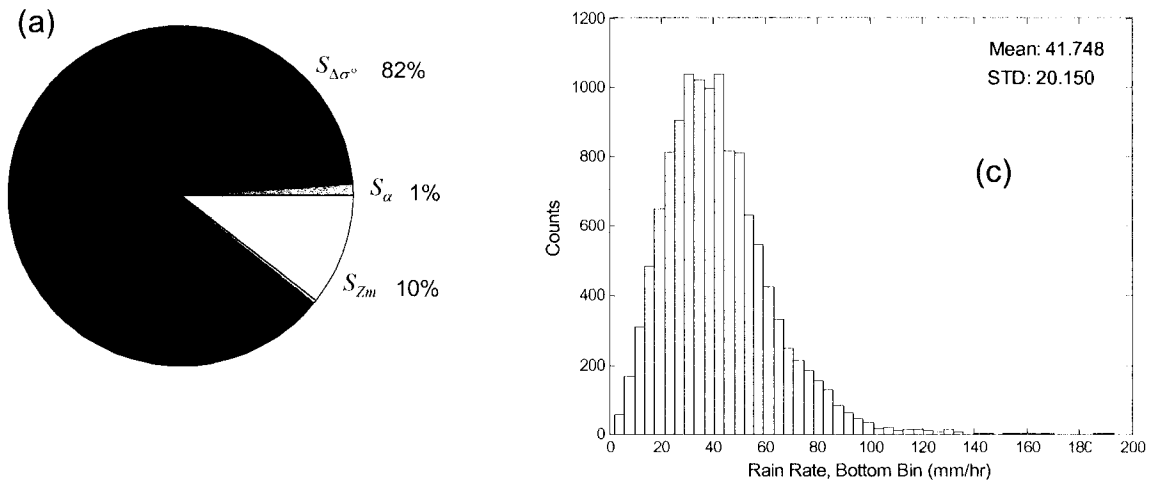

(d)

Sobol First order indexes	
S_α	0.010432
S_a	0
S_b	0
$S_{\Delta\sigma^0}$	0.816718
S_{Zm}	0.097970
Sobol total order Indexes	
$S_{T\alpha}$	0.067722
S_{Ta}	8.33e-016
S_{Tb}	8.33e-016
$S_{T\Delta\sigma^0}$	0.907246
S_{TZm}	0.120368

Figure 7.30. $N_w = 40{,}500$ $D_o = 1.35$. TRMM-like over land. The pie chart in part (a) shows the variance decomposition of the first-order sensitivity indices. Part (b) shows the total sensitivity indices. A histogram of the bottom-bin estimated rainfall is shown in part (c). Part (d) is a listing of the raw outputs from the method of Sobol' sensitivity analysis method. In this simulation, there is some higher-order interaction with α and the model is not additive.

The SA results for the N_w, D_o pairs listed in Table 7.1 are plotted using the input factor distributions corresponding to land. These are shown in Figure 7.31.

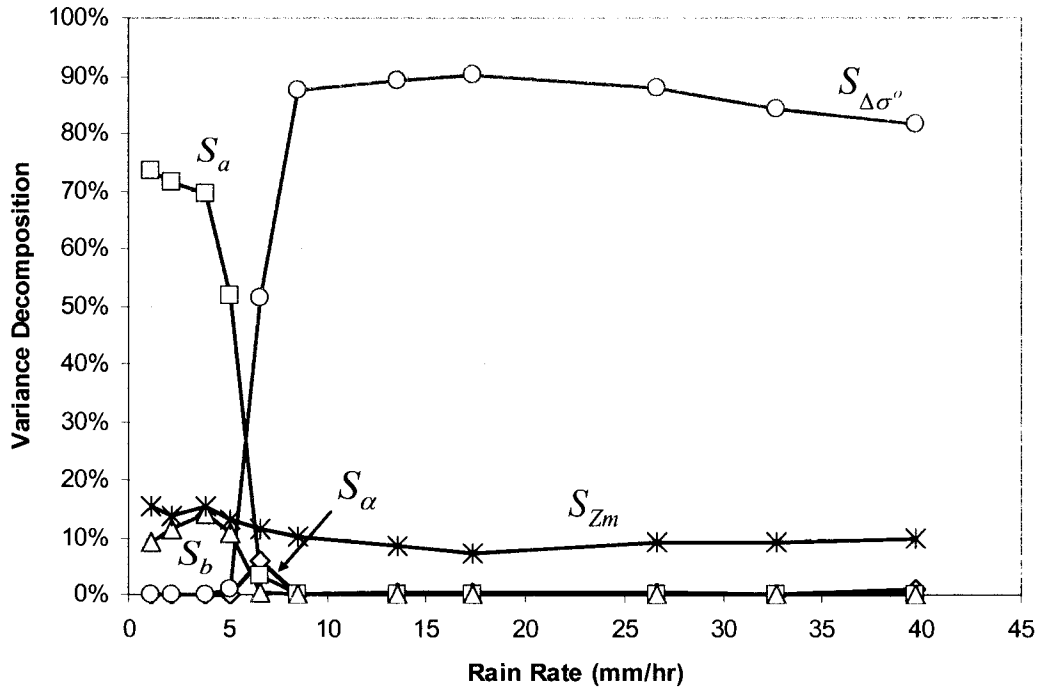

Figure 7.31. Graph showing the first-order variance decomposition of the important factors in the TRMM-like algorithm over LAND. The PDF assumptions used for the input factors are listed in Table 7.4. The factors *a* and *b* have significant impact in the low rainfall region. Their influence diminishes as the algorithm transitions to the high rainfall rate calculation. At low rain rates, a and b dominate and α has no effect. At high rain rates, the error in $\Delta\sigma^\circ$ dominates followed by the error in Z_m. As the rain rate and attenuation levels increase, attenuation becomes more important and requires more correction.

In this scenario, the error contribution from $\Delta\sigma^\circ$ has been increased over that of the error used for the ocean analysis. From the SA results, there is little contribution by α to the total output variance throughout the entire simulated rainfall range. At low rain rates, the error in *a* followed by the error in *b*, while the contribution from α and $\Delta\sigma^\circ$ are negligible. In the higher rain-rate region, the $\Delta\sigma^\circ$ input is weighted more heavily than HB in the retrieval algorithm. A transition between HB and $\Delta\sigma^\circ$ methods occurs in the range around 5-8 mm/hr. In both the lower and upper regions, the sum of the three first-order sensitivity factors is approximately 100% at each rain-rate simulation indicating that the TL model of (7.20) is additive. However, in the transition region, the model is not additive and higher-order sensitivity interactions occur.

Above the transition, the greater error in $\Delta\sigma^\circ$ dominates the rain-rate variance. As expected, the contribution from the error in $\Delta\sigma^\circ$ declines with increasing rain rate because the true-$\Delta\sigma^\circ$ values increase and the error associated with this variable decreases as a percentage of its true value and hence its contribution to output variance decreases. The error in measured reflectivity contributes little to total output variance throughout the range.

From UA, the standard and normalized standard error vs. rain rate for the profiles of Table 7.1 for the TL algorithm over LAND are shown in Figure 7.32.

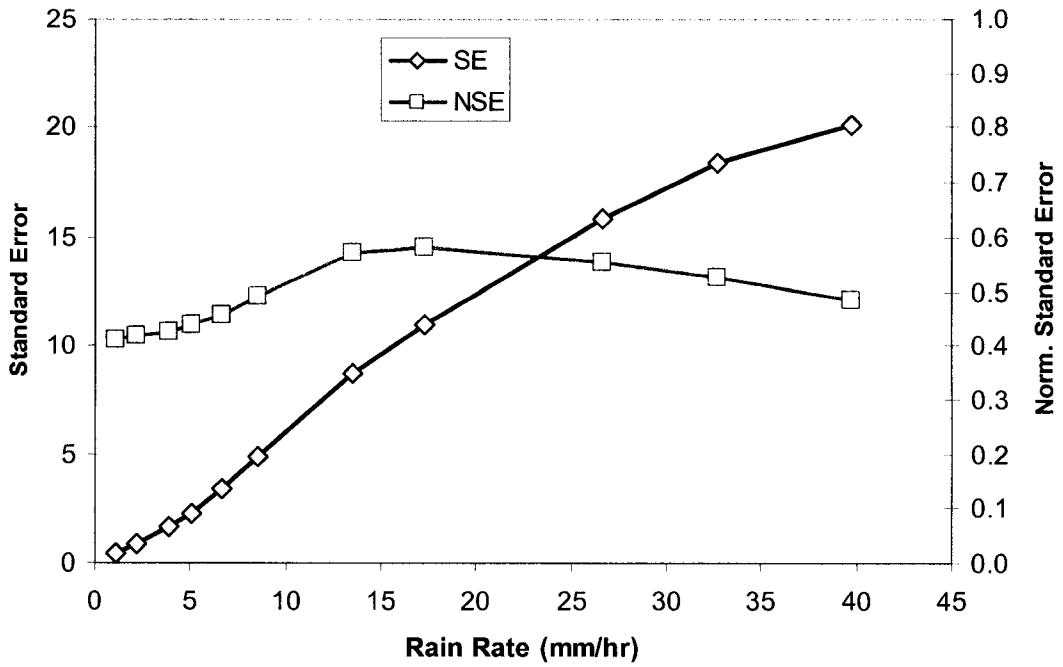

Figure 7.32. Graph showing the standard error and normalized standard error of the simulated rain rate only in the bottom bin. Data for TRMM-like over LAND.

Because of the greater error in $\Delta\sigma^\circ$, there is obviously greater standard error in the rain-rate calculations. The NSE values have a maximum at about 0.58 and then decline at higher rain rates.

Table 7.5 shows a listing of the variance decomposition results for each of the estimated rainfall rates based on the N_w, D_o values in Table 7.1.

Table 7.5. List of the variance decomposition results for the TRMM-like algorithm over land. The column on the left is estimated rain rate in mm/hr based on the N_w, D_o pairs listed in Table 7.1

Rain Rate (mm/hr)	S_α	S_a	S_b	$S_{\Delta\sigma^\circ}$	S_{Zm}
1.09	0.0%	0.0%	9.3%	0.0%	15.4%
2.14	0.0%	0.0%	11.6%	0.0%	13.8%
3.87	0.1%	0.1%	14.0%	0.0%	15.6%
5.10	0.0%	0.0%	10.7%	1.0%	13.1%
6.65	6.0%	6.0%	0.4%	51.4%	11.4%
8.56	0.0%	0.0%	0.0%	87.6%	10.0%
13.52	0.2%	0.2%	0.0%	89.1%	8.5%
17.33	0.3%	0.3%	0.0%	90.2%	7.2%
26.64	0.4%	0.4%	0.0%	88.0%	9.2%
32.65	0.0%	0.0%	0.0%	84.1%	9.2%
39.73	1.0%	1.0%	0.0%	81.7%	9.8%

7.5 SUMMARY

The sensitivity analyses performed on the TRMM-like algorithm over both ocean and land, with assumed factor distributions (Table 7.2, Table 7.4), show differences in factor variance decomposition depending on the rainfall region, low or high.

The majority of the variance in the low rain-rate region is due to the error in the *a* coefficients. At low rain rates, the contribution from α is negligible or small corresponding to small amounts of attenuation, and hence, requiring small amounts of attenuation correction. Also in this region, the model primarily uses the HB solution ignoring $\Delta\sigma^\circ$ in its calculations, hence the contribution from $\Delta\sigma^\circ$ in total output variance is negligible. A set of uniform PDFs for the *a* and *b* coefficients in the low rainfall region was estimated from disdrometer data. These PDFs were used in the SA/UA in this region.

In the lower rain-rate region, where the TRMM algorithm uses only the HB solution, the values of $\Delta\sigma^\circ$ are limited to be greater than 0.5 dB. At low rain rates, when the true value of

$\Delta\sigma^\circ$ is small, and when using its normal distribution with a 1 or 3 dB standard deviation, in the sampling procedure, it is likely that negative $\Delta\sigma^\circ$ values will be created. In reality, $\Delta\sigma^\circ$ is never negative, and as a result, when $\Delta\sigma^\circ$ is less than 0.5 dB, it is artificially set to 0.5 dB. Also, in the lower region, when ζ is small, less than 0.2 (corresponding to small PIA), it is assumed that it is a better measure of PIA than $\Delta\sigma^\circ$, and as such, $\Delta\sigma^\circ$ is set to 0.5 dB thereby decreasing its influence and heavily weighting the HB solution. The TRMM model is additive in the low rain-rate region as the first-order sensitivity indices, S_i, sum to approximately one in each N_w, D_o simulation. (Refer to Figure 7.18 and Figure 7.31)

In the transition region, around 5-8 mm/hr, the models for both ocean and land are not additive and display higher-order sensitivity terms. Above the transition region, for higher rain-rates, the TRMM algorithm increasingly weights the contribution from $\Delta\sigma^\circ$ and uses it to calculate rain rate. Hence the error from $\Delta\sigma^\circ$ is very important in this region. In fact, it becomes the dominant error source, far greater than that from Z_m. Note that in both cases, land and ocean, that in the higher rain-rate region, as the rate increases, the error contribution from $\Delta\sigma^\circ$ decreases as its fixed relative error (1 or 3 dB) decreases as a percentage of its true value.

In the high rainfall region (above about 5 mm/hr), the a and b terms in the $R = a\, Z_e^{\,b}$ relation, have no effect on output variance in the algorithm's operation. The reason for this is that the new a and b values in (7.19) are calculated from the quadratic equation using ε instead of the input a and b values listed in Table 7.2 and Table 7.4. Variance in $\Delta\sigma^\circ$ is implicitly applied to the calculation of the new final ε which is used to calculate the new a' and b' coefficients after the α-correction is done. More accurate PDFs for the log polynomials are not available, consequently, the errors in the log fits were implicitly incorporated using $\Delta\sigma^\circ$ and Z_m. The TRMM model is additive in the high rain-rate region.

The S_i indices plotted in Figure 7.18 and Figure 7.31 indicate that the most improvement or reduction in total rainfall-rate variance in the lower region could be made by decreasing the

variance or error in the a coefficient. The second most important factor is the b coefficient. From a systems engineering perspective, two questions need to be asked: first) are the standard errors good enough; and second) if not, what would it take to reduce the errors in a and b to reduce the overall variance and increase the measurement accuracy? This improvement in a and b could be done by calculating more and better Z-R regressions from more disdrometer data allowing more accurate and detailed histograms to be analyzed.

In the higher rainfall-rate region, the output variance can be decreased by reducing the error in $\Delta\sigma^{\circ}$. This could be effected by improved sampling, better radar calibration, or perhaps some other technique to independently measure total path integrated attenuation.

The SA and UA performed on the TRMM algorithm have at least one shortcoming: the assumption is made that both the k-Z and R-Z relationships described by (7.1) and (7.2) are accurate, or at least more accurate than the uncertainty in the output variable. The TRMM model used in these analyses is based on those relationships, the parameters used therein are based on data taken from several regions around the globe from which fitted values for α, β, a, and b are derived. Of course, both the a and b coefficients have no direct impact on the variance in the high rainfall region as the algorithm uses the log polynomials to calculate new R-Z coefficients. However, the log polynomials are derived from measurements and curve fitting. These coefficients, do however have a significant impact in the low rainfall-rate region as the algorithm does not implement α-correction in this region and the a and b coefficients are used directly in the estimation of rainfall rate. It is also clear that many other N_w, D_o and rain-rate combinations could be used in the simulations and analyses. The values listed in Table 7.1 were selected to be representative of the expected rainfall range and DSD parameter types.

This work focuses on how to apportion the variance in the output of a model to the uncertainty in the input factors which is referred to as input uncertainty. The assumption is

made that the model is reasonably accurate. SA and UA have no means to diagnose the contribution to error of the model structure itself, only through the variance in the input factors.

CHAPTER 8

SYSTEMS ENGINEERING ANALYSIS: GPM PROFILE-OPTIMIZATION METHOD

8.1 INTRODUCTION

In chapters three through five, three retrieval methods were described which are applicable for the dual-frequency capabilities of GPM. The first, single-loop method is applicable below rain rates of about 10-15 mm/hr as its operation is limited by incorrect convergence above that level (it also depends on rain-region height). The second, dual-loop method, is intended to be used for higher rain rates where the single-loop method fails. The third, profile-optimization method, is also intended for operation in the regime where the single-loop method fails, and it can be readily used over the entire rain-rate spectrum from low to high rates. In each of the dual-frequency retrieval methods, the enhanced attenuation of the Ka-band signal will limit the maximum rain-rate retrieval to the 20-30 mm/hr rate depending on the height of the rain region and the resultant total path attenuation. In order to better compare the total range of rain rate with that of the TRMM-like (TL) algorithm discussed in Chapter 7, this chapter describes the systems engineering analysis (uncertainty and sensitivity analyses) of the GPM profile-optimization method described in Chapter 5. The dual-loop method could have been SA/UA analyzed, but as it builds on the principles of the single-loop, it was viewed as more constructive to analyze the GPM profile-optimization method.

In section 8.2, principles of SA/UA from Chapter 6 are applied to the GPM profile-optimization method to derive a model suitable for sensitivity and uncertainty analysis. The input factors are described along with their probability density functions (PDFs). A description

of the D_o, N_w profiles used to perform the SA/UA is given. Section 8.3 shows the results of the sensitivity and uncertainty analyses using the Method of Sobol'. In section 8.4, a comparison of the profile-optimization results is made with preliminary SA results obtained from the single-loop retrieval method of Chapter 3. Section 8.5 summarizes the results.

8.2 UA AND SA APPLIED TO GPM

This section describes how uncertainty and sensitivity analyses are applied to the GPM profile-optimization algorithm with the objective of determining the importance of each of the input factors in the variance of the rainfall-rate estimation. It also lists the assumptions used for the input factors as well as the sample profiles used in the simulations.

8.2.1 Model

Using equations (5.1) through (5.13), a model for the optimization algorithm can be constructed according to the sensitivity analysis guidelines of Chapter 6 of the form,

$$R(r) = f(Z_{m1}, Z_{m2}) \tag{8.1}$$

where the rain rate (mm/hr) at altitude or range r, $R(r)$, is a function of the input factors. Using this model, for factor inputs consisting of Z_{m1} and Z_{m2}, the estimated rain-rate profile can be calculated at each bin of the input reflectivity profiles. Although the input profiles are many bins high (12 in this case, with bin spacing of 0.25 km, representing a vertical rain column 3-km in height), the sensitivity analysis is performed on the calculated rain rate in the bottom bin nearest the ground as it is deemed most important. The higher, remaining bins are used by the profile-optimization method to calculate the entire profile, but only the rain rate from the bottom bin is used to perform SA and UA.

8.2.2 Input Factors

To perform SA and UA, points are sampled (using LPτ sampling) from the distributions of each of the input factors to form k, N x 1vectors, and the Method of Sobol' is used, drawing one

set of points for each model evaluation comprised of one sample from each input factor where k is the number of factors, and N is the number of samples.

As indicated in (8.1), only two factors ($k = 2$) are used to perform the SA/UA on the GPM profile-optimization method. Both input factors are vectors (profiles of reflectivity versus altitude) and have associated error probability distribution functions which are used to incorporate simulated measurement error into each bin of each reflectivity profile. The associated random measurement error of each Z_m bin can be up to 0.5-dB standard deviation from a zero mean, normal distribution. In the simulations, this error is added in each bin of each profile. Similar to the process and method described in section 7.3.2, a trigger variable is used for both Z_{m1} and Z_{m2} to map the error-laden vectors to the SA/UA process.

The PDFs for Z_{m1} and Z_{m2} are shown in Table 8.1. Note that for each bin, in each reflectivity profile, random error is added by drawing samples from the specified PDF and algebraically adding the random error sample to the baseline reflectivity profile.

Table 8.1. List of the input factors and their distributions for the GPM profile-optimization rainfall-rate sensitivity/uncertainty analyses. Both input reflectivity factors have identical error distributions. The trigger variables are discrete uniform-random variables.

Factor Name	Probability Distribution
Z_{m1}	N{0, 0.5 dB}
Trigger Z_{m1}	U{1, 1000}
Z_{m2}	N{0, 0.5 dB}
Trigger Z_{m2}	U{1, 1000}

The two trigger variables are shown in the table, and are discrete uniform random variables ranging from 1 to 1000. The uniform distribution is represented by U{low, high}, and the normal distribution is N{mean, standard deviation}.

8.2.3 Tested DSD and Rain-Rate Combinations

In order to make an appropriate and similar comparison to the results from the TL analyses

which tested vertical rain profiles, the DSDs used for these GPM analyses were chosen to simulate near-vertical profiles for rain. The reflectivity profiles used in the simulations are then based on the DSD profiles. Both the $\log(N_w)$ and D_o profiles exhibit slight slants in their vertical profiles and consequently, the resultant rain profile for each DSD combination is near vertical. The DSD pairs and rainfall rates used in performing the SA/UA are listed in Table 8.2. It should be noted that the table shows the values of N_w in linear scale. In the actual simulations, the log of these values is used to create the linear, $\log(N_w)$ profiles. Note that log = $\log_{10}$, and ln = $\log_e$. The rain rate is listed for only the bottom bin and is slightly smaller at the top bin such that from top to bottom, the rain rate increases slightly.

Table 8.2. List of the N_w, D_o profiles that were used to create the Z_{m1} (13.6 GHz) and Z_{m2} (35.6 GHz) profiles. The expected rain rate in the bottom bin is shown in the right column. The actual N_w profiles were linear in $\log(N_w)$ with the N_w values given in the table.

N_w Top	N_w Bottom	D_o Top	D_o Bottom	Rain Rate Bottom Bin
2500	2100	1.10	1.15	1.03
3000	2500	1.10	1.20	1.50
3500	3000	1.20	1.25	2.19
5000	4500	1.25	1.30	3.94
5000	4500	1.40	1.45	6.57
5000	4500	1.50	1.55	8.95
5000	4500	1.65	1.70	13.72
6000	5500	1.65	1.70	16.77
6000	5500	1.75	1.80	21.80

Although many combinations of $\log(N_w)$ and D_o could be used for these sensitivity analyses, some with less slope, and some with more slope, the above sets meet the purpose here to measure the importance of error in Z_{m1} and Z_{m2} on the output variance in rain rate and determine the relative importance of each factor.

By way of example, two figures derived from the first and last sets (rows) in Table 8.2 are shown along with the simulated DSD-based measured-reflectivity profiles. Figure 8.1 shows the profiles for N_w: log(2500)-log(2100), D_o:1.10-1.15.

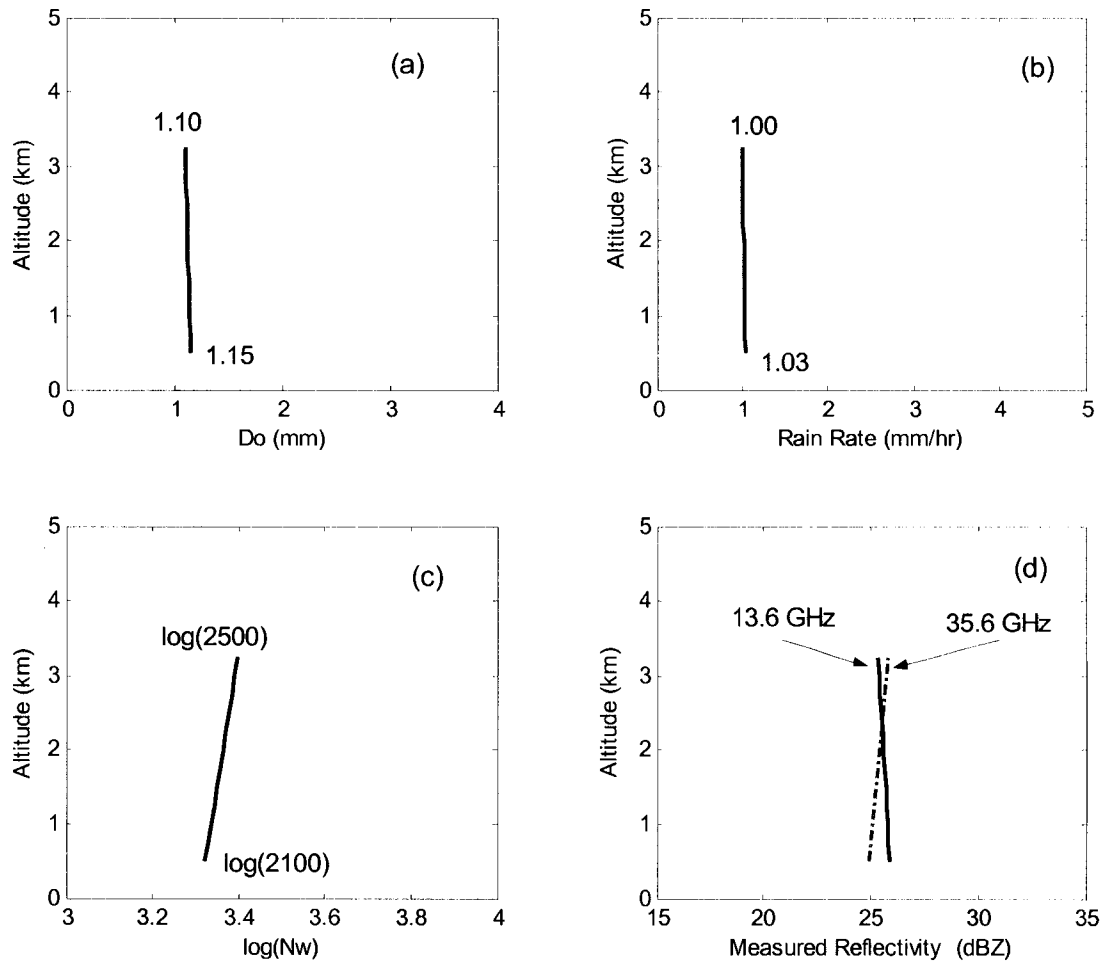

Figure 8.1. Graphic showing the DSD, rain rate and reflectivity profiles for N_w: log(2500)-log(2100) D_o 1.10-1.15.

Figure 8.1(a) shows the D_o profile, and panel (b) shows the rain-rate profile. Note that there is a slight slope to the profile, top to bottom, with the desired rain rate in the bottom bin. Figure 8.1(c) shows the log(N_w) profile and panel (d) shows the 13.6 and 35.6-GHz reflectivity profiles. In the top bin, the reflectivity from the 13.6 GHz signal is less than that of the 35.6 GHz signal. At the lower altitudes, where path attenuation is larger, the relative magnitude of the two signals switches.

An example of the profiles for N_w: log(6000)-log(5500), D_o: 1.75-1.80 is shown in Figure 8.2.

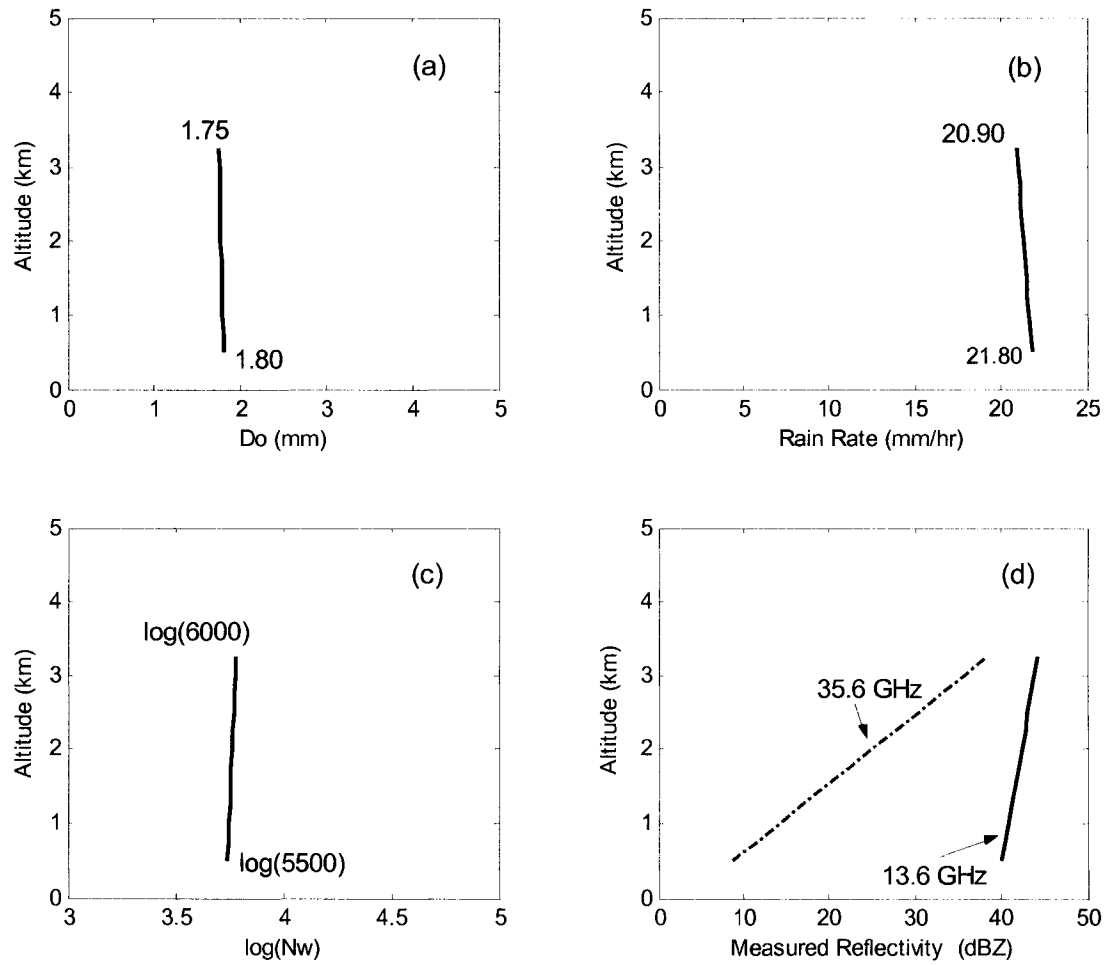

Figure 8.2. Graphic showing the DSD, rain rate and reflectivity profiles for N_w: log(6000)-log(5500), D_o: 1.75-1.80.

The linear D_o and calculated rain-rate profiles are shown in Figure 8.2 (a) and (b). The linear log(N_w) profile is shown in Figure 8.2(c). Figure 8.2(d) shows the two reflectivity profiles for 13.6 and 35.6-GHz radar signals. In this scenario, the bottom-bin 35.6-GHz reflectivity (about 7 dBZ) is below the expected noise floor of 11 dBZ. However, for simulation purposes, it is included here to represent the upper end of practical retrieval. In an actual retrieval, one or more bottom bins would be truncated due to the noise-floor constraint.

8.3 RESULTS

Sensitivity and uncertainty analyses of the model shown in (8.1), with factor definitions listed in Table 8.1, were performed using the Method of Sobol' variance decomposition technique for each of the reflectivity profiles determined by the DSD and rain-rate sets listed in Table 8.2. 6144 samples (N = 6144) were used for each SA/UA. Twelve random restarts (see Chapter 5) were performed on each sample to find the final DSD and rain-rate profiles.

8.3.1 SA/UA Plots

The SA/UA results for N_w: log(2500)-log(2100), D_o: 1.10-1.15 are shown in Figure 8.3. Panel (a) shows a pie chart of the first-order sensitivity indices. Panel(b) shows the total-order indices. A histogram of the bottom-bin rain rate is shown in panel (c). Panel (d) shows the raw values computed by the method of Sobol'. The total of the two first-order indices is much less than 100% indicating that there is significant higher-order interaction in the factors. The pie chart in panel (a) shows $S_{Z_{m1}}$ = 9% and $S_{Z_{m2}}$ = 34%, and the remainder of the output variance, about 57%, is due to higher-order interactions between $S_{Z_{m1}}$ and $S_{Z_{m2}}$. Because of the interactions, the sum of the total sensitivity indices is greater than one. There is a small positive bias in the measurement with the mean rain rate being calculated as 1.26 mm/hr compared to the expected value of 1.09 mm/hr.

The SA/UA results for N_w: log(3000)-log(2500), D_o: 1.10-1.20 are shown in Figure 8.4. Panel (a) shows a pie chart of the first-order sensitivity indices. Panel(b) shows the total-order indices. A histogram of the bottom-bin rain rate is shown in panel (c). Panel (d) shows the raw values computed by the method of Sobol'. The total of the first-order indices is much less than 100% indicating that there is significant higher-order interaction in the factors. The pie chart in panel (a) shows that $S_{Z_{m1}}$ = 11% and $S_{Z_{m2}}$ = 39%, and the remainder, about 50%, is due to higher-order interactions between $S_{Z_{m1}}$ and $S_{Z_{m2}}$. Because of the interactions, the sum of the

total sensitivity indices is greater than one as shown in part (d). There is a small positive bias in the measurement with the mean rain rate being calculated as 1.77 mm/hr compared to the expected value of 1.50 mm/hr.

The SA/UA results for N_w: log(3500)-log(3000), D_o: 1.20-1.25 are shown in Figure 8.5. Panel (a) shows a pie chart of the first-order sensitivity indices. Panel(b) shows the total-order indices. A histogram of the bottom-bin rain rate is shown in panel (c). Panel (d) shows the raw values computed by the method of Sobol'. The sum of the first-order indices is slightly less than 100% indicating that there is some higher-order interaction in the factors. The pie chart in panel (a) shows that $S_{Z_{m1}} = 8\%$ and $S_{Z_{m2}} = 69\%$, and the remainder of the output variance, about 23%, is due to higher-order interactions between $S_{Z_{m1}}$ and $S_{Z_{m2}}$. Because of the interactions, the sum of the total sensitivity indices is greater than one, and the sum of the first-order indices is less than one as shown in part (d). The amount of higher-order interaction is decreasing with increasing rain rate. There is a small positive bias in the measurement with the mean rain rate being calculated as 2.48 mm/hr compared to the expected value of 2.19 mm/hr.

The SA/UA results for N_w: log(5000)-log(4500), D_o: 1.25-1.30 are shown in Figure 8.6. Panel (a) shows a pie chart of the first-order sensitivity indices. Panel(b) shows the total-order indices. A histogram of the bottom-bin rain rate is shown in panel (c). Panel (d) shows the raw values computed by the method of Sobol'. The sum of the first-order indices is almost equal to 100% indicating that there is little higher-order interaction in the factors. The pie chart in panel (a) shows $S_{Z_{m1}} = 7\%$ and $S_{Z_{m2}} = 87\%$, and a small amount of higher-order interactions between $S_{Z_{m1}}$ and $S_{Z_{m2}}$. There is a small positive bias in the measurement with the mean rain rate being calculated as 4.32 mm/hr compared to the expected value of 3.94 mm/hr.

The SA/UA results for N_w: log(5000)-log(4500), D_o: 1.40-1.45 are shown in Figure 8.7. Panel (a) shows a pie chart of the first-order sensitivity indices. Panel(b) shows the total-order indices. A histogram of the bottom-bin rain rate is shown in panel (c). The bimodal distribution

is caused by the additional random error in the reflectivity profiles. The histogram is expected to have a single peak, but a second peak occurs below about 4 mm/hr rainfall rate. This second peak is caused by an artificial bias induced in the reflectivity profiles when random error is added to them. Normally, the random error is distributed with zero mean about each reflectivity profile. However, in some cases, the random error creates a bias between the two profiles, and for those profiles, the profile-optimization method finds correct, but less than expected rainfall rates. Panel (d) shows the raw values computed by the method of Sobol'. The pie chart in Figure 8.7 (a) shows $S_{Z_{m1}}$ = 4% and $S_{Z_{m2}}$ = 92%. The sum of the first-order indices is nearly equal to 100% indicating that there is little higher-order interaction in the factors and all the variance in the output can be explained by the errors in the two input factors individually. There is no bias in the measurement with the mean rain rate being calculated as 6.47 mm/hr compared to the expected value of 6.57 mm/hr.

The SA/UA results for N_w: log(5000)-log(4500), D_o: 1.50-1.55 are shown in Figure 8.8. Panel (a) shows a pie chart of the first-order sensitivity indices. Panel (b) shows the total-order indices. A histogram of the bottom-bin rain rate is shown in panel (c). Like the previous figure, the bimodal distribution is caused by the additional random error in the reflectivity profiles. The histogram is expected to have a single peak, but a second peak occurs below about 5.5 mm/hr rainfall rate. This second peak is caused by an artificial bias induced in the reflectivity profiles when random error is added to them. Normally, the random error is distributed with zero mean about each reflectivity profile. However, in some cases, the random error creates a small bias or artificial offset between the two profiles, and based on those profiles, the profile-optimization method finds correct, but less than expected rainfall rates. Panel (d) shows the raw values computed by the method of Sobol'. The sum of the first-order indices is nearly equal to 100% indicating that there is little higher-order interaction in the factors. The pie chart

in panel (a) shows $S_{Z_{m1}}$ = 3% and $S_{Z_{m2}}$ = 91%. There is no bias in the measurement with the mean rain rate being calculated as 8.78 mm/hr compared to the expected value of 8.95 mm/hr.

The SA/UA results for N_w: log(5000)-log(4500), D_o: 1.65-1.70 are shown in Figure 8.9. Panel (a) shows a pie chart of the first-order sensitivity indices. Panel(b) shows the total-order indices. A histogram of the bottom-bin rain rate is shown in panel (c). Panel (d) shows the raw values computed by the method of Sobol'. The pie chart in panel (a) shows $S_{Z_{m1}}$ = 1% and $S_{Z_{m2}}$ = 98%. There is no higher-order interaction between the two factors. There is no bias in the measurement with the mean rain rate being calculated as 13.6 mm/hr compared to the expected value of 13.6 mm/hr.

The SA/UA results for N_w: log(6000)-log(5500), D_o: 1.65-1.70 are shown in Figure 8.10. Panel (a) shows a pie chart of the first-order sensitivity indices. Panel(b) shows the total-order indices. A histogram of the bottom-bin rain rate is shown in panel (c). Panel (d) shows the raw values computed by the method of Sobol'. The pie chart in panel (a) shows $S_{Z_{m1}}$ = 1% and $S_{Z_{m2}}$ = 99%. There is no higher-order interaction between the two factors. There is no bias in the measurement with the mean rain rate being calculated as 16.7 mm/hr compared to the expected value of 16.8 mm/hr.

The SA/UA results for N_w: log(6000)-log(5500), D_o: 1.75-1.80 are shown in Figure 8.11. Panel (a) shows a pie chart of the first-order sensitivity indices. Panel(b) shows the total-order indices. A histogram of the bottom-bin rain rate is shown in panel (c). Panel (d) shows the raw values computed by the method of Sobol'. The pie chart in panel (a) shows $S_{Z_{m1}}$ = 1% and $S_{Z_{m2}}$ = 98%. There is no higher-order interaction between the two factors. There is no bias in the measurement with the mean rain rate being calculated as 21.7 mm/hr compared to the expected value of 21.8 mm/hr.

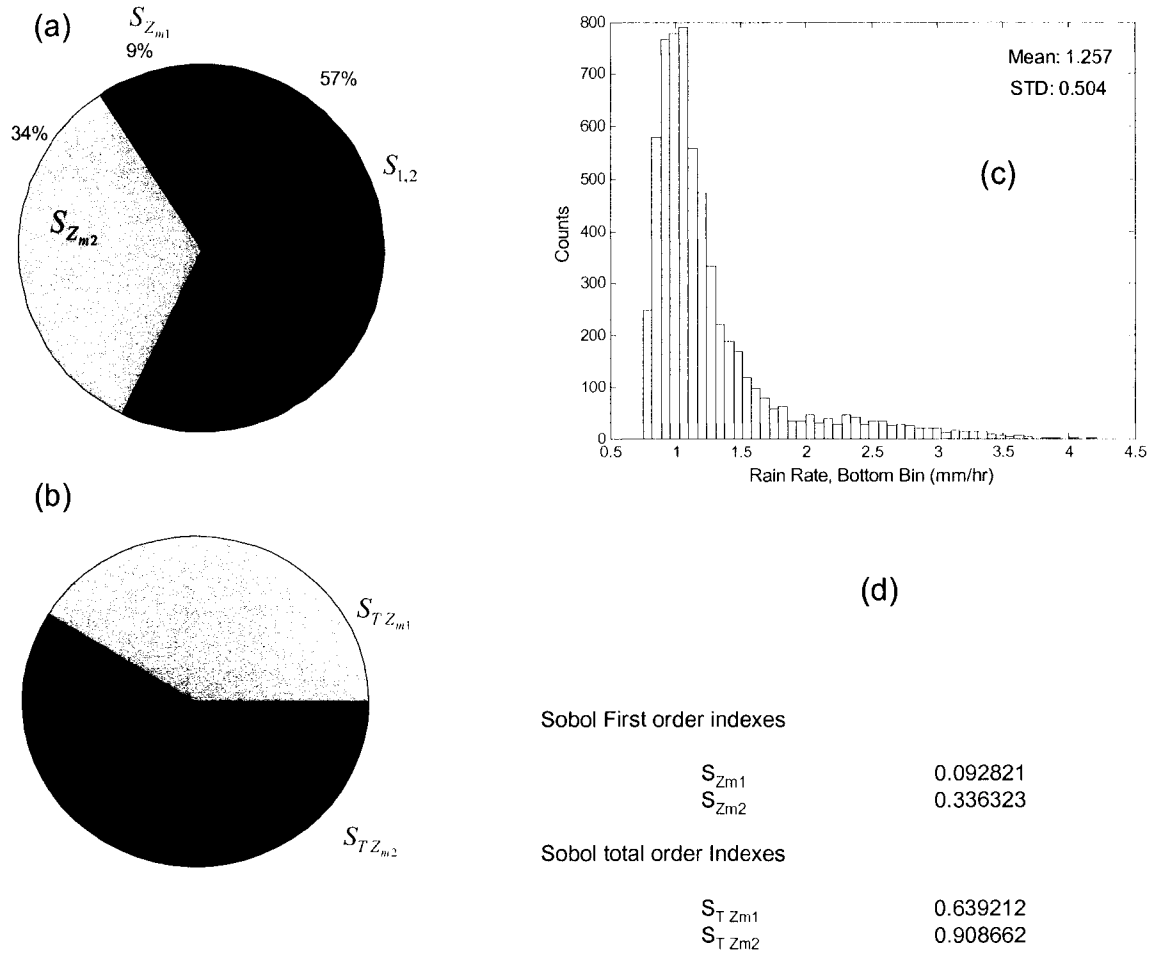

Figure 8.3 SA/UA results for GPM profile-optimization method for N_w: log(2500)-log(2100), D_o: 1.10-1.15. The pie chart in panel(a) shows the first-order indices for Z_{m1} and Z_{m2}. Their sum is less than 100% indicating that there is significant higher-order interaction between the two factors. In this case, about 57% of the output variance is due to higher-order interactions. The pie chart in panel (b) shows pictorially the values for the total-sensitivity indices. When there is higher-order interactions, the sum of the total sensitivity indices can be greater than one. A histogram of the bottom-bin rain rate calculations is shown in panel (c). Panel (d) lists the raw output values from the method of Sobol' procedure.

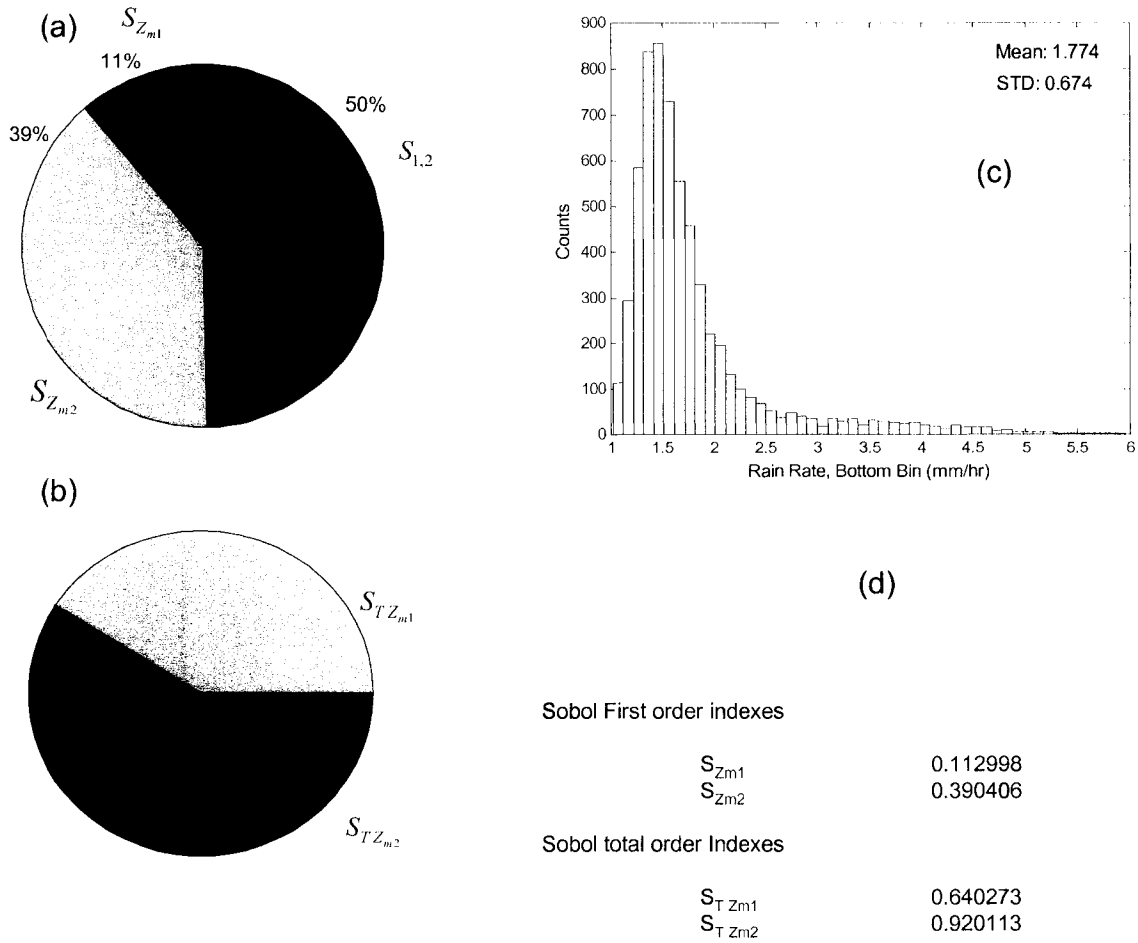

Figure 8.4. SA/UA results for GPM profile optimization method for N_w: log(3000)-log(2500), D_o: 1.10-1.20. The pie chart in panel(a) shows the first-order indices for Z_{m1} and Z_{m2}. Their sum is less than 100% indicating that there is significant higher-order interaction between the two factors. In this case, about 50% of the output variance is due to higher-order interactions. The pie chart in panel (b) shows pictorially the values for the total-sensitivity indices. When there is higher-order interactions, the sum of the total sensitivity indices can be greater than one. A histogram of the bottom-bin rain rate calculations is shown in panel (c). Panel (d) lists the raw output values from the method of Sobol' procedure.

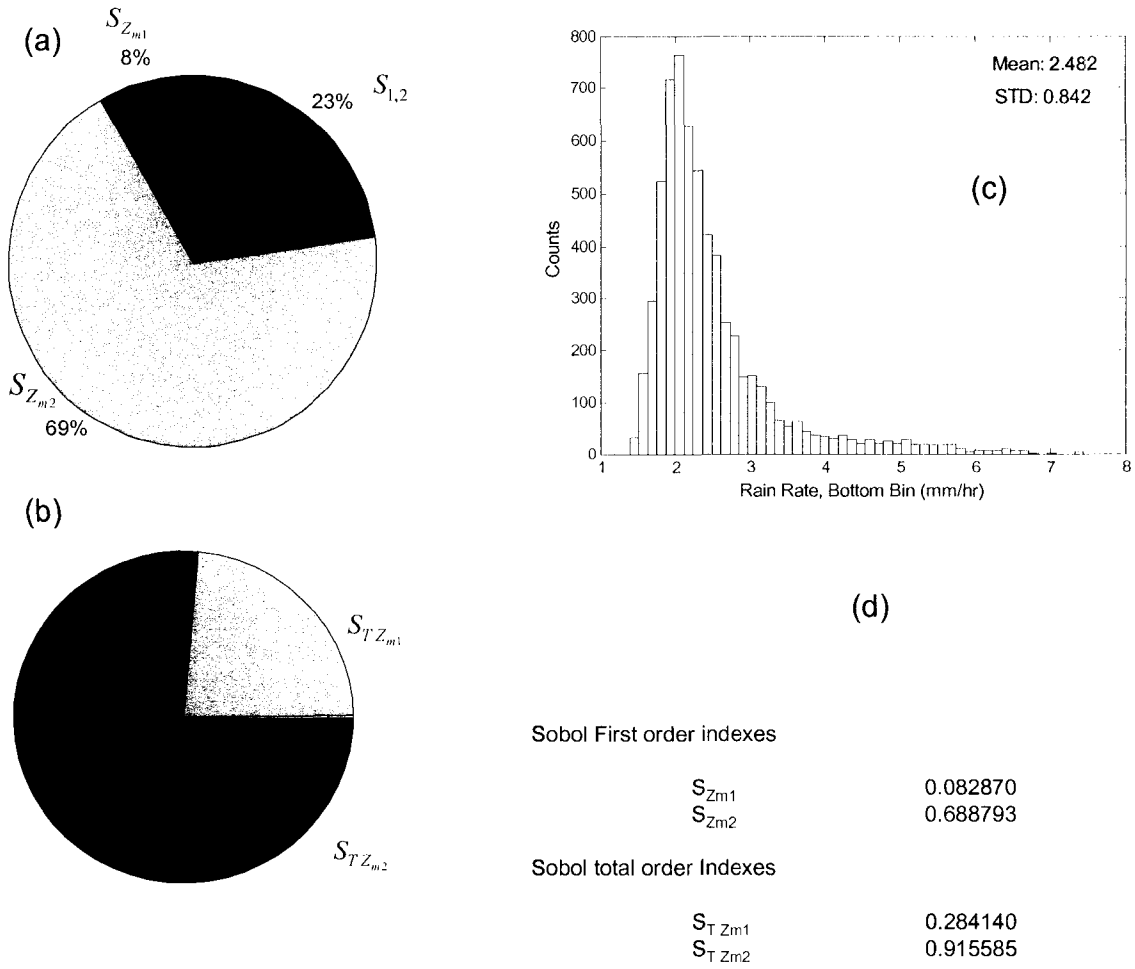

Figure 8.5. SA/UA results for GPM profile optimization method for N_w: log(3500)-log(3000), D_o: 1.20-1. 25. The pie chart in panel(a) shows the first-order indices for Z_{m1} and Z_{m2}. Their sum is less than 100% indicating that there is some higher-order interaction between the two factors. In this case, about 23% of the output variance is due to higher-order interactions. The pie chart in panel (b) shows pictorially the values for the total-sensitivity indices. When there is higher-order interaction, the sum of the total sensitivity indices can be greater than one. A histogram of the bottom-bin rain rate calculations is shown in panel (c). Panel (d) lists the raw output values from the method of Sobol' procedure.

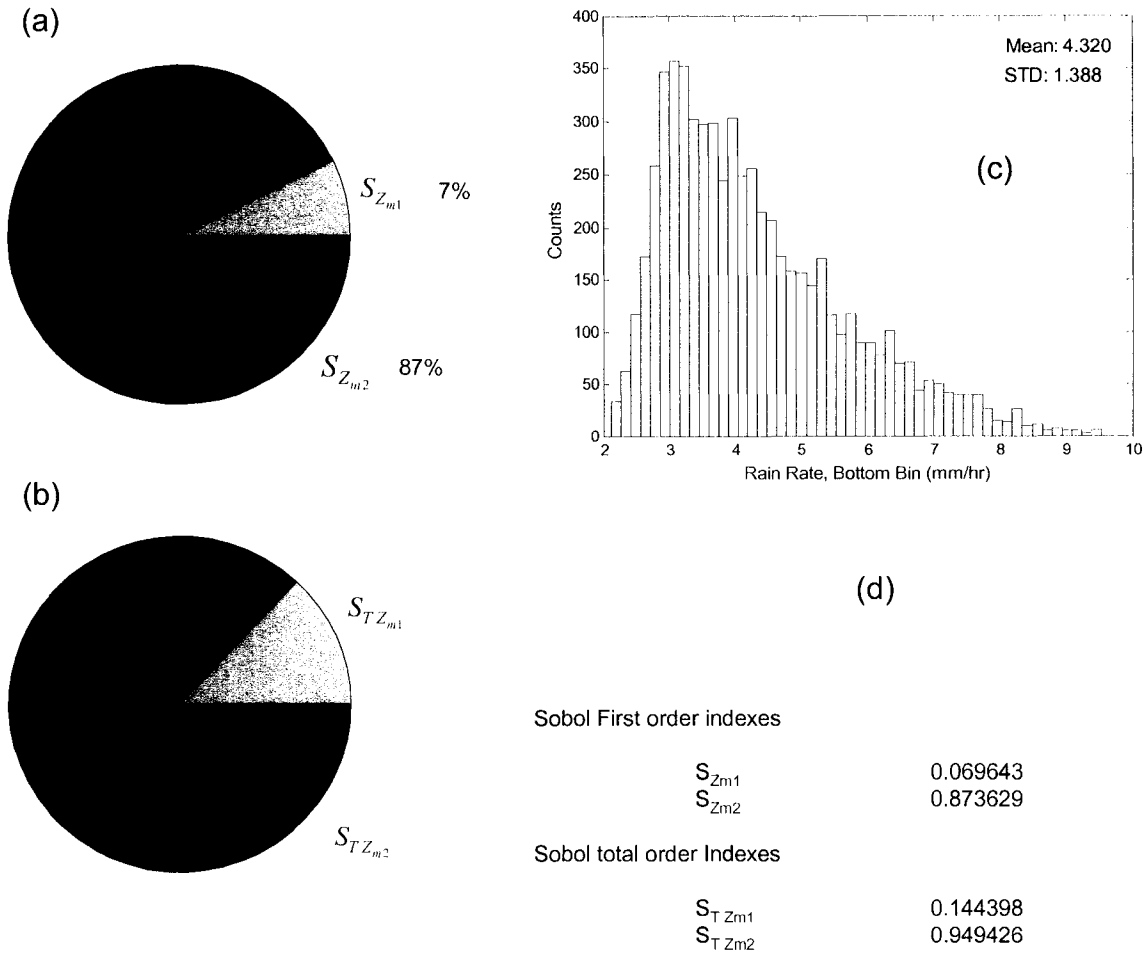

Figure 8.6. SA/UA results for GPM profile optimization method for N_w: log(5000)-log(4500), D_o: 1.25-1.30. The pie chart in panel(a) shows the first-order indices for Z_{m1} and Z_{m2}. Their sum is almost 100% indicating that there is little higher-order interaction between the two factors. The pie chart in panel (b) shows pictorially the values for the total-sensitivity indices. A histogram of the bottom-bin rain rate calculations is shown in panel (c). Panel (d) lists the raw output values from the method of Sobol' procedure.

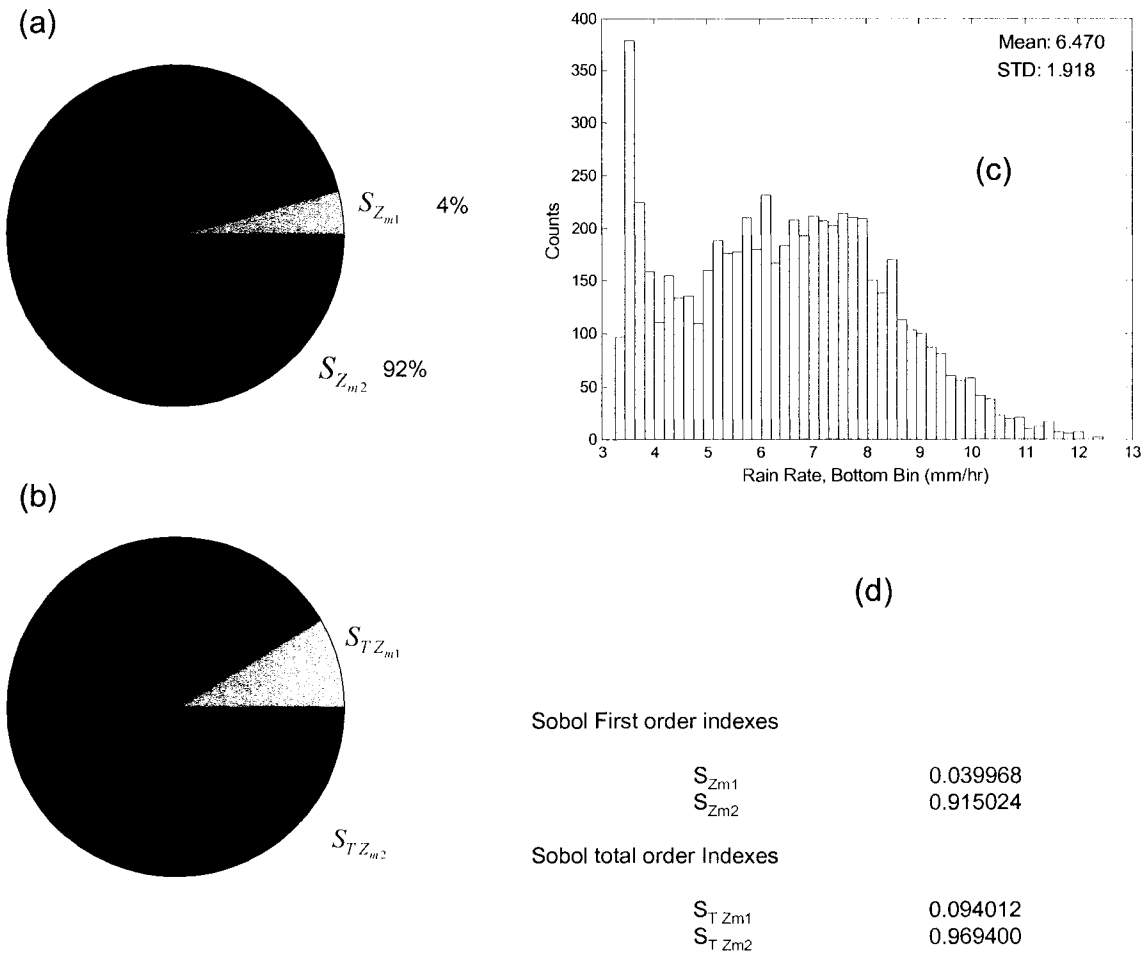

Figure 8.7. SA/UA results for GPM profile optimization method for N_w: log(5000)-log(4500), D_o: 1.40-1.45. The pie chart in panel(a) shows the first-order indices for Z_{m1} and Z_{m2}. Their sum is almost 100% indicating that there is no higher-order interaction between the two factors. The pie chart in panel (b) shows pictorially the values for the total-sensitivity indices. A histogram of the bottom-bin rain rate calculations is shown in panel (c). The bimodal distribution, with a second peak below about 4 mm/hr occurs because of a random bias created in the reflectivity profiles when random error is added. When this bias occurs, the profile-optimization method correctly determines the DSDs and rainfall rate though they are less than expected. Panel (d) lists the raw output values from the method of Sobol' procedure.

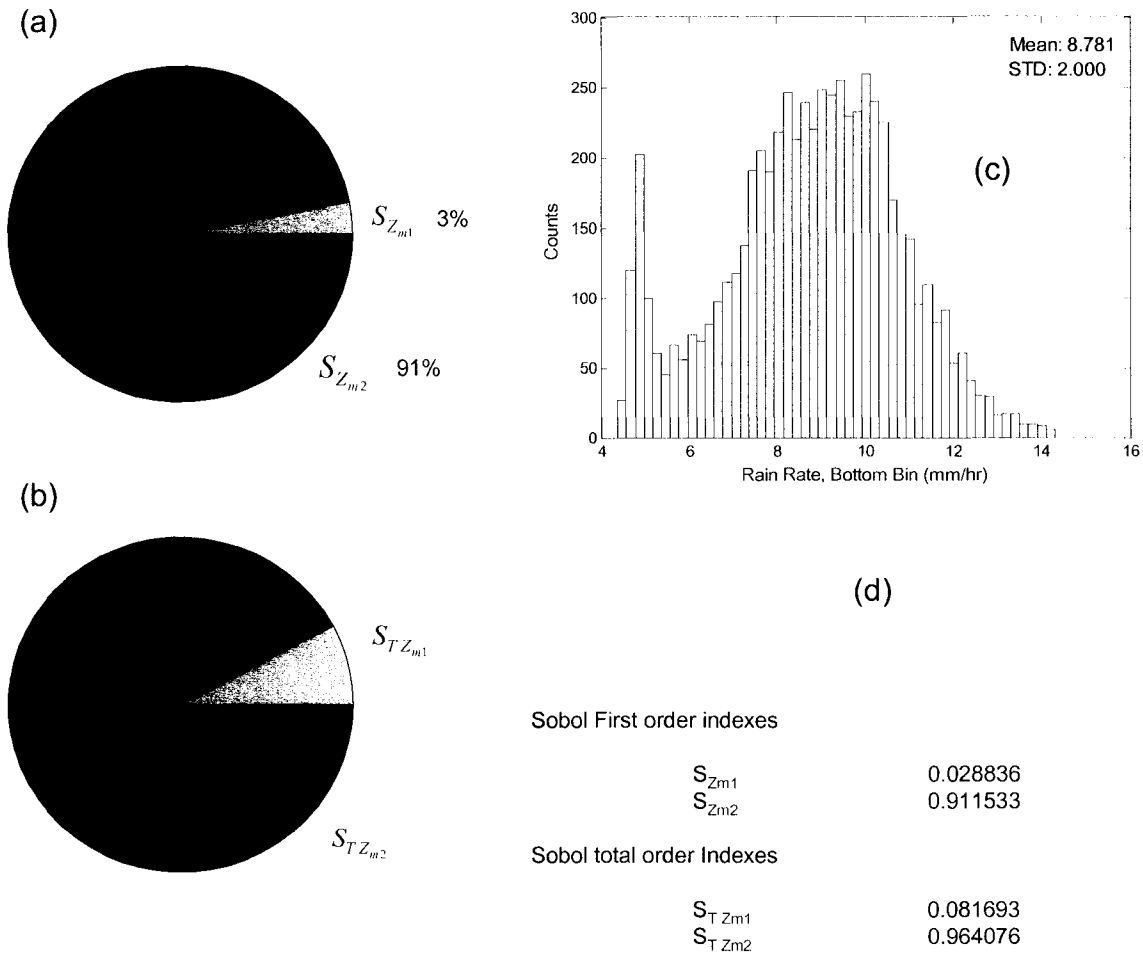

Figure 8.8. SA/UA results for GPM profile optimization method for N_w: log(5000)-log(4500), D_o: 1.50-1.55. The pie chart in panel(a) shows the first-order indices for Z_{m1} and Z_{m2}. Their sum is almost 100% indicating that there is little higher-order interaction between the two factors. The pie chart in panel (b) shows pictorially the values for the total-sensitivity indices. A histogram of the bottom-bin rain rate calculations is shown in panel (c). The bimodal distribution, with a second peak below about 5.5 mm/hr occurs because of a random bias created in the reflectivity profiles when random error is added. When this bias occurs, the profile-optimization method correctly determines the DSDs and rainfall rate though they are less than expected. Panel (d) lists the raw output values from the method of Sobol' procedure.

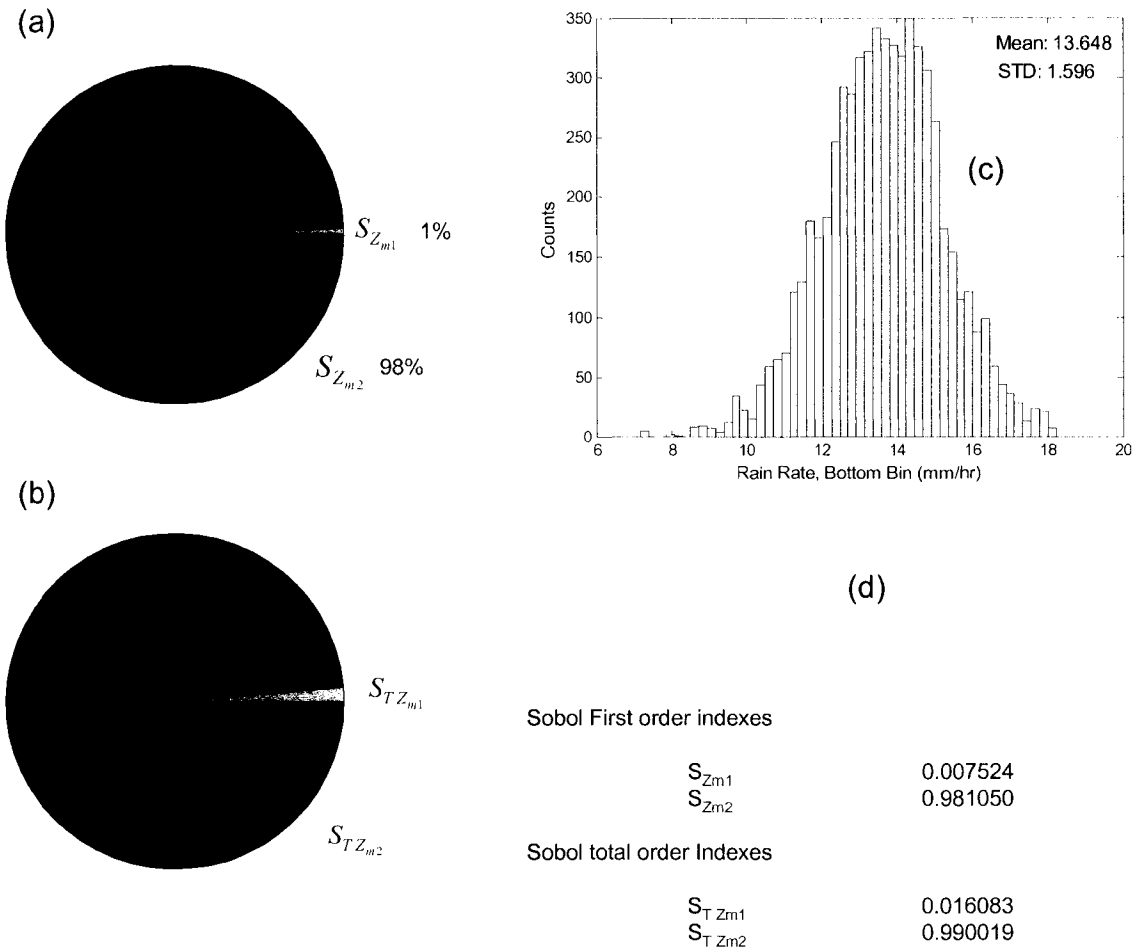

Figure 8.9. SA/UA results for GPM profile optimization method for N_w: log(5000)-log(4500), D_o: 1.65-1.70. The pie chart in panel(a) shows the first-order indices for Z_{m1} and Z_{m2}. Their sum is almost 100% indicating no higher-order interaction. The pie chart in panel (b) shows pictorially the values for the total-sensitivity indices. A histogram of the bottom-bin rain rate calculations is shown in panel (b). Panel (c) lists the raw output values from the method of Sobol' procedure.

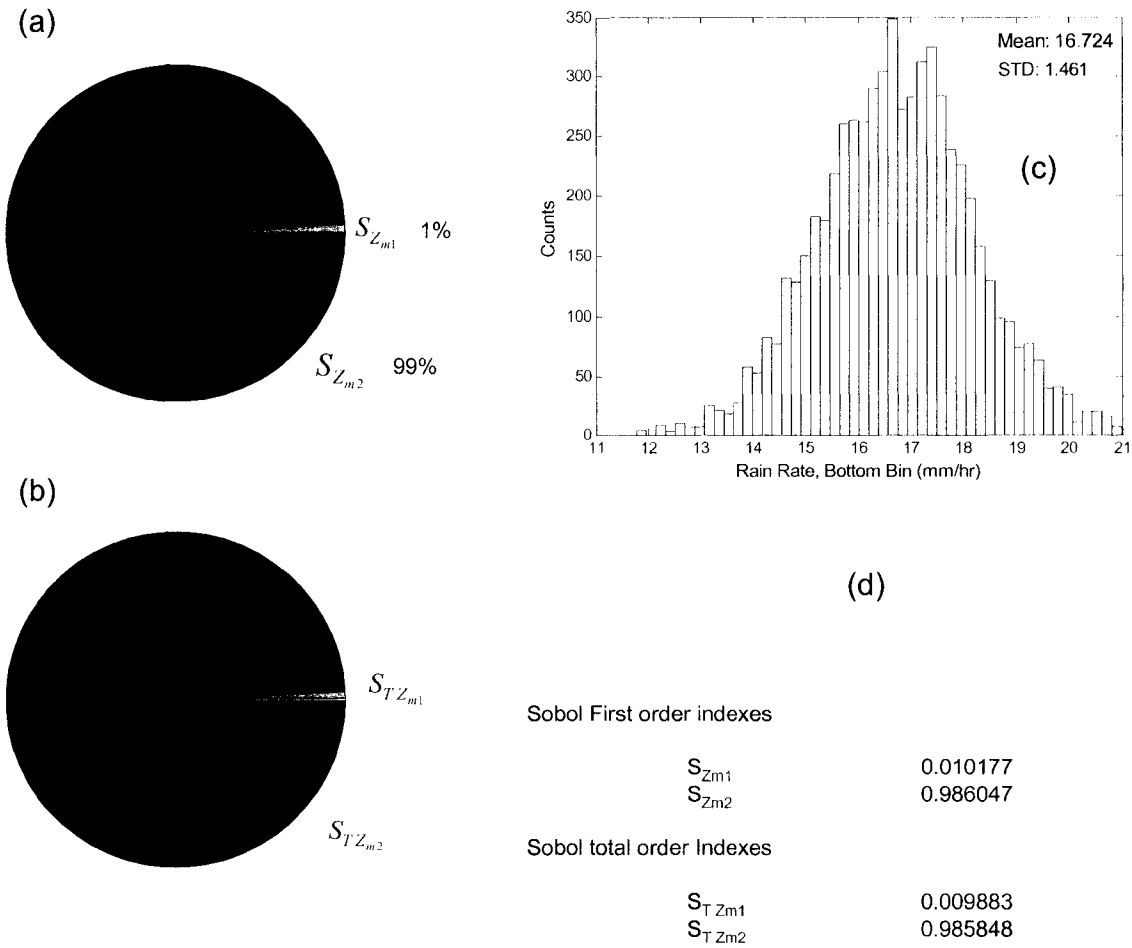

Figure 8.10. SA/UA results for GPM profile optimization method for N_w: log(6000)-log(5500), D_o: 1.65-1.70. The pie chart in panel(a) shows the first-order indices for Z_{m1} and Z_{m2}. Their sum is about 100% indicating no higher-order interaction between the two factors. The pie chart in panel (b) shows pictorially the values for the total-sensitivity indices. A histogram of the bottom-bin rain rate calculations is shown in panel (c). Panel (d) lists the raw output values from the method of Sobol' procedure.

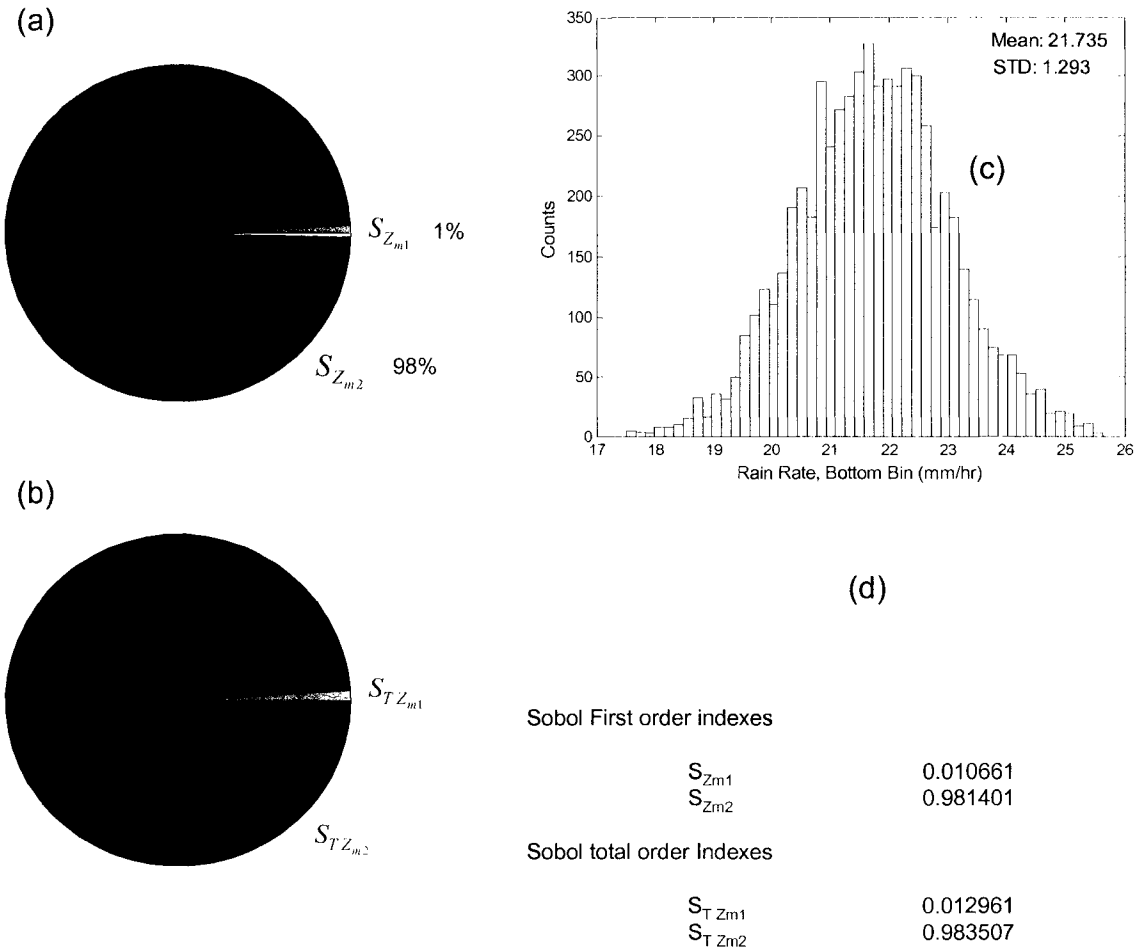

Figure 8.11. SA/UA results for GPM profile optimization method for N_w: log(6000)-log(5500), D_o: 1.75-1.80. The pie chart in panel(a) shows the first-order indices for Z_{m1} and Z_{m2}. Their sum is about 100% indicating no higher-order interaction between the two factors. The pie chart in panel (b) shows pictorially the values for the total-sensitivity indices. A histogram of the bottom-bin rain rate calculations is shown in panel (c). Panel (d) lists the raw output values from the method of Sobol' procedure.

8.3.2 GPM Sensitivity Analysis Listings

For a model that is additive, that is, it has no higher-order interactions between the input factors, the sum of the first-order indices is 100%. Note that the first-order indices are percentage values that indicate how much of the model output variance can be apportioned to each specific input factor. When there are higher-order effects, in other words, interactions between the input factors that manifest themselves as a percentage of the total output variance, then the sum of the first-order effects and interaction terms is 100%. Due to a limited number of samples used in any SA procedure, the sum of the first and total effects is usually not exactly 100% (but approaches 100%) and may vary a few percentage points either below or above. In this scenario, the values of the sensitivity indices are still valid approximations for their relative contributions to variance in the model output.

From the SA analyses, a plot of the first and higher-order sensitivity indices percentage values for all the rain rates listed in Table 8.2 is shown in Figure 8.12.

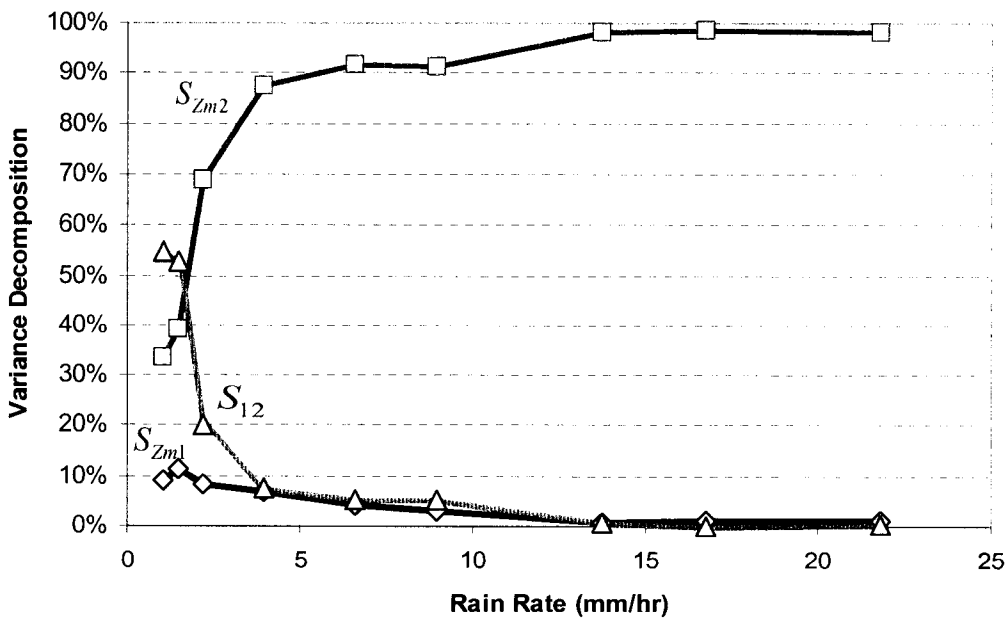

Figure 8.12. Graph showing the first and higher-order variance decomposition of the two input factors for the GPM profile-optimization method. At low rain rates, the model is not additive where significant higher-order interactions are present. At higher rain rates, the model is additive. The error in Z_{m2} is the primary contributor to total output variance throughout the entire rain rate region.

In Figure 8.12, at low rain rates, there is significant higher-order interaction between the two factors accounting for up to 57% of the variance in the calculation of the estimated rainfall rate. Because there are only two input factors, any higher-order interaction is attributed solely to those two factors, and this interaction is shown in the figure. As the rain rate increases, along with increasing levels of reflectivity and increasing magnitude of DSD parameters, the interaction decreases and the variance in the output can be singularly attributed to each input factor alone. At the higher rain rates, the sum of the two first-order indices approaches 100%. It should be noted that throughout the spectrum of rain rates, the contribution to output variance from the error in Z_{m2} is dominant and that the error in Z_{m1} contributes relatively little.

Table 8.3 is a tabular-form listing of the variance decomposition results for first and higher-order interactions for each of the rainfall rates listed in Table 8.2.

Table 8.3. List of the variance decomposition results for the GPM profile-optimization method. The column on the left is rain rate in mm/hr. The first-order and total-order indices are shown for both factors. At low rain rates, there is significant higher-order interaction. At higher rain rates, the model becomes additive. The amount of interaction between the two factors is shown in the two columns on the right. The numbers differ slightly, but show good overall agreement, because they are derived separately from S_{Zm1} and S_{Zm2}.

	First-Order Indices			Total Order		Interaction	
Rain Rate (mm/hr)	S_{Zm1}	S_{Zm2}	$S_{Zm1}+S_{Zm2}$	$S_{T,Zm1}$	$S_{T,Zm2}$	$S_{12}(Z_{m1})$	$S_{12}(Z_{m2})$
1.03	9.3%	33.6%	42.9%	63.9%	90.9%	54.6%	57.2%
1.50	11.3%	39.0%	50.3%	64.0%	92.0%	52.7%	53.0%
2.19	8.3%	68.9%	77.2%	28.4%	91.6%	20.1%	22.7%
3.94	7.0%	87.4%	94.3%	14.4%	94.9%	7.5%	7.6%
6.57	4.0%	91.5%	95.5%	9.4%	96.9%	5.4%	5.4%
8.95	2.9%	91.2%	94.0%	8.2%	96.4%	5.3%	5.3%
13.72	0.8%	98.1%	98.9%	1.6%	99.0%	0.9%	0.9%
16.77	1.0%	98.6%	99.6%	1.0%	98.6%	0.0%	0.0%
21.8	1.1%	98.1%	99.2%	1.3%	98.4%	0.2%	0.2%

These values were used to make the chart of Figure 8.12. The column on the left is rain rate in mm/hr which can be correlated to the simulated DSD profiles using Table 8.2. The second and third columns show the first-order index values for S_{Zm1} and S_{Zm2}. Column three shows the sum of the two, first-order indices. It should be noted that at low rain rates, below approximately 3 - 5 mm/hr, that the sum of the two, first-order indices is significantly less than 100%. This is a result of higher-order interactions which can be confirmed by examining the values in the right two columns for the interaction terms. At higher rain rates, the sum of the first-order indices approaches 100% indicating that the model becomes additive and the output variance can be attributed to each input factor singularly. The total-order indices $S_{T,Zm1}$ and $S_{T,Zm2}$ are shown in columns five and six. The total-order indices are the sum of the first order and interaction indices of each factor (see (6.13) for a description of higher-order interaction). Note that when the model is not additive that the sum of the two, total-order indices is greater than 100% and that when it becomes additive (reduced higher-order interactions) that the sum of the total-order indices approaches 100% as the sum of the first-order indices also approaches 100%. In this case, the total sensitivity index for factor Z_{m1} can be written as,

$$S_{T,Z_{m1}} = S_{Z_{m1}} + S_{12} \tag{8.2}$$

where S_{Zm1} represents the first-order index for Z_{m1}, and S_{12} represents the interaction between Z_{m1} and Z_{m2}. For Z_{m2}, the total-order index is written as,

$$S_{T,Z_{m2}} = S_{Z_{m2}} + S_{12} \tag{8.3}$$

If the higher-order interaction is zero, $S_{12} = 0$, then the value of the total-order sensitivity index for each factor equals the value of its respective first-order index. The two columns on the right show the amount of the higher-order interaction in percent for S_{12}, with each column being based on its respective factor.

Note that there is good agreement between the S_{12} values based on each of their respective first-order and total-order indices. For example, $S_{12}(Z_{m1}) = S_{T,Zm1} - S_{Zm1}$ and $S_{12}(Z_{m2}) = S_{T,Zm2} -$

S_{Zm2}. At low rain rates, there is significant higher-order interaction. At higher rain rates, the model becomes additive and the interactions diminish. The amount of output variance due to interaction between the two factors is shown in the two columns on the right. Normally, the numbers in the two columns would match exactly, but due to a limited number of samples used in the analysis, there is a minor discrepancy between some of the values in the two columns.

An example is useful to demonstrate how a model can exhibit higher-order interactions. In this example, assume a simple linear model with two input factors given by,

$$y = x_1 + x_2 \tag{8.4}$$

where the output y is the sum of x_1 and x_2. In this scenario, the two inputs do not interact to form the output. If x_1 is zero, then the output is determined by x_2 alone, and vice versa. As described in Chapter 6, this model is additive, with no sensitivity interaction between x_1 and x_2. For an example of a non-additive model, which exhibits higher-order interaction, examine the model,

$$y = x_1 \sin(x_2) \tag{8.5}$$

In this case, the value of y is determined by the product of x_1 and a function of x_2. If x_1 is small, or zero, then the output is small or zero regardless of the value of x_2. If x_2 is small or zero, then the output is also small or zero regardless of the value of x_1. In this case, there is an interaction or coupling between the two factors to determine the output. The variance of the output will be comprised of both first-order and higher-order sensitivity-index terms.

In the GPM profile-optimization algorithm, at low rain rates, a coupling occurs between Z_{m1} and Z_{m2} to cause a higher-order sensitivity interaction.

8.3.3 GPM Uncertainty Analysis Listings

From UA, the standard deviation (standard error (SE)) and normalized standard error (NSE) vs. rain rate for the profiles of Table 8.2 are shown in Figure 8.13. Throughout the rain-

rate spectrum the NSE decreases with increasing rain rates. The SE begins small at low rain rates, peaks at about 8-10 mm/hr, and then decreases with higher rain rates.

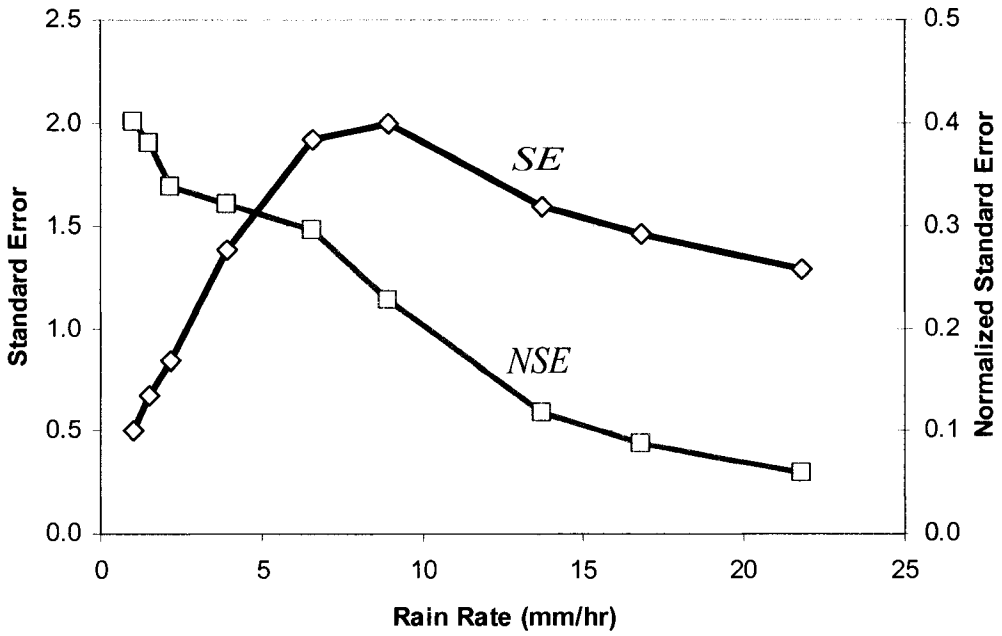

Figure 8.13. Graph showing the results from the UA of the GPM profile optimization method. The standard error and normalized standard error are shown vs. rain rate.

8.4 SA COMPARISON WITH SINGLE-LOOP RETRIEVAL METHOD

The results from the previous sections show that the error associated with Z_{m2} is the greatest contributor to output variance. As a preliminary, independent verification of this phenomenon, i.e., that the error in Z_{m2} dominates GPM dual-frequency-type retrieval algorithms' output variance, three of the DSD cases tested with the GPM profile-optimization algorithm were analyzed using the single-loop retrieval algorithm described in Chapter 3 that iterate to DSD-profile solutions in the correct convergence region. The test cases and their sensitivity analysis results, based on 3072 samples (model evaluations), are listed in Table 8.4 .

Table 8.4. List of the variance decomposition results, using 3072 samples, for the GPM single-loop retrieval method using three of the DSD profiles listed in Table 8.2. The column on the left is rain rate in mm/hr. The first-order and total-order indices are shown for both factors. The amount of interaction between the two factors is shown in the two columns on the right. The interaction column values are derived in the same manner as those in Table 8.3.

Rain Rate (mm/hr)	First-Order Indices			Total Order		Interaction	
	S_{Zm1}	S_{Zm2}	$S_{Zm1} + S_{Zm2}$	$S_{T,Zm1}$	$S_{T,Zm2}$	$S_{12}(Z_{m1})$	$S_{12}(Z_{m2})$
1.50	12.9%	24.9%	37.8%	67.4%	79.4%	54.5%	54.5%
3.94	4.3%	30.4%	34.7%	67.8%	93.9%	63.5%	63.5%
8.95	0.7%	51.4%	52.1%	45.2%	95.9%	44.5%	44.5%

For these three data sets, the preliminary sensitivity analysis results indicate that the error in Z_{m2} dominates the variance of the single-loop estimated rain-rate output as it also dominates in the GPM profile-optimization model. The data also indicate a substantial amount of higher-order interaction between the two input factors. It should be noted that in contrast to the GPM profile-optimization method, where at higher rain rates the interaction became negligible, that the higher-order interaction in the single-loop algorithm does not become negligible but seems to persist. For example, at a rainfall rate of 3.94 mm/hr, the S_{12} term is 63.5 %, and at 8.95 mm/hr, the S_{12} contribution is 44.5%.

8.5 SUMMARY

The GPM profile-optimization method has been restated in an algorithm compatible with sensitivity and uncertainty analysis procedures. As such, it requires only two input factors (vectors) for analysis, Z_{m1} and Z_{m2}. The probability density functions were described for each of the factors and a method described whereby random error is added to each bin of each profile to account for these error distributions. As with the TL algorithm, this GPM method also uses trigger variables for both input factors as each is a vector and not a single value. A table was given showing the DSDs and rain rate values for near vertical rainfall. The $\log(N_w)$ and D_o profiles are assumed linear and slightly sloped with respect to each other.

The sensitivity analyses performed on the GPM profile-optimization method show differences in factor variance decomposition depending on the rainfall region, low or high. At low rainfall rates, there is significant higher-order interaction between the two factors. At higher rain rates, the higher-order interactions diminish and all the variance in the output (rain rate calculation) can be singularly attributed to each of the input factors.

It should be noted that most of the variance in the rainfall calculation can be attributed to the error in Z_{m2}, with the error in Z_{m1} contributing proportionately less. In fact, at higher rain rates, above about 5 mm/hr, the contribution to total output variance from Z_{m1} is negligible with nearly all of it coming from Z_{m2}. These analyses indicate that the error in Z_{m2} is much more important than the error in Z_{m1} and future work should concentrate on improving the accuracy of Z_{m2}. Preliminary sensitivity and uncertainty analyses were performed using the single-loop retrieval method described in Chapter 3 which also indicate the dominance of the error in Z_{m2} on the output variance. These single-loop SA/UA also indicate a large amount of higher-order sensitivity interaction. Both the profile-optimization and single-loop methods indicate that Z_{m2} contributes the greatest amount to the output variance, and both algorithms would benefit from greater knowledge of Z_{m2} or its error reduction.

CHAPTER 9

SUMMARY AND FUTURE WORK

9.1 SUMMARY

This work has addressed some of the systems engineering aspects of the planned Global Precipitation Measurement (GPM) mission. In particular, a review was given of the GPM mission and its science requirements which have been demonstrated to drive all other system factors such as the type and accuracy of the retrieval algorithms, satellite hardware (for this discussion limited to the radar), sensitivity analysis of the proposed algorithms, and expected and required feedback to the system designers and mission architects. This work focused on the systems engineering aspects of the retrieval algorithms.

The iterative dual-frequency retrieval algorithm was analyzed, discussed and cast in terms of a single-loop control-system model that could be used for drop-size-distribution (DSD) parameter retrieval. Knowing the DSD values, then the rainfall rate can be calculated at each resolution volume. In particular, it was shown that the single-loop model retrieves the correct DSD values when the normalized-slope parameter N_w, and median volume diameter D_o values, as a pair, are in the correct convergence region for which the solution is single valued. For those N_w, D_o pairs that are in the incorrect convergence region, multiple solutions exist to the retrieval equations and the algorithm incorrectly estimates the DSD values because of insufficient constraints. As a result of the incorrect convergence region for this method, it is estimated that about half the global rainfall rate will be incorrectly estimated by this technique. Because of the multi-valued solution space, the single-loop algorithm is limited to accurate rain-rate retrieval below about 10-14 mm/hr.

Two methods to increase the robustness of the single-loop dual-frequency algorithm and extend its useful range to higher rainfall rates up to more than 20 mm/hr where the limiting factor in rain-rate retrieval becomes attenuation of the Ka-band signal and the dual-frequency radar's noise floor instead of the multi-valued solution space were proposed and examined. One method showed how a dual-loop model with a profile constraint on N_w could be used to fit a linear function to the $\log(N_w)$ vertical profile, analyze the residuals between the linear function and $\log(N_w)$ profiles, and find the best-fit DSD-retrieval solution. The second method, based on profile optimization, assumes that the profiles for D_o and $\log(N_w)$ can be approximated by linear functions and that these functions could be found using a random-restart non-linear optimization process. The optimization process finds top and bottom DSD values such that a cost function is minimized between the input measured reflectivity profiles and internally generated profiles using the selected top and bottom DSD values. Both of these techniques, in comparison with the single-loop method, incorporate an additional constraint on the DSD profiles, and subsequently do not suffer from the effects of the regions of convergence. However, they do impose an additional constraint which may affect the estimated DSD values. Several examples of the performance of both of these methods were given and explained for rainfall retrievals in incorrect convergence region showing that the methods correctly retrieve the DSD profiles given simulated input profiles.

A brief overview was given of sensitivity and uncertainty analysis and how these methods can be used to quantify the variance in the output of a model given uncertain input factors (parameters). Both first-order and total-sensitivity indices were described and how they can be used to determine the relative importance of each input factor as part of the total unconditional output variance of a system model. The described sensitivity analysis method is implemented using variance decomposition techniques. Two methods of performing variance decomposition were described: the first was the Correlation Ratio which computes first-order sensitivity indices and can be computed using Monte Carlo methods with several types of factor sampling.

The second technique is the Method of Sobol' which more efficiently computes both first- and total-order sensitivity indices and uses a factor sampling method proposed by Sobol' called LPτ. The sensitivity indices calculated using both methods are normalized such that their values correspond to percentage contribution of the total output variance if the models are additive and serve as indicators of a factor's relative importance. If the model is not additive, then higher-order interactions are present and the sum of the first-order indices is less than one. This work implemented the method of Sobol' to perform variance decomposition and sensitivity analysis as it is computationally more efficient and provides more information than the correlation ratio. Sensitivity analysis methods using variance decomposition techniques (Method of Sobol' and Correlation Ratio) require probability density functions for each of the input factors than can be sampled and a system model than can be expressed in terms of each of the input factors. Uncertainty analysis is a natural benefit of sensitivity analysis as it describes the uncertainty in the model output without apportioning the uncertainty to any one input factor. The outputs of uncertainty analysis are descriptive statistics such as mean and standard deviation.

An overview of the Tropical Rainfall Monitoring Mission (TRMM) was given along with the necessary equations to construct a system model compliant with sensitivity and uncertainty analysis methods. Distributions for each of the input factors were derived and explained. The distributions for the input factors a and b in the $R = a\ Z^{b}$ relationship were derived from empirical disdrometer data and indicate that both the a and b coefficients could be reasonably described by uniform probability density functions. Both sensitivity and uncertainty analysis methods were executed on a TRMM-like system model and results were given for precipitation simulations over both ocean and land. These results showed that at low rainfall rates, the error in the a coefficient dominates the output variance. The second most important factor is the error in the coefficient b followed closely by the error in measured reflectivity, Z_m. At higher rain rates, where the TRMM-like model transitions to using a modified Hitschfeld-Bordan and $\Delta\sigma^{\circ}$ method to correct for attenuation, and the coefficients a and b are calculated using log

polynomials, the primary contributor to output variance is $\Delta\sigma^\circ$ followed by Z_m. Over ocean, the error in $\Delta\sigma^\circ$ is assumed to be 1-dB standard deviation while over land, the error in $\Delta\sigma^\circ$ is assumed to be 3-dB standard deviation. Note that when the error in $\Delta\sigma^\circ$ is increased, it contributes proportionately more to output variance and as such the error in Z_m contributes less. In all cases, the contribution from α was small or negligible, especially at low rain rates where little or no attenuation correction is performed. In the low-rain region, where little attenuation correction is needed, it obviously contributes little to output variance. In higher rain-rate regions, where attenuation correction becomes much more important, the error in both $\Delta\sigma^\circ$ and Z_m continue to dominate the output variance with the error in α contributing little to output variance (rain rate calculation).

In order to perform systems engineering analysis on a GPM dual-frequency algorithm, the GPM profile-optimization method was restated in an algorithm compatible with SA/UA methods. As such, it requires only two input factors, the measured reflectivity profiles for Z_{m1} and Z_{m2}. Probability density functions were assumed for the error in each reflectivity profile. Based on known DSD parameters and rainfall rates, measured reflectivity profiles were generated and error was added to each bin of each profile to create an array of reflectivity profiles with error. Trigger variables were used to map the LPτ-sampled random variables to the profiles with error. A block diagram of the method used to perform the sensitivity analysis for both TRMM and GPM algorithms is shown in Figure 9.1.

Professional software called SIMLAB [53] is used to generate the LPτ random variables in the *.sam file (sample file). An external GPM or TRMM model is executed which reads the *.sam file, processes the respective model and saves computed output data to a *.dat file (output data file) for subsequent processing by SIMLAB. SIMLAB then uses the method of Sobol' to perform variance decomposition and provide the sensitivity analysis indices. For the GPM profile-optimization-based retrieval algorithm, the sensitivity and uncertainty analyses (using

the variance decomposition technique) showed significant higher-order interaction at low rain rates, less than 5 mm/hr, and decreased higher-order interaction above that level.

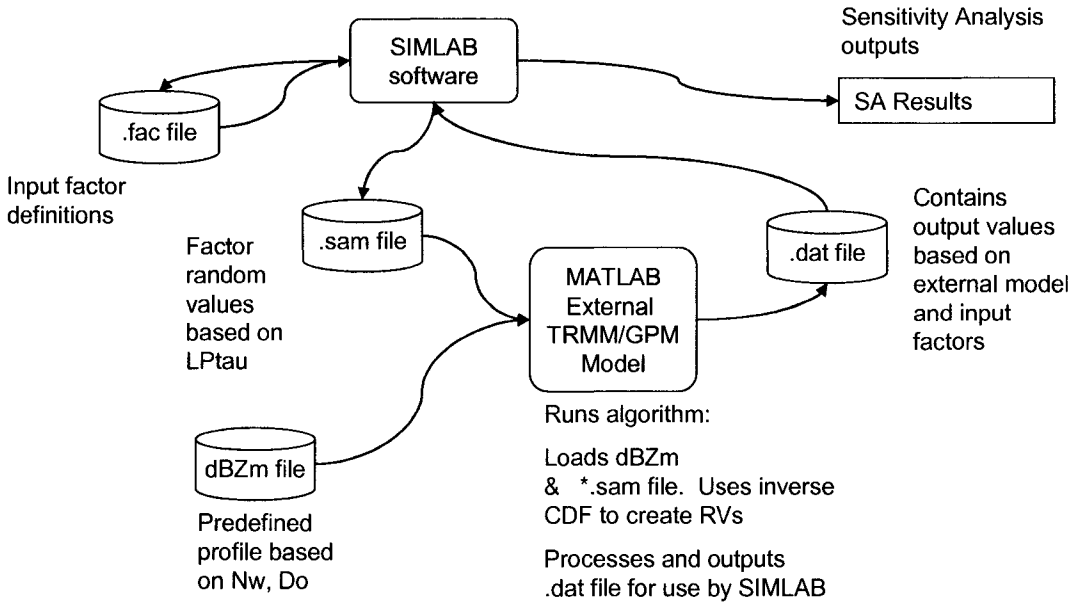

Figure 9.1. Block diagram of the procedure used to perform sensitivity and uncertainty analysis for both the TRMM and GPM algorithms. Professional software called SIMLAB is used to generate LPτ-sampled random variables in a *.sam file (sample file). An external program reads the *.sam file, executes the model, and when complete saves the output date to a *.dat file (output data file) for processing by SIMLAB.

In all parts of the tested rain-rate regime, from about 1 to 20 mm/hr, the error in Z_{m2} contributed the most to output variance. In fact, above about 5 mm/hr, the contribution from Z_{m1} was negligible. These results show that the error in Z_{m2} contributes the most to the error in the output of the retrieval algorithm and than significant accuracy improvement can be made in the algorithm by better measurement of Z_{m2}.

As a means to verify and corroborate this finding, i.e., that Z_{m2} is the greatest contributor to output variance in the tested dual-frequency retrieval algorithms, a preliminary version of the dual-frequency single-loop model was constructed and executed using variance decomposition techniques using the same factor distributions and simulated profiles as the profile-optimization method. Of the nine profiles tested with the profile-optimization method, only three profiles

(1.50, 3.94 and 8.95 mm/hr) were tested with the single-loop method because it is limited by the incorrect convergence region to about 10-14 mm/hr rainfall rate. These three profiles were viewed as representative of a region where both algorithms are expected to retrieve similar profiles and comparison would be valid between their respective sensitivity indices. The results from the single-loop sensitivity analysis showed that the error in Z_{m2} dominates the output variance confirming the results found with the profile-optimization algorithm. In addition, there is significant higher-order interaction between the two input factors, again confirming the results found from the profile-optimization method at rain rates below about 5 mm/hr.

In comparison with the TRMM-like algorithm, which showed that the error in the coefficients a and b at low rain rates dominated the output variance, and at higher rain rates, the error in $\Delta\sigma^{\circ}$ dominated the output error, the output error in the two tested GPM dual-frequency algorithms is dominated by the error in Z_{m2}. Based on the limited analysis described herein, and from a systems engineering analysis viewpoint, it appears that increasing the accuracy and reducing the error in Z_{m2} will provide the greatest benefit to overall system-retrieval accuracy.

9.2 FUTURE WORK

The following are suggestions for future work in this area of research:

- The simple one-region microphysical model used in this research for the single-loop, dual-loop and profile optimization methods should be improved to account for the melting layer and snow region above the melting layer.
- The dual-loop retrieval method should be extended to make it more fully automated in its retrieval process.
- Work that was begun using a two-variable profile-optimization method should be continued. This method uses the single-loop algorithm to determine the DSD points in the top bin. Those top DSD values are then used in the optimization method requiring the optimizer to only find the bottom two points resulting in a less computationally expensive DSD retrieval procedure.
- In the TRMM sensitivity analysis work, a study should be performed to determine an alternative, or more explicit representation of the errors in the a and b coefficients when the log polynomials are invoked.
- The sensitivity analysis of the TRMM-like algorithm should be extended to include the melting and snow regions.
- For GPM sensitivity analysis work, other models and methods should be studied including the single-loop method, the dual-loop method, and a dual-frequency method which uses the surface-reference technique.

BIBLIOGRAPHY

[1] Alexander Kossiakoff and William N. Sweet, *Systems Engineering: Principles and Practice*, John Wiley & Sons, Inc., 2003.

[2] Andrew P. Sage, *Systems Engineering*, John Wiley & Sons, Inc., 1992.

[3] GPM Science Reference, http://gpm.gsfc.nasa.gov/science.html

[4] W. J. Adams, et al., "Global Precipitation Measurement—Report 8," White Paper, NASA/TM—2002-211609.

[5] Global Precipitation Measurement (GPM) Systems Engineering Management Plan (SEMP), National Aeronautics and Space Administration (NASA), Feb. 1, 2002.

[6] Irene Bibyk, "Plans for Global Precipitation Measurement Ground Validation," NASA GPM Ground Validation 3rd GPM Workshop, Noordwijk, The Netherlands, June 25, 2003.

[7] V. Chandrasekar, H. Fukatsu, K. Mubarak, "Global Mapping of Attenuation at Ku- and Ka-Band," IEEE Trans. Geoscience and Remote Sensing, Vol. 41, No. 10, October 2003, pp. 2166-2176.

[8] Toshio Iguchi, Toshiaki Kozu, Robert Meneghini, Jun Awaka, Ken'ichi Okamoto, "Rain-Profiling Algorithm for the TRMM Precipitation Radar," Journal of Applied Meteorology, Vol. 39, December 2000, 2038-2052.

[9] R. Mardiana, T. Iguchi, N. Takahashi, H. Hanado, "Dual-Frequency Rain Profiling Method Without the Use of Surface Reference Technique." Geoscience and Remote Sensing Symposium, 2003, IGARSS '03, proceedings, Vol. 3, 21-25 July 2003.

[10] R. Meneghini, H. Kumagai, J. R. Wang, T. Iguchi, T. Kozu, " Microphysical Retrievals over Stratiform Rain Using Measurements from an Airborne Dual-Wavelength Radar-Radiometer," IEEE Trans. Geoscience and Remote Sensing, Vol. 35, No. 3, May 1997, pp. 487-506.

[11] L. Liao, Robert Meneghini, Toshio Iguchi, Andrew Detwiler, "Validation of Snow Parameters as Derived from Dual-Wavelength Airborne Radar." 31st Int'l Conference on Radar Meteorology, Seattle, Washington, August 6-12, 2003.

[12] R. Meneghini, L. Liao, T. Iguchi, "Integral Equations for a Dual-Wavelength Radar," Geoscience and Remote Sensing Symposium, IGARSS '02, Vol. 1, 24-28 June 2002.

[13] V. Chandrasekar, R. Meneghini, I. Zawadzki, "Global and Local Precipitation Measurements by Radar," Meteorological Monographs Series, Vol. 30, No. 52, August 2003, ISBN 1-878220-57-8.

[14] R. Mardiana, T. Iguchi, N. Takahashi, "A Dual-Frequency Rain Profiling Method Without the Use of a Surface Reference Technique," IEEE Trans. Geoscience and Remote Sensing, Vol. 42, No. 10, October 2004, 2214-2225.

[15] J. E. Testud, S. Oury, P. Amayenc, and R. A. Black, "The Concept of Normalized Distribution to Describe Raindrop Spectra: A Tool for Cloud Physics and Cloud Remote Sensing," *J. Appl. Meteor.*, vol. 40, Issue 6, 2001, pp. 1118-1140.

[16] V. N. Bringi, Taiwen Tang, and V. Chandrasekar, "Evaluation of a New Polarimetrically Based Z-R Relation," J. Atmospheric and Oceanic Technology, Vol. 21, April 2004, 612-623.

[17] L. Liao, R. Meneghini, "On Study of Air/Space-borne Dual-Wavelength Radar for Estimates of Rain Profiles," 3rd Int'l Ocean-Atmosphere Conference, Beijing, China, June 28-30, 2004.

[18] N. Takahashi, T. Iguchi, "DPR Overview/Requirements: System Requirements Review," presentation, June 4-5, 2002.

[19] V. N. Bringi, V. Chandrasekar, J. Hubbert, "Raindrop Size Distribution in Different Climatic Regimes from Disdrometer and Dual-Polarized Radar Analysis," *J. Atmos. Sci.*, Vol. 60, January 2003, 354-365.

[20] V. Chandrasekar, Basim Zafar, "Precipitation Type Determination From Spaceborne Radar Observations," *IEEE Trans. Geoscience and Remote Sensing*, Vol. 42, No. 10, October 2004, 2248-2253.

[21] C. R. Rose, V. Chandrasekar, "A Systems Approach to GPM Dual-Frequency Retrieval," *IEEE Trans. Geoscience and Remote Sensing*, Vol. 43, No.8, August 2005, 1816-1826.

[22] C. R. Rose, V. Chandrasekar, "System Engineering Approach to GPM Retrieval Algorithms", *2nd International TRMM Conference*, Nara, Japan, September 2004.

[23] V. Chandrasekar, K. Mubarak and S. Lim, "Estimation of Raindrop Size Distribution from TRMM Precipitation Radar Observations," *Geoscience and Remote Sensing Symposium*, 2003, IGARSS03, Vol. 3, 21-25 July 2003, pp. 1712-1714.

[24] X. Hu, R. Shonkwiler and M. Spruill, "Random Restart in Global Optimization," Georgia Tech School of Mathematics, 1997.

[25] Andrea Saltelli, Stefano Tarantola, Francesca Campolongo, Marco Ratto, *Sensitivity Analysis in Practice: A Guide to Assessing Scientific Models*, J. Wiley & Sons, 2004.

[26] Andrea Saltelli, Karen Chan, E. Marian Scott, *Sensitivity Analysis*, John Wiley & Sons, 2000.

[27] A. Saltelli, S. Tarantola, F. Campolongo, "Sensitivity Analysis as an Ingredient of Modeling," Statistical Science, 2000, Vol. 15, No. 4, 377-395.

[28] Richard C. Dorf, *Modern Control Systems*, 3rd Edition, Addison-Wesley Publishing Co., 1981.

[29] A. Saltelli, S. Tarantola, K. P-S. Chan, "A Quantitative Model-Independent Method for Global Sensitivity Analysis of Model Output," *Technometrics*, Vol. 41, No.1, Feb. 1999.

[30] Michael D. McKay, "Evaluating Prediction Uncertainty," NUREG/CR-6311, LA-12915-MS, 1997.

[31] Michael D. McKay, John D. Morrison, Stephen C. Upton, "Evaluating Prediction Uncertainty in Simulation Models," Los Alamos National Laboratory, LA-UR-98-1362, 1998.

[32] I. Sobol', "Sensitivity Analysis for Nonlinear Mathematical Models." *Math. Modelling Comput. Exp.* 1 (1993) 407-414.

[33] I. M. Sobol', "Global Sensitivity Indices for Nonlinear Mathematical Models and Their Monte Carlo Estimates," Mathematics and Computers in Simulation, Vol. 55, Issue 103, Feb. 2001.

[34] A. Saltelli, "Making Best Use of Model Evaluations to Compute Sensitivity Indices," Computer Physics Communications, Vol. 145, pp.280-297, 2002.

[35] R. I. Cukier, H. B. Levine, K. E. Shuler, "Nonlinear Sensitivity Analysis of Multiparameter Model Systems," *Journal of Computational Physics*, 26, 1-42, 1978.

[36] Andrea Saltelli, Ricardo Bolado, "An Alternative Way to Compute Fourier Amplitude Sensitivity Test (FAST)," *Computation Statistics & Data Anaysis.*, Vol. 26, 445-460, 1998.

[37] Michael D. McKay, "Latin Hypercube Sampling as a Tool in Uncertainty Analysis of Computer Models," Proceedings of the 1992 Winter Simulation Conference.

[38] Karen Chan, Andrea Saltelli, Stefano Tarantola, "Sensitivity Analysis of Model Output: Variance-Based Methods Make the Difference," Proceedings 1997 Winter Simulation Conference.

[39] Toshimitsu Homma and Andrea Saltelli, "Importance Measures in Global Sensitivity Analysis of Nonlinear Models," *Rel. Engr. and Sys. Safety*, Vo. 52, 1-17, 1996.

[40] Paul Bratley and Bennett L. Fox, "Algorithm 659: Implementing Sobol's Quasi-Random Sequence Generator," *Trans. Mathematical Software*, Vol. 14, No. 1, March 1988, 88-100.

[41] Tropical Rainfall Measuring Mission (TRMM), Overview and Project Summary. JAXA Website. http://www.jaxa.jp/missions/projects/sat/eos/trmm/index_e.html

[42] TRMM Science Data and Information System, Vol. 3, Release 5.03, National Space Development Agency of Japan (NASDA) and National Aeronautics and Space Administration (NASA), 2000.

[43] TRMM Satellite Validation Office, http://trmm-fc.gsfc.nasa.gov/trmm_gv.

[44] TSDIS TRMM official web site, http://tsdis02.nascom.nasa.gov, 2001.

[45] Description of the 2A25 algorithm. TRMM Data Products. *Data Products and Descriptions*. http://trmm.gsfc.nasa.gov/data_dir/ProductStatus.html

[46] R. Meneghini, T. Iguchi, T. Kozu, L. Liao, K. Okamoto, J. A. Jones, and J. Kwiatkowski, "Use of the Surface Reference Technique for Path Attenuation Estimates from the TRMM Precipitation Radar," *J. Appl. Meteor.*, 39, 2053-2070, 2000.

[47] T. Iguchi, R. Meneghini, "Intercomparison of Single-Frequency Methods for Retrieving a Vertical Rain Profile from Air-borne or Space Borne Radar Data," *J. Atmos. Oceanic Technol.*, Vol. 11, 1507-1516, 1994.

[48] C. Kummerow, et al., "The Status of the Tropical Rainfall Measuring Mission (TRMM) after Two Years in Orbit," *Journal of Applied Meteorology*, Vol. 39, No. 12, pp. 1965-1982, 2000.

[49] M. Saisana, A. Saltelli, and S. Tarantola, "Uncertainty and Sensitivity Analysis Techniques as Tools for the Quality Assessment of Composite Indicators," *Journal of the Royal Statistical Society A*, Vol. 168, Issue 2, pp 307, March 2005.

[50] Toshiaki Kozu and Toshio Iguchi, "Drop Size Distribution (DSD) Models for TRMM 2A25." Included in the TRMM PR User's Manual, 2000.

[51] John Kwiatkowski, Robert Meneghini and Ali Tokay, "On Incorporating Drop Size Measurements into the TRMM Satellite Radar Rain Retrieval Algorithm," TRMM International Science Conference, 22-26 July 2002, Honolulu, Hawaii 2P.12 p. 23.

[52] V. N. Bringi and V. Chandrasekar, *Polarimetric Doppler Weather Radar*, Cambridge University Press, 2001.

[53] Andrea Saltelli and Stefano Tarantola, *SIMLAB, Simulation Environment for Uncertainty and Sensitivity Analysis*, software v 2.2, http://www.jrc.cec.eu.int/uasa/prj-sa-soft.asp.